Novel quantum phenomena and excitation modes in type-I superconductors and magnetic vortices

Ricardo Zarzuela Fernández

ADVERTIMENT. La consulta d'aquesta tesi queda condicionada a l'acceptació de les següents condicions d'ús: La difusió d'aquesta tesi per mitjà del servei TDX (**www.tdx.cat**) i a través del Dipòsit Digital de la UB (**diposit.ub.edu**) ha estat autoritzada pels titulars dels drets de propietat intel·lectual únicament per a usos privats emmarcats en activitats d'investigació i docència. No s'autoritza la seva reproducció amb finalitats de lucre ni la seva difusió i posada a disposició des d'un lloc aliè al servei TDX ni al Dipòsit Digital de la UB. No s'autoritza la presentació del seu contingut en una finestra o marc aliè a TDX o al Dipòsit Digital de la UB (framing). Aquesta reserva de drets afecta tant al resum de presentació de la tesi com als seus continguts. En la utilització o cita de parts de la tesi és obligat indicar el nom de la persona autora.

ADVERTENCIA. La consulta de esta tesis queda condicionada a la aceptación de las siguientes condiciones de uso: La difusión de esta tesis por medio del servicio TDR (**www.tdx.cat**) y a través del Repositorio Digital de la UB (**diposit.ub.edu**) ha sido autorizada por los titulares de los derechos de propiedad intelectual únicamente para usos privados enmarcados en actividades de investigación y docencia. No se autoriza su reproducción con finalidades de lucro ni su difusión y puesta a disposición desde un sitio ajeno al servicio TDR o al Repositorio Digital de la UB. No se autoriza la presentación de su contenido en una ventana o marco ajeno a TDR o al Repositorio Digital de la UB (framing). Esta reserva de derechos afecta tanto al resumen de presentación de la tesis como a sus contenidos. En la utilización o cita de partes de la tesis es obligado indicar el nombre de la persona autora.

WARNING. On having consulted this thesis you're accepting the following use conditions: Spreading this thesis by the TDX (**www.tdx.cat**) service and by the UB Digital Repository (**diposit.ub.edu**) has been authorized by the titular of the intellectual property rights only for private uses placed in investigation and teaching activities. Reproduction with lucrative aims is not authorized nor its spreading and availability from a site foreign to the TDX service or to the UB Digital Repository. Introducing its content in a window or frame foreign to the TDX service or to the UB Digital Repository is not authorized (framing). Those rights affect to the presentation summary of the thesis as well as to its contents. In the using or citation of parts of the thesis it's obliged to indicate the name of the author.

Novel quantum phenomena and excitation modes in type-I superconductors and magnetic vortices

by

Ricardo Zarzuela Fernández

a dissertation presented to

The Departament de Física Fonamental of the Faculty of Physics

in partial fulfillment of the requirements
for the degree of Doctor per la UB
in the subject of Condensed Matter Physics
Programa de Doctorat de Física

Advisors: Prof. Javier Tejada Palacios and Prof. Eugene Chudnovsky
Tutor: Prof. Javier Tejada Palacios

Universitat de Barcelona

September 2014

Contents

Acknowledgements

Quiero aprovechar estas líneas para agradecer a todas aquellas personas que han contribuido directa o indirectamente a la consecución de esta tesis doctoral.

Considero necesario empezar la lista de agradecimientos por mis codirectores. Quiero agradecer al Dr. Javier Tejada Palacios la confianza depositada en mí cuando decidí volver al Grup de Magnetisme después de unos años dedicados a profundizar en el conocimiento de la geometría algebraica. También quiero agradecerle el hecho de proponerme que parte de mi tesis tuviera un contenido experimental, ya que esto me ha permitido aprender los entresijos y dificultades del mundo experimental además de reafirmarme en la opinión de que los modelos teóricos deben de servir para explicar resultados experimentales o, en su defecto, predecirlos. Por último, quiero darle las gracias al Dr. Tejada por las discusiones científicas, charlas, debates, etc. mantenidos a lo largo de estos años de doctorado. He aprendido mucho más de lo que él mismo puede llegar a imaginar.

Debo extender estos agradecimientos al Dr. Eugene Chudnovsky. Creo que no habría podido tener ni desear un mejor referente como físico teórico. Siempre han sido fascinantes nuestros encuentros y discusiones científicas y no puedo sino afirmar que a lo largo de estos años he intentado alcanzar ese grado de clarividencia científica que le permite describir cualquier fenómeno de la naturaleza mediante 'simples' modelos matemáticos. Gracias por insuflarme el espíritu de la escuela de Landau, además de por mostrarme la importancia que para un teórico tiene el conocimiento y la comprensión del mundo experimental, lo cuál muchas veces supone el éxito de un modelo o una teoría.

En segundo lugar, querría también darles las gracias a los Drs. Joan Manel Hernàndez Ferràs y Antoni García Santiago con los cuales he tenido el placer de investigar conjuntamente. Destaco no solo su valía científica y todo lo aprendido durante las discusiones que hemos mantenido a lo largo de estos años, sino también todos los grandes momentos vividos en congresos, celebraciones de grupo, extensas tandas de mediciones, etc. Vuestra actitud y la manera como nos acogísteis y nos habéis tratado a los doctorandos ha sido siempre ejemplar, y es uno de los motivos por los que existe tal comunión entre los miembros (presentes y pasados) de nuestro grupo. Quiero agradecerle especialmente a Toni la cuidadosa y precisa lectura de esta tesis, la cual me ha permitido mejorar notablemente la calidad de este manuscrito.

Es de recibo mostrarles mi agradecimiento a los que han sido mis compañeros en el Grup de Magnetisme a lo largo de estos años de aventura doctoral: Diego, Saül, Sergi, Cris, Víctor, Gianluca, Ferràn, Gerard, Carla, Antonio y Jesús. Nos hemos apoyado mútuamente, hemos vivido grandes momentos juntos, nos hemos divertido en el despacho y en laboratorio, y me llevo grandes recuerdos vuestros además de vuestra amistad. Creo que no podría haber encontrado mejores compañeros que vosotros. Quiero hacer dos menciones especiales: la primera es para Saül, al cual quiero agradecer el aprendizaje y la paciencia que tuvo conmigo en el laboratorio en mis inicios, además de las intensas discusiones científicas que hemos mantenido juntos. Aparte de considerarte un buen amigo, eres uno de aquellos colaboradores con los que más he disfrutado trabajando. La segunda mención es para Diego: te considero un gran amigo desde hace ya muchos años y para mi ha sido un verdadero placer compartir contigo despacho y trabajo. Han sido innumerables las risas, confidencias, discusiones científicas y charlas sobre lo divino y lo humano que hemos mantenido durante la tesis. Espero que sean muchas más en los próximos años y espero verte pronto defendiendo la tuya.

Deseo darles las gracias también a algunos de mis mejores amigos: Xavier, Alejandro, Guadaira, Estefanía, Ezequiel, Pau, Jorge, Mireia, Roger, Mercedes y Jordi. Os agradezco todo el apoyo recibido por vosotros y las vivencias que hemos compartido a lo largo de estos años. Compartir el proceso doctoral con alguno de vosotros, aún perteneciendo a disciplinas distintas, ha sido una experiencia que nunca olvidaré. Gracias a todos por haber estado siempre ahí cuando os he necesitado.

Deseo agradecer también a Israel, Daniel, David y Antonio su amistad y apoyo desde tiempos inmemoriales. Tengo la suerte de consideraros amigos míos casi desde que entré en la carrera, lo cual os agradezco. Finalmente seré un doctor más entre vosotros, hecho que me alegra inmensamente.

Me gustaría extender estos agradecimientos a Gemma, Carles, Xavier, Roger, Marina, Noelia, Albert, Lluís, etc. Gracias por todo lo que hemos vivido estos años, por vuestra amistad y por vuestro apoyo.

No puedo sino darle las gracias a Bernat por su amistad fraguada en el campo de las Matemáticas. Compartimos cursos de doctorado y estudiamos el Rotman juntos, algo de lo que uno no se olvida fácilmente. Gracias por el apoyo durante los años que ha durado esta tesis y espero verte defender en breve también.

Debo agradecer a Felipe, Sergio, Alejandro, Josep, Eduard, Berta, Anna, Alberto, Daniel, Gerard, Miquel P., Miquel T., Guaica, Ioana, Jone, Cristina y un sinfín más de personas que me han brindado su amistad y me han apoyado a lo largo de estos años de arduo y gratificante trabajo.

Por último, quiero agradecerles a mis padres todo lo que me han brindado en esta vida y que, en cierta manera, confluye en esta tesis. No os puedo agradecer lo suficiente el apoyo incondicional que siempre me habéis ofrecido y la confianza ciega depositada en cada uno de mis actos y de mis decisiones. Me habéis respaldado siempre sin pedir nada a cambio. Por todo ello, esta tesis es tanto vuestra como mía.

Preface

This thesis reports on the studies I have conducted during my doctoral years at the Grup de Magnetisme of the University of Barcelona. My research has focused primarily on the exploration of quantum dynamics and excitations modes at low temperatures in type-I superconductors and magnetic vortices, two well-known systems within condensed matter physics. The motivation for this topic of research is twofold. First, both Prof. Javier Tejada and Prof. Eugene Chudnovsky are pioneers in the observation and modeling of macroscopic quantum tunneling in mesoscopic magnetic systems. Their unique ability to foresee the existence of macroscopic quantum phenomena in the most unexpected physical systems has played a crucial role in showing that macroscopic quantum tunneling is of rather general character. Type-I superconductors and magnetic vortices are no exception to this. Second, some unanticipated experimental results made us refocus the final objectives of the doctoral research. In the case of type-I superconductivity, the study of the topological irreversibility in disks made of lead with defects by means of relaxation measurements led to the observation of a non thermal behavior of the magnetic viscosity at very low temperatures, which opened the exciting field of the quantum tunneling of normal-superconductor interfaces in type-I superconductors. We were suprised by the fact that no report on this quantum magnetization dynamics of lead –or any other type-I superconductor– in the intermediate state was found, even further if we take into account that the first studies of the intermediate state by L. Landau date back to 1938. In the case of magnetic vortices, for a flat disk geometry of the specimen the vortex state presents two well-defined polarizations of the vortex core with the same ground-state energy at zero applied transverse field. This bistability made the magnetic vortex a promising candidate to observe quantum tunneling of the polarization of the vortex core, but the corresponding energy barrier setting apart both equilibrium states was high enough to prevent the tunneling process to occur. On the other hand, low-temperature dynamics of the vortex state –excited by the application of in-plane magnetic fields– turned out to be very rich, especially with the discovery of the quantum diffusion of the magnetic vortex core from pinning potentials during the gyrotropic motion.

The manuscript is organized as follows: The first two chapters are devoted to the low-temperature dynamics of normal-superconductor interfaces in a type-I superconductor. Chapter 1 illustrates the study of the magnetic irreversibility in disk-shaped lead samples by means of hysteresis loops and relaxation measurements along the descending branch within the intermediate state. The dynamics of normal-superconductor interfaces were explored as a function of both the temperature and the magnetic field, which led to the experimental evidence of the phenomenon of quantum tunneling of these interfaces. In Chapter 2 a theoretical model of quantum tunneling of normal-superconductor interfaces pinned by planar defects is developed, which describes well the thermal dependence of the magnetic viscosity discussed in the previous chapter at zero field. According to this model, there would be the chance of a controlled measurement of quantum depinning of the interface in a type-I superconductor.

Chapters 3 and 4 are devoted to the study of the excitations modes and low-temperature dynamics of the vortex state. In Chapter 3, I discuss how the elastic nature of the vortex core line –ignored in the vast majority of the previous research– affects the excitation spectrum of magnetic vortices, which yields the introduction of a novel family of spin waves related specifically to the gyrotropic motion of the vortex. Effects of the magnetic field and dissipation have been considered. It is worth remarking that the predicted axial excitation modes have been confirmed experimentally earlier this year. Chapter 4 deals with the exploration of the magnetic irreversibility in flat disks with the vortex state at low temperatures by means of hysteresis loops, zero-field-cooled and field-cooled measurements, and relaxation measurements along the descending branch. This led to the experimental discovery of the quantum depinning of the vortex core line. A theoretical model describing this tunneling process is also developed in Chapter 4, from which estimates of the parameters of the pinning potential can be obtained by fitting the model to the experimental results.

In Chapter 5 superconductivity and magnetic vortices become intertwined. A device consisting of a ferromagnetic Josephson junction with the vortex state is proposed as a new tool to study the displacement of the vortex core in the nanometric scale –due to the quantum diffusion from a pinning well, for instance. I have calculated analytically the effect of the motion of the vortex core on the Josephson current. In Chapter 6 an outline of the conclusions of the thesis is presented and some perspectives of future work are proposed. The manuscript ends with two appendices, a list of all the publications resulting from my work during the doctoral years and a bibliography. In the appendices I have included a brief description of the mathematical techniques concerning the functional derivation and the Gaussian integration that are used in chapters 1–4.

I have attempted to write a self-contained thesis. Therefore, every chapter begins with an illustration of the state of the art in the corresponding field, both experimentally and theoretically, if required. Then the experimental protocols/measurements are introduced and/or the theoretical models are developed. Finally, discussion of the results is conducted. All derivations are either self-contained within the chapters or use results discussed in previous chapters or in the appendices. It is worth remarking that no ”Conclusions” section is present in the chapters. The underlying reason is my preference in a more fluid structure where the discussion and conclusions are intertwined. Furthermore, the first section of Chapter 6 is devoted to the general conclusions of the thesis, so that a ”Conclusions” section in every other chapter would be redundant. To conclude, all formulas appearing in the manuscript have been derived within the CGS unit system. In doing so, appealing formulas are obtained and the reader can focus on the intrinsic difficulties of the expression. On the contrary, explicit calculations and estimates are given in SI units. The reason is that, nowadays, the International System of units is commonly used worldwide by the scientific community. Finally, in Chapters 1 and 2 an explicit difference between the magnetic field strength H and the magnetic field –also known as magnetic induction– B is made due to their relevance in the physical properties of superconductors (Meissner effect, for instance). In the other chapters, the magnetic field strength will be referred to simply as magnetic field.

Ricardo Zarzuela Fernández,
September 2014

Resumen en castellano

Esta tesis recopila la amplia mayoría de los trabajos que he realizado durante mi doctorado en el Grup de Magnetisme de la Universidad de Barcelona. Mi proyecto de investigación doctoral se centró principalmente en la exploración de la dinámica cuántica y de los modos de excitación a bajas temperaturas en los superconductores tipo-I y en los vórtices magnéticos, dos sistemas físicos bien conocidos dentro de la física de la materia condensada. La elección de este tema de investigación viene motivada principalmente por el deseo de los doctores Javier Tejada Palacios y Eugene Chudnovsky de explorar la fenomenología cuántica macroscópica en la más amplia gama de sistemas físicos posibles. Entre esta fenomenología cabe destacar el efecto túnel macroscópico, de cuyo descubrimiento y predicción teórica en sistemas magnéticos son pioneros mis codirectores. El contenido de esta tesis se extiende a lo largo de los primeros cinco capítulos. Los dos primeros están dedicados al efecto túnel de interficies normal-superconductor (N-S) en superconductores tipo-I, tanto desde un punto de vista experimental (Capítulo 1) como teórico (Capítulo 2). Los siguientes dos capítulos están dedicados a los vórtices magnéticos, desarrollando el modelo teórico de excitaciones axiales asociado al movimiento girótropo del núcleo vorticial en el Capítulo 3 y estudiando experimental y teóricamente el efecto túnel del núcleo vorticial a través de barreras de anclaje en el Capítulo 4. Finalmente, en el Capítulo 5 se estudia teóricamente el efecto de la presencia del estado vórtice en la capa ferromagnética (F) de una unión Josephson de tipo S/F/S sobre la corriente Josephson. Especial atención se presta a la dependencia de esta corriente con el desplazamiento del núcleo vorticial a lo largo de la capa ferromagnética en forma de disco plano. Con este último capítulo se logra entrelazar los dos sistemas anteriores, desconexos a priori. A continuación, se contextualizará el trabajo brevemente y se expondrán de manera concisa tanto el estado del arte como los resultados más relevantes obtenidos en esta tesis para cada uno de los tres bloques recién comentados.

Efecto túnel de interficies normal-superconductor en superconductores tipo-I

La superconductividad ha demostrado ser uno de los campos más activos de la física de la materia condensada desde su descubrimiento en 1911, tanto por sus excepcionales propiedades físicas como por sus aplicaciones tecnológicas. Un superconductor perfecto se caracteriza por mostrar resistencia cero ante el flujo de corriente eléctrica y por comportarse como un diamagneto perfecto –expulsión completa de la inducción magnética dentro del espécimen– cuando su temperatura es inferior a una temperatura crítica T_c. La existencia de un gap de energía entre el estado fundamental y la banda de excitaciones (de cuasipartículas) representa la tercera característica asociada tradicionalmente a la superconductividad perfecta. El estado superconductor representa un verdadero estado termodinámico del sistema debido a su independencia de la historia magnética en el proceso de transición de la fase normal a la fase superconductora. Por otra parte, éste puede ser destruido mediante la aplicación de un campo magnético lo suficientemente intenso, cuyo valor mínimo se conoce como campo magnético crítico H_c. La dependencia térmica de este campo termodinámico determina el diagrama de fases de un superconductor perfecto.

Esta caracterización de la superconductividad perfecta es estrictamente válida para superconductores tipo-I puros – libres de defectos, impurezas, etc. Un superconductor tipo-I se define como todo aquel material superconductor cuya tensión superficial en las interficies normal-superconductor resulta ser positiva, lo que se traduce en una minimización del área total de estas interficies debido a que su formación es desfavorable energéticamente. Cuando la geometría del espécimen es tal que se producen efectos desmagnetizantes en la dirección del campo magnético externo, existe un rango de campos magnéticos $H_c' < H < H_c$ en el que la inducción magnética penetra gradualmente dentro del superconductor. Esta fase termodinámica se conoce como el estado intermedio y se caracteriza por una alternancia de zonas normales y zonas superconductoras dentro del espécimen, cuya estructura geométrica depende de su historia magnética y suele ser exótica.

El estado intermedio presenta una fuerte irreversibilidad magnética con dos contribuciones complementarias. La primera de ellas está asociada a la presencia de defectos en la muestra, de manera que el flujo magnético queda atrapado por la acción de centros de anclaje. La segunda contribución tiene un origen puramente geométrico y ocurre cuando el espécimen presenta una geometría planoparalela con las superficies transversales al campo magnético externo –e.g. un disco plano con el campo magnético aplicado a lo largo de su eje de rotación. El atrapamiento de flujo sucede por la existencia de lo que se conoce como barrera geométrica. La penetración de flujo magnético ocurre mediante una topología tubular cerrada mientras que una topología laminar bien definida es observada durante el correspondiente proceso de expulsión. Cabe destacar el hecho de que la histéresis magnética presente en muestras libres de estrés con estas geometrías es debida a la diferencia topológica entre la fase de flujo tubular (topológicamente cerrada) y la fase de flujo laminar (topológicamente abierta). Esta propiedad intrínseca del estado intermedio se conoce como irreversibilidad topológica.

La fase de flujo tubular representa la topología de equilibrio del estado intermedio. Uno de los objetivos de esta tesis consistió en estudiar la robustez de la metasestabilidad asociada al estado intermedio para discos planos de plomo (tipo-I) con defectos de estrés y la dinámica inherente al decaimiento de una estructura topológica metaestable hacia la correspondiente estructura de equilibrio. Para ello se realizaron experimentos de relajación magnética en un amplio rango de temperaturas y campos magnéticos, tomando como estado inicial las estructuras multidominio presentes a lo largo de la rama descendiente de los ciclos de histéresis. Se observó que la componente irreversible de la magnetización de estos sistemas evoluciona con el tiempo según una dependencia logarítmica, lo cual implica la existencia de una distribución amplia de barreras de energía asociadas a los defectos presentes en los discos. La viscosidad magnética muestra dos régimenes bien diferenciados para un campo magnético dado, los cuales se corresponden con las dinámicas cuántica y térmica de la magnetización de la estructura multidominio. La temperatura de transición entre ambos régimenes muestra una dependencia decreciente con el incremento del campo magnético aplicado. Esta dinámica magnética se atribuye al movimiento de interficies normal-superconductor a través del paisaje de pozos de potencial asociados a la presencia de defectos, los cuales tienden a ralentizar (bloquear) este movimiento.

Otro de los objetivos de esta tesis fue la modelización teórica de esta dinámica y, en particular, del efecto túnel de las interficies normal-superconductor a través de las barreras de anclaje. El modelo desarrollado trata la interficie normal-superconductor como una variedad 2D elástica sometida a la atracción de un potencial de pinning creado por un defecto planar. La barrera de anclaje puede ser controlada mediante la inyección de una supercorriente que ejerce una fuerza de tipo Lorentz sobre la interficie. El modelo se construye asumiendo la ausencia de campo magnético aplicado. El ritmo de relajación a cualquier temperatura se calcula mediante el método del instantón/termón dentro del marco de la teoría de Caldeira-Leggett y la correspondiente dinámica euclídea de la interficie normal-superconductor en un superconductor tipo-I resulta ser enteramente disipativa. La temperatura de transición puede ser descrita en función de los parámetros microscópicos del superconductor a partir de la teoría de Landau sobre las transiciones de fase. La difusión cuántica de la interficie normal-superconductor a través del pozo de potencial ocurre mediante la nucleación de una protuberancia en la interficie. Por último, la anchura promedio del pozo de potencial resulta ser de unos pocos nanómetros.

Modos de excitación axial en el estado vórtice y efecto túnel del núcleo vorticial a través de barreras de anclaje

Los avances en litografía óptica y de haz de electrones producidos en los últimos 10—20 años permiten hoy en día la fabricación de (matrices compuestas de) estructuras magnéticas de tamaño (sub)micrométrico con propiedades magnéticas bien definidas y controladas. Entre éstas cabe destacar los discos planos de tamaño mesoscópico fabricados a partir de un material ferromagnético, debido a sus inusuales propiedades magnéticas y sus potenciales aplicaciones tanto tecnológicas como biomédicas. Estos discos magnéticos muestran una amplia gama de configuraciones de equilibrio debido a las restricciones geométricas impuestas sobre su campo de espines. La mayoría de las aplicaciones de estos sistemas se basa en las propiedades estáticas y dinámicas del estado fundamental conocido como *estado vórtice*, el cuál se caracteriza por presentar un campo de magnetización cuya circulación es no nula en el plano del disco y por la existencia del núcleo vorticial —una pequeña área del plano del disco en la que los espines de la estructura magnética presentan una componente no nula en la dirección transversal al mismo. Formalmente hablando, este estado fundamental consiste en un solitón topológico ajustado a la forma del disco. El tamaño de este núcleo es del orden de la longitud de intercambio del material ferromagnético y muestra una débil dependencia con la anchura del disco.

La dinámica del estado vórtice en el régimen de bajas frecuencias se caracteriza por el movimiento espiral como un todo del núcleo vorticial. Esta excitación, conocida como el modo girótropo del vórtice, es equivalente a la precesión uniforme del momento magnético del disco debido al vórtice y puede ser inducida mediante la aplicación de un campo magnético en el plano del disco. Este modo de excitación es intrínsecamente distinto de las excitaciones magnónicas convencionales en ferromagnetos y presenta la menor de las energías dentro del espectro de excitaciones del estado vórtice. Además, cabe remarcar el hecho de que el modo girótropo influye en la estructura del espectro de magnones del vórtice magnético. La presencia de defectos estructurales en estos discos magnéticos puede afectar tanto a la dinámica como a la magnetización del estado vórtice: La detección cuantitativa del efecto Barkhausen y la observación de fluctuaciones en la frecuencia del movimiento girótropo del núcleo vorticial, las cuales están correlacionadas con la distribución espacial de defectos, ejemplifican este fenómeno. La temperatura también juega un papel relevante en las propiedades del estado vórtice puesto que no solamente las magnitudes físicas que lo caracterizan dependen explícitamente de ella, si no que al decrecer la temperatura el atrapamiento del núcleo vorticial por parte de los pozos de potencial asociados a los defectos será más efectivo al disponer el sistema de menor agitación térmica.

Debido a cuán fuerte es la interacción de intercambio entre los espines que constituyen el núcleo vorticial, éste se comporta como una entidad per se de tamaño mesoscópico. La rigidez del núcleo vorticial a lo largo del eje de simetría del disco ha sido una hipótesis inherente a la mayoría de modelos teóricos sobre excitaciones magnónicas del estado vórtice en discos magnéticos. El hecho de que la presencia de centros de anclaje afecte la dinámica girótropa del vórtice contradice dicha hipótesis. Por el contrario, esto es indicativo de la naturaleza elástica del núcleo vorticial en la dirección axial del disco. Con respecto al estado vórtice, el primer objetivo de esta tesis fue estudiar bajo qué condiciones el modo girótropo era compatible con una dispersión espacial semejante a las ondas de espín de longitud de onda finita presentes en un ferromagneto. Una extensión de la ecuación de Thiele ha sido obtenida mediante el formalismo Lagrangiano, la cual se caracteriza por 1) presentar una elasticidad finita cuyo origen es la interacción de intercambio, y 2) presentar una masa efectiva no nula asociada al núcleo vorticial, cuyo origen radica en las interacciones dipolares de largo alcance. El correspondiente espectro de excitaciones axiales presenta dos ramas bien definidas, una asociada al modo girótropo cuyo gap es precisamente la frecuencia girótropa del disco, y la otra originada por la masa efectiva. Este espectro también se puede derivar dentro del marco de la mecánica cuántica, obteniendo una discretización explícita del vector de onda. El efecto del campo magnético sobre el espectro de excitaciones también ha sido estudiado, demostrando que tan solo la componente transversal afecta a los modos axiales. La disipación es tenida en cuenta en este modelo mediante la adición de un término disipativo –lineal con la velocidad del núcleo vorticial– a la ecuación de Thiele elástica. Cabe destacar que los modos de excitación aquí presentados han sido observados experimentalmente por primera vez este mismo año.

El segundo de los objetivos en este bloque fue explorar la irreversibilidad magnética en discos con el estado vórtice y su dinámica a bajas temperaturas, lo cual se llevó a cabo mediante medidas de 1) ciclos de histéresis en un amplio rango de temperaturas, 2) curvas de magnetización *zero-field-cooled* y *field-cooled* a diferentes campos y, por último, 3) relajaciones magnéticas a bajas temperaturas tomando los estados vórtice presentes a lo largo de la rama descendiente de los ciclos de histéresis como estado inicial, en matrices de discos magnéticos hechos de permalloy. El campo magnético se aplicaba por defecto en el plano de los discos. Como resultado de este estudio se observó que la curva de magnetización *field-cooled* representa el equilibrio magnético del sistema. Además, la evolución temporal de la componente irreversible de la magnetización de estos sistemas sigue una dependencia logarítmica, lo cual implica de nuevo la existencia de una distribución amplia de barreras de energía asociadas a los defectos presentes en los discos. El análisis de la viscosidad magnética asociada a estos procesos de relajación permite distinguir de nuevo una transición entre los régimenes de dinámica térmica y de difusión cuántica. El comportamiento no térmico a bajas temperaturas se atribuye al efecto túnel de un segmento del núcleo vorticial a través de las barreras de anclaje durante el proceso de relajación hacia su posición de equilibrio. Experimentalmente no se ha observado ninguna dependencia de la temperatura de transición con el grosor de los discos magnéticos –fijado su diámetro–, hecho que refuerza la hipótesis de que tan solo un segmento del núcleo vorticial es el que participa en el proceso de túnel cuántico mediante una deformación elástica del mismo.

El último de los objetivos con respecto al estado vórtice fue modelizar este efecto túnel. Para ello el núcleo vorticial se describe como una variedad 1D elástica sometida a la atracción de un potencial de anclaje creado por un defecto lineal –el cual proporciona el atrapamiento más intenso para este tipo de estructuras. La validez del modelo se extiende a campos magnéticos externos que perturben ligeramente el estado vórtice. El ritmo de relajación a cualquier temperatura se calcula de nuevo mediante el método del instantón/termón dentro del marco de la teoría de Caldeira-Leggett y la dependencia funcional de la temperatura de transición con el campo puede ser derivada a partir de la teoría de Landau sobre las transiciones de fase. La dinámica euclídea del núcleo vorticial resulta ser disipativa. La amplitud de la deformación durante el proceso de túnel es de décimas de nanómetros, compatible con la anchura del correspondiente pozo de potencial.

Unión Josephson con el estado vórtice

Una unión Josephson consiste en dos regiones superconductoras separadas por una capa de un material no superconductor, a través de la cual se acoplan débilmente. Este dispositivo –pieza básica en el diseño de circuitos y dispositivos de alta sensibilidad– muestra el que se conoce como efecto Josephson, consistente en el flujo de supercorriente a través de la unión aun en el caso de no aplicar una diferencia de potencial entre las dos regiones superconductoras. Este efecto tiene su origen en el efecto túnel de pares de Cooper a través de la capa no superconductora. En esta tesis se planteó estudiar cuál sería el efecto sobre la corriente Josephson si como capa no superconductora se escogiera un disco magnético con el estado vórtice –las dos regiones superconductoras están compuestas por el mismo material. Se ha calculado analíticamente la dependencia de la corriente Josephson con la posición del núcleo vorticial en el plano del disco para desplazamientos pequeños y se ha observado en las pertinentes simulaciones que la variación relativa de esta corriente inducida por desplazamientos hasta la décima de la longitud de intercambio del material ferromagnético es detectable experimentalmente. Por lo tanto, la unión Josephson podría utilizarse para medir el movimiento del núcleo vorticial a escala atómica.

Chapter 1

Superconductivity

1.1 Introduction

Superconductivity was discovered by Kamerlingh Onnes in 1911 in the course of his studies of the electrical conductivity of pure metals at low temperatures [1]. This state of matter consists of the fermionic condensation of electrons in a solid: Below a certain critical temperature, near the Fermi surface pairs of electrons of opposite spin form a bound state called the Cooper pair. The net attraction between the (normally repulsive) electrons is provided by an interaction through the lattice. Cooper pairs themselves form a condensate due to their boson-like behavior. Therefore, superconductivity is a macroscopic quantum state characterized by the existence of a non-zero collective wavefunction of the condensed Cooper pairs.

Three features have been traditionally considered to be the hallmarks of perfect superconductors. Perfect conductivity is the first one: Below a critical temperature T_c, the superconducting material has zero electrical resistance (see Fig. 1.1a). The complete disappearance of resistance is most sensitively probed by observing the persistence of supercurrents circulating in a superconducting ring. These supercurrents have been observed to flow without measurable decrease for years.

The second hallmark, discovered by W. Meissner and R. Ochsenfeld in 1933, is the perfect diamagnetism of superconductors (see Fig. 1.1b), that is, magnetic flux is expelled from a superconducting material below T_c [2]. Meissner effect leads to the definition of a true equilibrium thermodynamic state associated with superconductivity, because of its independence on the magnetic history of the specimen. As a consequence, the superconducting transition is indeed a phase transition. Figure 1.2 shows the phase diagram of the normal-superconductor (N-S) transition in the phase space (T, H). For each temperature $T < T_c$ there exists a thermodynamic critical magnetic field $H_c(T)$ at which superconductivity is destroyed. This critical field is related to the difference in the Helmholtz free

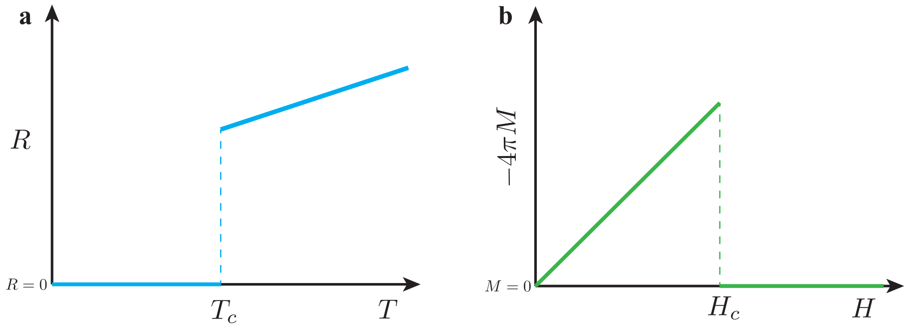

Figure 1.1: Sketch of (a) the resistance vs. temperature and of (b) the first magnetization curve of a perfect superconductor.

energy density (at zero field) between the normal and the superconducting state according to the identity

$$\frac{1}{8\pi}H_c^2(T) = \mathcal{F}_n(T,0) - \mathcal{F}_s(T,0), \tag{1.1}$$

where $H_c^2(T)/8\pi$ is referred to as the condensation energy of the superconducting state and the subscript $n(s)$ refers to the normal(superconducting) state.

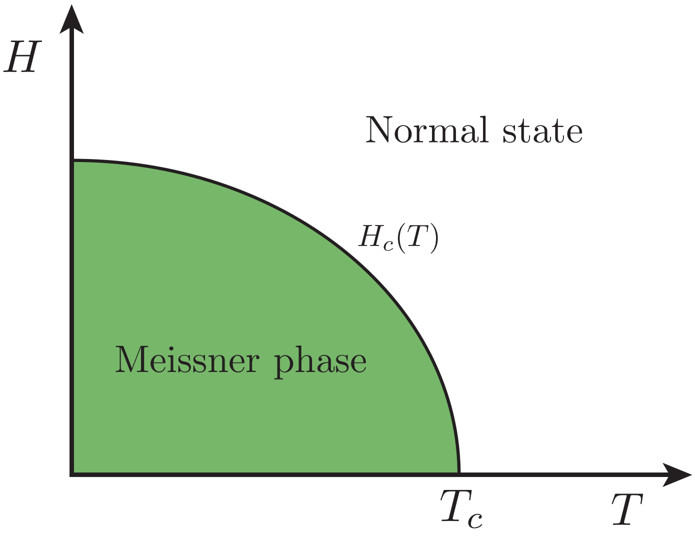

Figure 1.2: Schematic phase diagram (T, H) of a perfect superconductor.

The last hallmark of perfect superconductivity is the existence of an energy gap between the ground state and the band of quasiparticle excitations. An indirect observation of this energy gap in superconductors comes from heat capacity measurements: A discontinuous increase in the specific heat at zero field is observed through the N-S phase transition from the normal state. Furthermore, the specific heat is supressed rapidly below T_c, showing an exponential decay at low temperatures. This phenomenon is depicted in Fig. 1.3. The discontinuity in the specific heat at the critical temperature is a signature of the second order nature of the N-S phase transition. Microscopic theory predicts that the heat capacity approaches zero asymptotically as $C \sim e^{-\Delta(0)/k_{\rm B}T}$ due to the presence of the gap in the energy spectrum, where $\Delta(0)$ is the value of such gap at zero temperature.

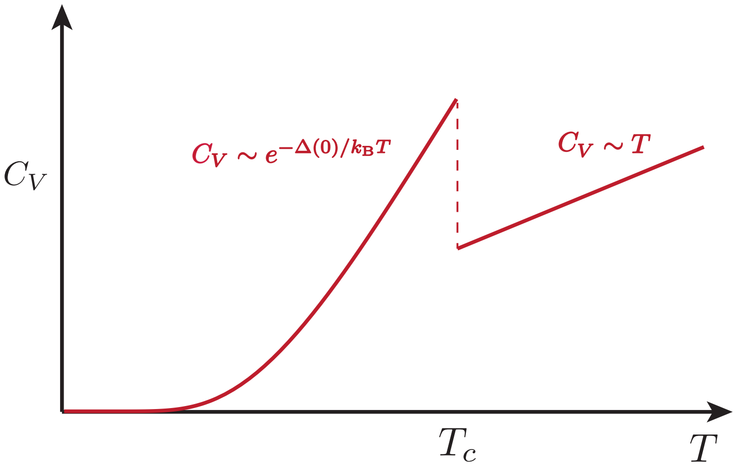

Figure 1.3: Sketch of the thermal dependence of the specific heat at zero field for a perfect superconductor.

1.2 Ginzburg-Landau theory

The first theoretical framework capable of describing the experimental (electrodynamic) features of superconductivity and predicting new ones was developed by V.L. Ginzburg and L. Landau in 1950 [3]. The keystone of this theory of superconductivity is the concept of order parameter arising from the Landau theory of second-order phase transitions [4]. Ginzburg and Landau introduced a complex order parameter $\psi(\vec{r})$ associated with superconductivity, so that in the normal state (the ordered phase) its value equals zero, whereas $\psi(\vec{r})$ becomes non-zero when the system undegoes the N-S transition to the superconducting state (the disordered phase). The exact physical significance of this order parameter is unknown to the theory. A microscopic derivation of the Ginzburg-Landau equations [Eqs. (1.6) and (1.7)] based on Gor'kov many-body extension of the BCS theory [5] leads the order parameter to be identified with the thermal average $\langle\hat{\Psi}_\uparrow(\vec{r})\hat{\Psi}_\downarrow(\vec{r})\rangle$, where $\hat{\Psi}_\alpha(\vec{r})$ is the Fermi field operator that destroys an electron of spin α at the point $\vec{r}$. Therefore, the order parameter can be understood as being the amplitude probability of finding a Cooper pair at the point $\vec{r}$, so that superconductivity turns out to be a macroscopic quantum state characterized by the non-zero value of the collective wavefunction of the superconducting carriers.

1.2.1 Ginzburg-Landau functional

The Helmholtz free energy is assumed to be a real analytic function and to preserve the symmetry of the ordered phase. In the vicinity of the critical temperature T_c, where $\psi \simeq 0$, one can therefore expand the free energy as a Taylor series of the order parameter ψ. In the case of a homogenous superconductor in the absence of a magnetic field, this expansion becomes

$$F_s(T,0) = F_n(T,0) + \alpha(T)|\psi|^2 + \frac{1}{2}\beta|\psi|^4, \tag{1.2}$$

where $\alpha(T) = a(T - T_c)$ and a, β are positive constants. The positivity of β is required to insure thermodynamic stability of the ground state. This expansion must be generalized to describe situations where the superconducting state is inhomogenous, that is, where the order parameter varies in space, $\psi(\vec{r}) = \psi_0(\vec{r})e^{i\Phi(\vec{r})}$. In this case, the expansion (1.2) holds for the free energy density.

With account of the correspondence $\psi(\vec{r}) \leftrightarrow \langle\hat{\Psi}_\uparrow(\vec{r})\hat{\Psi}_\downarrow(\vec{r})\rangle$ from microscopic theory, the following self-correlation condition for the order parameter holds

$$\psi(\vec{r}) = \int \mathrm{d}^3\vec{r}'\mathcal{K}(\vec{r}-\vec{r}')\psi(\vec{r}'), \tag{1.3}$$

where the kernel of the integral operator stems from finite-range interactions. Near a second-order phase transition not only is the order parameter small, but also its spatial variation is slow. Thus the expansion $\psi(\vec{r}') \simeq \psi(\vec{r}) + \nabla\psi(\vec{r})\cdot\vec{R} + \frac{1}{2}\vec{R}\cdot\left(\frac{\partial^2\psi}{\partial\vec{r}\partial\vec{r}}(\vec{r})\right)\cdot\vec{R}$ holds, where $\vec{R} = \vec{r}'-\vec{r}$, and the self-correlation condition becomes

$$\begin{aligned}\psi(\vec{r}) &\simeq \left[\int \mathrm{d}^3\vec{R}\;\mathcal{K}(\vec{R})\right]\psi(\vec{r}) + \frac{1}{2}\left[\frac{1}{3}\int \mathrm{d}^3\vec{R}\;R^2\mathcal{K}(\vec{R})\right]\nabla^2\psi(\vec{r}) \\ &\simeq \tilde{\mu}_0\psi(\vec{r}) + \frac{1}{6}\tilde{\mu}_2\nabla^2\psi(\vec{r}),\end{aligned} \tag{1.4}$$

where $\tilde{\mu}_i$ is the i-th moment of the kernel. The contribution of these nonlocal corrections to the free energy density is given by the terms $\tilde{\mu}_0|\psi(\vec{r})|^2$ and $\frac{1}{6}\tilde{\mu}_2|\nabla\psi(\vec{r})|^2$, respectively. The former can be absorbed into the α term of Eq. (1.2). Normalization of the coefficients in the free energy is chosen so that the prefactor of $|\nabla\psi|^2$ becomes $\hbar^2/2m^\star$, with $m^\star$ being an effective mass. In so doing, the gradient term mimics the quantum mechanical kinetic energy and therefore it should be regarded as the kinetic energy contribution of the superconducting carriers to the free energy.

In the presence of a magnetic field, described by a vector potential $\vec{A}$, the expansion of the free energy density is generalized by adding the magnetic pressure term, $\mathcal{F}_H(\vec{r}) = \frac{1}{8\pi}\vec{B}^2(\vec{r})$, and by applying the minimal coupling $\nabla \to \nabla - \frac{ie^\star}{\hbar c}\vec{A}$ to the kinetic energy term, with $e^\star$ being an effective charge. Finally, the Ginzburg-Landau free energy functional becomes

$$\begin{aligned} F_s[T,\psi,\vec{A}] =& F_n(T,0) + \int_V \mathrm{d}^3\vec{r} \Bigg\{ \alpha(T)|\psi(\vec{r})|^2 + \frac{1}{2}\beta|\psi(\vec{r})|^4 + \frac{1}{8\pi}\vec{B}^2(\vec{r}) \\ & + \frac{\hbar^2}{2m^\star}\left|\left[\nabla - \frac{ie^\star}{\hbar c}\vec{A}(\vec{r})\right]\psi(\vec{r})\right|^2 \Bigg\}. \end{aligned} \tag{1.5}$$

Minimization of the free energy functional with respect to $\bar{\psi}(\vec{r})$ and $\vec{A}(\vec{r})$ [see Appendix A] yields the Ginzburg-Landau equations

$$-\frac{\hbar^2}{2m^\star}\left[\nabla - \frac{ie^\star}{\hbar c}\vec{A}(\vec{r})\right]^2 \psi(\vec{r}) + \alpha(T)\psi(\vec{r}) + \beta|\psi(\vec{r})|^2\psi(\vec{r}) = 0, \tag{1.6}$$

and

$$\nabla \times \vec{B}(\vec{r}) = \frac{4\pi}{c}\vec{j}(\vec{r}), \qquad \text{(Ampère's law)} \tag{1.7}$$

where

$$\begin{aligned} \vec{j}(\vec{r}) &= \frac{e^\star}{m^\star}\mathrm{Re}\left\{\bar{\psi}(\vec{r})\left[-i\hbar\nabla - \frac{e^\star}{c}\vec{A}(\vec{r})\right]\psi(\vec{r})\right\} \\ &= i\frac{\hbar e^\star}{2m^\star}\left[\psi(\vec{r})\nabla\bar{\psi}(\vec{r}) - \bar{\psi}(\vec{r})\nabla\psi(\vec{r})\right] - \frac{e^{\star 2}}{m^\star c}|\psi(\vec{r})|^2\vec{A}(\vec{r}), \end{aligned} \tag{1.8}$$

represents the supercurrent density. Cooper pairs are the superconducting carriers according to the microscopic theory, which implies $m^\star = 2m_e$ and $e^\star = -2e$ for the values of the effective mass and charge respectively.

A natural boundary condition on ψ arises from the surface term in the minimization process of the Ginzburg-Landau functional with respect to $\bar{\psi}$. It ensures that no supercurrent flows through the boundary surface ∂V and is given by

$$\left[\nabla - \frac{ie^\star}{\hbar c}\vec{A}(\vec{r})\right]\psi \cdot \hat{n} = 0 \quad \text{on } \partial V, \tag{1.9}$$

where $\hat{n}$ denotes the normal vector to the boundary surface. This boundary condition is only correct for an insulator-superconductor (I-S) interface according to the microscopic theory [6]. A more general boundary condition is required for a S-N metal interface, where proximity effects occur. It is given by [6]

$$\left[\nabla - \frac{ie^\star}{\hbar c}\vec{A}(\vec{r})\right]\psi\cdot\hat{n} = -\gamma\psi \quad \text{on } \partial V, \tag{1.10}$$

where γ is a real-valued constant. This boundary condition also implies $\vec{j}\cdot\vec{n} = 0$ on the boundary surface.

Thermodynamic fluctuations are neglected by the Ginzburg-Landau theory due to its mean-field nature. The occurrence of fluctuations in phase transitions is a universal phenomenon and their effects become important for some interval of temperatures near the critical one. According to the Ginzburg criterion [3], when fluctuations of the order parameter are of the same magnitude as the order parameter itself the Ginzburg-Landau theory breaks down. This happens in the temperature interval

$$\frac{|T-T_c|}{T_c} \sim \begin{cases} 10^{-16} & \text{(clean superconductor)} \\ 10^{-6} & \text{(dirty superconductor)} \end{cases} \tag{1.11}$$

for typical 3D superconductors, so that it is not possible to observe fluctuations in this case. For this reason the Ginzburg-Landau theory has been so successful in describing superconductivity and the corresponding phase transition. On the other hand, fluctuation effects are larger for lower dimensionality, so that it is possible to observe the breakdown of the Ginzburg-Landau theory in one and two dimensions.

1.2.2 Gauge invariance and characteristic lengths

The Ginzburg-Landau free energy functional (1.5) preserves global $U(1)$ symmetry by construction, which is the underlying symmetry of the ordered phase. In the absence of a magnetic field it becomes

$$F_s[T,\psi] = F_n(T,0) + \int_V \mathrm{d}^3\vec{r}\left\{\alpha(T)|\psi(\vec{r})|^2 + \frac{1}{2}\beta|\psi(\vec{r})|^4 + \frac{\hbar^2}{2m^\star}\left|\nabla\psi(\vec{r})\right|^2\right\}. \tag{1.12}$$

The value of the field ψ in the ground state is obtained via minimization of the above functional, which requires homogeneity of the order parameter (the contribution of the gradient term to the free energy is always positive) and minimization of the potential term. The corresponding values are

$$\begin{aligned} |\psi| &= 0 & T > T_c, \\ |\psi| &= \left[\tfrac{|\alpha(T)|}{\beta}\right]^{1/2} & T < T_c. \end{aligned} \tag{1.13}$$

The high temperature phase shows a unique ground state at $\psi = 0$, sharing the $U(1)$ symmetry of the free energy. On the contrary, the ground state of the disordered phase is degenerate and the vacuum states are asymmetric under $U(1)$: The orientations in the complex plane define the vacuum states. Application of a $U(1)$ transformation to any of the vacuum states will lead to a different orientation describing a different vacuum state.

Lowering the temperature below T_c leads the ground state $\psi = 0$ to become unstable, and thus the field ψ to condensate into one of the vacuum states ψ_0. This spontaneous choice of ground state (among the set of equally likely vacuum states) is known as *spontaneous breaking* of the global $U(1)$ symmetry. Goldstone theorem provides the appearance of one massless scalar particle (the Nambu-Goldstone boson) in the spectrum of excitations due to symmetry breaking.

Another feature of the Ginzburg-Landau theory is its preservation of the $U(1)$ gauge symmetry: The free energy functional (1.5) is invariant under the gauge transformations

$$\vec{A}(\vec{r}) \rightarrow \vec{A}(\vec{r}) + \nabla\chi(\vec{r}) \tag{1.14}$$

$$\psi(\vec{r}) \rightarrow \psi(\vec{r}) e^{i\frac{e^\star}{\hbar c}\chi(\vec{r})} \tag{1.15}$$

of the order parameter $\psi(\vec{r})$ (Higgs field) and of the gauge field $\vec{A}(\vec{r})$. A deep insight into the physical content of the Ginzburg-Landau theory can be gained by expanding the order parameter perturbatively around the ground state. For $T < T_c$ this expansion takes the form

$$\psi(\vec{r}) = [\psi_0 + \eta(\vec{r})]\, e^{i\theta(\vec{r})}, \tag{1.16}$$

where $\eta(\vec{r})$ and $\theta(\vec{r})$ are two real scalar fields that parametrize the perturbation of the Higgs field. The vacuum state $\psi_0 = [|\alpha(T)|/\beta]^{1/2}$ is chosen to be real. Introduction of Eq. (1.16) into the Ginzburg-Landau functional leads to the following expansion:

$$\begin{aligned} F_s[T,\psi,\vec{A}] \simeq F_s[T,\psi_0,\vec{0}] + \int_V \mathrm{d}^3\vec{r} \Bigg\{ & 2|\alpha(T)|\eta^2 + \frac{\hbar^2}{2m^\star}|\nabla\eta|^2 + 2\sqrt{|\alpha(T)|\beta}\eta^3 \\ & + \frac{1}{2}\beta\eta^4 + \frac{\hbar^2}{2m^\star}(\psi_0+\eta)^2 \left|\nabla\theta - \frac{e^\star}{\hbar c}\vec{A}\right|^2 + \frac{1}{8\pi}|\nabla\times\vec{A}|^2 \Bigg\}. \end{aligned} \tag{1.17}$$

Cubic and quartic terms in the above expansion can be neglected due to η being a perturbation of the modulus of the order parameter. For this same reason $\psi_0 + \eta \simeq \psi_0$ also holds. The gauge transformation

$$\vec{A}(\vec{r}) \rightarrow \vec{A}(\vec{r}) - \frac{\hbar c}{e^\star}\nabla\theta(\vec{r}) \tag{1.18}$$

$$\psi(\vec{r}) \rightarrow \psi(\vec{r})e^{-i\theta(\vec{r})} = \psi_0 + \eta(\vec{r}) \tag{1.19}$$

removes the gauge symmetry from the free energy functional, which now becomes

$$F_s[T,\psi,\vec{A}] \simeq F_s[T,\psi_0,\vec{0}] + \int_V \mathrm{d}^3\vec{r} \left\{ 2|\alpha(T)|\eta^2 + \frac{\hbar^2}{2m^\star}|\nabla\eta|^2 + \frac{e^{\star 2}\psi_0^2}{2m^\star c^2}|\vec{A}|^2 \right. \\ \left. + \frac{1}{8\pi}|\nabla\times\vec{A}|^2 \right\}. \tag{1.20}$$

This expansion clearly shows that there is a massive gauge field and that the Higgs field has one massive component (presence of quadratic terms on the fields). Massification of the gauge field happens at the expense of the field θ (the Nambu-Goldstone field), which dissapears in the process of gauge fixing. This is the keystone of the Anderson-Higgs mechanism [7, 8].

Remarkably, some electrodynamic features of superconductivity emerge naturally from the dynamical generation of the mass of the fields in the Ginzburg-Landau theory: Minimization of the functional (1.20) with respect to the fields $\vec{A}$ and η yields the following set of differential equations

$$\nabla\times\nabla\times\vec{A} + \frac{1}{\lambda_{\mathrm{L}}^2}\vec{A} = 0, \tag{1.21}$$

$$\nabla^2\eta - \frac{1}{\xi_{\mathrm{GL}}^2}\eta = 0, \tag{1.22}$$

where $\lambda_{\mathrm{L}} = \left[\frac{m^\star c^2}{4\pi e^{\star 2}\psi_0^2}\right]^{1/2}$ is the *London penetration length* and $\xi_{\mathrm{GL}} = \left[\frac{\hbar^2}{4m^\star|\alpha|}\right]^{1/2}$ is the Ginzburg-Landau *coherence length*. Application of the curl operator on Eq. (1.21) leads to the differential equation

$$\nabla^2\vec{B} - \frac{1}{\lambda_{\mathrm{L}}^2}\vec{B} = 0, \tag{1.23}$$

where the second Maxwell equation $\nabla\cdot\vec{B} = 0$ has been taken into consideration. Both Eqs. (1.22) and (1.23) are time-independent Klein-Gordon equations, so that their respectives masses are $m_\eta c = \hbar/\xi_{\mathrm{GL}}$ for the perturbation of the modulus of the order parameter and $m_A c = \hbar/\lambda_{\mathrm{L}}$ for the gauge field. Under the assumption of an I-S interface along the YZ plane, the solutions of these differential equations are

$$\vec{B}_{\parallel}(x) = \vec{B}_{\parallel}(0)e^{-x/\lambda_{\mathrm{L}}}, \; B_x = 0 \quad \text{and} \quad \eta(x) = \eta(0)e^{-x/\xi_{\mathrm{GL}}}, \tag{1.24}$$

for a superconductor occupying the region $x > 0$. Therefore, the coherence length measures the spatial response of the superconductor to a perturbation (generated in this case by the interface). In other words, ξ_{GL} represents a measure of the distance over which self-correlation of the order parameter extends. Microscopic theory relates the coherence length to the characteristic size of the Cooper pairs, which means that the weak interaction coupling the electrons into the Cooper pair is short-ranged. On the other hand, λ_{L} represents the length scale over which a magnetic field (parallel to the superconductor surface) is able to penetrate into the superconductor. Consequently, the Meissner effect is nothing but the massification of the gauge field $\vec{A}$ through the onset of a finite condensate density.

The same perturbative expansion of the Ginzburg-Landau functional around the ground state can be performed for $T > T_c$ (normal phase), where the ground state is $\psi_0 = 0$. In this case, the quadratic expansion of the free energy on the pertubative fields yields a massless gauge field (the magnetic field is not screened from the interior of the material) and a natural length scale for the spatial variation of the field η, $\xi_{\mathrm{GL}} = \left[\frac{\hbar^2}{2m^\star\alpha}\right]^{1/2}$, which corresponds to the coherence length. This definition of ξ_{GL} differs by a prefactor from the former obtained in the superconducting case. From this point forward, the latter will be the standard definition of the coherence length.

1.2.3 Classification of superconductors

In the Ginzburg-Landau theory the divergence of both λ_{L} and ξ_{GL} near the critical temperature is characterized by the critical exponent $\nu = 1/2$, that is

$$\begin{aligned}\lambda_{\mathrm{L}}(T) &= \left(\frac{m^\star c^2\beta}{4\pi e^{\star 2} a T_c}\right)^{1/2}\left|1-\frac{T}{T_c}\right|^{-1/2}, \\ \xi_{\mathrm{GL}}(T) &= \left(\frac{\hbar^2}{2m^\star a T_c}\right)^{1/2}\left|1-\frac{T}{T_c}\right|^{-1/2}.\end{aligned} \tag{1.25}$$

The *Ginzburg-Landau parameter* is defined as the ratio

$$\kappa \equiv \frac{\lambda_{\mathrm{L}}}{\xi_{\mathrm{GL}}} = \frac{m^\star c}{e^\star \hbar}\left(\frac{\beta}{2\pi}\right)^{1/2}, \tag{1.26}$$

which is temperature independent. Its value plays a critical role in determining the thermodynamic stability of the system to the formation of domains with N-S interfaces, and hence in the classification of superconductivity.

The Gibbs free energy is an appropiate tool to study this thermodynamic stability: It is defined as the Legendre transform of the Helmholtz free energy of the system with respect to the magnetic field $\vec{B}$, $\mathcal{G} = \mathcal{F} - \vec{H}\cdot\vec{B}/4\pi$. Within the framework of the Ginzburg-Landau theory it becomes

$$\begin{aligned}\mathcal{G}(T,\psi,\vec{H}) =& \mathcal{F}_{\mathrm{n}}(T,0)+\alpha(T)|\psi(\vec{r})|^2+\frac{1}{2}\beta|\psi(\vec{r})|^4+\frac{1}{8\pi}\vec{B}^2(\vec{r})\\ &+\frac{\hbar^2}{2m^\star}\left|\left[\nabla-\frac{ie^\star}{\hbar c}\vec{A}(\vec{r})\right]\psi(\vec{r})\right|^2-\frac{1}{4\pi}\vec{H}\cdot\vec{B}(\vec{r})\end{aligned} \tag{1.27}$$

Assume a homogenous bulk superconductor in a magnetic field (strength) $\vec{H}$. In the superconducting state, which is characterized by a non-zero order parameter $\psi=\sqrt{|\alpha|/\beta}e^{i\theta}$ and $\vec{B}=0$, Eq. (1.27) takes the form

$$\mathcal{G}_{\mathrm{s}}=\mathcal{F}_{\mathrm{n}}+\alpha|\psi|^2+\frac{1}{2}\beta|\psi|^4=\mathcal{F}_{\mathrm{n}}-\frac{\alpha^2}{2\beta}, \tag{1.28}$$

where the London gauge $\vec{A}=\frac{\hbar c}{e^\star}\nabla\theta=0$ has been chosen. In the normal state ψ vanishes and $\vec{B}=\vec{H}$, so that the Gibbs free energy density becomes

$$\mathcal{G}_{\mathrm{n}}=\mathcal{F}_{\mathrm{n}}+\frac{\vec{B}^2}{8\pi}-\frac{\vec{H}\cdot\vec{B}}{4\pi}=\mathcal{F}_{\mathrm{n}}-\frac{\vec{H}^2}{8\pi}. \tag{1.29}$$

The system condenses into the superconducting state only if it minimizes the Gibbs free energy, that is, if the condition

$$\mathcal{G}_{\mathrm{s}}-\mathcal{G}_{\mathrm{n}}=\frac{\vec{H}^2}{8\pi}-\frac{\alpha^2}{2\beta}<0 \tag{1.30}$$

holds. Consequently, there is a critical magnetic field above which superconductivity cannot occur,

$$H_c(T)=\left[\frac{4\pi\alpha^2(T)}{\beta}\right]^{1/2}. \tag{1.31}$$

Consider a N-S interface along the YZ plane with the superconductor occupying the region $x>0$ and with the magnetic field strength applied along the Y axis (parallel to the phase boundary). Thus both the order parameter $\psi(\vec{r})$ and the magnetic field $\vec{B}(\vec{r})=B(\vec{r})\hat{e}_y$ depend only on the coordinate x. Far from the interface both normal and superconducting regions are homogeneous, which yields the following boundary conditions for the order parameter:

$$\lim_{x\to\infty}\psi(x)=\psi_0=[|\alpha|/\beta]^{1/2}, \quad \lim_{x\to-\infty}\psi(x)=0. \tag{1.32}$$

With regard to the magnetic field, the boundary condition $\lim_{x\to\infty}B(x)=0$ applies due to the Meissner effect. At the other boundary, condition $\lim_{x\to-\infty}B(x)=H_c$

is imposed to guarantee the stability of the interface: if $\lim\limits_{x\to-\infty} B(x) < H_c$, the inequality (1.30) holds and therefore the normal region condenses into the superconducting state (stable phase). For $\lim\limits_{x\to-\infty} B(x) > H_c$, penetration of the magnetic field into the superconducting region according to Eq. (1.24) implies that some material on the superconducting side close to the interface would be driven normal. This means that superconductivity would be unstable. In brief, the boundary conditions for the magnetic field are

$$\lim_{x\to\infty} B(x) = 0, \qquad \lim_{x\to-\infty} B(x) = H_c. \tag{1.33}$$

The surface tension σ of the N-S interface is defined as follows: the above boundary conditions yield the equality $\lim\limits_{x\to\infty} \mathcal{G}_{\mathrm{n}}(x) = \lim\limits_{x\to-\infty} \mathcal{G}_{\mathrm{s}}(x)$ between the normal and superconducting Gibbs free energy densities deep inside the corresponding regions. This in turn leads to the definition of a bulk Gibbs free energy density as $\mathcal{G}_{\mathrm{Bulk}} \equiv \lim\limits_{x\to\infty} \mathcal{G}_{\mathrm{n}}(x) = \mathcal{F}_{\mathrm{n}} - \frac{H_c^2}{8\pi}$. The presence of the N-S phase boundary results in an additional contribution to the Gibbs free energy density, which is just the difference $\mathcal{G} - \mathcal{G}_{\mathrm{Bulk}}$ with $\mathcal{G}$ being the total Gibbs free energy density of the sample. Hence the surface tension of the N-S interface becomes

$$\sigma\mathcal{A} = \int_V \mathrm{d}^3\vec{r}\,\{\mathcal{G} - \mathcal{G}_{\mathrm{Bulk}}\}\,, \tag{1.34}$$

where $\mathcal{A}$ is the interface area. Equivalently,

$$\begin{aligned}\sigma &= \int_{\mathbb{R}} \mathrm{d}x \Bigg\{ \frac{H_c^2}{8\pi} + \alpha(T)|\psi(x)|^2 + \frac{1}{2}\beta|\psi(x)|^4 + \frac{\hbar^2}{2m^\star}\left|\left[\nabla - \frac{ie^\star}{\hbar c}\vec{A}(x)\right]\psi(x)\right|^2 \\ &\qquad + \frac{B^2(x)}{8\pi} - \frac{H_c B(x)}{4\pi}\Bigg\} \\ &= \int_{\mathbb{R}} \mathrm{d}x \Bigg\{ \alpha(T)|\psi(x)|^2 + \frac{1}{2}\beta|\psi(x)|^4 + \frac{\hbar^2}{2m^\star}\left|\frac{d\psi(x)}{dx}\right|^2 + \frac{e^{\star 2}}{2m^\star c^2}A^2(x)|\psi(x)|^2 \\ &\qquad + \frac{(B(x) - H_c)^2}{8\pi}\Bigg\},\end{aligned} \tag{1.35}$$

where the gauge $\vec{A}(x) = A(x)\hat{e}_z$ $[B(x) = -dA(x)/dx]$ has been chosen. Multiplication of the first Ginzburg-Landau equation (1.6) by $\bar{\psi}$ and integration over x yields the identity

$$\int_{\mathbb{R}} \mathrm{d}x \left\{ \alpha(T)|\psi(x)|^2 + \beta|\psi(x)|^4 + \frac{\hbar^2}{2m^\star}\left|\frac{d\psi(x)}{dx}\right|^2 + \frac{e^{\star 2}}{2m^\star c^2}A^2(x)|\psi(x)|^2 \right\} = 0, \tag{1.36}$$

which leads to the following simplification of Eq. (1.35):

$$\sigma = \frac{H_c^2}{8\pi} \int_{\mathbb{R}} \mathrm{d}x \left\{ -\frac{|\psi(x)|^4}{\psi_0^4} + \left(\frac{B^2(x)}{H_c^2} - 1 \right)^2 \right\}. \tag{1.37}$$

The surface tension of the interface is the result of the difference between the energy gain due to the condensation into the superconducting state and the energy cost of expelling the magnetic field from the superconducting region. In the regime $\xi_{\mathrm{GL}} \gg \lambda_{\mathrm{L}}$ ($\kappa \ll 1$), there is a region of thickness $\xi_{\mathrm{GL}} - \lambda_{\mathrm{L}} > 0$ where the second term is already large but the first one is small due to the order parameter slowly approaching its bulk value (see Fig. 1.4a). Therefore $\sigma > 0$ in this regime. On the contrary, in the regime $\xi_{\mathrm{GL}} \ll \lambda_{\mathrm{L}}$ ($\kappa \gg 1$) there is a region of thickness $\lambda_{\mathrm{L}} - \xi_{\mathrm{GL}} > 0$ where the condensate is nearly fully developed and the magnetic field is not completely expelled (see Fig. 1.4b), so that the first term of Eq. (1.37) dominates and hence the surface tension is negative.

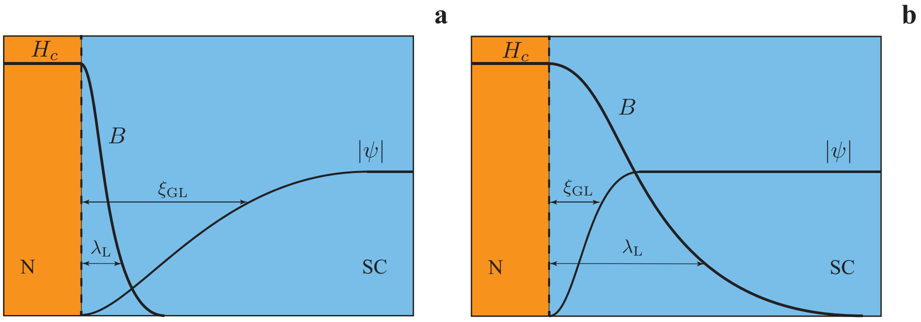

Figure 1.4: Schematic diagram of a N-S interface for $\kappa \ll 1$ [panel (a)] and for $\kappa \gg 1$ [panel (b)]. Decay of the magnetic field takes place on a scale λ_{L}, whereas the variation of the Cooper-pair condensate density occurs on a scale ξ_{GL}.

A deep insight into the dependence of the surface tension on the Ginzburg-Landau parameter requires the numerical solution of the Ginzburg-Landau equations (1.6) and (1.7) with the boundary conditions (1.30) and (1.33). Qualitatively, it has been shown that as κ increases the surface tension decreases from positive values to negative ones. A detailed analysis of this functional dependence shows that the critical value of the Ginzburg-Landau parameter at which σ vanishes is $\kappa_c = 1/\sqrt{2}$. Superconductors for which the surface tension of N-S interfaces is positive are called *type-I*, whereas *type-II* superconductors are those for which this surface tension is negative. This classification can be done in terms of the Ginzburg-Landau parameter according to the previous discussion, that is, $\kappa < 1/\sqrt{2}$ or $\kappa > 1/\sqrt{2}$ determines whether the superconductor is type-I or type-II respectively. The electrodynamic properties of superconductors change dramatically depending on the type of superconductivity.

Type-I superconductors

Formation of N-S interfaces is energetically unfavourable in type-I superconductors due to their surface tension being positive. Therefore, such superconductors tend to minimize the total area of these phase boundaries. The way this minimization takes place is cumbersome because it strongly depends on the shape of the specimen and so on the corresponding demagnetizing effects: in type-I superconductors the penetration of the magnetic field happens in a way that minimizes the total Gibbs free energy, which also contains the energy of the demagnetizing field generated by the sample.

If the magnetic field strength is applied in a direction so that the resulting demagnetizing field vanishes, N-S interfaces are not allowed to form and the magnetic field is expelled according to the Meissner effect. Furthermore, the equilibrium state in the bulk is uniform and is described by the order parameter ψ_0. Experimentally, their behavior corresponds to that of perfect superconductors introduced at the beginning of this chapter (see Figures 1.1-1.3).

On the contrary, when the demagnetizing field is non-zero there exists a magnetic field strength H_c' above which the magnetic field is able to penetrate the superconductor. For field strengths $H_c' < H < H_c$ the sample consists of alternating domains of normal-metal and superconductor. This multi-domain structure shows exotic patterns that depend on the magnetic history of the specimen and on its geometry. Such regime in a type-I superconductor is called the *intemediate state* and will be extensively discussed in the next section.

Type-II superconductors

Surface tension of N-S interfaces is negative for type-II superconductors, which tend to maximize the total area of these phase boundaries. Penetration of magnetic field into the sample is energetically favourable and therefore the fall of perfect diamagnetism, one of the hallmarks of perfect superconductivity, is a signature of this type of superconductivity. Experimentally, there exists a critical field H_{c1} (lower critical field) from which a continuous increase in magnetic flux penetration is observed. The magnetic field reaches $B = H$ at a second critical field H_{c2} (upper critical field) where the specimen becomes normal. This behavior is depicted in Fig. 1.5. The regime $H_{c1} < H < H_{c2}$ represents a new thermodynamic superconducting state called the (*Abrikosov*) *mixed state.*

A feature of type-II superconductivity is that magnetic flux does not penetrate randomly the superconductor. On the contrary, it is quantized at the microscopic

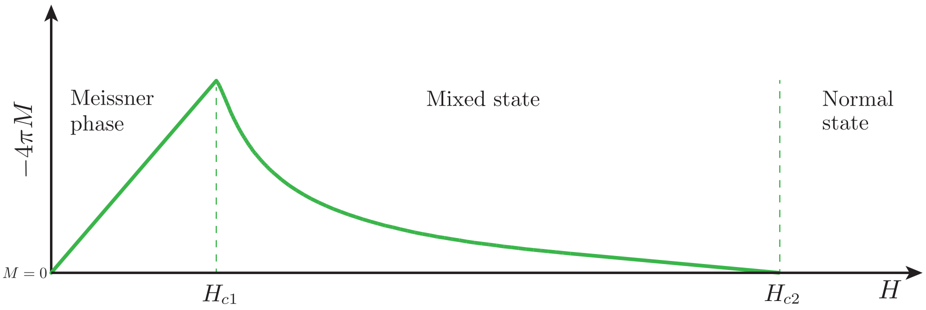

Figure 1.5: Sketch of the first magnetization curve for an ideal type-II superconductor.

scale: Let S be an arbitrary surface with its boundary ∂S lying inside the superconductor. Eq. (1.8) yields the identity

$$\int_{\partial S} \vec{j} \cdot \mathrm{d}\vec{l} = \frac{\hbar e^{\star}}{m^{\star}} |\psi|^2 \int_{\partial S} \nabla\theta \cdot \mathrm{d}\vec{l} - \frac{e^{\star 2}}{m^{\star} c} |\psi|^2 \Phi(S), \tag{1.38}$$

where $\Phi(S) = \int_{\partial S} \vec{A} \cdot \mathrm{d}\vec{l}$ is the magnetic flux through the surface. The circulation of $\nabla\theta$ over ∂S represents the change of phase of the condensate wavefunction along the closed path, which must be an integer multiple of 2π to guarantee the continuity of ψ. Consequently,

$$\Phi^{\star}(S) = \Phi(S) + \frac{m^{\star} c}{e^{\star 2} |\psi|^2} \int_{\partial S} \vec{j} \cdot \mathrm{d}\vec{l} = n\Phi_0, \quad n \in \mathbf{Z}, \tag{1.39}$$

where $\Phi_0 = \frac{hc}{|e^{\star}|}$ is the flux quantum. In fact, it is not the magnetic flux but the fluxoid $\Phi^{\star}(S)$ that is quantized. For a contour ∂S deep inside the superconductor, the second term of Eq. (1.39) can be neglected due to the Meissner effect (the supercurrent vanishes far from interfaces) and then the magnetic flux is the quantized magnitude. Therefore, the smallest amount of magnetic flux that can penetrate a superconductor is one flux quantum Φ_0 and it does so in the form of a vortex line. The size of its core is of order the coherence length ξ_{GL}. The resulting structure of vortex lines becomes stable under the spatial configuration of a two-dimensional lattice.

For magnetic field strengths slightly above H_{c1} the Gibbs free energy can be expanded as

$$\mathcal{G}(T,H) \simeq \mathcal{G}(T,0) + n_{\mathrm{L}} \frac{\mathcal{E}_v}{L} + \frac{1}{V} \sum_{i<j} \mathcal{E}^{ij} - \frac{1}{4\pi} \vec{H} \cdot \vec{B}, \tag{1.40}$$

where n_{L} represents the surface density of vortex lines, $\mathcal{E}_v = L\left(\frac{\Phi_0}{4\pi\lambda_{\mathrm{L}}}\right)^2 K_0\left(\frac{1}{\kappa}\right)$ is the energy of a vortex line and $\mathcal{E}^{ij}$ represents the (repulsive) interaction energy between the pair (i,j) of vortex lines. K_0 is the zero-th order modified Bessel function of imaginary argument. This expansion has been done considering a rectangular geometry with cross section $\mathcal{A}$ and thickness L ($V = \mathcal{A}L$) for the sake of simplicity. The magnetic field strength is applied perpendicular to this cross section.

Just above the lower critical field the interaction energy term can be neglected because the vortex lines are far from each other (penetration of only a few vortex lines in the superconductor) and $\mathcal{E}^{ij}$ decreases exponentially for long distances. The magnetic field due to the lattice of vortex lines is $B = n_{\mathrm{L}}\Phi_0$ and therefore the Gibbs free energy becomes

$$\mathcal{G}(T,H) \simeq \mathcal{G}(T,0) + n_{\mathrm{L}}\left(\frac{\mathcal{E}_v}{L} - \frac{1}{4\pi}H\Phi_0\right). \tag{1.41}$$

According to this expression, the onset of magnetic flux penetration happens at the magnetic field strength $H = \frac{4\pi}{\Phi_0}\frac{\mathcal{E}_v}{L}$, which can be identified with H_{c1},

$$H_{c1}(T) = \frac{\Phi_0}{4\pi\lambda_{\mathrm{L}}^2(T)}K_0\left(\frac{1}{\kappa}\right) \xrightarrow{\kappa\gg 1} \frac{\Phi_0}{4\pi\lambda_{\mathrm{L}}^2(T)}\ln\kappa. \tag{1.42}$$

On the other hand, superconducting domains begin to nucleate for magnetic field strengths just below H_{c2}, that is, the upper critical field determines the onset of superconductivity. In this regime, the magnetic field is approximately uniform across the sample. In the region of nucleation the order parameter is vanishingly small, so that the first Ginzburg-Landau equation (1.6) can be linearized to obtain

$$-\frac{\hbar^2}{2m^\star}\left[\nabla - \frac{ie^\star}{\hbar c}\vec{A}(\vec{r})\right]^2\psi(\vec{r}) + \alpha(T)\psi(\vec{r}) = 0. \tag{1.43}$$

This equation is formally identical to the Schrödinger equation for a particle with energy $-\alpha$, mass $m^\star$ and charge $e^\star$ in a uniform magnetic field $\vec{B} \simeq H\hat{e}_z$. Calculation of its spectrum for the case of an infinite medium yields the inequality

$$-\alpha \geq \left(n + \frac{1}{2}\right)\hbar\omega_c, \quad n \in \mathbf{N}, \tag{1.44}$$

where $\omega_c = |e^\star|H/m^\star c$ is the cyclotron frequency of the particle. The highest field at which superconductivity can occur corresponds to the lowest eigenvalue of the above inequality, which is given by the expression

$$H_{c2}(T) = \frac{2m^\star c}{\hbar|e^\star|}|\alpha(T)| = \frac{\Phi_0}{2\pi\xi_{\mathrm{GL}}^2(T)}. \tag{1.45}$$

Comparison of this field to the thermodynamic critical field H_c leads to the identity

$$H_{c2} = \sqrt{2}\kappa H_c, \tag{1.46}$$

which for type-II superconductors implies $H_{c2} > H_c$ ($\kappa > 1/\sqrt{2}$). In the regime $H_c < H < H_{c2}$ an ordered superconducting phase ($\psi \neq 0$) will appear in the sample, which cannot correspond to the complete exclusion of magnetic field due to this being energetically unfavorable according to Eq. (1.30). This phase is the Abrikosov mixed state, which is characterized by a lattice arrangement of the vortex lines (see Fig. 1.6a). The mean-field phase diagram in the (T, H) plane of a conventional (low T_c) type-II superconductor is shown in Fig. 1.6b.

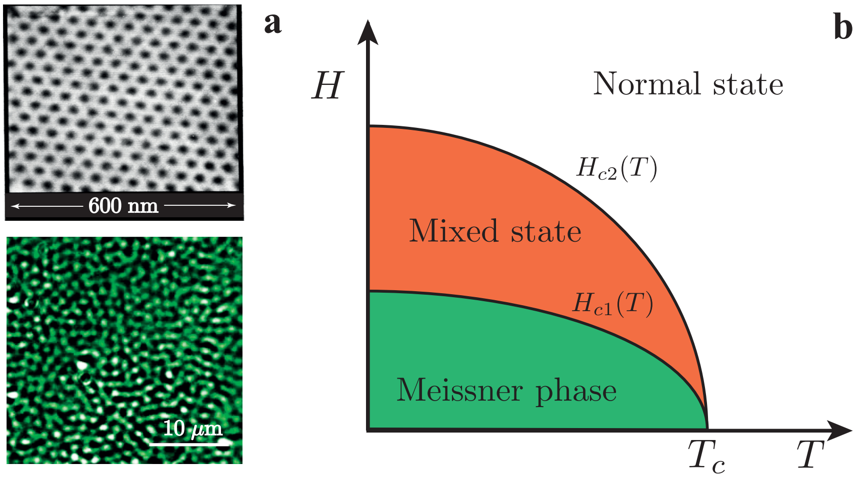

Figure 1.6: (a) STM (scanning-tunneling-microscope) image at $T = 1.8$ K in $B = 1$ T (top) and magneto-optical image at $T = 4.0$ K in $H = 8$ Oe (bottom) of a NbSe$_2$ crystal. The images have been adapted from Refs. [9] and [10]. (b) Mean-field phase diagram in the (T, H) plane of a conventional (low T_c) type-II superconductor.

So far no description of the order parameter has been provided for the mixed state. The full non-linear Ginzburg-Landau equation is required to calculate ψ in this superconducting phase. For magnetic field strengths slightly below H_{c2}, analytical solutions of Eq. (1.6) can be obtained: A. Abrikosov considered that ψ could be expressed as a linear superposition of the degenerate solutions of the linearized Ginzburg-Landau equation (1.43) and that the probability density $|\psi|^2$ should preserve the symmetry of the vortex lattice in the XY plane. The functional dependence chosen for the order parameter was [11]

$$\psi(x,y) = \sum_{n\in\mathbb{Z}} C_n \exp\left(inky\right) \exp\left(-\frac{1}{2\xi_{\mathrm{GL}}^2}\left[x + n\frac{\Phi_0 k}{2\pi H_{c2}}\right]^2\right), \tag{1.47}$$

where C_n are complex coefficients. Periodicity of $|\psi|^2$ is guaranteed by imposing the periodicity condition $C_{n+\nu} = C_n$ with ν being an integer. In so doing, the wavefunction (1.47) becomes quasiperiodic with a period $b = 2\pi/k$ in the y direction and with a quasiperiod $a = 2\pi\nu\xi_{\mathrm{GL}}^2/b$ in the x direction. Clearly, the area of the unit cell is $ab = 2\pi\nu\xi_{\mathrm{GL}}^2$ and so ν corresponds to the number of vortices per unit cell.

The coefficients $\{C_n\}_{n=1}^{\nu}$ are fixed by imposing the stationariness of the free energy with respect to a variation of ψ. Introducing the Abrikosov parameter $\beta_A = V\int_V |\psi(\vec{r})|^4\,\mathrm{d}^3\vec{r}/\left(\int_V |\psi(\vec{r})|^2\,\mathrm{d}^3\vec{r}\right)^2$, which depends on the symmetry of the lattice and turns out to be field independent for $H \lesssim H_{c2}$, the magnetic induction (volume average of the magnetic field) and the magnetization of the system become

$$B = H - \frac{H_{c2} - H}{\beta_A(2\kappa^2 - 1)}, \qquad \bar{M} = \frac{H - H_{c2}}{4\pi\beta_A(2\kappa^2 - 1)}. \tag{1.48}$$

The lowest free-energy solution is obtained for a triangular (hexagonal) lattice, characterized by $\nu = 2$, $b = \sqrt{3}a$ and $C_1 = iC_0$. The corresponding value of the Abrikosov parameter is $\beta_A = 1.16$. Some consequences of Abrikosov's calculation are worth to be pointed out: Slightly below H_{c2}, 1) the volume average of the magnetization increases linearly with the magnetic field strength and its slope is a function of the Ginzburg-Landau parameter κ; and 2) the magnetic field inside the superconductor varies periodically according to the symmetry of the vortex lattice.

Another interesting regime of the mixed state is given by $H_{c1} \ll H \ll H_{c2}$, which exists for type-II superconductors with $\kappa \gg 1$. In this regime there is a densely packed lattice of vortex lines with vortex-vortex spacing d satisfying $\xi_{\mathrm{GL}} \ll d \ll \lambda_{\mathrm{L}}$. Inequality $d \gg \xi_{\mathrm{GL}}$ implies that the magnetic field $\vec{B}(\vec{r})$ is described accurately by the solution of the inhomogenous London equation

$$\vec{B}(\vec{r}) + \lambda_{\mathrm{L}}^2 \nabla\times\nabla\times\vec{B}(\vec{r}) = \Phi_0\left(\sum_i \delta^2(\vec{r} - \vec{r}_i)\right)\hat{e}_z, \tag{1.49}$$

where i runs over all vortices in the lattice. Solution of this equation using Fourier analysis yields the following expressions for the magnetic induction and the magnetization of the superconductor [12]:

$$B = H - H_{c1}\frac{\ln\left(\gamma\frac{d}{\xi_{\mathrm{GL}}}\right)}{\ln\kappa}, \quad \bar{M} = -\frac{H_{c1}}{4\pi}\frac{\ln\left(\gamma\frac{d}{\xi_{\mathrm{GL}}}\right)}{\ln\kappa}, \tag{1.50}$$

where $\gamma = 0.628$ and $d^2 = 2\Phi_0/\sqrt{3}B$ for the triangular lattice. Thus $\bar{M}$ increases logarithmically with increasing magnetic field strength. The dependences of the magnetization on H described by Eqs. (1.48) and (1.50) agree well with experimental data for type-II superconductors (see Fig. 1.5).

The description of superconductivity made so far corresponds to the ideal (homogenous) case. The presence of various kinds of inhomogeneities (such as defects, impurities, grain boundaries, etc.) in a real superconductor results in a nonideal (inhomogenous) behavior. For a type-II superconductor in the mixed state, these inhomogeneities act as pinning centers for the vortex lines due to the effective interaction between them. Consequently, there is a distortion of the vortex lattice from the ideal (triangular) case.

Interaction between vortex lines yields the Lorentz force density $\vec{f}_L = \frac{1}{c}\vec{j}_s \times \vec{B}$ acting on the vortex-line lattice, where $\vec{j}_s$ is the total volume-averaged supercurrent density and $\vec{B}$ is the magnetic induction. For a distorted vortex lattice, the total supercurrent at the points corresponding to vortex lines is non-zero and therefore a net transverse driving (Lorentz) force appears. On the contrary, $\vec{j}_s$ vanishes at the points with vortex lines in the case of a uniform (undistorted) lattice. Application of a transport current $\vec{J}$ makes the vortex lines to be subjected to the same kind of driving force, $\frac{1}{c}\vec{J} \times \vec{B}$, so that even in this case a net force can be produced on the vortex lattice. Vortex lines begin to move sideways for strong enough driving forces. This motion of magnetic flux creates an electric field that, in the presence of the transport current, creates a dissipation [13]. Thus the appearance of an Ohmic resistance due to the motion of vortex lines in type-II superconductors means the fall of perfect conductivity and a major setback in the possible technological applications of this kind of materials.

With respect to the third hallmark of perfect superconductivity, when both type-I and type-II superconductors are doped with magnetic impurities there exists a concentration range where the material remains superconducting but the gap vanishes. Hence superconductivity appears not to be connected with the existence of the energy gap.

To conclude this section, it is important to remark that type-II superconductors are the most abundant in nature and the ones presenting the highest critical temperatures. Furthermore, even bulk type-I superconductors can become type-II by lowering its dimensionality (thin slabs) or by doping them with impurities, for instance.

1.3 The intermediate state in type-I superconductors

1.3.1 Theoretical description

Demagnetizing effects are responsible for the magnetic flux penetration in (pure) type-I superconductors. Even though the surface tension is positive, a multi-domain structure of normal-metal and superconducting regions appears for magnetic field strengths $H'_c < H < H_c$, where H'_c strongly depends on the shape of the specimen. Complex geometric patterns of N-S interfaces occur for samples of general shape due to the non-uniformity of the demagnetizing field. Therefore, a rigorous (theoretical) description of this pattern formation is cumbersome.

Despite the complexity of this picture, the main features of the intermediate state can be obtained by restricting its study to the special case of an ellipsoid: such shape symmetry provides a uniform demagnetizing field across the sample, whose linear dependence on the magnetization is given by

$$\vec{H}_d = -\hat{N} \cdot \vec{M}, \tag{1.51}$$

where $\hat{N}$ is the demagnetizing tensor due to dipolar fields. This tensor becomes diagonal on the basis of main axes of the ellipsoid, $\hat{N}_{\alpha\beta} = n_\alpha \delta_{\alpha\beta}$, with n_α, $\alpha \in \{x, y, z\}$ being the demagnetizing factors along the Cartesian axes. Suppose that a magnetic field strength $\vec{H}_0$ is applied along one of these axes and let n be the corresponding demagnetizing factor. The field strength inside the ellipsoid is then given by

$$\vec{H} = \vec{H}_0 + \vec{H}_d = \vec{H}_0 - n\vec{M} \tag{1.52}$$

and, if the condition $-4\pi\vec{M} = \vec{H}$ of perfect diamagnetism holds, it becomes

$$\vec{H} = \frac{1}{1 - \frac{n}{4\pi}} \vec{H}_0. \tag{1.53}$$

This identity implies that the magnetic field strength inside the superconductor is enhanced by a factor $1/(1 - \frac{n}{4\pi}) \geq 1$ compared to the applied one.

Let now the applied field strength be gradually raised from zero. When it reaches the value $H'_c \equiv (1 - \frac{n}{4\pi})H_c$, the field strength inside the superconductor becomes equal to the critical field H_c and therefore the ellipsoid should be driven into the normal state. But were this to happen the magnetization of the sample would become zero and hence $H = H_0 = H'_c < H_c$. This leads to a completely normal sample in a field strength smaller than H_c, which cannot happen according to Eq. (1.30). The so-called intermediate state represents the solution to this paradox, that is, the coexistence of both normal and superconducting phases in equilibrium.

From the discussion leading to the boundary conditions (1.10) for the magnetic field, it is clear that a stationary N-S phase boundary will only exist where the internal field is exactly H_c and, consequently, the magnetic field on the normal side will be $B = H_c$. On the other hand, the interfaces between normal-metal and superconducting domains must lie parallel to the local direction of the magnetic field: The interface can be locally identified with the YZ plane via an appropiate (point dependent) rotation of the axes, which implies that locally both $\vec{H}$ and $\vec{B}$ depend only on the x coordinate. From the second Maxwell equation, $\nabla \cdot \vec{B} = 0$, the identity $B_x(x) \equiv \text{const}$ holds and the application of Eq. (1.23) to the x-component of the magnetic field yields $B_x \equiv 0$ in the superconducting domain. Finally, the continuity of the normal component of $\vec{B}$ across the interface implies $B_x \equiv 0$ in both domains, which proves the above claim.

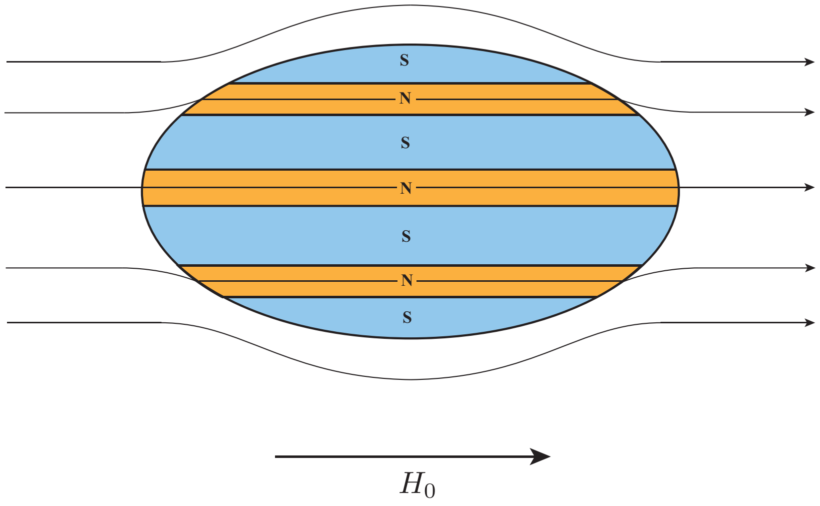

Figure 1.7: Multi-domain structure of alternating normal (N, chrome yellow) and superconducting (S, blue) laminae for an ellipsoidal type-I superconductor in the intermediate state.

The simple geometry of laminar domains will be considered from this point forward, which still retains the main magnetic and thermodynamic features of the intermediate state: For $H_c' < H_0 < H_c$ the type-I superconductor is assumed to split into an arrangement of alternating normal and superconducting laminae, whose sizes are small compared to the sample dimensions but large compared to the London penetration length. The N-S interfaces lie parallel to the applied magnetic field (see Fig. 1.7) and the internal field is equal to H_c across the sample. Let $d_n(d_s)$ be the average thickness of the normal (superconducting) laminae and

ρ_s be the fraction of the maximum cross section being in the superconducting state. Hence $\rho_s = d_s/(d_n + d_s)$ and the magnetic induction through the sample becomes $B = (1 - \rho_s)H_c$. The volume average of the magnetization is then given by $4\pi\bar{M} = B - H = B - H_c$ and, with account of Eq. (1.52), the identity

$$H_c = H = \frac{H_0}{1 - \frac{n}{4\pi}\rho_s} \tag{1.54}$$

follows. This determines the dependence of the fraction ρ_s on the ratio H_0/H_c and thus the values of B and $\bar{M}$ for applied field strengths H_0 between H_c' and H_c. These dependences are shown in Fig. 1.8.

Thermodynamic stability of the intermediate state stems from the fact that it minimizes the Gibbs free energy of a type-I superconductor in the range of field strengths $H_c' < H_0 < H_c$: The differential of the Gibbs free energy density is given by the expression $d\mathcal{G} = -\bar{M}dH_0$ at constant temperature. This identity neglects the energy term arising from the establishment of the applied field, $\frac{H_0^2}{8\pi}$, because one is solely interested in the contribution from the superconducting sample. On the other hand, the contribution to the Gibbs potential associated to the presence of N-S interfaces is neglected for the time being. Consequently, the Gibbs free energy density becomes

$$\mathcal{G}(H_0) = \mathcal{G}_s(0) - \int_0^{H_0} \bar{M}\,\mathrm{d}H_0, \tag{1.55}$$

where $\mathcal{G}_s(0)$ is the free energy density of the superconducting state at zero field. In the regime $0 < H_0 < H_c'$ the ellipsoid is totally superconducting ($\rho_s = 1$), so that with account of the identity $4\pi\bar{M} = -H = H_0/(1 - \frac{n}{4\pi})$ the Gibbs free energy density becomes

$$\mathcal{G}(H_0) = \mathcal{G}_\mathrm{s}(0) + \frac{1}{1 - \frac{n}{4\pi}}\frac{H_0^2}{8\pi}. \tag{1.56}$$

In the range of field strengths $H_c' < H_0 < H_c$ the ellipsoid is in the intermediate state and $4\pi\bar{M} = -\rho_s H_c$. Hence

$$\mathcal{G}(H_0) = \mathcal{G}_\mathrm{n}(0) - \frac{(H_0 - H_c)^2}{2n}, \tag{1.57}$$

where $\mathcal{G}_\mathrm{n}(0) = \mathcal{G}_\mathrm{s}(0) + \dfrac{H_c^2}{8\pi}$ is the Gibbs free energy density of the normal state. Finally, for $H_0 > H_c$ the sample is completely normal and $\bar{M} = 0$, which leads to $\mathcal{G}(H_0) = \mathcal{G}_n(0)$. Figure 1.9 shows an sketch of the dependence of $\mathcal{G}$ on the applied field strength, which clearly shows that the intermediate state (in this simplified model of planar laminae) has a lower free energy than both the pure

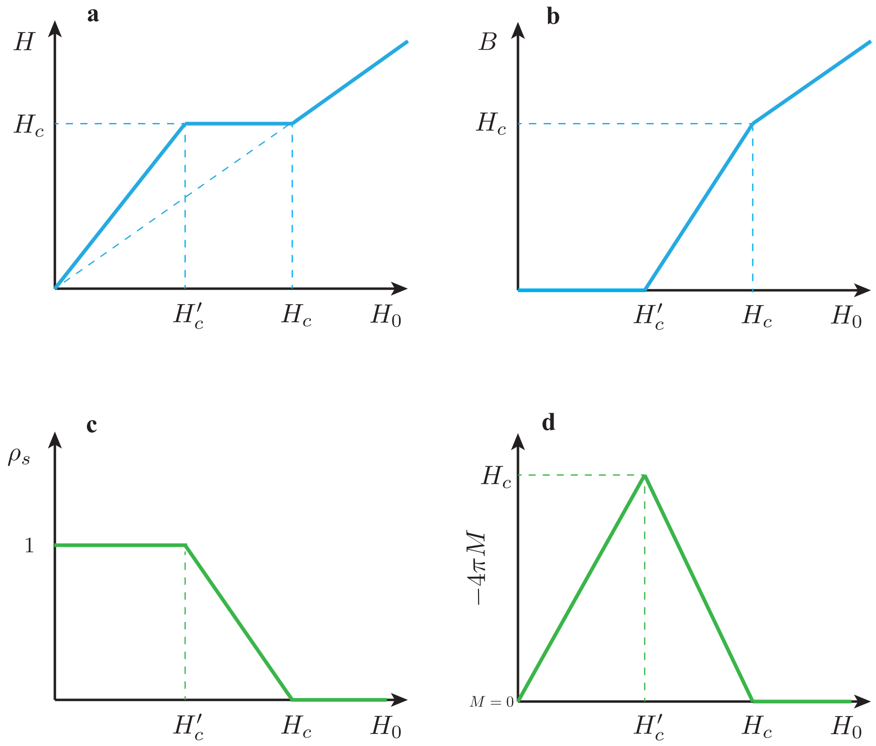

Figure 1.8: Sketches of the dependence on the applied magnetic field strength of (a) the (internal) magnetic field strength H, (b) the magnetic induction B, (c) the superconducting fraction of the sample ρ_s, and (d) the volume average of the magnetization $-4\pi M$.

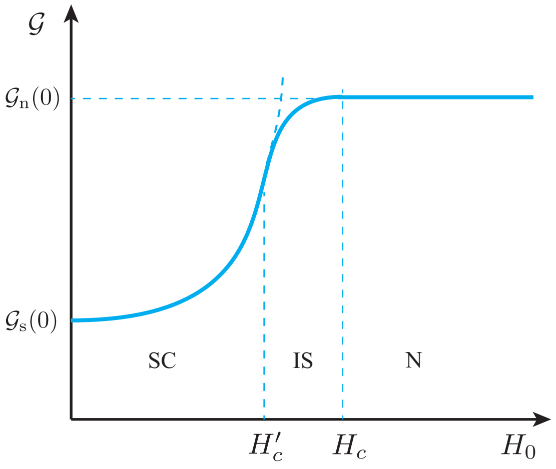

Figure 1.9: Schematic diagram of the Gibbs free energy density for a specimen with non-zero demagnetizing factor.

superconducting and the pure normal states would have in the regime $H_c' < H_0 < H_c$.

In order to estimate the values of d_n and d_s within this simple model, both the presence of N-S phase boundaries and the effects of the deformation of the field lines near the surface of the sample must be considered: Interfaces between normal-metal and superconducting domains contribute to the Gibbs free energy density with an extra term $\sigma\mathcal{A}$, where $\mathcal{A}$ is the total area of the interfaces. The surface tension (1.37) can be described in terms of a characteristic length $\bar{\Delta}$ as $\sigma = \frac{H_c^2}{8\pi}\bar{\Delta}$. A broadening of the normal laminae near the surface of the specimen occurs to maintain the value H_c of the local field at the interfaces (see Fig. 1.10a). This deformation translates into a loss of condensation energy and a modification of the magnetic field energy (near the surface) with respect to the ideal planar laminae model, see Eq. (1.57). A. Fortini and E. Paumier studied this more realistic multi-domain structure under the assumption of semi-infinite normal-metal/superconducting regions [14], and obtained the following expression for the reduced free energy $g = \mathcal{G}/\frac{H_c^2}{8\pi}$:

$$g = -\rho_s + \frac{\rho_s h_0^2}{1 - \frac{n}{4\pi}\rho_s} + 2\left(\frac{2\bar{\Delta}}{L}(g_M h_0^2 + g_C)\right)^{1/2}, \tag{1.58}$$

where $h_0 = H_0/H_c$ is the reduced field and L is the thickness of the sample. The functions g_M and g_C determine corrections to the Gibbs free energy (of the ideal laminar case) and correspond to the magnetic energy due to the domain ends and to the increment of the condensation energy due to the increment of volume of the normal-metal domains, respectively. Furthermore, the equilibrium value of the period $d = d_s + d_n$ of the multi-domain structure is

$$d = \left(\frac{2\bar{\Delta} L}{g_M h_0^2 + g_C} \right)^{1/2} , \tag{1.59}$$

where the restriction $L \gg d$ must hold.

Minimization of the Gibbs free energy (1.58) with respect to ρ_s yields the equlibrium value $\rho_s = \rho_{s,0} + \delta\rho_s$, where $\rho_{s,0} = (1 - h_0)/\frac{n}{4\pi}$ is the superconducting fraction within the ideal laminar model [see Eq. (1.54)] and $\delta\rho_s$ is given by

$$\delta\rho_s = -\frac{h_0}{n/2\pi} \frac{g_M' h_0^2 + g_C'}{(g_M h_0^2 + g_C)^{1/2}} \left(\frac{2\bar{\Delta}}{L} \right)^{1/2} , \tag{1.60}$$

where the functions g_M, g_C and their derivatives are evaluated at $\rho_{s,0}$ [this evaluation also occurs in Eq. (1.59)]. Neglecting the correction $\delta\rho_s$, the identity $h = 1 - \frac{n}{4\pi}\rho_s$ holds. The assumption of a semi-infinite geometry implies that the validity of this model reduces to flat ellipsoidal samples (such as disks and thin slabs), which in turn implies demagnetizing factors $n/4\pi$ close to one. The Landau limit corresponds to the case $\frac{n}{4\pi} = 1$, where $g_M h_0^2 + g_C$ can be identified with twice the Landau function

$$\begin{aligned} 2\Psi_L(h_0) = (g_M h_0^2 + g_C)_{\frac{n}{4\pi}=1} = \frac{1}{\pi} \Bigg[& \frac{(1+h_0)^4}{2} \ln(1+h_0) + \frac{(1-h_0)^4}{2} \ln(1-h_0) \\ & - \frac{(1+h_0^2)^2}{2} \ln(1+h_0^2) - 2h_0^2 \ln(8h_0) \Bigg] . \end{aligned} \tag{1.61}$$

The correction $\delta\rho_s$ gives rise to deviations in both the magnetic field strengths in the normal-metal laminae and the magnetic moment $\bar{M}$ of the sample

$$\frac{\delta H}{H_c} = \frac{n/4\pi}{1 - \frac{n}{4\pi}\rho_{s,0}} \delta\rho_s, \quad \delta\bar{M} = -\frac{H_c}{h_0} \delta\rho_s. \tag{1.62}$$

Therefore the effect of the deformation of the N-S interfaces near the surface on the electrodynamic properties of the intermediate state is of order $(\bar{\Delta}/L)^{1/2}$. On the other hand, the field strengths at the phase transitions PS-IS (pure superconductor-intermediate state) and IS-NS (intermediate state-normal state) become slightly modified with respect to their values H_c' and H_c in the ideal laminar model and are given by

$$\begin{aligned} H_{\text{PS-IS}} &= H_c' + H_c' \left(\left[2 - \ln\left(8\left(1 - n/4\pi\right)\right)\right] \frac{n\bar{\Delta}}{\pi^2 L} \right)^{1/3}, & (1.63) \\ H_{\text{IS-NS}} &= H_c - O\left(\left(\bar{\Delta}/L \right)^{1/2} \right). & (1.64) \end{aligned}$$

Hence, the deviation of the field strengths from their ideal values is of order $(\bar{\Delta}/L)^{1/3}$ for the PS-IS phase transition and of order $(\bar{\Delta}/L)^{1/2}$ for the IS-NS phase transition.

According to this model, the internal field strength is uniform across the sample except for a region of size $\sim d$ near the external surface. Restricting the analysis of this field distortion to the line ℓ (see Fig. 1.10a), the minimum value of the field strength occurs at the point A and is given by $H_A = f(\rho_s) H_{\text{un}}$, where $H_{\text{un}} = H_c + \delta H$ is the undistorted field strength far from the external surface. The function f is a decreasing function of the superconducting fraction and satisfies $f(0) = 1$ and $f(1) = 0.648$. Consequently, the field strength H_A at the point A is less than H_{un} in the intermediate state. Assuming the identity $H_{\text{un}} = H_c$ from the ideal case (that is, neglecting the correction δH), this means that there exists a point in every normal domain where the internal field strength is less than the critical field, which contradicts the condition (1.30). This argument lead L. Landau to develop the *branched* model, in which each normal domain splits recursively into two laminae as it approaches the surface, becoming extremely thinner at the surface itself [15]. Fortini and Paumier estimated that the spatial extension of the field-distortion region is d at most, so that the branching of the normal laminae is most likely to occur with a few splittings in the medium range of ρ_s.

1.3.2 Experimental description

Experimentally, the intemediate state has been revealed by means of different techniques. The first resolution of its domain structure was due to A. Meshkovsky and A. Shalnikov, who used a bismuth probe to explore the magnetic field distribution between two hemispheres of tin of diameter $2R = 4$ cm [16, 17]. Another technique relies on the tendency of ferromagnetic powders to accumulate in regions of high magnetic flux density. B. Balashova and Yu. Sharvin observed rich and complex patterns in the intermediate state by spreading 1 μm nickel powder on the outside of a tin sphere [18]. Spreading superconducting powders on a type-I sample, which tend to accumulate in regions with low flux density, represents the complementary technique. Finally, magneto-optic methods based on the Faraday effect have proved themselves to be a valuable technique to explore the intricacy of the domain structure, especially the dynamic effects: W. De Sorbo *et al.* and B. Goodman *et al.* recorded dynamic phenomena of the intermediate state through

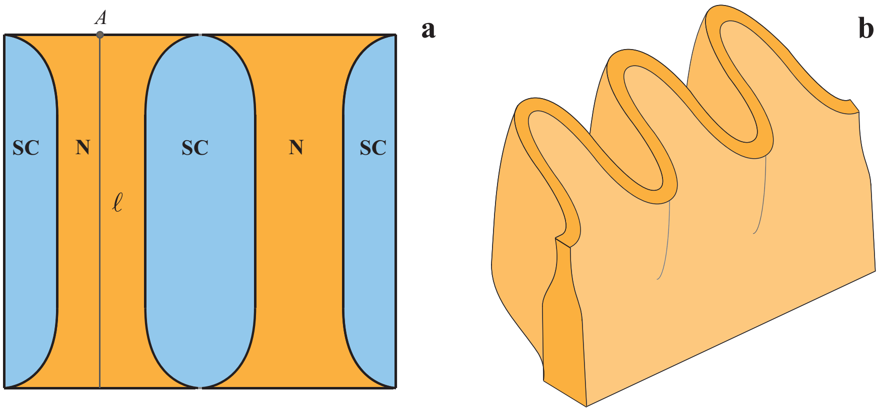

Figure 1.10: (a) Unbranched laminar model of the multi-domain structure of a flat ellipsoidal specimen in the intermediate state. (b) Perspective view of a corrugated normal-metal lamina. The amplitude of corrugation decreases with depth from the surface of the sample.

motion pictures [19, 20] and high-speed photography [21, 22]. More recently, R. Prozorov *et al.* used magneto-optic techniques to explore the topological hysteresis in the intermediate state of lead for different shapes [23, 24]. It should be remarked, however, that magneto-optic methods are best suited only to flat surfaces.

Experiments have unravelled the commonness of the unbranched multi-domain structure in the intermediate state: for typical values of the surface tension ($\bar{\Delta} \sim 10^{-4} - 10^{-5}$ cm), multiple branching only occurs for extremely thick samples, whereas for typical specimen dimensions ($L \sim 1$ cm) the normal laminae should split into one or two branches at most. Therefore the unbranched model appears to be more favourable energetically than the branched one, despite the fact that there exist points in the normal domains (such as A) where the field strength may be appreciably less than H_c. Nevertheless, branching cannot be excluded for type-I superconductors with low values of $\bar{\Delta}$. Corrugations in the normal laminae near the external surface (see Fig. 1.10b) are observed in practice, whose development is the mechanism through which the unbranched multi-domain structure minimizes its free energy. Rather than being an exception, nonequilibrium structures of the intermediate state are often obtained experimentally. High reduced temperature T/T_c, high reduced field and low Ginzburg-Landau parameter κ are found to favor the attainment of equilibrium structures.

From this point forward, the analysis of the dynamics and the topology of the intermediate state will be restricted to disk-shaped samples with small thickness-to-radius aspect ratio β in a transverse field strength. First of all, a reversible penetration of magnetic flux along the corners of the specimen is observed at the

PS-IS transition as the field strength increases (see Fig. 1.11b). The opposite normal domains in the corners are separated at the equator of the disk by a Meissner phase and the peripheral N-S boundary moves inward during this stage. The reversibility of this process is due to the high increase of interfacial area (and the corresponding surface energy) with penetration. Figure 1.11c represents the onset of irreversible flux penetration, where magnetic flux tubes can form and migrate towards the center of the disk. The magnetic field strength H_p at which this occurs is called the penetration field. A superconducting ring exists near the edge of the sample even after considerable flux penetration and, as flux accumulates in the center of the disk (due to the field being increased), the peripheral N-S interface moves outward again. This Meissner phase, however, prevents the exit of normal domains from inside the sample as the field strength is decreased and therefore the flux penetration becomes irreversible.

It is worth remarking the concept of geometrical barrier: the formation of an intermediate phase inside the superconducting sample becomes energetically favorable above some field H_m, but a potential barrier arising at the sample edge (the geometrical barrier) impedes the transition into this thermodynamic state. Hence, metastability arises in the sample. The penetration field of the geometrical barrier, H_g, is defined as the field strength up to which the geometrical barrier prevents the penetration of normal domains into the inner part of the specimen. It corresponds to the field strength above which the free energy of the Meissner state exceeds the minimal energy of the state containing one magnetic flux tube at the edge of the sample. Equivalently, it corresponds to the field strength above which the internal field at the sample equator reaches the critical field (so that two opposite normal domains nucleated at the corners can become linked through the equator and form a flux tube). But were the flux tubes to overcome somehow this geometrical barrier, the metastable state would decay. This situation can happen, in principle, as soon as the metastability arises, so that inequalities $H_m \leq H_p \leq H_g$ among the above field strengths are expected to hold. The theoretical dependences of the metastability field and the penetration field of the geometrical barrier on the aspect ratio are $H_m \simeq \beta$ and $H_g \simeq \sqrt{\beta}$. Finally, the geometrical barrier is gradually depressed by the formation of the intermediate phase inside the sample and it is completely destroyed at some field called the irreversibility field of the geometrical barrier, where the uniform intermediate state becomes the equilibrium of the system.

As discussed in Ref. [25], thermal fluctuations are the most plausible mechanism by which the magnetic flux tubes surmount the geometrical energy barrier: (Thermal) fluctuations of the equilibrium shape of a normal domain are possible provided that the energy of the domain remains the same. On the contrary, fluctuations of the radial length of the domain are forbidden due to the increase of the

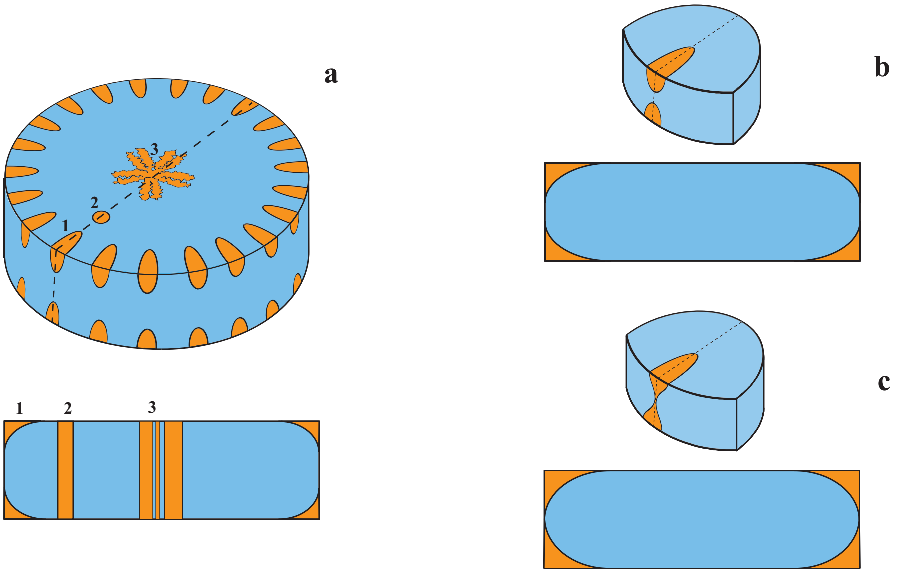

Figure 1.11: (a) Sketch of the multi-domain structure for a disk-shaped specimen with small β in the intermediate state. The bottom picture depicts the cross section along the dashed line. (b) Part of the disk near its edge in the regime of reversible penetration (top) and cross section along the dashed line (bottom). (c) Part of the disk near its edge at the onset of irreversible flux penetration (top) and cross section along the dashed line (bottom). Blue regions correspond to the Meissner phase and chrome yellow ones to the normal domains. These figures have been adapted from Ref. [25].

energy associated to the change of the shielding current distribution. Therefore, two opposite domains at the corners of the disk can become connected due to fluctuations (increase) of their thickness at the equator and then begin to spread from the edge for $H \geq H_m$, where the intermediate phase is favorable inside the sample. At this stage the equatorial (internal) field strength is lower than H_c, so that a Meissner domain nucleates at the equator confining a part of the normal domain out of the edge of the sample. Finally, interaction with the shielding current makes the confined flux experience a driving (Lorentz) force that moves it away from the edge, therefore migrating afterwards towards the center. Figure 1.12 sketches the different stages of the magnetic flux tube nucleation. This picture is valid in the case of weak pinning, because the pinning of N-S interfaces depresses thermal fluctuations of the shape of normal domains. Strong pinning leads to a complete suppresion of these fluctuations, which results in the penetration field increasing up to H_g. This effect has been observed experimentally by DeSorbo and Healy [26].

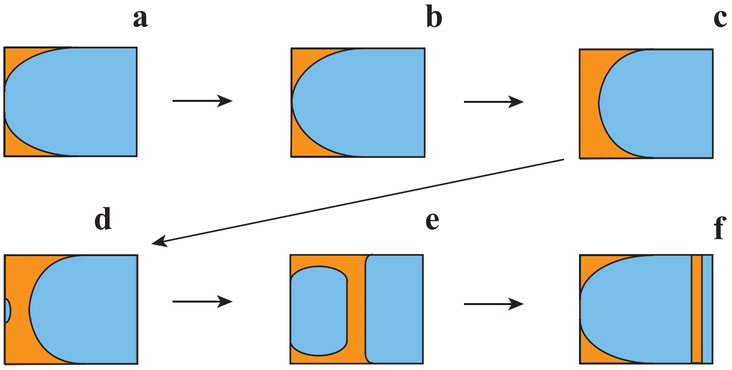

Figure 1.12: Schematic time sequence of a flux tube nucleation, where the pictures correspond to cross sections along a part of the disk near its edge in analogy with Figs. 1.11b and 1.11c. (a) The opposite normal domains in the corners are separated at the equator by the Meissner phase. (b) These two domains become connected and (c) begin to spread from the edge towards the center of the specimen. (d) Meissner phase restores at the equator and (e) the normal domain expands towards the center. (f) Finally, a magnetic flux tube separates from the normal domains at the edge and migrates inside the sample. Blue regions correspond to the Meissner phase and chrome yellow ones to the normal domains. These pictures have been adapted from [25].

The formation of a honeycomb structure (a hexagonal array of flux tubes in three dimensions) is usually observed from the accumulation of magnetic flux tubes inside the sample. Once such a structure is formed, it requires the coalescence or splitting of the flux tubes to reach a new equilibrium under the change of any of the thermodynamic variables (T, H_0). This is the so-called suprafroth state [27]. On the other hand, the perfection of the sample governs the degree of supercooling, the corresponding number of superconducting nuclei and their rate of growth in the NS-IS transition. Superconducting domains tend to spread into laminae after nucleation and normal regions migrate towards the edge of the disk, forming complex (random) labyrinthine patterns. Finally, the flux expulsion from flat disks is usually incomplete.

In recent years R. Prozorov and coworkers have pointed out a striking new feature of the intermediate state, the topological hysteresis: Measurements of $M(H)$ loops in type-I superconductors reveal the presence of magnetic hysteresis, which has been generally atributted to impurities, grain boundaries, etc. In two seminal works, the authors studied different samples made of pure 99.9999% lead with different shapes [rectangles, disks, cones and (hemi)spheres] and with different degrees of stress by means of both magnetometry and magneto-optic methods, which allowed them to correlate the macroscopic hysteretic behavior with the observed flux patterns [23, 24]. They observed that the more stressed the sample is, the bigger the magnetic hysteresis becomes. This pinning-induced hysteresis is characterized by becoming larger at the lower H_0, with its maximum at zero field strength. In the case of the stress-free (disk and rectangular) samples, however, the observed magnetic hysteresis is characterized by vanishing in the limit $H_0 \to 0$ and by reaching its maximum at the ballpark of H_c' (see Fig. 1.13a). Therefore, the origin of this hysteresis is of a different kind. Magneto-optic images showed that tubular topology is destroyed by pinning, turning into a laminar pattern or even into a nonequilibrium dendrite-like topology for strong disorder/pinning. In the case of the above stress-free samples, the tubular (closed) topology is observed upon flux penetration, whereas a well-defined laminar (open) topology is oberved upon flux exit (see Fig. 1.13b). A remarkable conclusion from Prozorov's work is that the magnetic hysteresis exhibited by the disk-shaped and rectangular stress-free samples at intermediate fields is due to the topological difference between the (topologically closed) flux tube phase and the (topologically open) laminar phase, therefore being an intrinsic property of the intermediate state.

Other shapes such as cones and (hemi)spheres were also studied by R. Prozorov and coworkers, which show no magnetic hysteresis and with tubular topology dominating both flux penetration and flux exit in the intermediate state. Unlike the previous cases (disks and rectangles), these samples (ellipsoidal shape) have no geometrical barrier and, furthermore, formation of flux tubes is always observed through the process of field cooling/warming them. Therefore, the authors con-

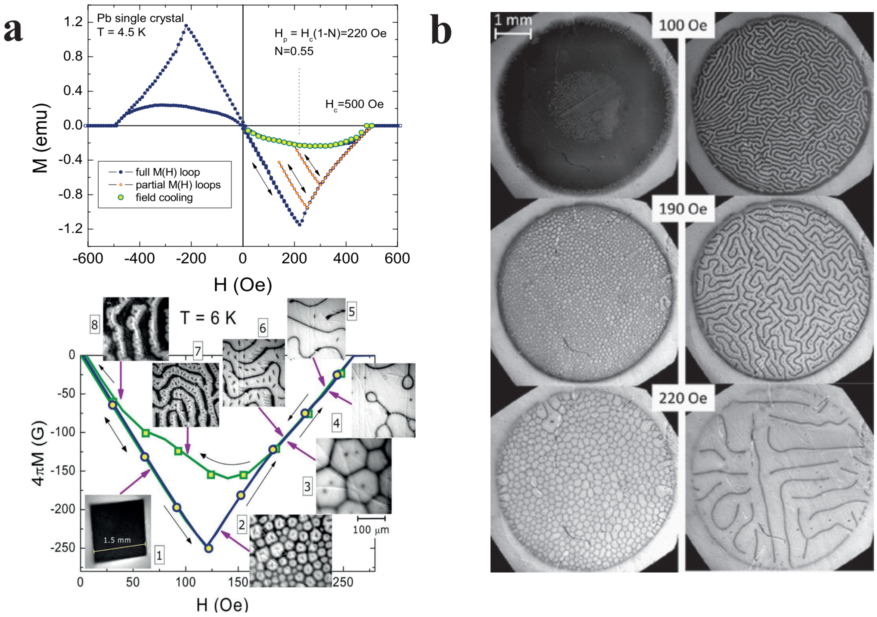

Figure 1.13: (a) Magnetization curves for a disk-shaped Pb single crystal at $T = 4.5$ K (top) and for a rectangular Pb sample at $T = 6$ K (bottom). Both are stress-free samples. The insets of the bottom image are the corresponding magneto-optical images obtained at the field strengths indicated by the arrows. The numbers indicate the sequence of images according to the magnetic field history. (b) Topology of the magnetic flux distribution for a disk-shaped Pb single crystal in the intermediate state at $T = 5$ K. Left column corresponds to the process of increasing the magnetic field strength after a zero field cooling (ZFC) and the right column corresponds to the process of decreasing the field strength. These images have been adapted from Refs. [23] and [24].

cluded that the flux tubular pattern represents the equilibrium topology of the intermediate state. On the other hand, the hysteretic descending branch coincides with the field-cooled magnetization curve in stress-free samples, indicating that the observed laminar structures correspond to a succession of equlibrium states that would be followed during the flux expulsion as the magnetic field strength decreases. This open topology is unstable in the presence of forces (Lorentz or gradient of the condensation energy) and, in the particular case of flat samples, this structure is formed as a flux-percolative state at high fields whereas it splits into flux tubes at smaller fields.

As a final remark, observation of a (closed) tubular pattern on flux penetration and an open topology on flux exit is quite typical for samples with two flat surfaces perpendicular to the applied field.

1.4 Magnetic irreversibility and quantum dynamics in lead

The intermediate state of type-I superconductivity offers a rich and wide variety of nonequilibrium multi-domain structures, which depend, among other factors, on the magnetic (temperature and field) history of the specimen. As discussed in the previous section, it is experimentally found that a closed flux tubular structure is a generic feature of the intermediate state of pinning-free samples upon flux penetration, representing the equilibrium topology of this thermodynamic phase. A natural question to arise is how robust metastability is and what kind of dynamics will be observed when a metastable state decays towards the equilibrium.

Metastability arises in the form of laminar structures (open topology) along the states of the hysteretic descending branch corresponding to the intermediate phase for weak-pinning type-I superconductors with a flat disk-shaped geometry. Relaxation measuments, based on the temporal measurement of the magnetization after the sample is driven into a metastable state, are best suited for studying magnetic hysteresis (metastability) and for clarifying some of its dynamic properties. E. Chudnovsky and coworkers conducted magnetic characterization and relaxation experiments in the temperature range $1.8 - 8$ K on two disk samples of octogonal shape made of pure 99.999% lead and annealed at two different temperatures [28]. The resulting isothermal magnetization curves made the authors conclude that they were dealing with a pure type-I Pb superconductor in a weakly pinned intermediate state. Once having applied a magnetic field strength $H_0 > H_c(T)$, isothermal temporal evolution of the remnant magnetization (in zero field) was recorded. A logarithmic time dependence of the remnant magnetization was found at all temperatures, which indicates the existence of a broad distribution of energy barriers acting as a source for metastability.

The so-called magnetic viscosity, which in the present case is defined as the rate at which the normalized remnant magnetization decreases logarithmically, shows a plateau for both samples in the limit $T \to 0$, that is, it does not extrapolate to zero as the samples are cooled down. This fact points towards the underbarrier quantum tunneling as the mechanism of escape from the metastable states. A phenomenological model was proposed by E. Chudnovsky to explain this quantum process: Remnant magnetization corresponds to the zero-field point of the hysteretic descending branch, which shows a (metastable) laminar topology. Therefore, these nonthermal relaxations appear to be due to quantum diffusion of the N-S interfaces via the formation (or decay) of mesoscopic surface bumps. The rate of decay from the metastable state is proportional to $\exp(-B)$, where the WKB exponent is given by $B = U/k_{\mathrm{B}}T$ in the thermally assisted regime and by $B = I_{\mathrm{eff}}/\hbar$ in the quantum regime. I_{eff} is a temperature-independent effective action and U is the energy barrier to be overcome, which in the present case is provided by local pinning associated to defects. The crossover temperature from thermal to quantum regime can be defined as the temperature at which both expression of the WKB exponent coincide, $T_Q = \hbar U/k_{\mathrm{B}}I_{\mathrm{eff}}$. The following rough estimate of the effective action is considered

$$I_{\mathrm{eff}} \simeq \frac{\eta}{4\pi}(\bar{a}L)^2, \tag{1.65}$$

where η is the drag coefficient and L and $\bar{a}$ are the lateral size and the height of the bump, respectively. Magnetic viscosity measurements lead to an experimental value in the ballpark of $4-5$ K for the crossover temperature, from which the estimates $L \sim 90$ nm (comparable to the coherence length of Pb) and $a \sim 1$ nm are obtained under the assumption of $I_{\mathrm{eff}} \lesssim 25\hbar$. These values are quite plausible and yield the estimate $U \sim 100$ K for the average pinning energy barrier.

1.4.1 Experimental results

As a natural extension of this work, experiments to investigate the effect of an external magnetic field on the low-temperature dynamics of N-S interfaces in type-I Pb superconductors were conducted in collaboration with S. Vélez and A. García-Santiago. The sample studied was a thin disk of extremely pure (99.999 at.%) type-I superconducting Pb with a surface area of 40 mm^2 and a thickness of 0.2 mm. It was annealed during one hour at 280 °C in glycerol and nitrogen atmosphere to reduce mechanical stress from defects. Magnetic measurements were carried out in a commercial superconducting quantum interference device (SQUID) magnetometer at temperature values from $T = 1.80$ K to $T = 7.00$ K with a low temperature stability better than 0.01 K. A configuration of the applied magnetic field parallel to the revolution axis of the sample is used in this set-up, with strengths H_0 up to 1 kOe. Isothermal magnetization curves, $M(H_0)$, were measured after the sample had been first zero-field-cooled (ZFC) from the normal state down to the desired temperature. At each T value, the first magnetization curve, $M_{\text{1st}}(H_0)$, was measured by sweeping H_0 from zero up to the normal state, and the descending branch of the corresponding hysteresis cycle, $M_{\text{des}}(H_0)$, was measured by subsequently sweeping H_0 back to zero. The magnetic field dependence of the field-cooled (FC) magnetization, $M_{\text{FC}}(H_0)$, was also registered at different temperatures by cooling the sample from the normal state down to each T value under different values of H_0. Finally, the isothermal time evolution of the remnant magnetization obtained at different H_0 values along $M_{\text{des}}(H_0)$ was recorded. The results were analyzed in terms of the reduced magnitudes $h_0 \equiv H_0/H_c$ and $m \equiv M/H_c$, with $H_c(T) = H_{c0}\,(1 - (T/T_c)^2)$[29]. Fitting the expression of $H_c(T)$ to experimental data obtained from the $M(H_0)$ curves produced values of $H_{c0} = 802 \pm 2$ Oe and $T_c = 7.23 \pm 0.02$ K for this sample, which agree fairly well with typical values found in similar samples [30].

A detail of the $m_{\text{1st}}(h_0)$ curves and $m_{\text{des}}(h_0)$ branches measured at $T = 2.00$ K (solid squares) and $T = 6.00$ K (solid circles) is plotted in Fig. 1.14 for the range of reduced field strengths $0 \leq h_0 \leq 0.35$, where the magnetic hysteresis cycles exhibit the strongest irreversibility. In this region, the two $m_{\text{1st}}(h_0)$ curves largely superimpose whereas the $m_{\text{des}}(h_0)$ branches depend on the value of T. Actually, the $m_{\text{des}}(h_0)$ branches obtained as T increases progressively from 2.00 K to 6.00 K (not shown) span the space bound by the two branches in the figure, whereas all the corresponding $m_{\text{1st}}(h_0)$ curves scale onto a single one, in good agreement with previous results obtained in similar samples [31]. Fig. 1.14 also presents the $m_{\text{FC}}(h_0)$ values obtained at $T = 2.00$ K (open squares) and $T = 6.00$ K (open circles). Both curves practically superimpose in this representation in a similar way as the two $m_{\text{1st}}(h_0)$ curves do.

As discussed in the previous section, in a defect-free sample $m_{\text{1st}}(h_0)$ should follow a series of equilibrium states corresponding to the flux penetration as h_0 increases, whereas $m_{\text{des}}(h_0)$ and $m_{\text{FC}}(h_0)$ should actually coincide. In the present sample other sources of irreversibility, such as stress defects, are present. Thus, the ability of the system to trap magnetic flux during the expulsion is enhanced with respect to the defect-free case and is substantially influenced by temperature [31]. This corroborates the differences observed in Fig. 1.14 among the $m_{\text{des}}(h_0)$ branches at different T values and between these and $m_{\text{FC}}(h_0)$. In this case, only the latter would follow the energy minima for flux expulsion, whereas $m_{\text{1st}}(h)$ would still define the equilibrium for flux penetration, as it is confirmed by the fact that the magnetization did not evolve with time starting anywhere along this curve [31].

In this context, the pinning energy barriers associated with defects should

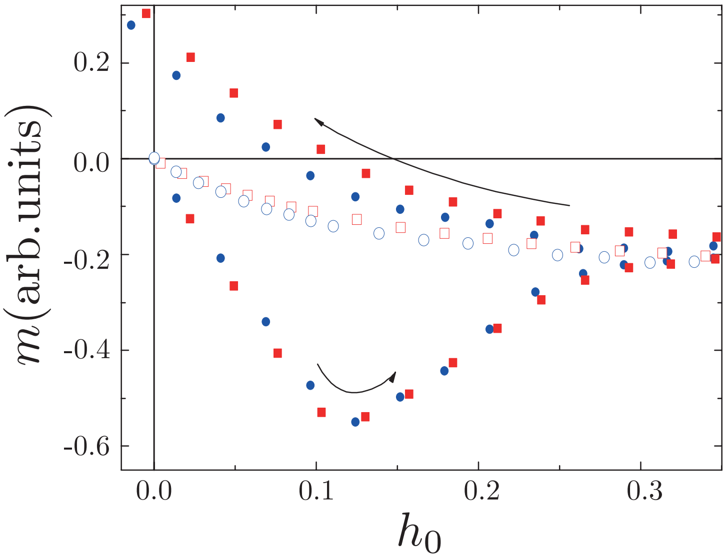

Figure 1.14: First magnetization curves (left-to-right arrow) and descending branches (right-to-left arrow) of the hysteresis cycles measured at 2.00 K (solid squares) and 6.00 K (solid circles) when the magnetic field is applied parallel to the revolution axis of the sample after a ZFC process. The magnetic field dependence of the FC magnetization at the same temperatures is included (open squares for 2.00 K, open circles for 6.00 K). The data are plotted using the reduced $m(h_0)$ representation. The region of h_0 values up to 0.35 has been chosen to show the irreversible part of the hysteresis cycles in detail.

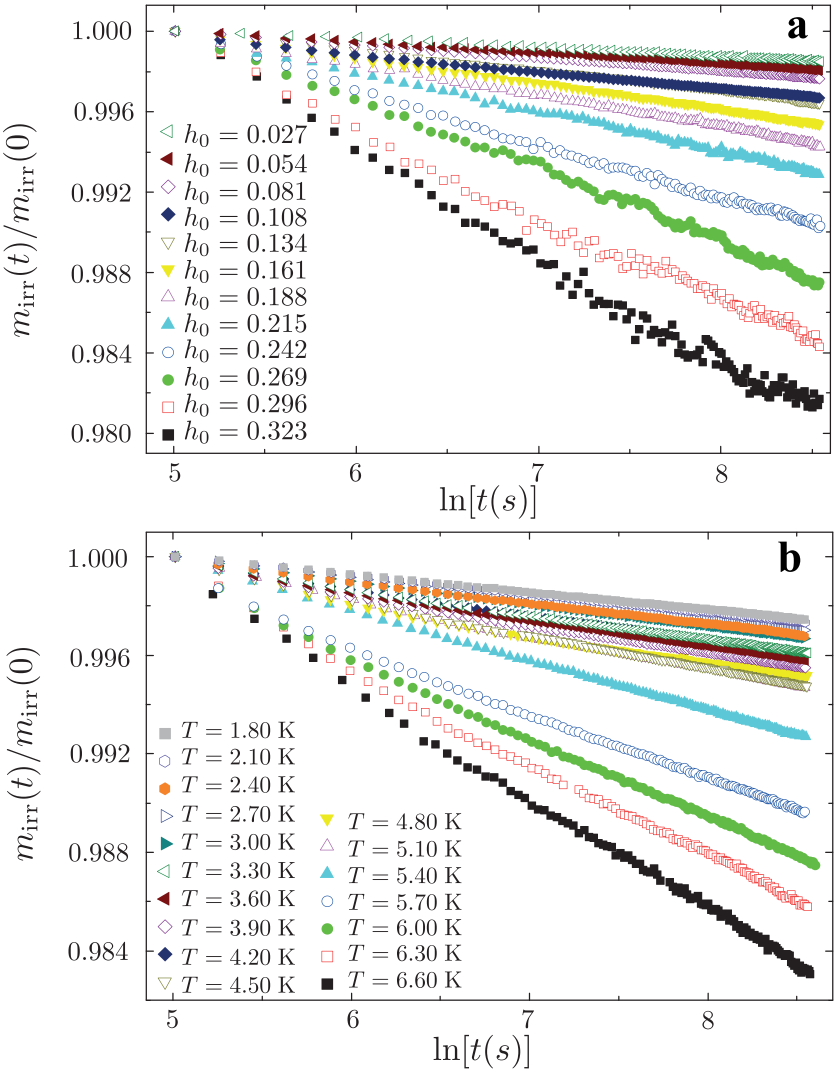

Figure 1.15: Logarithmic time evolution of the normalized reduced irreversible magnetization of the sample, $m_{\rm irr}(t)/m_{\rm irr}(0)$, (a) measured for different h_0 values from 0.027 (uppermost curve) to 0.323 (lowermost curve) in steps of 0.027 at $T =$ 2.00 K, and (b) at different T values from 1.80 K (uppermost curve) to 6.60 K (lowermost curve) in steps of 0.30 K for $h_0 = 0.10$.

provide a multiplicity of metastable states along $m_{\text{des}}(h_0)$ that would originate time-dependent phenomena just as in magnetic materials [32]. For a broad distribution of barriers, as it should be expected in this sample according to the preparation procedure, the reduced irreversible magnetization, m_{irr}, should evolve with time following a logarithmic dependence. Such magnetization is defined as $m_{\text{irr}}(t) \equiv m(t) - m_{\text{eq}}$ and is considered as the amount of reduced magnetization, $m(t)$, that deviates from the magnetic equilibrium state, m_{eq}, which is given by the appropriate $m_{\text{FC}}(h_0)$ value. Panel (a) in Fig. 1.15 shows $m_{\text{irr}}(t)/m_{\text{irr}}(0)$ as a function of $\ln(t)$ for several h_0 values from 0.027 (uppermost curve) to 0.323 (lowermost curve) in steps of 0.027 at $T = 2.00$ K, whereas panel (b) shows the same representation at different T values from 1.80 K (uppermost curve) to 6.60 K (lowermost curve) in steps of 0.30 K for $h_0 = 0.10$. A good linear dependence is observed for all curves in both panels and is also found for all combinations of h_0 and T values explored. Fitting of the whole data set to the law $m_{\text{irr}}(t) = m_{\text{irr}}(0)[1 - S\ln(t)]$ determines the dependence of the magnetic viscosity on temperature and reduced magnetic field, $S(T, h_0)$.

Panel (a) in Fig. 1.16 shows the $S(T)$ curves obtained for $h_0 = 0.00$ (squares), $h_0 = 0.10$ (circles), $h_0 = 0.15$ (upward triangles), $h_0 = 0.20$ (downward triangles), and $h_0 = 0.25$ (rhombuses), while panel (b) shows the $S(h_0)$ curves obtained at $T = 2.00$ K (squares), $T = 4.00$ K (circles), and $T = 5.00$ K (upward triangles). As T increases, two regimes can be identified in panel (a) for all h_0 values but 0.25: S exhibits a practically constant plateau, S_Q, up to some critical temperature T_Q, above which it increases with T. The behavior of $S(T)$ in the second regime is the common signature of thermal activation processes, while the occurrence of S_Q is an indication that magnetic relaxation in the first regime should be ascribed to quantum phenomena instead [32]. The value of the plateau changes progressively from $S_Q(0.00) \sim 0.0005$ to $S_Q(0.20) \sim 0.0020$, whereas the crossover temperature tends to decrease from $T_Q(0.00) \sim 5.4$ K to $T_Q(0.20) \sim 4.0$ K. At the same time, the slope of $S(T)$ above T_Q grows as h_0 increases. In particular, only the increasing regime in $S(T)$ can be observed for $h_0 = 0.25$ in the whole temperature range of our experiments. The shape of the curve in this case prompts to estimate T_Q at somewhere around 2.0 K. On the other hand, two successive regimes can be also distinguished in panel (b): as h_0 increases, the three curves superimpose onto a single one that rises slowly up to $h_0 \sim 0.12$, while above this value they separate progressively and become steeper. In particular, the curve at $T = 5.00$ K deviates at $h_0 \sim 0.12$, whereas the curve at $T = 4.00$ K deflects at $h_0 \sim 0.17$, indicating that these h_0 values determine the crossover reduced magnetic field strength, h_Q, that separates the quantum and thermal regimes at these temperatures. In conformity with what has been remarked for panel (a), the first increasing region of $S(h_0)$ in panel (b) shows actually the dependence of the tunneling rate on the reduced

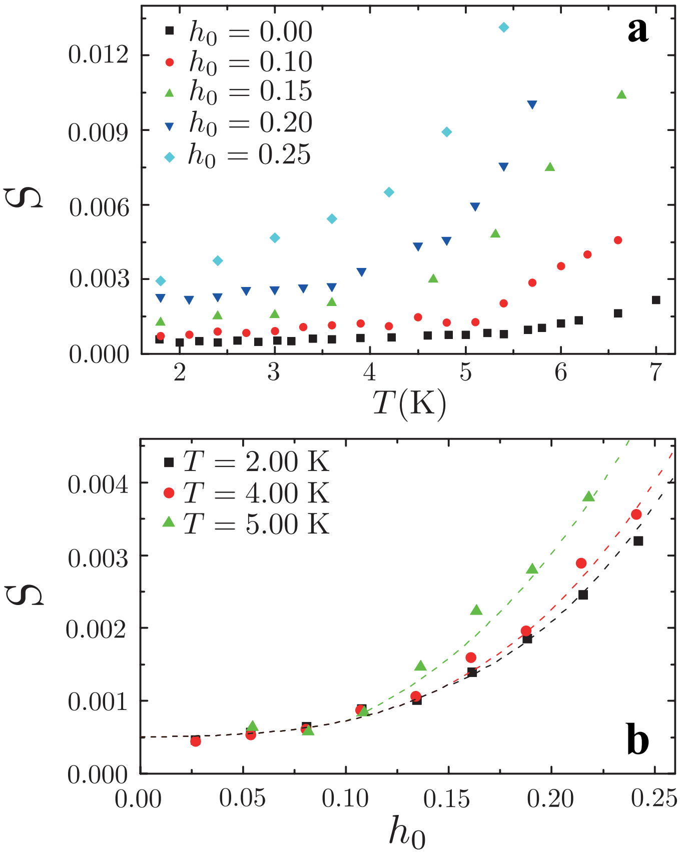

Figure 1.16: (a) Temperature dependence of the magnetic viscosity, $S(T)$, obtained for $h_0 = 0.00$ (squares), $h_0 = 0.10$ (circles), $h_0 = 0.15$ (upward triangles), $h_0 = 0.20$ (downward triangles), and $h_0 = 0.25$ (rhombuses). (b) Reduced magnetic field dependence of the magnetic viscosity, $S(h_0)$, obtained for $T = 2.00$ K (squares), $T = 4.00$ K (circles), and $T = 5.00$ K (upward triangles). The dashed lines are guides to the eye.

magnetic field strength, $S_Q(h_0)$.

1.4.2 Discussion

The origin of a remnant magnetic state that relaxes towards equilibrium lies in the capability of stress defects to pin the N-S interfaces when the magnetic field is reduced from the normal state in a magnetic history dependent process. The onset of such state along $m_{\text{des}}(h_0)$ takes place at a certain temperature-dependent magnetic field strength, the so-called reduced irreversibility field, $h^\star(T)$, that can be identified experimentally as the point at which $m_{\text{des}}(h_0)$ departs from $m_{1\text{st}}(h_0)$ [31]. According to the discussion conducted in Ref. [31], the decreasing dependence of $h^\star$ on temperature implies that the increment of the strength of the applied magnetic field has an important influence on the reduction of the strength of the pinning energy barriers that control metastability. Therefore, the motion of normal-superconducting interfaces along the sample would be less obstructed by defects and, as a consequence, the magnetization should evolve faster with time. This would explain why the slope of $S(T)$ in the thermal regime and the value of S_Q grow as h_0 increases in Fig. 1.15.

Within the framework of Chudnovsky's model [28], magnetic relaxation in type-I superconductors occurs due to the formation and decay of bumps at the N-S interfaces when they are pinned at the defects. These bumps are characterized by a lateral size L and a height $\bar{a}$, which should both depend on the field strength h_0. The energy barrier associated with the bump is independent of $L(h_0)$ and can be generally expressed as $U_B(h) = \sigma\pi[\bar{a}(h_0)]^2$, where $\sigma = \xi_{\text{GL}} H_c^2/(3\sqrt{2}\pi)$ is the surface tension of the interface, which actually does not depend on the magnetic field. The theoretical expression for the magnetic viscosity in the quantum regime is given by $S_Q(h_0) = A(h_0)e^{-I_{\text{eff}}(h_0)/\hbar}$, where the prefactor can be assumed to contribute much less than the exponent, which is dominated by the dissipative term of the Caldeira-Leggett effective action, $I_{\text{eff}}(h) \approx (\eta/4\pi)[L(h_0)\bar{a}(h_0)]^2$. Here $\eta = \sqrt{\lambda_L \xi_{\text{GL}}} H_c^2/(2\rho_n c^2)$ is the drag coefficient and ρ_n is the normal-state resistivity, which can be considered magnetic field independent in the present experimental conditions [33]. Consequently, η does not depend on h_0, and $L(h_0)$ and $\bar{a}(h_0)$ can be established in terms of their zero magnetic field values as

$$\frac{U_B(h_0)}{U_B(0)} = \left[\frac{\bar{a}(h_0)}{\bar{a}(0)}\right]^2, \quad \frac{T_Q(h_0)}{T_Q(0)} = \left[\frac{L(0)}{L(h_0)}\right]^2, \tag{1.66}$$

where the energy barrier and the crossover temperature are related via the expression $T_Q = \hbar U_B/k_{\text{B}} I_{\text{eff}}$. As it has been discussed, both U_B and T_Q decrease as h_0 increases, and this translates through Eq. (1.66) into a reduction of the height $\bar{a}(h_0)$ and an enlargement of the lateral size $L(h_0)$ of the bump. Therefore, the main effect of the increment of the magnetic field is to flatten the bumps of the N-S interfaces pinned by the defects, so for large values of h_0 the energy barrier becomes weak enough to avoid the experimental observation of T_Q, as it happens in Fig. 1.16a for $h_0 = 0.25$.

Finally, the increasing dependence observed experimentally for $S_Q(h_0)$ in Fig. 1.16 implies that $I_{\text{eff}}(h_0)$ should be a decreasing function. Considering the expression given above for $I_{\text{eff}}(h_0)$ and taking into account Eq. (1.66), we may then infer that the ratio $U_B(h_0)/T_Q(h_0)$ should also show a decreasing dependence. As both T_Q and U_B diminish with h_0, if this relation is to be fulfilled in the h_0 range of Fig. 1.16, the variation of $U_B(h_0)$ should be steeper than that of $T_Q(h_0)$. This appears to be supported by the behavior of the curves in Fig. 1.16a: As h_0 goes from 0.00 to 0.20, the decrease in the value of T_Q turns out to be slower than the increase in the slope of $S(T)$ above T_Q, which should be in fact related with the decrease of U_B if thermal activation processes are positively involved in this regime. Further experimental work is needed to confirm the validity of this conjecture.

Chapter 2

Quantum tunneling in type-I superconductors

2.1 Macroscopic quantum tunneling

2.1.1 Introduction

Macroscopic quantum tunneling refers to the situation when an object consisting of many degrees of freedom, coupled to a dissipative environment, escapes from a metastable well via underbarrier quantum tunneling [34, 35]. In condensed matter this phenomenon was first observed through measurements of tunneling of the macroscopic magnetic flux created by a superconducting current in a circuit interrupted by a Josephson junction [36]. Another example is tunneling of magnetization in solids [32]. In cases of the magnetic flux or the magnetic moment of a nanoparticle, the tunneling object is described by one or two macroscopic coordinates that depend on time, like in a problem of a tunneling particle in quantum mechanics. The environment enters the problem through interaction of these macroscopic coordinates with microscopic excitations of the medium. Equally interesting, but significantly more involved, is the problem of tunneling of a macroscopic field between two distinct configurations. Most common examples are tunneling of vortex lines in type-II superconductors [37–39] and tunneling of domain walls in magnets [40–42]. The essential difference between the last two examples is that tunneling of vortex lines is determined by their predominantly dissipative dynamics [43–47], while tunneling of the spin-field is affected by dissipation to a much lesser degree. Recently, a conceptually similar problem of the escape of a fractional vortex from the long Josephson junction has been studied [48, 49]. Theory that describes quantum tunneling of extended condensed-matter objects involves space-time instantons that are similar to the instantons studied in relativistic field models [50, 51]. Examples that are available for experimental

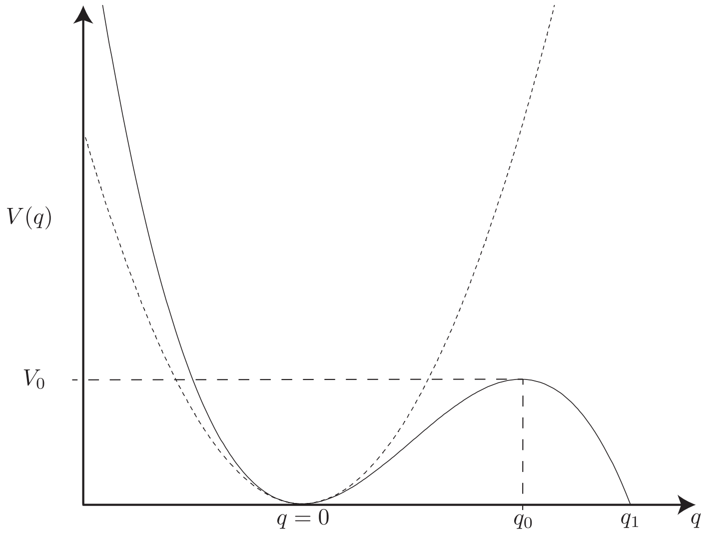

Figure 2.1: Metastable potential for a one-dimensional system.

studies are limited. Consequently, any new example of tunneling of an extended object must be of significant interest.

Before proceeding to develop the theoretical framework concerning macroscopic quantum tunneling, it is important to make some considerations about the problem itself. To simplify the discussion the case of a one-dimensional system will be considered, but the conclusions can be straightforwardly extended to higher dimensions or even to a field-theory description of the system. Therefore, consider a *macroscopic* one-dimensional system (described by a variable q) in a potential of the kind given by Fig. 2.1. In the present framework, the term 'macroscopic' must be understood as the system being large enough to behave classically during most of the measurement (observation) time. Equivalently, quantum transitions must be very rare. With respect to the potential depicted in Fig. 2.1, this condition translates into the probability of underbarrier quantum tunneling being quite small. Furthermore, the system is assumed to be weakly perturbed by the interaction with the measuring devices due to its macroscopic character. This means that the value of q is not driven far away from its measured value as a result of the observation process.

Secondly, the system is initially driven into *metastability*, so that it is prepared in a state consisting of low-lying *energy levels* near the bottom of the metastable well ($q = 0$ in Fig. 2.1). The very existence of this metastable state implies that the probability of thermal barrier hopping is also small. The corresponding transition rate Γ at a temperature T, defined as the probability per unit time of thermal fluctuations driving the system over the energy barrier, has the following Arrhenius-like dependence on the ratio $V_0/k_\mathrm{B}T$ [52]:

$$\Gamma = \frac{\omega_0}{2\pi}\exp\left(-\frac{V_0}{k_B T}\right), \tag{2.1}$$

where V_0 is the height of the energy barrier and ω_0 is the frequency associated to the harmonic approximation of the energy potential near $q = 0$. Thus, a long lifetime of the metastable state requires the thermal energy to be small compared to V_0. Thirdly, in the case of q representing a position of space, solution of the Schödinger equation with account of the potential $V(q)$ leads to a set of nonlocalized eigenstates on the left-hand side of the barrier. Hence, the concept of 'energy levels of the metastable state' proposed in the second hypothesis of the macroscopic quantum tunneling problem appears to be misleading. In fact, this setback can be overcome by considering the harmonic approximation of the potential well in the case of Fig. 2.1 (see dashed line) or, in a more general situation, an infinite barrier approximating the potential well to the left of the barrier near its bottom. This guarantees the locality of the eigenstates and therefore a correct definition of the energy levels.

To conclude, the last of the assumptions consists of the system being in thermal equilibrium with a thermal bath at temperature T. This means by definition that the system interacts with the environment and that this interaction is responsible for the thermalization. Notice that it should be strong enough to bring the system to (thermal) equilibrium during the lifetime of the metastable state, a requirement equivalent to the condition $\Gamma\tau_\mathrm{R} \ll 1$, with τ_R being the thermal relaxation time. For a macroscopic system this condition usually holds due to the exponential smallness of Γ, as it will be shown later [Eq. (2.1) proves this statement in the thermal regime case]. On the other hand, the time-energy uncertainty relation yields the width $\Delta E \sim \hbar/\tau_\mathrm{R}$ in the energy of the system, which is non-zero for finite values of τ_R. The description of the system changes drastically depending on whether the spacing between the energy levels ($\hbar\omega_0$ according to the harmonic approximation of the metastable well, Fig. 2.1) is greater than this width or not: If the inequality $\omega_0\tau_\mathrm{R} \gg 1$ holds, the effect of the interaction with the environment reduces to the system being in a mixed state according to the thermal (Boltzmann) distribution over well-defined energy levels of finite width. On the contrary, the condition $\omega_0\tau_\mathrm{R} \ll 1$ implies such a broad blurring of the energy levels that a correct description of the system requires the environmental degrees of freedom to be taken into consideration explicitely. The former represents the case of main interest in the macroscopic quantum tunneling problem.

2.1.2 Transition rate from a metastable state

Consider a macroscopic system described by a Hamiltonian $\hat{\mathcal{H}}_\mathrm{s} = \hat{\mathcal{H}}_0 + \hat{V}$, where the operator $\hat{V}$ represents a perturbative potential. Let $\{|n\rangle\}$ and $\{\epsilon_n\}$ be respectively the set of eigenstates and eigenvalues of the time-independent hamiltonian $\hat{\mathcal{H}}_0$. For the sake of simplicity, a time-independent perturbation will be considered in the following derivation. Assume that initially the system is prepared in the state $|\Psi(0)\rangle = |n\rangle$, where $|\psi(t)\rangle$ represents the system wavefunction at $t \geq 0$. The probability of remaining in the state $|n\rangle$ is given by

$$P_{n,n}(t) = |\langle n|\Psi(t)\rangle|^2 \,. \tag{2.2}$$

The probability amplitudes can be factorized as the products $\langle m|\Psi(t)\rangle = e^{-i\epsilon_m t/\hbar} c_m(t), \forall m$. The function c_n satisfies the Schrödinger equation

$$i\hbar \dot{c}_n(t) = \sum_m e^{i\omega_{nm}t} V_{nm} c_m(t), \tag{2.3}$$

where $\omega_{nm} = (\epsilon_n - \epsilon_m)/\hbar$ is the transition frequency between the (n,m)-th levels and $V_{nm} = \langle n|\hat{V}|m\rangle$. According to the perturbative nature of the operator $\hat{V}$, perturbation theory leads to the following asymptotic expansions for the functions c_m:

$$\begin{aligned} c_n(t) &= 1 + c_n^{(1)}(t) + c_n^{(2)}(t) + \ldots, \\ c_m(t) &= c_m^{(1)}(t) + c_m^{(2)}(t) + \ldots, \qquad \forall m \neq n \end{aligned} \tag{2.4}$$

where $c_k^{(p)}(t) = O(\hat{V}^p)\ \forall k$ describes the p-th order perturbative term. Notice that the initial conditions $c_m(0) = \delta_{nm}\ \forall m$ have been used. Therefore, Eq. (2.3) becomes

$$\begin{aligned} i\hbar \frac{d}{dt} \ln c_n(t) &= i\hbar \frac{\dot{c}_n(t)}{c_n(t)} = V_{nn} + \sum_{m\neq n} e^{i\omega_{nm}t} V_{nm} \frac{c_m(t)}{c_n(t)} \\ &= V_{nn} + \sum_{m\neq n} e^{i\omega_{nm}t} V_{nm} \frac{c_m^{(1)}(t)}{1} + O(\hat{V}^3), \end{aligned} \tag{2.5}$$

where only the lowest orders in the perturbative expansions of the functions c_m have been considered. With account of the expressions for the first order terms in Eq. (2.5) [53], the above equation becomes

$$i\hbar \frac{d}{dt} \ln c_n(t) = V_{nn} + \sum_{m\neq n} \frac{|V_{nm}|^2}{i\hbar} \int_0^t du\, e^{-i\omega_{mn}u}. \tag{2.6}$$

At this point one consideration should be made: The above integrals diverge in the regime $t \gg 1$ for the case of (quasi)resonant energy levels. Distribution theory must be invoked to deal with these divergences, so that one obtains the identities

$$\frac{1}{i\hbar}\int_0^t \mathrm{d}u\, e^{-i\omega_{mn}u} = \lim_{\eta\to 0}\frac{1}{\epsilon_n-\epsilon_m+i\hbar\eta}, \qquad t \gg 1, \tag{2.7}$$

where the limit must be understood in a distributional sense. For transitions from a discrete state to a continuum spectrum (which corresponds to the case of the energy barrier depicted in Fig. 2.1), the Sokhotski-Plemelj theorem (see Appendix B) leads to the identity between distributions

$$\lim_{\eta\to 0}\frac{1}{\epsilon_n-\epsilon_m+i\hbar\eta} = \mathcal{P}\left(\frac{1}{\epsilon_n-\epsilon_m}\right) - i\pi\delta(\epsilon_n-\epsilon_m), \tag{2.8}$$

where $\mathcal{P}$ stands for the Cauchy principal value prescription. Therefore, Eq. (2.6) becomes

$$\begin{aligned} i\hbar\frac{d}{dt}\ln c_n(t) &= \Delta_n \Rightarrow c_n(t) = c_n(0)e^{-i\Delta_n t/\hbar} = e^{-i\Delta_n t/\hbar} \qquad t \gg 1 \\ \mathrm{Re}\ \Delta_\mathrm{n} &= V_{nn} + \mathcal{P}\sum_{m\neq n}\frac{|V_{nm}|^2}{\epsilon_n-\epsilon_m} + O(\hat{V}^3) \equiv E_n - \epsilon_n \\ \mathrm{Im}\ \Delta_\mathrm{n} &= -\frac{\hbar}{2}\left(\frac{2\pi}{\hbar}\sum_{m\neq n}|V_{nm}|^2\delta(\epsilon_n-\epsilon_m)\right) \equiv -\frac{\hbar}{2}\Gamma_n, \end{aligned} \tag{2.9}$$

where the sums mean integration over the energy domain. Notice that E_n is analogous to the perturbative correction (up to second order) for the energy of the state $|n\rangle$ in the case of the non-degenerate time-independent perturbation theory and that Γ_n represents Fermi's second golden rule. Consequently, the probability amplitude of the state $|n\rangle$ turns out to be

$$\langle n|\Psi(t)\rangle = e^{-i\epsilon_n t/\hbar}c_n(t) = e^{-iE_n t/\hbar}e^{-\Gamma_n t/2} \tag{2.10}$$

and hence the dwell probability becomes

$$P_{nn}(t) = \exp\left(-\Gamma_n t\right), \tag{2.11}$$

that is, it decays exponentially. This dependence is typical of the intermediate time scale and is characterized by Γ_n, the rate of escape out of the state $|n\rangle$. For practical purposes (time scale of observation/measurement) this dependence remains always valid. Notice that the time evolution of $|n\rangle$ (eigenstate of $\hat{\mathcal{H}}_0$) is given by $e^{-i(E_n-i\hbar\Gamma_n/2)t/\hbar}|n\rangle$ (plus other perturbative corrections associated with the remaining eigenstates). In analogy with the time evolution of the eigenstates of $\hat{\mathcal{H}}_{\rm s}$, $|E\rangle \to e^{-iEt/\hbar}|E\rangle$, the energy of the state $|n\rangle$ appears to be a complex scalar with imaginary part $-\hbar\Gamma_n/2$. This identification is rather formal and (along with the analytical continuation of the free energy) provides a unified framework to study both the true thermodynamic equilibrium and the long-living metastability.

The exponential decay with time of the dwell probability is a general feature of the metastable states of macroscopic systems, whether the transition/escape mechanism is of (pure) quantum origin or thermally assisted: In the regime $\omega_0\tau_{\rm R} \gg 1$ considered, every metastable state is characterized by an energy E_n (with the corresponding width ΔE_n due to the interaction with the environment) and by a transition rate Γ_n. Furthermore, the decay of the metastable states occurs according to the law (2.11) and this behaviour is found at any temperature T of the bath. Two competing mechanisms contribute to the escape rate out of a metastable state, namely the quantum diffusion through the energy barrier (for instance, see the above derivation of Γ_n) and the barrier hopping assisted by thermal fluctuations. The transition from the quantum to the thermal regime occurs at the so-called *crossover temperature* $T_{\rm cr}$.

A complex energy associated with the eigenstates of the metastable well, $\Delta_n = E_n - i\frac{\hbar}{2}\Gamma_n$, can be formally introduced to treat both magnitudes in a unified manner. This leads to a complex extension of the Hamitonian of the macroscopic system over the basis $\{|n\rangle\}$ of states corresponding to the energy levels of the metastable well, which is given by $\hat{\mathcal{H}}_{\rm s}|n\rangle = \Delta_n|n\rangle\ \forall n$. On the other hand, the system of interest is not isolated but weakly coupled (in the sense specified in the next subsection) to a dissipative system, namely the thermal bath. Such a situation is properly described by means of the density matrix formalism: The macroscopic system in consideration can be embedded into an extended one (system + environment) that is described by the Hamiltonian $\mathcal{H} = \mathcal{H}_{\rm s} + \mathcal{H}_{\rm b} + \mathcal{H}_{\rm int}$, where $\mathcal{H}_{\rm b}$ and $\mathcal{H}_{\rm int}$ represent respectively the Hamiltonian of the thermal bath and the weak interaction between the environment and the system. Only physical observables measured on the macroscopic subsystem are of interest, so that the reduced density operator for the subsystem, $\hat{\rho}_{\rm s}$, provides a complete description of the problem. It is obtained from the partial trace $\hat{\rho}_{\rm s} = {\rm Tr}_{W_{\rm b}^H}[\hat{\rho}]$, where $\hat{\rho}$ is the density matrix operator for the extended system and $W_{\rm b}^H$ is the Hilbert space of states of the environment. Its time evolution is ruled by the density matrix equation [54]

$$\begin{aligned} \frac{d}{dt}\hat{\rho}_{\rm s} &= -\frac{i}{\hbar}\left[\hat{\mathcal{H}}_{\rm s}, \hat{\rho}_{\rm s}\right] + \mathcal{R}[\hat{\rho}_{\rm s}], \qquad (2.12) \\ \mathcal{R}[\hat{\rho}_{\rm s}](t) &\equiv -\frac{1}{\hbar^2}\int_0^t {\rm d}\tau\ \frac{1}{\mathcal{Z}_{\rm b}}{\rm Tr}_{\rm W_b^H}\left[\hat{\mathcal{H}}_{\rm int}, \left[\hat{\mathcal{H}}_{\rm int}(-\tau)_{\rm I}, \hat{\rho}_{\rm s}\exp(-\beta\hat{\mathcal{H}}_{\rm b})\right]\right], \end{aligned}$$

where $\beta = 1/k_{\mathrm{B}}T$ is the reciprocal of the thermal energy, $\mathcal{Z}_{\mathrm{b}} = \mathrm{Tr}_{W_{\mathrm{b}}^{H}}\left[e^{-\beta\hat{\mathcal{H}}_{\mathrm{b}}}\right]$ is the partition function of the thermal bath, $\hat{\mathcal{H}}_{\mathrm{int}}(\tau)_I = \hat{U}_0^{\dagger}(\tau)\hat{\mathcal{H}}_{\mathrm{int}}\hat{U}_0(\tau)$ is the coupling Hamiltonian in the interaction picture and $\hat{U}_0(\tau) = e^{-i(\hat{\mathcal{H}}_{\mathrm{s}}+\hat{\mathcal{H}}_{\mathrm{b}})\tau/\hbar}$. The commutator in the above equation represents the conservative term whereas the second term describes the relaxation of the subsystem in consideration. A detailed analysis of the projection of Eq. (2.12) onto the adiabatic basis of the macroscopic subsystem leads to its equilibrium solution being

$$\hat{\rho}_{\mathrm{s}}^{\mathrm{eq}} = \frac{e^{-\beta\hat{\mathcal{H}}_{\mathrm{s}}}}{\mathcal{Z}_{\mathrm{s}}}, \quad \mathcal{Z}_{\mathrm{s}} = \mathrm{Tr}_{W_{\mathrm{s}}^{H}}\left[e^{-\beta\hat{\mathcal{H}}_{\mathrm{s}}}\right], \tag{2.13}$$

which is known as the *statistical operator*. As before, $\mathcal{Z}_{\mathrm{s}}$ and W_{s}^{H} represent respectively the partition function and the Hilbert space of states associated with the mestastable well of the macroscopic subsystem. The transition rate can be defined as the physical observable $\hat{\Gamma} = -\frac{2}{\hbar}\mathrm{Im}\,\hat{\mathcal{H}}_{\mathrm{s}}$. With account of the analytical continuation of the partition function, the expectation value of the transition rate out of the metastable state can be obtained by means of the expression

$$\Gamma \equiv \langle\hat{\Gamma}\rangle = \mathrm{Tr}_{\mathrm{W}_{\mathrm{s}}^{\mathrm{H}}}\left[\hat{\rho}_{\mathrm{s}}\hat{\Gamma}\right] = \frac{\sum_{\mathrm{n}}\Gamma_{\mathrm{n}}\mathrm{e}^{-\beta\Delta_{\mathrm{n}}}}{\mathcal{Z}_{\mathrm{s}}}, \tag{2.14}$$

which is the Boltzmann average of the rates of escape Γ_n. The analytical continuation of the Helmholtz free energy is obtained through the relation $\mathcal{F}_{\mathrm{s}} = -\frac{1}{\beta}\ln\mathcal{Z}_{\mathrm{s}}$. With account of the exponentially smallness of $\mathrm{Im}\,\Delta_n$, expansion of the imaginary part of the free energy leads to the identity $\mathrm{Im}\,\mathcal{F}_{\mathrm{s}} = \sum_n \mathrm{Im}(\Delta_n)e^{-\beta\Delta_n}/\mathcal{Z}_{\mathrm{s}}$, from which the following simple expression for the transition rate is obtained [50, 51, 55, 56]:

$$\Gamma = -\frac{2}{\hbar}\mathrm{Im}\,\mathcal{F}_{\mathrm{s}}. \tag{2.15}$$

Taking into consideration the expansion of the complex logarithm for exponentially small values of the imaginary part of its argument, the above formula can be recast as

$$\Gamma = \frac{2}{\hbar\beta}\frac{\mathrm{Im}\,\mathcal{Z}_{\mathrm{s}}}{\mathrm{Re}\,\mathcal{Z}_{\mathrm{s}}}. \tag{2.16}$$

As commented in the introduction, the applicability of these results extends beyond the class of problems for which they have been derived. In fact, these formulas allow the calculation of the transition rate out of any metastable state within the framework of quantum field theory, provided that it is small and that the system has thermalized with the environment. In the next subsection, a path-integral formulation of these calculations is provided.

2.1.3 Path-integral formulation

A profound connection between quantum field theory and statistical mechanics arises from the notion of Wick rotation: This geometric transformation acts on spacetime, leaving the n-dimensional coordinate space invariant and transforming the time domain according to $t \to \tau = it$, where t is the ordinary time coordinate. This shift of the time coordinate to pure imaginary values leads to a formal equivalence between the geometries of the Minkowski manifold $(\mathbf{R}^{n+1}, g^{\mathrm{M}})$ and the Euclidean manifold $(\mathbf{R}^{n+1}, g^{\mathrm{E}})$, where the corresponding metrics are given by $g^{\mathrm{M}}_{\alpha\beta} = \mathrm{diag}(-1, 1, \overset{(n)}{\ldots}, 1)$ (Minkowski) and $g^{\mathrm{E}}_{\alpha\beta} = \mathrm{diag}(1, \overset{(n+1)}{\ldots}, 1)$ (Euclidean) on the orthogonal basis. This fact was pointed out in 1906 by H. Poincaré in the context of special relativity [57].

Let $\hat{U}(t, t')$ be the time evolution operator of the macroscopic subsystem. Assuming the time independence of its Hamiltonian, the propagator has the form $\hat{U}(t, t') = e^{-i\mathcal{H}_{\mathrm{s}}(t-t')/\hbar}$. Application of the Wick rotation to the propagator of the subsystem yields the correspondence

$$\hat{U}(t, 0) = e^{-i\mathcal{H}_{\mathrm{s}}t/\hbar} \xleftrightarrow{\text{Wick}} e^{-\mathcal{H}_{\mathrm{s}}\tau/\hbar} \xleftrightarrow{\tau\equiv\hbar\beta} e^{-\beta\mathcal{H}_{\mathrm{s}}}, \tag{2.17}$$

where the right-hand side term is the Boltzmann factor. Let $\{x_\alpha\}_\alpha$ be the set of coordinates of the thermal bath. A well-known result from Feynman's path integral formulation of quantum mechanics is that the transition amplitude for the extended system to go from coordinates $(q_i, \{x_{\alpha,i}\}_\alpha)$ at time $t = t_i$ to $(q_f, \{x_{\alpha,f}\}_\alpha)$ at time $t = t_f$ is given by the path integral

$$\left\langle q_f, \{x_{\alpha,f}\}_\alpha \left| e^{-i\hat{\mathcal{H}}(t_f - t_i)/\hbar} \right| q_i, \{x_{\alpha,i}\}_\alpha \right\rangle = \int_{q(t_i)=q_i}^{q(t_f)=q_f} \mathcal{D}[q(t)] \tag{2.18}$$
$$\prod_\alpha \int_{x_\alpha(t_i)=x_{\alpha,i}}^{x_\alpha(t_f)=x_{\alpha,f}} \mathcal{D}[x_\alpha(t)] \exp\left(\frac{i}{\hbar} \int_{t_i}^{t_f} \mathrm{d}t \, \mathcal{L}(q, \dot{q}, \{x_\alpha\}, \{\dot{x}_\alpha\}, t) \right),$$

with $\mathcal{L}$ being the Lagrangian of the extended system and $\dot{q}$ $(\dot{x}_\alpha)$ representing (ordinary) time derivative of the coordinate q (x_α). With account of the correspondence (2.17) the euclidean version of the above Green's function is obtained,

$$\left\langle q_f, \{x_{\alpha,f}\}_\alpha \left| e^{-\hat{\mathcal{H}}(\tau_f - \tau_i)/\hbar} \right| q_i, \{x_{\alpha,i}\}_\alpha \right\rangle = \int_{q(\tau_i)=q_i}^{q(\tau_f)=q_f} \mathcal{D}[q(\tau)] \times \tag{2.19}$$
$$\prod_\alpha \int_{x_\alpha(\tau_i)=x_{\alpha,i}}^{x_\alpha(\tau_f)=x_{\alpha,f}} \mathcal{D}[x_\alpha(\tau)] \exp\left(-\frac{1}{\hbar} \int_{\tau_i}^{\tau_f} \mathrm{d}\tau \, \mathcal{L}_{\mathrm{E}}(q, \dot{q}_\tau, \{x_\alpha\}, \{\dot{x}_{\alpha,\tau}\}, \tau) \right),$$

where $\mathcal{L}_{\mathrm{E}} \equiv -\mathcal{L}[t \to -i\tau]$ is the euclidean version of the total Lagrangian and $\dot{q}_\tau$ $(\dot{x}_{\alpha,\tau})$ represents the derivative with respect to τ of the coordinate q (x_α).

The extended system is assumed to be very weakly coupled to some *super-bath*, so that it does not behave like an isolated system in a pure quantum state but like a system in a mixed state in equilibrium at the temperature of the bath. Then, according to the discussion leading to Eq. (2.13), the density matrix operator associated with the extended system is $\hat{\rho} = e^{-\beta\hat{\mathcal{H}}}/\mathrm{Tr}_{W^H}\left[e^{-\beta\hat{\mathcal{H}}}\right]$, with $W^H = W^H_{\mathrm{s}} \otimes W^H_{\mathrm{b}}$ being the Hilbert space of states of the extended system. Therefore, the reduced density matrix operator $\hat{\rho}_{\mathrm{s}}$ becomes

$$\hat{\rho}_{\mathrm{s}} = \mathrm{Tr}_{W^H_{\mathrm{b}}}[\hat{\rho}] = \frac{\mathrm{Tr}_{W^H_{\mathrm{b}}}\left[e^{-\beta\hat{\mathcal{H}}}\right]}{\mathrm{Tr}_{W^H}\left[e^{-\beta\hat{\mathcal{H}}}\right]} \overset{\text{Equilibrium}}{\Longrightarrow} \rho^{\mathrm{eq}}_{\mathrm{s}}. \tag{2.20}$$

With account of the identity $\mathrm{Tr}_{W^H}[\,\cdot\,] = \mathrm{Tr}_{W^H_{\mathrm{s}}}\left[\mathrm{Tr}_{W^H_{\mathrm{b}}}[\,\cdot\,]\right]$ and the definition (2.13) of the equilibrium reduced density operator $\hat{\rho}^{\mathrm{eq}}_{\mathrm{s}}$, the correspondence $\mathrm{Tr}_{W^H_{\mathrm{b}}}\left[e^{-\beta\hat{\mathcal{H}}}\right] \equiv e^{-\beta\hat{\mathcal{H}}_{\mathrm{s}}}$ can be derived. Completeness of the bases of system and environmental coordinates, $\{|q\rangle\}$ and $\{|x_\alpha\rangle\}_\alpha$, yields the following expression for the partition function of the macroscopic subsystem:

$$\begin{aligned} \mathcal{Z}_{\mathrm{s}} &= \mathrm{Tr}_{W^H_{\mathrm{s}}}\left[e^{-\beta\hat{\mathcal{H}}_{\mathrm{s}}}\right] = \mathrm{Tr}_{W^H}\left[e^{-\beta\hat{\mathcal{H}}}\right] \\ &= \int \mathrm{d}q \prod_\alpha \int \mathrm{d}x_\alpha \left\langle q, \{x_\alpha\}_\alpha \middle| e^{-\beta\hat{\mathcal{H}}} \middle| q, \{x_\alpha\}_\alpha \right\rangle, \end{aligned} \tag{2.21}$$

which, considering Eq. (2.19), leads to the formula

$$\mathcal{Z}_{\mathrm{s}} = \oint \mathcal{D}[q(\tau)] \prod_\alpha \oint \mathcal{D}[x_\alpha(\tau)] \exp\left(-\frac{1}{\hbar}\int_0^{\hbar\beta} \mathrm{d}\tau\, \mathcal{L}_{\mathrm{E}}(q, \dot{q}_\tau, \{x_\alpha\}, \{\dot{x}_{\alpha,\tau}\}, \tau)\right), \tag{2.22}$$

where the path-integrals are done over all periodic trajectories $(q(\tau), \{x_\alpha(\tau)\}_\alpha)$ in the coordinate space with imaginary-time period $\tau_p = \hbar\beta$.

The Lagrangian of the extended system can be split into the sum $\mathcal{L} = \mathcal{L}_{\mathrm{s}} + \mathcal{L}_{\mathrm{b}} + \mathcal{L}_{\mathrm{int}}$, where $\mathcal{L}_{\mathrm{b}}$ is the Lagrangian of the thermal bath and $\mathcal{L}_{\mathrm{int}}$ describes the weak interaction between the macroscopic subsystem and the environment. In the case depicted in Fig. 2.1, the Lagrangian of the subsystem is of the form $\mathcal{L}_{\mathrm{s}} = \frac{1}{2}M\dot{q}^2 - V(q)$ with M being the corresponding mass. In the next subsection, a concise but general description of both the environment and its interaction with the system of interest will be provided, which in turn will lead to the derivation of the transition rate for dissipative systems.

2.1.4 Caldeira-Leggett theory

Linearity of the response of the environment to the macroscopic system is the keystone of the Caldeira-Leggett theory [34, 35, 58]. It is in this sense that the coupling between both physical systems is assumed to be *weak*. This assumption leads to the environment being described as a set of harmonic oscillators, whose Lagrangian is given by

$$\mathcal{L}_{\text{env}}\left(\{x_\alpha\}_\alpha, \{\dot{x}_\alpha\}_\alpha, t\right) = \sum_\alpha \left(\frac{1}{2} m_\alpha \dot{x}_\alpha^2 - \frac{1}{2} m_\alpha \omega_\alpha^2 x_\alpha^2\right), \tag{2.23}$$

where m_α, ω_α and x_α are the mass, the frequency and the coordinate of the α-th oscillator. Furthermore, the Lagrangian representing the interaction can be chosen linear in both q and $\{x_\alpha\}_\alpha$, that is

$$\mathcal{L}_{\text{int}}\left(q, \dot{q}, \{x_\alpha\}_\alpha, \{\dot{x}_\alpha\}_\alpha, t\right) = -q \sum_\alpha C_\alpha x_\alpha - q^2 \sum_\alpha \frac{C_\alpha^2}{2 m_\alpha \omega_\alpha^2}, \tag{2.24}$$

where $\{C_\alpha\}_\alpha$ are coupling constants. The last term on the right-hand side has been added to cancel the renormalization of the potential V due to the interaction of the system with the set of oscillators modeling the environment. Euler-Lagrange equations for the Lagrangian of the extended system result in the classical equations of motion for the coordinates $q, \{x_\alpha\}_\alpha$,

$$M\ddot{q} + \frac{dV}{dq} + q \sum_\alpha \frac{C_\alpha^2}{m_\alpha \omega_\alpha^2} + \sum_\alpha C_\alpha x_\alpha = 0, \tag{2.25}$$

$$m_\alpha \ddot{x}_\alpha + m_\alpha \omega_\alpha^2 x_\alpha + C_\alpha q = 0. \tag{2.26}$$

A formal solution of Eq. (2.25) is obtained from the Langevin equation

$$M\ddot{q} + M \int_0^t \mathrm{d}\sigma \gamma(t-\sigma) \dot{q}(\sigma) + \frac{dV}{dq} = \xi(t), \tag{2.27}$$

where $\xi(t)$ represents a fluctuating force (that depends on the initial conditions of both systems) and the damping kernel is given by the expression

$$\gamma(t) = \frac{1}{M} \sum_\alpha \frac{C_\alpha^2}{m_\alpha \omega_\alpha^2} \cos(\omega_\alpha t). \tag{2.28}$$

Within the framework of the present theory, it is also assumed that the expectation value $\langle q(t) \rangle$ of the coordinate of the macroscopic system obeys an equation of the form (2.27) when condition $V_0 - E \gg \hbar\omega_0$ holds for the energy E of this subsystem [34].

The Euclidean version of the Lagrangian of the extended system is given by

$$\begin{aligned}\mathcal{L}_{\mathrm{E}}\left(q,\dot{q}_\tau,\{x_\alpha\}_\alpha,\{\dot{x}_{\alpha,\tau}\}_\alpha,\tau\right) = \frac{1}{2}M\dot{q}_\tau^2 + V(q) + \frac{1}{2}\sum_\alpha m_\alpha\left(\dot{x}_{\alpha,\tau}^2+\omega_\alpha^2 x_\alpha^2\right) \\ + q\sum_\alpha C_\alpha x_\alpha + q^2\sum_\alpha \frac{C_\alpha^2}{2m_\alpha\omega_\alpha^2}.\end{aligned} \tag{2.29}$$

Gaussian integration of the path integrals over $x_\alpha(\tau)$ [see Appendix B] in Eq. (2.22) yields the following expression for the partition function of the system as a path integral over periodic $q(\tau)$-trajectories:

$$\mathcal{Z}_{\mathrm{s}} \propto \oint \mathcal{D}[q(\tau)]\exp(-S_{\mathrm{eff}}/\hbar), \tag{2.30}$$

where the effective action is given by

$$\begin{aligned}S_{\mathrm{eff}}\left[q(\tau)\right] = \int_0^{\hbar\beta}\mathrm{d}\tau\left[\frac{1}{2}M\dot{q}^2+V(q)+q^2\sum_\alpha\frac{C_\alpha^2}{2m_\alpha\omega_\alpha^2}\right] \\ -\int_0^{\hbar\beta}\mathrm{d}\tau\int_0^{\hbar\beta}\mathrm{d}\tau' q(\tau)q(\tau')\mathcal{G}(\tau,\tau').\end{aligned} \tag{2.31}$$

The integral kernel $\mathcal{G}(\tau,\tau')$ splits into the sum $\mathcal{G}(\tau,\tau') = \sum_\alpha \frac{C_\alpha^2}{2m_\alpha}\mathcal{G}_{\omega_\alpha}(\tau,\tau')$, where $\mathcal{G}_{\omega_\alpha}(\tau,\tau')$ is the Euclidean version of the Green's function for the harmonic oscillator of frequency ω_α,

$$\left[-\partial_\tau^2+\omega_\alpha^2\right]\mathcal{G}_{\omega_\alpha}(\tau,\tau') = \delta(\tau-\tau'). \tag{2.32}$$

Matsubara representation of these imaginary-time propagators leads to the formula $\mathcal{G}_{\omega_\alpha}(\tau,\tau') = \frac{1}{\hbar\beta}\sum_{n\in\mathbf{Z}} D_\alpha(i\nu_n)e^{i\nu_n(\tau-\tau')}$, where $D_\alpha(i\nu_n) = \dfrac{1}{\omega_\alpha^2-(i\nu_n)^2}$ are the Fourier coefficients of the propagators and $\nu_n = 2\pi n/\hbar\beta$, $\forall n\in\mathbf{Z}$ are the Matsubara frequencies. These propagators can be split into the sum $\mathcal{G}_{\omega_\alpha,1}(\tau,\tau') + \mathcal{G}_{\omega_\alpha,2}(\tau,\tau')$, where

$$\mathcal{G}_{\omega_\alpha,1}(\tau,\tau') = \frac{1}{\omega_\alpha^2}\sum_{n\in\mathbf{Z}}\delta(\tau-\tau'-n\hbar\beta) = \frac{1}{\hbar\beta\omega_\alpha^2}\sum_{n\in\mathbf{Z}}e^{i\nu_n(\tau-\tau')}, \tag{2.33}$$

$$\mathcal{G}_{\omega_\alpha,2}(\tau,\tau') = \frac{-1}{\hbar\beta\omega_\alpha^2}\sum_{n\in\mathbf{Z}}\frac{\nu_n^2}{\nu_n^2+\omega_\alpha^2}e^{i\nu_n(\tau-\tau')}. \tag{2.34}$$

The second identity from Eq. (2.33) is derived using Poisson summation formula over the periodic sum of delta functions. Therefore, the integral kernel admits the

Fourier expansion

$$\begin{aligned}\mathcal{G}(\tau,\tau') &= \left(\sum_\alpha \frac{C_\alpha^2}{2m_\alpha\omega_\alpha^2}\right)\sum_{n\in\mathbf{Z}}\delta(\tau-\tau'-n\hbar\beta)-D(\tau-\tau'), \qquad (2.35)\\ D(\tau) &= \frac{1}{\hbar\beta}\sum_{n\in\mathbf{Z}}D(i\nu_n)e^{i\nu_n\tau}, \quad D(i\nu_n)=\sum_\alpha\frac{C_\alpha^2}{2m_\alpha\omega_\alpha^2}\frac{\nu_n^2}{\nu_n^2+\omega_\alpha^2}.\end{aligned}$$

Evaluation of the double integral term in the effective action (2.31) with account of the kernel $\mathcal{G}(\tau,\tau')+D(\tau-\tau')$ yields the local term

$$-\left(\sum_\alpha\frac{C_\alpha^2}{2m_\alpha\omega_\alpha^2}\right)\int_0^{\hbar\beta}q^2(\tau)\,\mathrm{d}\tau, \qquad (2.36)$$

which cancels with the third term on the right hand side of Eq. (2.31). Therefore, the effective action of the macroscopic system becomes

$$S_{\text{eff}}\left[q(\tau)\right]=\int_0^{\hbar\beta}\mathrm{d}\tau\left[\frac{1}{2}M\dot{q}^2+V(q)\right]+\int_0^{\hbar\beta}\mathrm{d}\tau\int_0^{\hbar\beta}\mathrm{d}\tau' D(\tau-\tau')q(\tau)q(\tau'). \qquad (2.37)$$

The spectral density of the bath is defined as $J(\omega)=\pi\sum_\alpha\frac{C_\alpha^2}{2m_\alpha\omega_\alpha}\delta(\omega-\omega_\alpha)$ and comparison with Eq. (2.28) leads to the relation

$$\gamma(t)=\frac{2}{\pi M}\int_0^\infty\mathrm{d}\omega\frac{J(\omega)}{\omega}\cos(\omega t). \qquad (2.38)$$

Its Laplace transform gives rise to the identity

$$\gamma^\star(s)\equiv(\mathcal{L}\gamma)(s)=\frac{1}{M}\sum_\alpha\frac{C_\alpha^2}{m_\alpha\omega_\alpha^2}\frac{s}{s^2+\omega_\alpha^2}, \qquad (2.39)$$

from which the following Fourier expansion of the integral kernel can be derived:

$$D(\tau)=\frac{M}{2\hbar\beta}\sum_{n\in\mathbf{Z}}|\nu_n|\gamma^\star(|\nu_n|)e^{i\nu_n\tau}. \qquad (2.40)$$

In the Ohmic regime, characterized by the spectral density $J(\omega)=M\gamma\omega$, the damping kernel becomes $\gamma(t)=2\gamma\delta(t)$. Hence, the dissipative term of Eq. (2.27) turns out to be $M\gamma\dot{q}(t)$, which means that the friction is linear with respect to the velocity. Furthermore, the corresponding Laplace transform is given by $\gamma^\star(s)=\gamma$, so that

$$D(\tau)=\frac{1}{2\hbar\beta}\sum_{n\in\mathbf{Z}}\eta|\nu_n|e^{i\nu_n\tau}, \qquad (2.41)$$

where $\eta = M\gamma$ is the friction coefficient of the system. Finally, with account of the above expression for the integral kernel, the effective action becomes

$$S_{\text{eff}}\left[q(\tau)\right] = \int_0^{\hbar\beta} \mathrm{d}\tau \left[\frac{1}{2}M\dot{q}^2 + V(q)\right] + \frac{\eta}{4\pi}\int_0^{\hbar\beta} \mathrm{d}\tau \int_{\mathbf{R}} \mathrm{d}\tau' \frac{(q(\tau)-q(\tau'))^2}{(\tau-\tau')^2}. \tag{2.42}$$

Therefore, the interaction of the macroscopic system with the environment translates into a non-local term in the effective action, known as the Caldeira-Leggett dissipative term.

Calculation of the partition function of the macroscopic system [Eq. (2.30)] can be done by the method of the steepest descent [59]: For a potential of the kind given in Fig. 2.1, the set of stationary trajectories of the effective action consists of three solutions. The first two are the imaginary-time-independent trajectories $q(\tau) = 0$ and $q(\tau) = q_0$, which correspond respectively to the relative minimum and relative maximum of the energy barrier. The remaining stationary trajectory satisfies the Euler-Lagrange equation of motion [see Appendix A]

$$\ddot{q}_b - \frac{dV}{dq}(q_b) - \frac{\eta}{\pi}\int_{\mathbf{R}} \mathrm{d}\tau' \frac{q_b(\tau) - q_b(\tau')}{(\tau-\tau')^2} = 0, \tag{2.43}$$

with boundary conditions $q_b(-\tau_p/2) = q_b(\tau_p/2) = 0$ and $q_b(0) = q_1$ (periodic trajectory with imaginary-time period τ_p). This trajectory is called *instanton* in the zero-temperature case and *thermon* for $T \neq 0$ (see [32] and references therein). Above the crossover temperature the thermon solution coincides with the maximum of the energy barrier. With account of Eq. (2.16), the transition rate can be written as $\Gamma(T) = A(T)e^{-B(T)}$ with $B(T)$ being $S_{\text{eff}}/\hbar$ evaluated at the instanton/thermon $q_b(\tau)$. The prefactor $A(T)$ is given by the formula [32, 51]

$$A(T) = \left(\frac{B(T)}{2\pi}\right)^{1/2} \left|\frac{\det \hat{D}_0}{\det' \hat{D}_1}\right|^{1/2}, \tag{2.44}$$

where $\hat{D}_0$ and $\hat{D}_1$ are the integro-differential operators

$$\hat{D}_0[q(\tau)] = \left[-\partial_\tau^2 + \partial_q^2 V(q=0)\right] q(\tau) + \frac{\eta}{\pi}\int_{\mathbf{R}} \mathrm{d}\tau' \frac{q(\tau)-q(\tau')}{(\tau-\tau')^2}, \tag{2.45}$$

$$\hat{D}_1[q(\tau)] = \left[-\partial_\tau^2 + \partial_q^2 V(q=q_b)\right] q(\tau) + \frac{\eta}{\pi}\int_{\mathbf{R}} \mathrm{d}\tau' \frac{q(\tau)-q(\tau')}{(\tau-\tau')^2}, \tag{2.46}$$

and $\det'$ means omission of the eigenvalue $\lambda_1 = 0$ in the product defining the determinant of the corresponding operator.

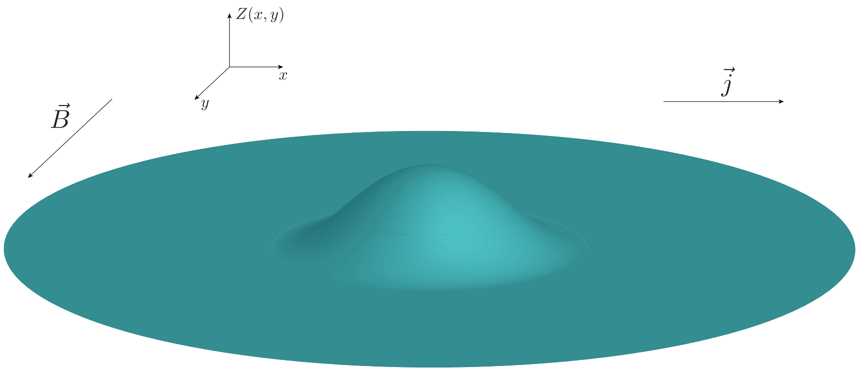

Figure 2.2: Interface between normal and superconducting domains in a type-I superconductor, pinned by a planar defect in the XY plane. Transport current parallel to the interface controls the energy barrier. Depinning of the interface occurs through quantum nucleation of a critical bump described by the instanton/thermon of the equations of motion in 2+1 dimensions.

2.2 Macroscopic Quantum Tunneling of Normal-Superconductor Interfaces

2.2.1 Introduction

Measurements discussed in Sec. 1.4 have elucidated the possibility of macroscopic quantum tunneling in type-I superconductors. Such superconductors (with lead being a prototypical system), unlike type-II superconductors, do not develop vortex lines when placed in the magnetic field. Instead, they exhibit the intermediate state in which the sample splits into normal and superconducting regions separated by planar interfaces of positive energy. Equilibrium states and dynamics of these interfaces have been discussed in Sec. 1.3, where the interface was treated as a classical object. In Sec. 1.4, however, it was noticed that slow temporal evolution of magnetization in a superconducting Pb sample was independent of temperature below a few kelvin. This observation points towards the possibility of quantum tunneling of interfaces in the potential landscape determined by pinning. In general the pinning potential would be due to random distribution of pinning centers or due to properties of the sample surface. In a polycrystalline sample it may also be due to extended pinning of interfaces by grain boundaries.

Modern atomic deposition techniques permit preparation of a pinning layer with controlled properties. This fact motivates the study of a well-defined problem in which the interface separating normal and superconducting regions is pinned by a planar defect. The corresponding pinning barrier can be controlled by a superconducting current that exerts a force on the interface. At low temperature the depinning of the interface would occur through quantum nucleation of a critical bump shown in Fig. 2.2. Somewhat similar problems in 1+1 dimensions have been studied for a flux line pinned by the interlayer atomic potential in a layered superconductor [44], for a flux line pinned by a columnar defect [60], and for fractional vortices in long Josephson junctions [48]. However, the two-dimensional nature of the interface, as compared to a one-dimensional flux line, makes the interface problem more challenging. Note that tunneling of two-dimensional objects has been studied theoretically in application to non-thermal dynamics of planar domain walls [40] and quantum nucleation of magnetic bubbles [61, 62]. These studies employed non-dissipative dynamics of the magnetization field because corrections coming from dissipation are not dominant for spin systems. On the contrary, the Euclidean dynamics of the interface in a type-I superconductor is entirely dissipative, described by integro-differential equations in 2+1 dimensions.

2.2.2 The model

The N-S interface is described by a smooth function $Z(x,y)$, see Fig. 2.2. The dimensionless Euclidean effective action associated with the interface is

$$\begin{aligned} B(T) =& \frac{\sigma}{\hbar}\oint \mathrm{d}\tau \int \mathrm{d}x\,\mathrm{d}y\left[1+(\boldsymbol{\nabla} Z)^2\right]^{\frac{1}{2}} + \frac{1}{\hbar}\oint \mathrm{d}\tau \int \mathrm{d}x\,\mathrm{d}y\, V\left[x,y,Z(x,y,\tau)\right] \\ &+ \frac{\eta}{4\pi\hbar}\oint \mathrm{d}\tau \int_{\mathbf{R}} \mathrm{d}\tau' \int \mathrm{d}x\,\mathrm{d}y \frac{\left[Z(x,y,\tau)-Z(x,y,\tau')\right]^2}{(\tau-\tau')^2}, \end{aligned} \tag{2.47}$$

where σ is the surface energy density of the interface and η is a drag coefficient. The former can be estimated in the limit $\kappa \ll 1$ with account of Eq. (1.37): In this limit the size of the region in the superconducting side where the exponential decay of the magnetic field (from its critical value down to zero) occurs is much smaller than the size of the region where the superconducting wavefunction varies (see Fig. 1.4). Therefore, considering the geometry of the N-S interface given in Sec. 1.2.3, the variation of B can be neglected in the domain $x > 0$, so that $B \simeq H_c$ for $x < 0$ and $B \simeq 0$ for $x > 0$. The functional dependence of the wavefunction can be approximated as $\psi(x) = \psi_0 \tanh\left(\frac{\kappa x}{\sqrt{2}\lambda_{\mathrm{L}}}\right)$ for $x > 0$ and zero otherwise. Introducing these dependences into (1.37) one obtains

$$\begin{aligned} \sigma &= \frac{H_c^2}{8\pi}\int_0^\infty \mathrm{d}x \left\{1-\frac{|\psi(x)|^4}{\psi_0^4}\right\} = \frac{H_c^2\lambda_{\mathrm{L}}}{4\sqrt{2}\pi\kappa}\int_0^\infty \mathrm{d}y\ \left[1-\tanh^4(y)\right] \\ &= \frac{H_c^2\xi_{\mathrm{GL}}}{3\sqrt{2}\pi}. \end{aligned} \tag{2.48}$$

The derivation of the drag coefficient follows that of Ref. [28]: A superconducting current parallel to the planar defect (and to the interface pinned by the defect) exerts a Lorentz force on the interface similar to the force acting on a vortex line in a type-II superconductor. It is assumed that the magnetic field is applied in the $\hat{y}$ direction and that the transport current of density j flows in the $\hat{x}$ direction. The driving force experienced by the $\mathrm{d}x\mathrm{d}y$ element of the interface in the $\hat{z}$ direction is given by

$$\frac{\mathrm{d}^2 F_z}{\mathrm{d}x\mathrm{d}y} = \frac{1}{c}\int \mathrm{d}z jB(z), \tag{2.49}$$

Here $B(z) = H_c \exp(-z/\delta)$ is the magnetic field inside the interface with $\delta = \sqrt{\xi_{\mathrm{GL}}\lambda_{\mathrm{L}}}$ [63]. In terms of the normal-state resistivity, ρ_n, the density of transport current can be expressed as $j = E/\rho_n$, where the electric field $E = (V/c)B$ is produced inside the interface moving at a speed V in the z direction. Thus, one has

$$\frac{\mathrm{d}^2 F_z}{\mathrm{d}x\mathrm{d}y} = \frac{V}{\rho_n c^2}\int \mathrm{d}z B^2(z) \equiv \eta V, \quad \text{with} \quad \eta = \frac{H_c^2\sqrt{\lambda_{\mathrm{L}}\xi_{\mathrm{GL}}}}{2\rho_n c^2}. \tag{2.50}$$

Note that both magnitudes depend on temperature via the London penetration depth and the coherence length. As the crossover temperature is small compared to the critical temperature of the type-I superconductor, it is fair to approximate the surface energy density and the drag coefficient by their values at $T = 0$ due to the asymptotic behaviour of λ_L and ξ_{GL} when $T \ll T_c$.

The first term in Eq. (2.47) is due to the elastic energy of the interface associated with its total area, the second term is due to the space-dependent potential energy, $V[x, y, Z(x, y, \tau)]$, of the interface inside the imperfect crystal, and the third term is the Caldeira-Leggett dissipative term [see Eq. (2.42)]. Same as for the flux lines, the inertial mass of the interface is neglected. Its dynamics in a type-I superconductor is dominated by friction. Pinning of the interface by a planar defect located in the XY plane is considered and the corresponding potential is chosen in the form

$$V_p = p\sigma \int \mathrm{d}x\,\mathrm{d}y \left(\frac{1}{2}\frac{Z^2}{a^2} - \frac{1}{4}\frac{Z^4}{a^4}\right), \tag{2.51}$$

that is symmetric with respect to the sign of the local displacement Z. It will be shown below that the effective potential becomes cubic on Z in the most interesting case when the transport current is close to the depinning current. Here $2a$ is roughly the width of the well that traps the interface and $p \lesssim 1$ is a dimensionless constant describing the strength of the pinning. The interface separates the normal state at $Z < 0$ from a superconducting state at $Z > 0$. Integration of Eq. (2.49) for a given value j of the density of transport current gives $\mathrm{d}^2F_z/(\mathrm{d}x\mathrm{d}y) = H_c\delta j/c$, so that the corresponding contribution to the potential can be obtained by writing

F_z as $-\nabla_Z V_L$, yielding

$$\frac{\mathrm{d}^2 V_L(Z)}{\mathrm{d}x\mathrm{d}y} = -\frac{H_c\delta}{c} j Z\,. \tag{2.52}$$

The total potential, $V(Z) = V_p(Z) + V_L(Z)$ is

$$V(Z) = p\sigma \int \mathrm{d}x\,\mathrm{d}y \left(-\bar{j}\tilde{Z} + \frac{\tilde{Z}^2}{2} - \frac{\tilde{Z}^4}{4}\right) \tag{2.53}$$

where we have introduced dimensionless $\tilde{Z} = Z/a$ and

$$\bar{j} = \frac{a\delta H_c}{pc\sigma} j = \frac{3\pi\sqrt{2\kappa a}}{pcH_c} j. \tag{2.54}$$

2.2.3 Effective action in the vicinity of the critical current

Measurable quantum depinning of the interface can occur only when the transport current is close to the critical current j_c that destroys the energy barrier. It therefore makes sense to study the problem at $j \to j_c$. Maxima and minima of the function

$$f(\bar{j}, \tilde{Z}) = -\bar{j}\tilde{Z} + \frac{\tilde{Z}^2}{2} - \frac{\tilde{Z}^4}{4} \tag{2.55}$$

that enters Eq. (2.53) are given by the roots of the equation $\tilde{Z}^3 - \tilde{Z} + \bar{j} = 0$. At $j^2 < 4/27$ it has three real roots corresponding to one minimum and two maxima of the potential on two sides of the pinning layer, whereas at $j^2 > 4/27$ there is one real root corresponding to the maximum of f. Consequently, the barrier disappears at $j^2 = 4/27$, providing the value of the critical current

$$\bar{j}_c = \frac{2}{3\sqrt{3}}\,, \quad j_c = \frac{2pcH_c}{9\pi\sqrt{6\kappa a}}\,. \tag{2.56}$$

At $\bar{j} = \bar{j}_c$ the minimum and the maximum of the potential combine into the inflection point $\tilde{Z} = \tilde{Z}_c$ given by the set of equations

$$\begin{aligned} 0 &= -\tilde{Z}_c^3 + \tilde{Z}_c - \bar{j}_c, \\ 0 &= -3\tilde{Z}_c^2 + 1, \end{aligned} \tag{2.57}$$

that correspond to zero first and second derivatives of f. The value of $\tilde{Z}_c$ deduced from these equations is $1/\sqrt{3}$. It is convenient to introduce a small parameter

$$\epsilon = 1 - j/j_c\,, \tag{2.58}$$

so that $j = j_c(1-\epsilon)$ and

$$\bar{j} = \bar{j}_c(1-\epsilon) = \frac{2}{3\sqrt{3}}(1-\epsilon)\,. \tag{2.59}$$

Let $\tilde{Z}_0(\bar{j})$ be the minimum of f (see Fig. 2.3) satisfying

$$\tilde{Z}_0^3 - \tilde{Z}_0 + \bar{j}_c(1-\epsilon) = 0\,. \tag{2.60}$$

Consider $\tilde{Z}' = \tilde{Z} - \tilde{Z}_0$. It is straightforward to find that the form of the potential in the vicinity of $\tilde{Z}_0$ is

$$f = f[\tilde{Z}_0(\bar{j})] + \frac{1}{2}(1-3\tilde{Z}_0^2)\tilde{Z}'^2 - \tilde{Z}_0\tilde{Z}'^3 - \frac{\tilde{Z}'^4}{4}\,. \tag{2.61}$$

At small ϵ one has $\tilde{Z}_0 \to \tilde{Z}_c = 1/\sqrt{3}$, so that $1 - 3\tilde{Z}_0^2$ in front of $\tilde{Z}'^2$ in Eq. (2.61) is small. The first term in Eq. (2.61) can be omitted as an unessential shift of energy, while the last term proportional to $\tilde{Z}'^4$ can be neglected due to its smallness compared to other $\tilde{Z}'$-dependent terms. Consequently, one obtains the effective potential

$$f_{\text{eff}}(\bar{j}, \tilde{Z}) = \frac{1}{2}(1-3\tilde{Z}_0^2)\tilde{Z}^2 - \tilde{Z}_0\tilde{Z}^3\,. \tag{2.62}$$

The dependence of $\tilde{Z}_0$ on ϵ can be obtained by substituting $\tilde{Z}_0(\epsilon) = \tilde{Z}_c[1-\beta(\epsilon)]$ into Eq. (2.60), from which the identity $\beta(\epsilon) = \sqrt{2\epsilon/3}$ holds to the lowest order on ϵ. Then $1 - 3\tilde{Z}_0^2 \approx 2\sqrt{2\epsilon/3}$ and

$$f_{\text{eff}}(\epsilon, \tilde{Z}) = \sqrt{\frac{2\epsilon}{3}}\tilde{Z}^2 - \frac{\tilde{Z}^3}{\sqrt{3}}\,. \tag{2.63}$$

The height of the effective potential is $\frac{8}{27}\sqrt{\frac{2}{3}}\epsilon^{3/2}$ and the width is $\sqrt{2\epsilon}$, see Fig. 2.3.

As follows from the equations of motion, smallness of ϵ results in $|\boldsymbol{\nabla} Z| \sim p\epsilon \ll 1$. This allows one to replace $[1 + (\boldsymbol{\nabla} Z)^2]^{\frac{1}{2}}$ in Eq. (2.47) with $1 + \frac{1}{2}(\boldsymbol{\nabla} Z)^2$. Introducing dimensionless variables

$$\begin{gathered} x_0 = \left(\frac{2p\sqrt{\epsilon}}{3\sqrt{3}}\frac{\xi_{\text{GL}} H_c^2}{\eta a^2}\right)\tau, \quad (x_1, x_2) = \left(\sqrt{2\epsilon/3}\,p\right)^{1/2}\frac{(x,y)}{a}, \\ v = V(x,y,Z)/\sigma p, \quad u = \frac{3}{\sqrt{2\epsilon}}\left(Z/a - \tilde{Z}_c(1 - \sqrt{2\epsilon/3})\right), \end{gathered} \tag{2.64}$$

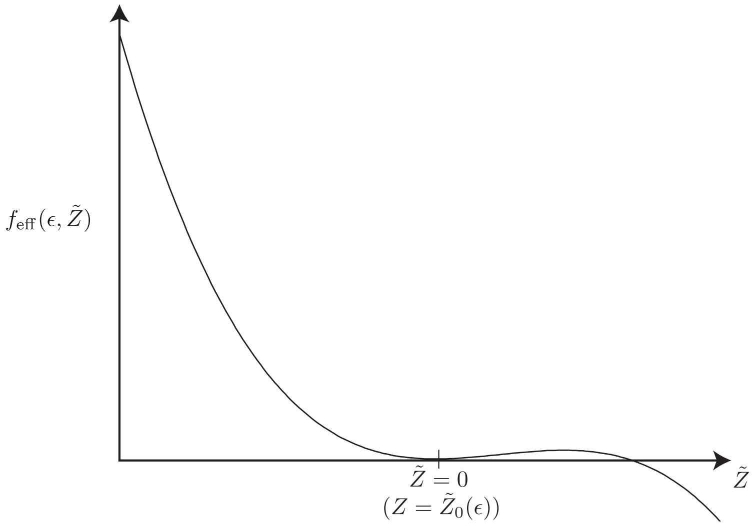

Figure 2.3: Effective potential for $\epsilon = 0.15$.

the WKB exponent of the transition rate becomes

$$\begin{aligned}B(T) =& \frac{\sqrt{\epsilon}}{3\sqrt{6}\pi p}\frac{\eta a^4}{\hbar}\oint \mathrm{d}x_0 \int \mathrm{d}x_1\,\mathrm{d}x_2 \left[\frac{1}{2}(\boldsymbol{\nabla} u)^2 + u^2 - \frac{u^3}{3}\right. \\ &\left. + \frac{1}{2}\int_{\mathbf{R}} \mathrm{d}x_0' \frac{[u(x_0,x_1,x_2) - u(x_0',x_1,x_2)]^2}{(x_0-x_0')^2}\right], \end{aligned} \tag{2.65}$$

where $\nabla = (\partial_1, \partial_2)$.

2.2.4 Instantons of the dissipative 2+1 model

Quantum depinning of the interface is given by the instanton (thermon) solution of the Euler-Lagrange equations of motion of the 2+1 field theory described by Eq. (2.65):

$$\sum_{\mu=0,1,2} \frac{\partial}{\partial x^\mu}\left[\frac{\delta \mathcal{L}}{\delta\left(\partial u/\partial x^\mu\right)}\right] - \frac{\partial \mathcal{L}}{\partial u} = 0\,. \tag{2.66}$$

This gives [see Appendix A]

$$\nabla^2 u - 2u + u^2 - 2\int_{\mathbf{R}} \mathrm{d}x_0' \frac{u(x_0,x_1,x_2) - u(x_0',x_1,x_2)}{(x_0-x_0')^2} = 0 \tag{2.67}$$

with the boundary conditions

$$\begin{aligned} &u(-\Omega/2, x_1, x_2) = u(\Omega/2, x_1, x_2) \quad \forall (x_1, x_2) \in \mathbf{R}^2, \\ &\max_{x_0 \in [-\Omega/2, \Omega/2]} u(x_0, x_1, x_2) = u(0, x_1, x_2) \quad \forall (x_1, x_2) \in \mathbf{R}^2, \end{aligned} \tag{2.68}$$

that must be periodic on imaginary time with the period $\hbar/(k_{\rm B}T)$. The corresponding period on x_0 is

$$\Omega = \left(\frac{2p\sqrt{\epsilon}}{3\sqrt{3}} \frac{\xi_{\rm GL} H_c^2}{\eta a^2} \right) \frac{\hbar}{k_{\rm B}T} \,. \tag{2.69}$$

This equation cannot be solved analytically, so we must proceed by means of numerical methods.

Zero temperature

Application of the Fourier transform

$$\hat{u}(\vec{\omega}) = \frac{1}{(2\pi)^{3/2}} \int_{\mathbf{R}^3} u(\vec{x}) e^{i\vec{\omega}\cdot\vec{x}} \, \mathrm{d}^3\vec{x} \tag{2.70}$$

to equation (2.67) yields

$$\hat{u}(\vec{\omega}) = \frac{(2\pi)^{-3/2}}{2 + 2\pi|\omega_0| + \omega_1^2 + \omega_2^2} \int_{\mathbf{R}^3} \mathrm{d}^3\vec{\omega}' \, \hat{u}(\vec{\omega} - \vec{\omega}') \hat{u}(\vec{\omega}'), \tag{2.71}$$

which is still an integral equation for $\hat{u}(\vec{\omega})$. The dimensionless effective action (2.65) in terms of $\hat{u}(\vec{\omega})$ becomes

$$\begin{aligned} B(T)\,[\hat{u}] = &\frac{\sqrt{\epsilon}}{3\sqrt{6}\pi p} \frac{\eta a^4}{\hbar} \left[\int_{\mathbf{R}^3} \mathrm{d}^3\vec{\omega} \; \hat{u}(\vec{\omega}) \hat{u}(-\vec{\omega}) \left(\frac{1}{2}(\omega_1^2 + \omega_2^2) + 1 + \pi|\omega_0| \right) - \right. \\ &\left. \frac{1}{3(2\pi)^{3/2}} \int_{\mathbf{R}^6} \mathrm{d}^3\vec{\omega} \, \mathrm{d}^3\vec{\omega}' \hat{u}(\vec{\omega}) \hat{u}(\vec{\omega}') \hat{u}(-\vec{\omega} - \vec{\omega}') \right]. \end{aligned} \tag{2.72}$$

Next, the field-theory extension of the algorithm introduced in Ref. [64] for the problem of dissipative quantum tunneling of a particle will be used in the computation of the instanton solution. It consists of the following steps:

1. Start with an initial aproximation $\hat{u}_0(\vec{\omega})$. Define the operator

$$\begin{aligned} &\hat{O} : \mathbf{R} \times \mathcal{L}^2(\mathbf{R}^3) \to \mathcal{L}^2(\mathbf{R}^3) \\ &(\lambda, \hat{u}(\vec{\omega})) \mapsto \frac{\lambda}{2 + 2\pi|\omega_0| + \omega_1^2 + \omega_2^2} \int_{\mathbf{R}^3} \mathrm{d}^3\vec{\omega}' \hat{u}(\vec{\omega} - \vec{\omega}') \hat{u}(\vec{\omega}') \end{aligned} \tag{2.73}$$

2. Let $\hat{u}_1(\vec{\omega}) = \hat{O}(\lambda_0, \hat{u}_0(\vec{\omega}))$ for an initial $\lambda_0 \in \mathbf{R}$.
3. Calculate $\lambda_1 = \lambda_0/\xi^2$ with $\xi = \frac{\hat{u}_1(\vec{\omega}=0)}{\hat{u}_0(\vec{\omega}=0)}$.
4. Find $\hat{u}_2(\vec{\omega}) = \hat{O}(\lambda_1, \hat{u}_1(\vec{\omega}))$.
5. Repeat steps (2) − (4) until the successive difference satisfies a preset convergence criterion.

The output is the pair $(\lambda_n, \hat{u}_n(\vec{\omega}))$. Finally, a rescaling of $\hat{u}_n$ by a factor $(2\pi)^{3/2}\lambda_n$ is applied to obtain the instanton solution.

Non-zero temperature

At $T \neq 0$ the period of the thermon solution is finite, given by Eq. (2.69). Hence, a solution of the type

$$u(x_0, x_1, x_2) = \sum_{n\in\mathbf{Z}} e^{i\omega_{0,n}x_0} u_n(x_1, x_2) \tag{2.74}$$

is considered, where $\omega_{0,n} = 2\pi n/\Omega$. Introducing into (2.67) the above functional dependence and applying a 2D Fourier transform one obtains

$$\hat{u}_n(\vec{\omega}) = \frac{1}{2 + 2\pi|\omega_{0,n}| + \vec{\omega}^2} \left(\frac{1}{2\pi} \sum_{p\in\mathbf{Z}} \int_{\mathbf{R}^2} \mathrm{d}^2\vec{\omega}' \hat{u}_{n-p}(\vec{\omega} - \vec{\omega}')\hat{u}_p(\vec{\omega}') \right), \tag{2.75}$$

which is the integral equation for $\hat{u}_n$ with $\vec{\omega} = (\omega_1, \omega_2)$. In terms of $\{\hat{u}_n(\vec{\omega})\}_n$ the WKB exponent of the transition rate becomes

$$\begin{aligned} B(T)\left[\{\hat{u}\}_n\right] =& \frac{\sqrt{\epsilon}}{3\sqrt{6}\pi p} \frac{\eta a^4}{\hbar} \left[\sum_{n\in\mathbf{Z}} \int_{\mathbf{R}^2} \mathrm{d}^2\vec{\omega}\ \hat{u}_n(\vec{\omega})\hat{u}_{-n}(-\vec{\omega}) \left(\frac{\vec{\omega}^2}{2} + 1 + \pi|\omega_{0,n}| \right) \right. \\ & \left. - \frac{1}{6\pi} \sum_{n,m\in\mathbf{Z}} \int_{\mathbf{R}^4} \mathrm{d}^2\vec{\omega}\, \mathrm{d}^2\vec{\omega}' \hat{u}_n(\vec{\omega})\hat{u}_m(\vec{\omega}')\hat{u}_{-n-m}(-\vec{\omega} - \vec{\omega}') \right] \Omega. \end{aligned} \tag{2.76}$$

The numerical algorithm used to calculate the thermon solution is analogous to the one used in the $T = 0$ case, which is a field-theory extension of the Waxman-Leggett algorithm [65].

Therefore, both procedures lead to the formula

$$B(T) = \frac{\eta a^4 \sqrt{\epsilon}}{p\hbar} I(T), \tag{2.77}$$

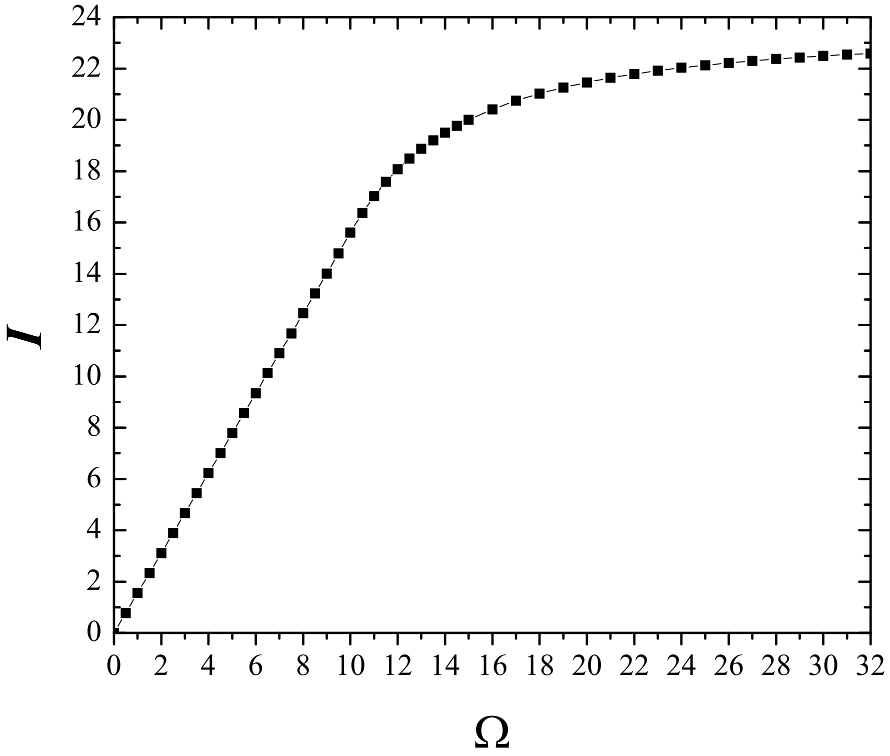

Figure 2.4: Temperature dependence of the depinning exponent: $I(T)$ versus Ω at zero field.

which is valid in the whole range of temperatures. The value of the integral depends on the value of T in comparison with the temperature, T_{cr}, of the crossover from quantum tunneling to thermal activation. Figure 2.4 shows the dependence of $I(T)$ on the period Ω. At $\Omega \gg \Omega_{\mathrm{cr}}$ ($T \ll T_{\mathrm{cr}}$) the numerical value of $I(T)$ is very close to $I(0)$, while at $\Omega \ll \Omega_{\mathrm{cr}}$ ($T \gg T_{\mathrm{cr}}$) one has the dependence $I(T) \propto \Omega$. In the latter case, the Boltzmann exponent $B(T) = V_0/(k_B T)$ is recovered with V_0 being the energy barrier for depinning. Nevertheless, as it will be shown below, the crossover temperature T_{cr} can be computed exactly.

2.2.5 Crossover temperature

The crossover temperature can be computed by means of theory of phase transitions [56, 58, 66]. Above T_{cr} the solution minimizing the instanton action is a function $u(x_0, x_1, x_2) = \bar{u}_0(x_1, x_2)$ that does not depend on x_0. Just below T_{cr}, the instanton solution can be split into the sum of $\bar{u}_0$ and a term that depends on x_0,

$$u(x_0, x_1, x_2) = \bar{u}_0(x_1, x_2) + u_1(x_1, x_2) \cos\left(\frac{2\pi}{\Omega} x_0\right) . \tag{2.78}$$

This identity is obtained by expanding $u(x_0, x_1, x_2)$ over the complete set of periodic functions $\{\cos[(2\pi n/\Omega)x_0]\}_{n\in\mathbf{Z}^+}$ and by using the fact that only the first term of the expansion survives when temperature approaches T_{cr} from below. The value of T_{cr} is independent of the choice of the basis of periodic functions [56, 58, 66].

The instanton action is proportional to

$$\int_{\mathbb{R}^2} \mathrm{d}x_1\, \mathrm{d}x_2 \Phi(x_1, x_2; u, \nabla u) , \tag{2.79}$$

where $\Phi(x_1, x_2; u, \nabla u)$ is the spatial action density. Using the expansion of u introduced above, one obtains

$$\Phi(x_1, x_2; u_1, \nabla u_1) = \Omega \left[\frac{1}{2}(\nabla \bar{u}_0)^2 + v(\bar{u}_0)\right] + \frac{\Omega}{4}(\nabla u_1)^2 + \Lambda u_1^2 + O(4) \tag{2.80}$$

with $v(u) = u^2 - u^3/3$ and

$$\Lambda = \frac{\Omega}{4} v''(\bar{u}_0) + \pi^2 . \tag{2.81}$$

If $\Lambda > 0$, the only $(u_1, \nabla u_1)$ minimizing Φ is $u_1 \equiv 0$, so the crossover temperature is defined by the equation

$$\min_{\vec{x}\in\mathbf{R}^2} \Lambda = \min_{\vec{x}\in\mathbf{R}^2} \frac{\Omega_{\mathrm{cr}}}{4} v''[\bar{u}_0(x_1, x_2)] + \pi^2 = 0 . \tag{2.82}$$

Notice that this minimum corresponds to the minimum of $v''[\bar{u}_0(x_1, x_2))]$. The equation of motion for $\bar{u}_0$ is

$$\nabla^2 \bar{u}_0 - 2\bar{u}_0 + \bar{u}_0^2 = 0 . \tag{2.83}$$

The solution corresponding to the minimum is spherically symmetric,

$$\bar{u}_0 = \bar{u}_0\left(r = \sqrt{x_1^2 + x_2^2}\right) , \tag{2.84}$$

satisfying boundary conditions: $\bar{u}_0 \to 0$ at $r \to \infty$ and $\bar{u}_0(0) = 3$, which is the width of the potential. Consequently,

$$\begin{aligned} &\min_{\vec{x}\in\mathbf{R}^2} v''[\bar{u}_0(x_1, x_2)] = \min_{\bar{u}_0\in[0,3]} v''(\bar{u}_0) \\ &= \min_{\bar{u}_0\in[0,3]} 2(1 - \bar{u}_0) = -4 . \end{aligned} \tag{2.85}$$

Then, according to equations (2.81) and (2.82), the crossover temperature is determined by the equation $\Omega(T_{\text{cr}}) = \pi^2$, which gives

$$T_{\text{cr}} = \frac{2p\sqrt{\epsilon}}{3\sqrt{3}\pi^2}\frac{\hbar\xi_{\text{GL}}H_c^2}{k_{\text{B}}\eta a^2} = \frac{4p\sqrt{\epsilon}}{3\pi^2\sqrt{3\kappa}}\frac{\hbar\rho_n c^2}{k_{\text{B}}a^2}\,. \tag{2.86}$$

2.2.6 Discussion

To guarantee the feasibility of the proposed experiment on quantum depinning of the interface from a planar defect in a type-I superconductor, two conditions must be satisfied: Firstly the dimensionless effective action of Eq. (2.77), which is the WKB exponent of the transition rate, should not exceed $30 - 40$ in order for the tunneling to occur on a reasonable time scale. Secondly, the crossover temperature determined by Eq. (2.86) better be not much less than 1 K. For a known superconductor, the two equations contain three parameters: the parameter $p \leq 1$ describing the strength of pinning, the parameter a describing the width of the pinning layer, and the parameter ϵ that controls how close the transport current should be to the depinning current. Therefore, one has to investigate how practical is the range of values of these parameters that can provide conditions $B \sim 30$ and $T_{\text{cr}} \sim 1$ K.

Consider lead as the prototypical example. The values of λ_{L} and ξ_{GL} in lead are 37 nm and 83 nm, respectively, giving $\kappa = \lambda_{\text{L}}/\xi_{\text{GL}} = 0.45$. The critical field strength is $H_c \approx 802$ Oe. The elastic energy of the interface is $\sigma \approx 0.4$ erg/cm^2. The normal state resistivity in the K range is $5 \times 10^{-11}\ \Omega \cdot \text{m} = 5.6 \times 10^{-21}$ s, while the drag coefficient is $\eta \approx 0.35$ erg·s/cm^4. Then equations (2.77) and (2.86) with conditions $B \sim 30$ and $T_{\text{cr}} \sim 1$ K give $a/p^{1/3} \sim 5.1$ nm and $a\sqrt{\epsilon} \sim 0.3$ nm. Note that these relations are specific for a two-dimensional elastic manifold pinned by a two-dimensional layer. In principle one could study pinning of the interface by a one-dimensional line of defects or even by a point defect. However, such choices would be less practical due to very small pinning barriers and, thus, strong thermal effects, even in the absence of the transport current.

If the pinning layer is not compatible with superconductivity, that is, it favors the normal phase, then at $2a < \xi_{\text{GL}}$ one should expect $p \sim 2a/\xi_{\text{GL}}$, giving $a \sim 1.79$ nm and $\epsilon \sim 0.03$. This means that observation of quantum escape of the interface from a pinning layer of thickness $2a \sim 3.6$ nm in a superconducting Pb sample at $T \sim 1$ K would require control of the transport current within three percent of the critical depinning current. All the above parameters are within experimental reach.

The model presented here is a theoretical extension of the phenomenological model introduced in Sec. 1.4: The expressions for the WKB exponent and the crossover temperature [see Eqs. (4) and (8) respectively in Ref. [28]] can be obtained from Eqs. (2.77) and (2.86) up to numerical factors with account of the identifications $a \sim \bar{a}$ and $p \sim (a/L)^2$, where L and $\bar{a}$ are respectively the lateral size and the height of the bump in the phenomenological model. The estimate of the lateral size is $L \sim \xi_{\mathrm{GL}}$ according to Chudnovsky's model, so that the corresponding value of the strength of the pinning turns out to be $p \sim 4 \cdot 10^{-4}$. On the other hand, Ref. [28] provides the value $\bar{a} \sim 1$ nm, which is compatible with condition $a \sim \bar{a}$ and the value of a obtained via the argument of feasibility.

To conclude, notice that the theoretical model of quantum tunneling of N-S interfaces presented in Sec. 2.2 is valid at zero magnetic field. Its extension to arbitrary applied magnetic field strengths is beyond the scope of this manuscript, but a qualitative description of the effect of the magnetic field strength on the transition rate can be provided. This effect is twofold: First, the higher the magnetic field strength is the thinner the superconducting regions in the intermediate state become [see Fig. 1.8c with $H_c' \simeq 0$]. This translates into the number of N-S interfaces increasing as the magnetic field strength rises (up to a certain value) and, thus, the formation of bumps becoming more probable. Equivalently, the prefactor $A(T)$ of the transition rate is multiplied by an increasing –up to a certain reduced magnetic field strength– function $N(h)$ accounting for the number of N-S interfaces. Second, the higher the magnetic field strength is the more magnetic flux lines must fit into the normal regions of the flat disk. As a result, a magnetic tension force is induced on the N-S interfaces that weakens the strength of the pinning potential by the planar defect. Therefore, the depth of the effective energy barrier $v(x_1, x_2, u, h)$ appearing in the WKB exponent $B(T)$ decreases as the reduced field strength h increases.

Chapter 3

Magnetic vortex state

3.1 Introduction

Magnetic systems at the nanoscale are crucial within condensed matter physics because a direct competition among interactions of pure quantum origin (such as the exchange interaction, which results from the electrostatic interaction and the overlap of one-electron orbitals), long-range interactions (for instance, magnetostatic/dipolar forces) and interactions with external fields arises, so that within this length scale their physical properties differ remarkably from those of individual systems (atoms, molecules, etc.) and bulk materials. Recent advances in optical and electron-beam lithography offer possibility to fabricate arrays of nano- and micro-size magnetic structures with controlled magnetic properties. For reasons such as these, nano-scaled magnetic systems have drawn the attention of physicists for the last twenty years and have been intensively studied.

Bulk magnetic systems tend to split into magnetic domains at zero field in order to minimize their total energy, in particular the magnetostatic contribution. It is well known that the thickness of the resulting domain walls, inside which spins rotate from one domain to the other, is given by the exchange length of the ferromagnetic material, $\Delta_0 \sim (E_{\mathrm{ex}}/E_{\mathrm{mag}})^{1/2}a$, where E_{ex} and E_{mag} are the exchange and magnetostatic contributions to the total energy, respectively, and a is the lattice spacing. Therefore, magnetic systems of size smaller than the exchange length exhibit the single domain (SD) as their ground state. In the case of permalloy (Py), which is the prototypical soft ferromagnetic material with negligibly small crystal-field anisotropy used in the fabrication of magnetic structures with the vortex state, the exchange length is about 10 nm. The critical size below which the specimen becomes SD depends on the balance between the exchange and magnetostatic energies, the type of the crystal-field anisotropy and the shape of the system.

Among such magnetic structures, mesoscopic circular disks made of soft ferromagnetic materials should be remarked because of their unusual magnetic properties and potential for technological and biomedical applications: (ultra-)high-density magnetic information storage [67, 68], ultrasmall magnetic field sensors [69], biomolecular carriers [70] and targeted cancer-cell destruction [71], to name a few. From this point forward the geometry of the structures will be that of a cylinder, characterized by the pair $(L,\ R)$ —thickness and radius, respectively. Due to geometric constains on the spin field, (sub)micron-size circular disks exhibit a rich landscape of magnetic equilibrium configurations. A deep and thorough theoretical study of the magnetic ground states for the cylindrical geometry was conducted by J. Ha and coworkers using micromagnetic principles and finite-element methods [72]: These authors studied the remnant states of disks made of Py based on the parameters (L, R). These remnant states were reached by first saturating magnetically the specimen using a large external magnetic field and then reducing it gradually to zero.

The resulting ground states can be classified into two categories, one consisting of the onion and vortex states and the buckle states defining the other one. Uniformity of the spin field is favored in the onion states due to the exchange interaction being the dominant one. Two mechanisms contribute to the formation of this kind of state, namely the *flowering* (the opening/closing of the magnetization along the axial direction) and the *onionization* (formation of an onion pattern in the plane of the disk, see Fig. 3.1a) processes. Twisted onion states belong to this category too (see Fig. 3.1b). The authors conclude that, as a rule of thumb, stability of the SD is guaranteed if $2R < \Delta_0$; otherwise the onion state develops. The vortex state (VS) is heavily dictated by the magnetostatic interaction and is characterized by the curling of the magnetization field, which winds either in (in-plane vortex) or perpendicular to (out-of-plane vortex) the plane of the disk at the vortex core (see Figs. 3.1c and 3.1d, respectively). This configuration of the spin field leaves virtually no magnetic charges.

The second category consists of the buckle states, which result from a balance between the exchange and the magnetostatic interactions so that the magnetization field in the disk plane buckles. These states can be classified according to the number of 'buckles' in the in-plane magnetization: The C state corresponds to the first-order buckling, the S state to the second-order buckling, etc. (see Figs. 3.1e and 3.1f). Fig. 3.2 shows the diagram of remnant states obtained by the authors, from which it is concluded that the aspect ratio $\beta = L/R$ does not determine the kind of magnetic pattern developed within the disk. On the contrary, the radius of the disk determines whether some in-plane buckling is sustainable and the thickness dictates whether a VS has lower energy than an onion state.

If not stated otherwise, room temperature will be considered from this point

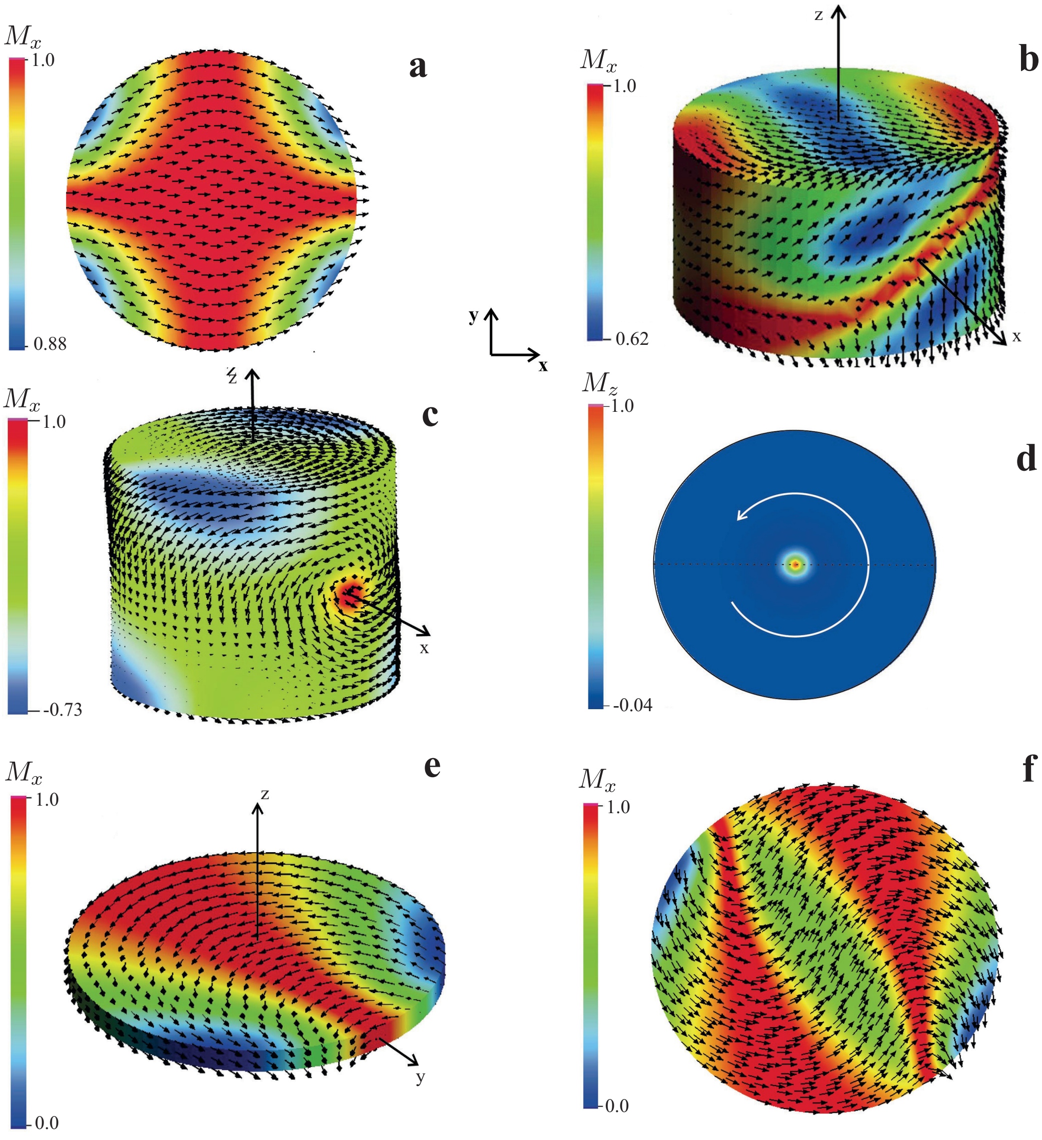

Figure 3.1: Micromagnetic study of ground states in permaloy circular disks. (a) Top view of the x-component of the magnetization for an onion state. Perspective views of (b) a twisted onion state and (c) an in-plane vortex state. (d) Top view of the z-component of the magnetization for an out-of-plane vortex state. (e) Perspective view of a C state and (f) top view of the x-component of the magnetization for a S state. Color coating reflects the variation of the corresponding component of the magnetization. The figure is adapted from Ref. [72].

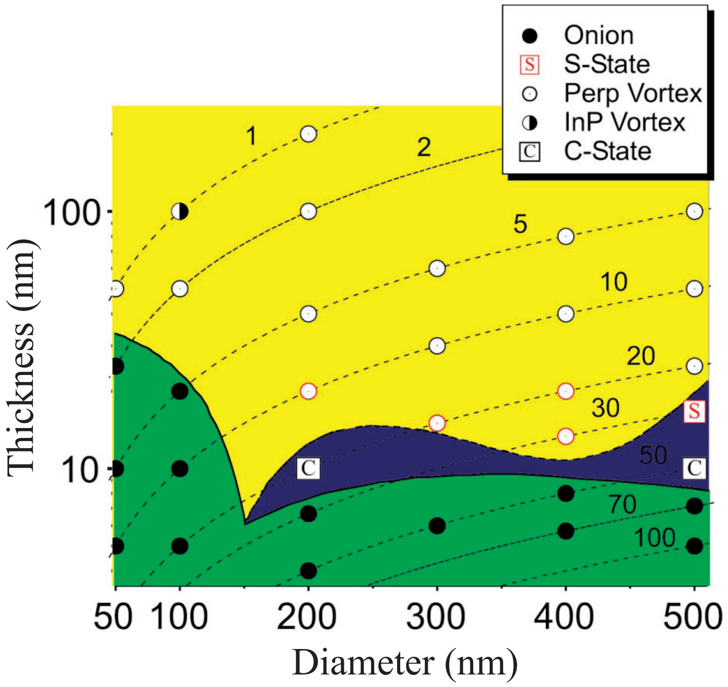

Figure 3.2: (L, R)-diagram of remnant states. Dashed lines are the iso-aspect-ratio lines. The true remnant states corresponding to red-coated data are onion states, but these ones collapse into the indicated states under small perturbations (thermal fluctuations and small fields with reversed polarity). The figure is extracted from Ref. [72].

forward.

3.1.1 Experimental results

One of the first experimental observations of the VS was conducted by R. Cowburn and coworkers, who studied arrays of submicron circular disks made of supermalloy ($Ni_{80}Fe_{14}Mo_5$) and fabricated by high-resolution electron beam lithography [73]. The ranges of their thickness and diameter were $[6, 15]$ nm and $[55, 500]$ nm, respectively. The interdot distance, defined as the spacing among the submicron circular dots, was set to be at least twice their radius, which ensures a negligible interdot magnetostatic interaction. Therefore, the magnetic properties of a single disk can be derived from the averaged magnetic properties measured on the whole array. According to the diagram shown in Fig. 3.2, the expected magnetic equilibrium configurations would be either the onion states/SD or the out-of-plane VS (referred to as VS from this point forward). Hysteresis loops measured by magneto-optical methods were used to determine the ground state of the circular disks, with the external magnetic field H being applied in the plane of the disks. The prototypical hysteresis loop for the VS was systematically observed, see Fig. 3.3. It is an antisymmetic curve as a function of the external magnetic field. Its descending branch is characterized by the magnetic moment retaining its saturation value (corresponding to a SD state) when the applied magnetic field is reduced from its (positive) saturation value to a critical field $H_\mathrm{n} > 0$, at which the magnetic moment drops sharply. The dependence of the magnetic moment on the external magnetic field is linear in the range $[0, H_\mathrm{n}]$, with $m(H = 0) \simeq 0$ in the absence of pinning. On the other hand, the ascending branch for positive values of H is characterized by the magnetic moment being linear with the external magnetic field from zero to a second critical field $H_\mathrm{an} > 0$, at which it increases sharply up to its saturation value. The low-field linear regime of these hysteresis loops is reversible.

Micromagnetic simulations assuming the presence of a VS within the circular disks led to reproduce almost identically the half loop just described. The vortex core (VC) is defined as the small area where the very weak uncompensated magnetic moment of the disk sticks out. From these simulations the authors concluded that the vortex structure is deformed when the magnetic field increases within the linear regime, so that the VC is displaced from the center of the disk towards the outer region, where it becomes unstable and the VS is anihilated at H_an (annihilation field). Furthermore, the displacement of the VC is perpendicular to the direction of the applied magnetic field. On the other hand, H_n (nucleation field) determines whether the SD state becomes unstable and a transition towards the VS occurs. The experimental values for the nucleation and annihilation fields can be recovered in these simulations if thermal fluctuations are taken into consideration.

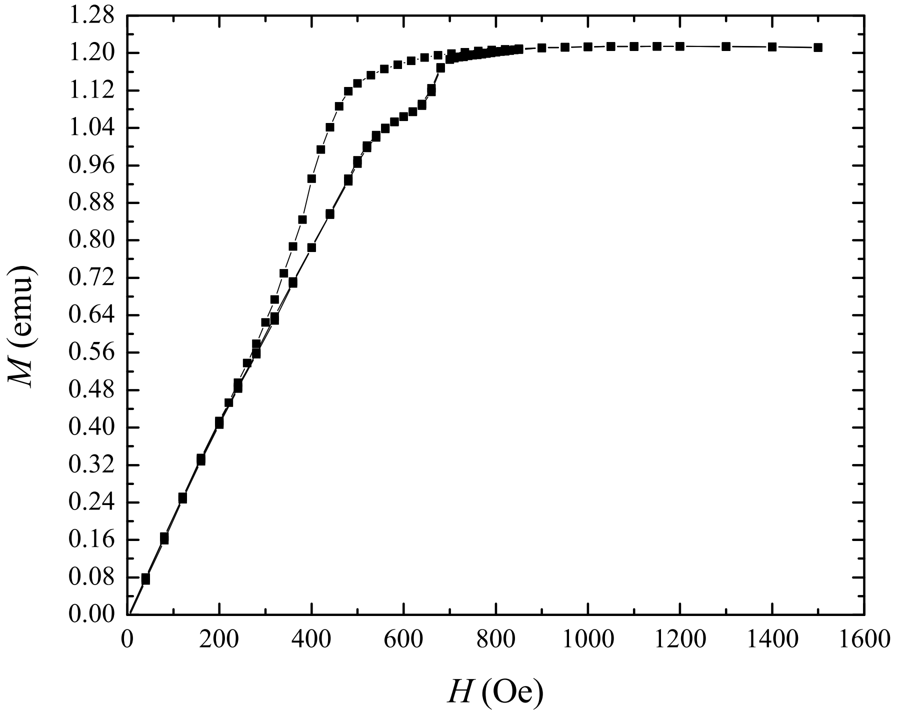

Figure 3.3: Half hysteresis loop of the VS for a Py ($Ni_{81}Fe_{19}$) disk with thickness $L = 95$ nm and radius $R = 1.5$ μm.

First direct observations of the vortex state were carried out by T. Shinjo *et al.* using magnetic force microscopy (MFM) [74] and by M. Schneider and coworkers using Lorentz transmission electron microscopy (LTEM) [75], see Fig. 3.4. Samples were made of Py ($Ni_{80}Fe_{20}$) and had the same thickness but different radius. The MFM technique allows to observe the presence of the VC in the form of a clearly contrasted spot (see Fig. 3.4a). Whether the contrast is dark or bright depends on the direction of the out-of-plane magnetization (referred to as the vortex polarization), which appears to be independent of the application of an in-plane external magnetic field (within the linear regime) and the vortex chirality -clockwise (CW) or counter-clockwise (CCW). By means of the LTEM technique one is able to observe the sense of rotation of the VS, see Fig. 3.4b, where dark and bright spots indicate CW and CCW chirality of the spin field, respectively. Schenider *et al.* concluded that changes in the chirality of the VS are more probable with the reversal of the magnetic field between saturation values before reaching the remnant state (field history $H_S \to 0 \to -H_S \to 0$, with H_S being the saturation field). Furthermore, measurements of the annihilation field by the latter technique led to its lack of correlation to the disk geometry (radius) for large diameters.

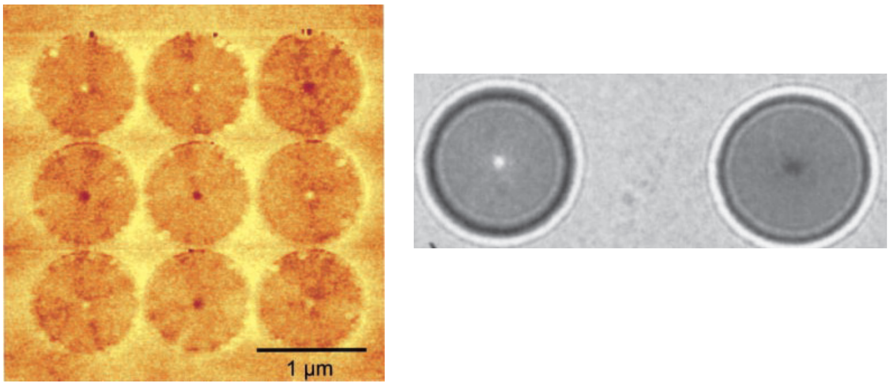

Figure 3.4: MFM (left) and LTEM (right) images of the VS. Bright (dark) contrast at the central spot of the disks indicates polarization $p = \pm 1$ of the VC in the case of the MFM image and CCW (CW) chirality in the case of the LTEM image. This figure has been adapted from Refs. [74, 75].

.

Lack of correlation between the vortex chirality and polarization can be also observed by means of MFM in the case of elliptical disks [76]. In the same work, Okuno and coworkers observed that the dependence of the magnetic reversal field (along the axis of the disk), H_r, on the radius of circular dots was small and concluded that this is due to the fact that the magnetization reversal of the VC does not depend on the outer spin-field distribution if the VC remains deep inside the disk. Hysteresis loops were also measured by means of SQUID magnetometry: For the in-plane configuration of the applied magnetic field the hysteresis loops corresponded to the prototypical ones depicted in Fig. 3.3. In the case of the external magnetic field being swept perpendicularly to the disk plane, the authors observed a smooth increase of the magnetic moment to the saturated value, with no sharp variation corresponding to the VC magnetization switching around H_r. This is due to the fact that, magnetically, the VC is a very small object.

M. Grimsditch and coworkers used the difracted magneto-optical Kerr effect (DMOKE) technique to investigate the high-order hysteresis loops of a square array of Py ($\mathrm{Ni_{81}Fe_{19}}$) disks with $(L, R) = (60, 800)$ nm and period $d = 1.6$ μm [77]. From the fitting of the measured high-order hysteresis loops to the theoretical shapes calculated with account of the form factors associated with the presence of a VS within the dots, the authors concluded that magnetic vortices are nucleated with a preferential chirality in the majority of the disks (coherent chirality) due to the presence of asymmetries in the dots shape. In Ref. [78] the authors studied the effect of the interdot magnetostatic interaction on the magnetic properties of arrays of circular dots with the VS. Disks of Py ($\mathrm{Ni_{81}Fe_{19}}$) with thickness $L = 80$ nm and radii $R \in \{0.2, 0.3, 0.4\}$ μm were considered. Rectangular arrays of these disks (with a fixed value of R) were fabricated, with the interdot distance along the Y axis being set to $\zeta_y = 2R$ and being variable along the X axis, $\zeta_x \in [30, 800]$ nm. The direction of the external magnetic field was set to the X axis. V. Novosad *et al.* observed that for a fixed interdot distance ζ_x both nucleation and annihilation fields are decreasing functions of the radius of the disk, whereas for a fixed radius both nucleation and annihilation fields are increasing functions of the interdot distance. On the other hand, the more packed the dots are within the array, the bigger its initial susceptibility is. The values of these three magnitudes tend to a plateau for ζ_x big enough. The authors also noticed that the shape of the hysteresis loops was sensitive to the angle between the lattice orientation and the applied magnetic field. In brief, magnetization reversal in arrays of ferromagnetic circular disks is controlled by magnetostatic interaction in the regime of small interdot distances.

3.1.2 Theoretical description

For an arbitrary geometry of the magnetic structure -defined by a volume V- the static magnetization-field distribution of the ground state, $\vec{M}(\vec{r})$, can be derived by functional minimization of the total energy

$$E[\vec{m}] = \int_V \mathrm{d}^3\vec{r} \left\{ \frac{A}{2} \sum_{i=x,y,z} [\nabla m_i(\vec{r})]^2 - M_S \left(\vec{H}_\mathrm{d}[\vec{m}] + \vec{H} \right) \cdot \vec{m}(\vec{r}) \right\} \tag{3.1}$$

corresponding to the sum of the exchange, magnetostatic and Zeeman contributions, respectively. Magnetocrystalline anisotropy is neglected for the time being. $\vec{m} = \vec{M}/M_S$ is the normalized magnetization field, $\vec{H}$ is the external magnetic field, $\vec{H}_\mathrm{d}$ is the demagnetizing field associated with the magnetization distribution, and M_S and A are the saturation magnetization and exchange stiffness constant of the ferromagnetic material, respectively.

Minimization of the above functional should be done with the constraint $|\vec{m}(\vec{r})| = 1$ within the volume of the system, which leads to the magnetization field being naturally mapped onto the complex plane by means of the stereographic projection,

$$m_x + i m_y = \frac{2w}{1+|w|^2}, \quad m_z = \frac{1-|w|^2}{1+|w|^2}, \tag{3.2}$$

where $w(\vec{r}) \in \mathbf{C}$ is a complex function. Restricting oneself to the case of a two-dimensional flat geometry in the XY plane, the stereographic parametrization becomes a mapping $w : \mathbf{C} \to \mathbf{S}^2$, that is, $w(z, \bar{z})$ is a function of the complex variable $z = x + iy$. Notice that $\mathbf{S}^2$ represents the three-dimensional sphere. In so doing, the functional for the exchange interaction becomes

$$E_\mathrm{ex}[\vec{m}] = AL \int_{\mathbf{R}^2} \mathrm{d}x\, \mathrm{d}y \, \frac{4}{(1+|w|^2)^2} \left(\frac{\partial w}{\partial z} \frac{\partial \bar{w}}{\partial \bar{z}} + \frac{\partial w}{\partial \bar{z}} \frac{\partial \bar{w}}{\partial z} \right), \tag{3.3}$$

where L is the thickness of the flat structure and independence on the coordinate z has been assumed. The topological charge (or vorticity) is defined as the degree of the mapping $w : \mathbf{C} \to S^2$,

$$\begin{aligned} \mathcal{Q} &= \frac{1}{4\pi} \int_{\mathbf{S}^2} \vec{m} \cdot \mathrm{d}^2\vec{S}, \\ &= \frac{1}{\pi} \int_{\mathbf{R}^2} \mathrm{d}x\, \mathrm{d}y \, \frac{1}{(1+|w|^2)^2} \left(\frac{\partial w}{\partial z} \frac{\partial \bar{w}}{\partial \bar{z}} - \frac{\partial w}{\partial \bar{z}} \frac{\partial \bar{w}}{\partial z} \right), \end{aligned} \tag{3.4}$$

where surface integration is done over the three-dimensional sphere. Notice that $\mathcal{Q}$ is a topological invariant of integer nature. Minimization of the functional (3.3) [see Appendix A] leads to the complex partial differential equation

$$\frac{\partial}{\partial z} \left(\frac{\partial w}{\partial \bar{z}} \right) = \frac{2\bar{w}}{1+|w|^2} \frac{\partial w}{\partial z} \frac{\partial w}{\partial \bar{z}}, \tag{3.5}$$

whose solutions are the extrema of the functional (3.3) and therefore (un)stable magnetic states of the exchange interaction. Holomorphicity of w is a sufficient condition to satisfy Eq. (3.5) because of the Cauchy-Riemann equations $[\partial w/\partial \bar{z} = 0]$. A. Belavin and A. Polyakov found the only family of solutions of the unbounded two-dimensional case with finite exchange energy, which are known as the Belavin-Polyakov (BP) solitons [79]. These solutions are defined by a rational function w of the complex variable z, so that zeros of the numerator (denominator) correspond to the centers of the solitons with positive (negative) topological charge and $|m_z| = 1$ for $|z| \to \infty$. D. Gross found another family of solutions of Eq. (3.5), the *merons*, defined by a parametrization of the form $w(z,\bar{z}) = f(z)/|f(z)|$ with f being an arbitrary holomorphic function [80]. These solutions exhibit zero out-of-plane component of the magnetization field everywhere, $m_z \equiv 0$, and their exchange energy density diverges at those points where $f(z) = 0$. Therefore, BP solitons (merons) are (un)stable magnetic configurations of the infinite planar ferromagnet.

A pseudo meron function can be introduced to avoid the divergences of the exchange energy density present in the pure meron case: On the contour $|f| = 1$ the pure meron solution overlaps $w(z) = f(z)$ continuously for any holomorphic function f, so that the complex function

$$w(z,\bar{z}) = \begin{cases} f(z) & |f(z)| \leq 1 \\ \frac{f(z)}{|f(z)|} & |f(z)| > 1 \end{cases} \tag{3.6}$$

turns out to be continuous. Notice that in the domain $\{z \in \mathbf{C}, |f(z)| \leq 1\}$ the magnetic structure is BP-soliton-like, whereas outside shows a meron-like behaviour. A realistic vortex-like magnetization-field distribution can be obtained by means of the holomorphic function

$$f(z) = i\left(\frac{z - z_0}{\lambda}\right)^n, \tag{3.7}$$

which represents a VS centered at the point z_0 of the flat space and where λ is an arbitrary real number characterizing the scale (size) of the soliton-like part (the vortex core) and n is an arbitrary integer number. The corresponding vorticity is $\mathcal{Q} = n$, so that positive values of n correspond to magnetic vortices.

The case $n = 1$ corresponds to the prototypical VS described in the previous subsections and, for a flat (finite) disk geometry and $z_0 = 0$, it satisfies the boundary conditions $\vec{m} \cdot \vec{n} = \dfrac{\partial \vec{m}}{\partial \vec{n}} \equiv 0$ on the lateral side of the circular dot. N. Usov and S. Peschany investigated the stability of this particular solution and proved that, even though the exchange energy associated to this family of solutions is invariant under translations $z \mapsto z + z_0$ and scaling transformations $z \mapsto \lambda z$ (which implies that there is no preferential choice of either center or scale), this magnetic structure stabilizes with respect to both VC displacement and VC size due to the magnetostatic interaction [81, 82]. This means that the equilibrium values of the parameters (z_0, λ) can be obtained by minimizing the total energy functional (3.1). Family of solutions corresponding to $n = \mathcal{Q} = 1$ is referred to as the *rigid vortex model* (RVM).

Composition of solutions of Eq. (3.5) with holomorphic functions also satisfies the same Euler-Lagrange equation. Therefore, solutions of the form (3.7) can be generalized to other shapes by means of conformal mappings, for which the choice of a complex function f based solely on symmetry arguments is cumbersome. The forthcoming theoretical development becomes simplified over the unit disk $\mathbf{D} = D(0,1)$, so that an arbitrary circular disk of radius R, $D(0,R)$, is mapped onto $\mathbf{D}$ via the (conformal) scaling $z \mapsto z/R$. From this point forward, complex variables and length scales are normalized according to this transformation. The conformal map $z \mapsto (z - z_0)/(1 - \overline{z_0} z)$ of the unit disk to itself yields the following family of solutions, referred to as the *two-vortex model* (2VM):

$$w(z,\bar{z}) = \begin{cases} \frac{i}{\lambda}\frac{z-z_0}{1-\overline{z_0}z} & |z-z_0| \leq \lambda|1-\overline{z_0}z| \\ i\frac{(z-z_0)|1-\overline{z_0}z|}{(1-\overline{z_0}z)|z-z_0|} & |z-z_0| > \lambda|1-\overline{z_0}z|. \end{cases} \tag{3.8}$$

The conformal mapping used preserves the boundary condition $\left.\dfrac{\partial \vec{m}}{\partial \vec{n}}\right|_{\partial\mathbf{D}} \equiv 0$ but magnetic charges on the side of the disk, $\vec{m} \cdot \vec{n}|_{\partial\mathbf{D}}$, appear. One can always rotate the frame of axis so that the coordinate z_0 of the vortex center becomes a real number. The total energy (3.1) can be calculated with account of Eqs. (3.2),(3.6),(3.7) for both the RVM and 2VM [83–85]:

$$\begin{aligned} E_{\mathrm{RVM}} &= \frac{\pi}{2}AL\left[\ln\left(1-z_0^2\right) - 2\ln\left(\lambda\right)\right] + (2\pi M_S)^2(R\lambda)^3\left[G(0) - G(\beta/\lambda)\right] \\ &\quad + 2M_S^2R^2L\left[z_0^2\sum_{\mu>0}F_\mu(\beta)I_\mu^2(z_0)\right] + E_Z, \qquad (3.9) \\ E_{\mathrm{2VM}} &= \pi AL\left[2 - \ln\left(\lambda\right)\right] + (2\pi M_S)^2(RR_\lambda)^3\left[G(0) - G(\beta/R_\lambda)\right] + (2\pi M_S)^2 \times \\ &\quad \frac{R^2L}{2}\left[z_0^2\left(z_0^2-2\right)^2F_1(\beta) + \left(1-z_0^2\right)^2\sum_{\mu\geq 2}z_0^{2\mu}F_\mu(\beta)\right] + E_Z, \qquad (3.10) \end{aligned}$$

where the constants depending solely on the disk geometry (that is, not depending on the parameters of the model) have been omitted. The contributions to the total energy in the above expressions are the exchange energy, the magnetostatic energy of the magnetic charges on the faces and side of the disk, and the Zeeman energy, respectively. Notice that $R_\lambda = \lambda(1-z_0^2)/(1-\lambda^2z_0^2)$ and that the magnetostatic function $G(x)$ is defined as

$$G(x) = \int_0^1 \int_0^1 \int_0^{2\pi} \int_0^{2\pi} \frac{\mathrm{d}\rho_1\, \mathrm{d}\rho_2\, \mathrm{d}\phi_1\, \mathrm{d}\phi_2\ \rho_1\rho_2\sigma(\rho_1,\phi_1)\sigma(\rho_2,\phi_2)}{(2\pi)^2\sqrt{x^2+\rho_1^2+\rho_2^2-2\rho_1\rho_2\cos(\phi_1-\phi_2)}}, \tag{3.11}$$

where $\sigma = \vec{m}\cdot\vec{n}|_{\text{face}} = m_z$ is the magnetic charge density on the faces of the disk, which depends on the model considered. The functions $F_\mu(\beta)$ and $I_\mu(z)$ are defined as

$$F_\mu(\beta) = \int_0^\infty \mathrm{d}t \frac{f(\beta t)}{t} J_\mu^2(t), \quad f(x) = 1 - \frac{1-e^{-x}}{x} \tag{3.12}$$

$$I_\mu(z) = 2\int_0^\pi \mathrm{d}\phi \frac{\sin\phi \sin(\mu\phi)}{\sqrt{1-2z\cos\phi + z^2}}, \tag{3.13}$$

where $J_\mu(x)$ is the Bessel function of the first kind and order μ. Suppose that the magnetic field is applied along the Y axis, $\vec{H} = H\hat{e}_y$. Thus, the Zeeman energy term turns out to be $E_Z = -HM_S\pi R^2 L\langle m_y\rangle$. Within the regime of small displacements of the VC, $z_0 \ll 1$, the average value of the Y-component of the normalized magnetization field is given by

$$\langle m_y\rangle_{\text{RVM}} \simeq z_0 + O(z_0^3), \tag{3.14}$$

$$\langle m_y\rangle_{\text{2VM}} \simeq \frac{4\pi}{144}\left[15z_0^4 + 34z_0^2 - 193\right] z_0. \tag{3.15}$$

Notice that the expression for $\langle m_y\rangle$ within the RVM is independent of the orientation of the external magnetic field.

RVM describes well the vortex structure in the regimes of small VC displacement ($z_0 \ll 1$) and the vortex center being outside the dot ($z_0 \gg 1$). For small displacements of the VC, expression (3.9) for the total energy can be approximated as

$$E|_{\text{RMV}} \simeq E[s=0] + M_S^2\pi R^2 L\left[a(\beta,R)z_0^2 - \frac{H}{M_S}z_0\right] + O(z_0^4), \tag{3.16}$$

$$a(\beta,R) = 2\pi F_1(\beta) - \frac{1}{2}\left(\frac{\Delta_0}{R}\right)^2,$$

where $a(\beta,R)$ must be postive defined to stabilize the vortex within the disk. The exchange length is defined as $\Delta_0 = \sqrt{A/M_S^2}$. Minimization with respect to the parameter z_0 yields the equilibrium displacement of the vortex center

$$\langle z_0\rangle|_{\text{eq}} = \frac{H}{2a(\beta,R)M_S}, \tag{3.17}$$

so that the average value of magnetization turns out to be [see Eq. (3.14)] $\langle\vec{M}\rangle|_{\text{eq}} = \chi_{\text{iso}}\vec{H}$, where $\chi_{\text{iso}} = \dfrac{1}{2a(\beta,R)}$ is the initial in-plane susceptibility of the isolated circular disk. The nucleation field is defined as the maximal magnetic field at which the initial SD state becomes unstable. The corresponding process of nucleation can be modeled by means of the RVM considering a vortex structure (3.7) with its center $z_0 = 1/\sin\phi_0$ located outside the disk ($\phi_0 = 0$ corresponds to the SD magnetic structure). Recalculating the total energy of the system and studying its stability with respect to the angle ϕ_0, one obtains a critical magnetic field below which instability of the SD state arises,

$$H_{\text{n,iso}}(\beta,R) = 4\pi M_S\left[F_1(\beta) - F_2(\beta) - \frac{1}{\pi}\left(\frac{\Delta_0}{R}\right)^2\right]. \tag{3.18}$$

Calculation of the annihilation field can be done within the 2VM: In Ref. [85] the assumption of $z_0\lambda$ being small —which is justified by numerical calculations— leads to the parameters of the total energy becoming decoupled if one considers the new pair (z_0, q), with $q = \lambda\left(1 - z_0^2\right)/\beta$. Therefore, the total energy splits into the sum $E[z_0, q] = E_1[z_0, H] + E_2[q]$ and the term depending solely on the VC displacement is given by

$$\begin{aligned}\frac{E_1[z_0,H]}{M_S^2\pi R^2 L} = 2\pi&\left[z_0^2\left(z_0^2-2\right)^2 F_1(\beta) + \left(1-z_0^2\right)^2\sum_{\mu\geq 2} z_0^{2\mu}F_\mu(\beta)\right]\\ &- \frac{H}{M_S}\langle m_y\rangle + \left(\frac{\Delta_0}{R}\right)^2 \ln\left(1-z_0^2\right).\end{aligned} \tag{3.19}$$

Instability of the VS arises at the annihilation field, where the displacement of the VC minimizing the energy (3.19) becomes a saddle point. That is,

$$\begin{aligned} 0 &= \frac{\partial E_1[\langle z_0\rangle_{\text{eq}}, H_{\text{an}}]}{\partial z_0}, \\ 0 &= \frac{\partial^2 E_1[\langle z_0\rangle_{\text{eq}}, H_{\text{an}}]}{\partial z_0^2}. \end{aligned} \tag{3.20}$$

This system of equations must be solved numerically and the resulting values of the annihilation field are plotted in Fig. 3.5. Theoretical predictions of the initial in-plane susceptibility and of the nucleation and annihilation fields agree reasonably well with the corresponding experimental values of these magnitudes, see Fig. 3.5.

The above results have been derived for an isolated disk. Generalization to the case of an array of dots, where interdot magnetostatic interactions play a significant role in the magnetization reversal processes, is straightforward [84]. Let again ζ_x

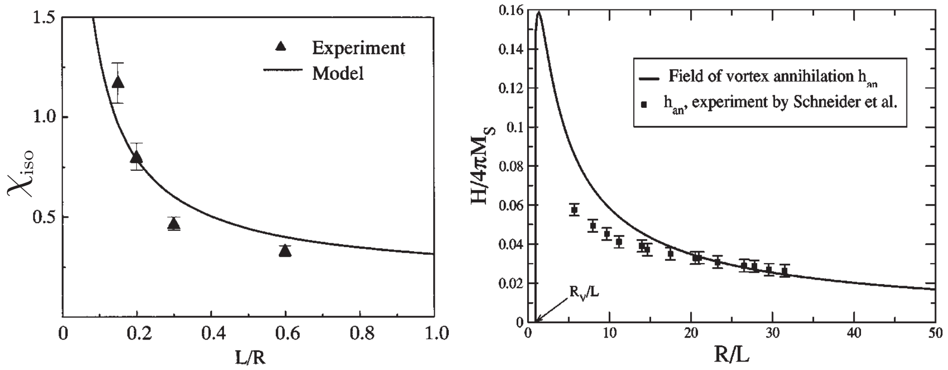

Figure 3.5: Initial in-plane susceptibility (left) and annihilation field (right) as a function of the aspect ratio. Solid lines and points represent theoretical dependences and experimental data, respectively. This figure has been adapted from Refs. [83, 85].

and ζ_y denote the interdot distances along the X and Y axes, respectively. Let $d_x = 2R + \zeta_x$ and $d_y = 2R + \zeta_y$ denote the unit cell sizes. The frame of axes is chosen so that $d_x \leq d_y$. Only the magnetostatic energy is affected by the interdot distance –exchange and Zeeman energies are single-disk quantities–, which for small displacements z_0 and within the RVM becomes

$$E_{\text{mag}}[z_0] = E_{\text{mag}}[0] + 2(\pi R M_S)^2 L \Lambda(\beta, \delta, \phi_H) z_0^2 + O(z_0^4), \tag{3.21}$$
$$\Lambda(\beta, \delta, \phi_H) = \frac{4\pi}{d_x d_y} \sum_{\vec{k}} f(kL) \frac{J_1^2(kR)}{k^2} \cos^2(\phi_{\vec{k}} - \phi_H),$$

where summation runs over vectors $\vec{k}$ of the reciprocal lattice, $\delta = d_x/R$ and $\phi_{\vec{k}}$ (ϕ_H) is the polar angle for the vector $\vec{k}$ ($\vec{H}$). Therefore, the expression for the total energy of an array of identical circular disks in the regime of small displacement of the VC is given by

$$E \simeq E[s=0] + M_S^2 \pi R^2 L \left[A(\beta, \delta, R, \phi_H) z_0^2 - \frac{H}{M_S} z_0 \right] + O(z_0^4), \tag{3.22}$$
$$A(\beta, \delta, R, \phi_H) = 2\pi \Lambda(\beta, \delta, \phi_H) - \frac{1}{2} \left(\frac{\Delta_0}{R} \right)^2,$$

so that the theoretical expression for the initial in-plane susceptibility of the array, χ_{array}, is analogous to the one derived for the single-disk case, but substituting $a(\beta, R)$ with $A(\beta, \delta, R, \phi_H)$: $\chi_{\text{array}} = \frac{1}{2A(\beta,\delta,R,\phi_H)}$. The nucleation field for the array of dots can be derived along the lines of the isolated-disk case, resulting in the expression

$$H_{\mathrm{n,array}}(\beta,\delta,R,\phi_H)=4\pi M_S\left[F(\beta,\delta,\phi_H)-\frac{1}{\pi}\left(\frac{\Delta_0}{R}\right)^2\right],\tag{3.23}$$

$$F(\beta,\delta,\phi_H)=-\frac{8\pi}{d_xd_y}\sum_{\vec{k}}f(kL)\frac{\cos^2(\phi_{\vec{k}}-\phi_H)}{k^2}[C_1(kR)\cos[2(\phi_{\vec{k}}-\phi_H)]+C_2(kR)],$$

$$C_1(x)=3J_1(x)J_3(x)-J_2^2(x),\ C_2(x)=-J_1(x)J_3(x)-J_0(x)J_2(x).$$

Once again, these formulas explain reasonably well the experimental results with regard to the effect of the interdot spacing on the magnetic properties of circular disks. Numerical calculations of the above magnitudes lead to conclude that the nucleation field decreases significantly when the interdot distance reduces, whereas χ_{array} increases.

A different approach can be taken to study the topology of the VS, not based on variational principles. A. Aharoni investigated analitically the curling of the magnetization field in flat circular disks, based on the ansatz $m_\rho=0, m_\phi=f(\rho)$ and $m_z=\sqrt{1-m_\phi^2}$ for the magnetization in cylindrical coordinates (ρ,ϕ,z) [86]. N. Usov and S. Peschany showed that the substitution $f(\rho)\to\sin\Theta(\rho)$ yields the relation $\tan\Theta(\rho)=\rho/b$, where b is the radius of the VC [81, 82]. Notice that $\Theta(\rho)=\pi/2$ $(m_z=0)$ outside the vortex core. With account of the expansion

$$\vec{M}(\Theta,\Phi)=M_S(\cos\Phi\sin\Theta,\sin\Phi\sin\Theta,\cos\Theta)\tag{3.24}$$

of the fixed-length magnetization vector in spherical coordinates, the following asymptotic expansion [87] of the static magnetization field for the VS will be used in the forthcoming calculations:

$$\begin{aligned}\Phi_0(x,y)&=\mathcal{Q}\tan^{-1}(y-y_v/x-x_v)+\phi_0,\\ \cos\Theta_0(\tilde{r})&=\begin{cases}p\left(1-C_1\left(\frac{\tilde{r}}{\Delta_0}\right)^2\right) & \tilde{r}\ll\Delta_0\\ C_2\left(\frac{\Delta_0}{\tilde{r}}\right)^{1/2}\exp(-\tilde{r}/\Delta_0) & \tilde{r}\gg\Delta_0\end{cases}\end{aligned}\tag{3.25}$$

where (x_v,y_v) are the coordinates of the VC center in the XY plane and $\tilde{r}$ represents the distance from it. $\phi_0=\pm\pi/2$ corresponds to chirality $C=\pm1$ of the magnetization vector in the dot plane, respectively, and C_1,C_2 are constants that can be obtained by imposing the smoothness condition on $\cos\Theta_0$ at $\tilde{r}=\Delta_0$ up to its first derivative. The corresponding values are $C_1=\frac{3}{7}$ and $C_2=\frac{4}{7}pe$, where e denotes Euler's number. It is important to remark that a magnetic vortex of fixed vorticity (in the present case, $\mathcal{Q}=1$) is defined topologically by its polarization p and its chirality C.

3.2 Dynamics of the vortex state

Topological singularity of the magnetic vortex structure leads the VC to behave as an independent entity because of the strong exchange interaction among its spins. This enriches the landscape of magnetic excitations present in submicron-size circular disks, which can be classified into two well-defined families. The first one consists of the low-frequency dynamics of the VS, characterized by the spiral-like precessional motion of the VC as a whole. The family of spin-waves excitations defines the second kind of dynamics for the vortex ground state.

3.2.1 Low-frequency dynamics

The spiral motion of the VC in Py circular disks was directly observed in Ref. [88] for the first time. J. Park and coworkers used time-resolved Kerr imaging to study the dynamics of the VS in individual Py ($Ni_{81}Fe_{19}$) disks with thickness $L = 60$ nm and diameters $2R \in \{0.5, 1, 2\}$ μm after the application of an in-plane magnetic-field pulse of amplitude 5 Oe and width 150 ps. Apart from the high-frequency dynamics (magnons), the authors observed a long-lived sub-GHz Kerr signal attributed to the gyrotropic motion of the VC. This excitation is known as the *gyrotropic mode*. S. Choe *et al.* studied the magnetization dynamics of micron-size magnetic vortex structures by means of time-resolved x-ray imaging –with a time resolution of about 70 ps– using fast in-plane AC pulses [89]. First, they found a subnanosecond dynamical response ruled by the polarization of the VC. A three-dimensional chirality in the vortex structure is induced by the out-of-plane component of the magnetization of the VC, which controls its precessional motion driven by the subnanosecond magnetic field pulse: The motion is (anti)parallel to the field on that time scale for (left) right-handed vortices. After the magnetic field pulse, the VC follows a gyrotropic motion towards its equilibrium position. The corresponding VC velocity is found to be one order of magnitude higher than the expected value calculated from the static susceptibility.

Detection of the gyrotropic mode was performed by V. Novosad and coworkers using a vector network analyzer to measure the excitation spectrum of micron-size Py ($Ni_{80}Fe_{20}$) circular disks of thicknesses $L \in \{20, 40\}$ nm and diameters $2R \in \{1, 2\}$ μm lithographed on top of microwave coplanar waveguides [90]. Application of an in-plane AC field of amplitude about 1 Oe leads to the excitation of the gyrotropic mode. The authors observed narrow resonant peaks within the subGHz range in the excitation spectra of the samples, which correspond to the gyrotropic motion of the VC as a whole. They also found a weak dependence of the gyrotropic frequency (gyrofrequency) on the application of an static in-plane magnetic field –which induces the initial displacement of the VC within the dot. This dependence becomes noticeable when $H \to H_{\mathrm{an}}$. The gyrofrequency scales with β, being an increasing function of the aspect ratio. This is indicative of the fact that the gyrotropic mode is dominated by magnetostatic interactions induced by the circular geometry of the dots.

In Ref. [91] magnetization reversal of the VS via excitation of the gyrotropic mode with bursts of an in-plane AC magnetic field was explored. The authors applied an in-plane sinusoidal field of amplitude 1 Oe and frequency 250 MHz, which is close to the expected value 244 MHz for the gyrofrequency of the vortex structure. This guarantees a permanent spiral-like precessional motion of the VC. Superimposed on this, a short magnetic field burst of 4 ns is applied and the resulting dynamics is studied by time-resolved X-ray imaging. Switching of the VC polarization can be detected through the change of the sense of gyration of the VC during its gyrotropic motion [See Eq. (3.27)]. It was observed that just a magnetic field strength of about 15 Oe is enough for the burst to change the direction of the out-of-plane component of the magnetization of the VC. This VC switching was reproduced by the authors using micromagnetic simulations, where they observed that this switching process occurs via the formation of a vortex-antivortex (V-AV) pair with equal polarizations. This V-AV pair splits and the antivortex moves towards the original vortex, both of them annihilating when they meet. Therefore, only the new vortex with opposite polarization remains in the magnetic structure.

It is worth pointing out that this scheme allows magnetization reversal of the VC in a controllable manner using short in-plane bursts of a very weak magnetic field compared to the switching of the VC polarization induced by the application of a perpendicular static magnetic field H opposite to the VC direction, with values for the reversal field of $H_\mathrm{r} \sim 5000$ Oe. G. de Loubens *et al.* used magnetic resonance force microscope (MRFM) spectroscopy to study the dependence of the gyrotropic mode on the application of a transversal magnetic field in single circular disks made of NiMnSb with thickness $L = 43.8$ nm and radius $R \in \{130, 520\}$ nm [92]. The gyrofrequency was found to split into two modes whose difference was linear with the field H and the aspect ratio β. These two gyrotropic modes induced by the magnetic field correspond to the two (opposite) polarizations of the VC and this bistability occurs within the range of magnetic fields $|H| < H_\mathrm{r}$.

Theoretical description

The gyrotropic motion of the VC can be described according to a collective variable approach, because it precesses towards the equilibrium position as a whole entity. The magnetization field of the vortex structure is therefore uniquely determined by the position of the center of the VC in the XY plane, represented by the coordinate vector $\vec{X} = (x, y)$ where $x(t)$ and $y(t)$ are time-dependent functions. The equation of motion for this collective variable can be obtained from the Landau-Lifshitz-

Gilbert equation [93] with account of the functional form $\vec{M}[\vec{r},t] = \vec{M}[\vec{r} - \vec{X}(t)]$ for the magnetization field,

$$\dot{\vec{X}} \times \vec{G} + \frac{\partial E(\vec{X})}{\partial \vec{X}} - \hat{D}\dot{\vec{X}} = 0, \tag{3.26}$$

which is known as *Thiele equation* [94]. The second term describes the restoring force acting on the system and $E(\vec{X})$ represents the potential energy of the vortex structure at the VC position $\vec{X}$. Exchange, magnetostatic, anisotropy (if not neglected) and Zeeman energies are the main contributions to this potential, but pinning might be considered when necessary [see Chapter 4]. The first and third term are the gyroscopic force and the dissipative (damping) force, respectively. They are completely characterized in terms of the gyrovector $\vec{G}$ and the damping tensor $\hat{D}$, with expressions

$$\vec{G} = L\frac{M_S}{\gamma}\int_{D(0,R)} \mathrm{d}^2\vec{r}\, \sin\Theta\left(\nabla_{\vec{r}}\Phi \times \nabla_{\vec{r}}\Theta\right), \tag{3.27}$$

$$D_{\alpha\beta} = -\alpha_{\mathrm{LLG}}L\frac{M_S}{\gamma}\int_{D(0,R)} \mathrm{d}^2\vec{r}\left(\frac{\partial\Theta}{\partial x_\alpha}\frac{\partial\Theta}{\partial x_\beta} + \sin^2\Theta\frac{\partial\Phi}{\partial x_\alpha}\frac{\partial\Phi}{\partial x_\beta}\right), \tag{3.28}$$

where γ is the gyromagnetic ratio and α_{LLG} is the Gilbert damping parameter. The damping tensor becomes diagonal for cylindrical geometries, $\hat{D} = D\hat{\mathbb{I}}$, with D being the damping coefficient. The values of the gyrovector and the damping coefficient can be calculated within the RVM [95, 96]:

$$\vec{G} = G\hat{e}_z, \quad G = 2\pi pQLM_S/\gamma, \tag{3.29}$$

$$D = -\alpha_{\mathrm{LLG}}[2 + \ln(R/R_c)]\pi LM_S/\gamma, \quad R_c(L) = 0.86\Delta_0\left(\frac{L}{\Delta_0}\right)^{1/3} \tag{3.30}$$

with the expression of R_c being valid for $L \geq \sqrt{2}\Delta_0$. The Thiele equation can be also derived from the Lagrangian formulation of the Landau-Lifshitz equation according to the principle of least action. This Lagrangian approach leads naturally to generalizations of the above equation, see Sec. 3.4.

Calculation of the gyrofrequency ω_{G} can be done from Thiele equation if 1) dissipation is neglected (it affects only the amplitude of the precessional motion, not its period), and 2) the regime of small displacements ($|\vec{X}| \ll R$) is considered. The gyrotropic frequency can be accurately calculated within the *two-vortices side surface charges free model* (2VSCFM), which is described by the holomorphic function $f(z) = icz + z_0 - \overline{z_0}z^2$ with $c \in \mathbf{R}$ and $z_0 \in \mathbf{C}$ (in the absence of applied magnetic field, it can be taken real). It verifies the boundary condition $\vec{m}\cdot\vec{n}|_{\partial\mathbf{D}} \equiv 0$, that is, no lateral surface charges are generated. The expression of the total energy for small displacements of the VC becomes [97, 98]

$$\begin{aligned} E[z_0] &= E[z_0 = 0] + M_S^2 \pi R^2 L a^\star(\beta, R) z_0^2 + O(z_0^3), \qquad (3.31) \\ a^\star(\beta, R) &= 8\pi F^\star(\beta) - \left(\frac{\Delta_0}{R}\right)^2, \quad F^\star(x) = \int_0^\infty \mathrm{d}t \frac{f(xt)}{t} \left(\int_0^1 \mathrm{d}\rho \rho J_1(t\rho)\right)^2, \end{aligned}$$

so that the restoring force becomes $\dfrac{\partial E}{\partial \vec{X}} = (2\pi M_S^2 L) a^\star(\beta, R) \vec{X}$. With account of the expression $\dot{\vec{X}} = \vec{\omega} \times \vec{X}$ for the velocity of the VC in a circular motion, with $\vec{\omega} = \omega \hat{e}_z$ being the angular frequency, one has $\dot{\vec{X}} \times \vec{G} = \omega G \vec{X}$. Therefore Eq. (3.26) yields the following expression for the gyrofrequency

$$\omega_\mathrm{G} = \frac{2\pi M_S^2 L a^\star(\beta, R)}{|G|} = \gamma M_S a^\star(\beta, R), \qquad (3.32)$$

where a magnetic vortex with topological charge $\mathcal{Q} = 1$ has been considered. Within the limit $\beta \ll 1$ the linear approximation $F^\star(\beta) \simeq \dfrac{5}{18\pi}\beta$ holds and the term $(\Delta_0/R)^2$ can be neglected because $\Delta_0 \ll R$. This leads to the linear dependence $\omega_\mathrm{G} = \dfrac{20}{9}\gamma M_S \beta$ for the gyrofrequency [98] in the regime of very small aspect ratios.

Fig. 3.6 shows comparison of experimental values (left) and micromagnetic simulations (right) for the gyrofrequency to the above theoretical predictions. The agreement between theory and experiments is satisfactory in the case of the gyrotropic mode. In Ref. [98], K. Guslienko and coworkers observed by means of micromagnetic simulations that the direction of the precessional motion (CW or CCW) of the VC is determined by the combination of the polarization and the chirality, in agreement with the experimental observations of Ref. [89].

3.2.2 Magnon dynamics

Whereas the gyrotropic motion of the VC represents the softest dynamical mode of the VS, high-frequency excitations occur in the form of conventional spin waves. High-frequency spin wave modes can be excited by low-amplitude short-duration magnetic field pulses and can be classified by a pair of integers (m, n), with $n \in \mathbf{N}$ corresponding to the number of axially symmetric nodes and $m \in \mathbf{Z}$ counting the number of azimuthal modes.

Ref. [99] reports the observation of dipole-dominated spin waves in an square array of Py circular dots with $(L, R) = (60, 400)$ nm and lattice period $d = 1.6$ μm. The authors observed two excitation modes in the VS with frequencies $f_1 \sim 8$ GHz and $f_2 \sim 12$ GHz using Brillouin light scattering (BLS) spectroscopy, showing no

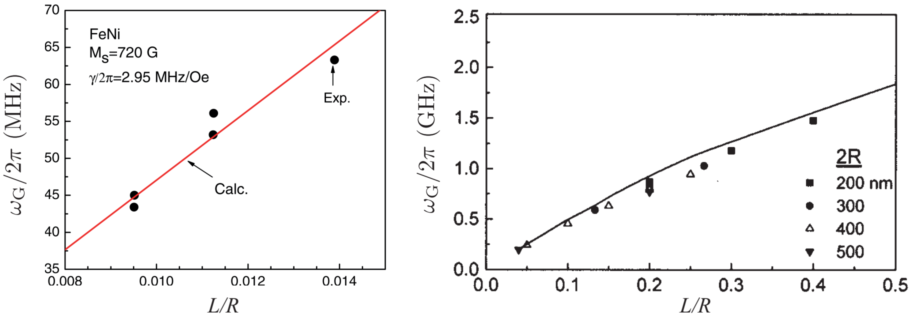

Figure 3.6: (Left) Experimental data for the gyrotropic frequency (symbols) and analytical dependence within the linear approximation (solid line) vs. the disk aspect ratio. (Right) Comparison of micromagnetic calculations (symbols) and theoretical dependence (solid line) given by Eq. (3.32) vs. the dot aspect ratio. This figure has been adapted from Refs. [97, 98].

dependence on (being slightly decreasing with) the strength of an in-plane applied magnetic field in the former (latter) case. V. Novosad *et al.* could reproduce these magnon modes by means of micromagnetic simulations, showing their radial nature and their localization at the edge and inside the disk (collective behavior far from both the edge and the VC), respectively. L. Giovannini and coworkers also used BLS to study spin wave excitations in an array of dots with $(L, R) = (15, 100)$ nm and interdot distance $2R$. The experimental results were interpreted within the framework of a hybrid micromagnetic simulation based on a dynamical matrix approach [100]. The authors concluded that at zero in-plane magnetic field 1) eigenfrequency of pure radial modes $(0, n)$ is an increasing function of the radial index n, and 2) the mode coupling effect (hybridization of $\pm m$ modes) is observed in many spin-wave modes. In general, application of transversal magnetic field pulses excites radially symmetric magnon modes.

On the other hand, in-plane magnetic field pulses generate spin-wave modes with azimuthal symmetry. C. Zaspel *et al.* used this scheme combined with time-resolved Kerr microscopy to study the excitation spectrum of Py ($\mathrm{Ni_{81}Fe_{19}}$) disks with thickness $L = 50$ nm and radii $R \in [250, 1000]$ nm [101]. A couple of peaks in the spectrum were clearly observed, one belonging to the sub-GHz range (identified with the gyrotropic mode) and the second one to the GHz range. These modes correspond to azimuthal modes with $|m| = 1$: This particular symmetry is unraveled by means of the polar Kerr rotation signal, where a phase shift of 2π in the time traces is observed when one moves around the azimuth of the dots. Another high-frequency $|m| = 1$ mode was also measured experimentally for some disks. From the theoretical model presented in Refs. [101, 102] one concludes that the azimuthal number corresponding to the gyrotropic mode is $m = -1$. The higher frequency modes belonging to the $|m| = 1$ class form a doublet, whose frequency splitting increases with the aspect ratio.

Broadband ferromagnetic resonance (FMR) in combination with Kerr imaging was used in Ref. [103] to study magnon dynamics of the VS in arrays of Py circular disks with $(L, R) = (30, 350)$ nm and with lattice period $d = 2$ μm. Transversal configuration of the transient magnetic field led to an excitation spectrum dominated by a peak at 9.3 GHz and two additional resonances with small amplitudes at 2.4 and 13.0 GHz. Homogeneity of the field pulse over the disks yields the dominant resonance being a uniform mode across the disk with mode number $(m, n) = (0, 0)$. The highest mode corresponds to a radial mode with $n = 2$. These two modes are also excited within the in-plane configuration of the pulse excitation. Furthermore, also the gyrotropic mode ($\omega_{\mathrm{G}} = 0.44$ GHz) is excited and two other resonant peaks appear at 6.00 and 7.25 GHz, which correspond to the azimuthal class $|m| = 1$. Kerr imaging of these latter modes led the authors to conclude that they are circularly polarized (with opposite chirality) and couple directly to the spatially antisymmetric torque profile of the excitation pulse. Furthermore, a substantial doublet splitting of 1.5 GHz is observed in the $|m| = 1$ class.

J. Park and coworkers studied the class $|m| = 1$ of azimuthal spin-wave modes in Py ($\mathrm{Ni}_{81}\mathrm{Fe}_{19}$) disks with $L = 20$ nm and $R \in \{0.7, 5.0\}$ μm using time-resolved Kerr microscopy [104]. Analysis of the corresponding spatially resolved spectral power and phase images led the authors to conclude that the chirality of the phase change in the $(\pm 1, 0)$ modes is determined by the polarization of the VC. Therefore, the azimuthal symmetry breaking of the $|m| = 1$ modes is due to the coupling between the gyroscopic motion of the VC (p fixes its sense of rotation) and magnon dynamics, with the doublet splitting increasing as β increases. In Ref. [105] a different approach was taken to confirm this hypothesis: The $|m| = 1$ class of azimuthal modes was studied in a set of punctured Py disks with thickness $L = 15$ nm and radii $R \in \{1, 6\}$ μm. The holes were located at the center of the disks and had a diameter $D = 100$ nm, which guarantees the absence of the VC structure at zero field. Power spectra of these disks show a single resonant peak corresponding to the $|m| = 1$ class, that is, the azimuthal modes $(\pm 1, 1)$ are degenerated. The absence of doublet structure is attributed to the lack of interaction with the gyrotropic motion of the VC, therefore confirming that the softest excitations of the VS –in the form of gyrotropic motion of the VC soliton– influence its magnon dynamics. Hybridization of the degenerate $(\pm 1, 1)$ modes was also observed by the authors using time-resolved Kerr microscopy. It is also reported that the values of the ($|m| = 1$)-class resonant frequency for punctured disks were higher than the corresponding values for regular disks. Furthermore, a scaling of the azimuthal excitation frequencies with $\beta^{1/2}$ is observed (as in [99]).

Theoretical description

C. Zaspel and B. Ivanov developed in Refs. [101, 102] a model describing the spin-wave excitation spectrum of azimuthal modes in ferromagnetic submicron circular disks. It is based on a linearized version of the Landau-Lifshitz equation and on vortex-magnon scattering. Considering the fixed-length spherical representation (3.24) of the magnetization field, angles Θ and Φ for small oscillations due to the presence of spin waves become

$$\Theta(\vec{r}) = \Theta_0(r) + \vartheta(r,\phi,t), \quad \Phi(\vec{r}) = \Phi_0(r,\phi) + \psi(r,\phi,t), \tag{3.33}$$

where (r,ϕ,z) represent the spherical coordinates and ϑ, ψ are small deviations from the ground state (3.25). Rigidity of the spin wave mode along the axis of the disk (no dependence on the variable z) is assumed. The choice of independent variables for this problem is the set $\{\vartheta, \mu\}$, with $\mu(r,\phi,t) = -\psi \sin\Theta_0$. It is convenient to split the radial and azimuthal dependences of this set, obtaining the ansatz

$$\vartheta(r,\phi,t) = f(r)\cos(m\phi + \omega t), \quad \mu(r,\phi,t) = g(r)\sin(m\phi + \omega t), \tag{3.34}$$

where ω is the frequency of the magnon mode and $\{f, g\}$ is the new set of (radial) independent functions. The demagnetizing field is given by $\vec{H}_\mathrm{d} = -\nabla U_\mathrm{d}$, where $U_\mathrm{d} = U_\mathrm{d,v} + U_\mathrm{d,s}$ is the magnetostatic potential generated by the volume and surface charge densities $-\nabla \cdot \vec{M}$ ($U_\mathrm{d,v}$) and $\vec{M} \cdot \hat{n}$ ($U_\mathrm{d,s}$), respectively. Introducing these dependences into Eq. (3.1) for the total energy and linearizing the resulting Landau-Lifshitz equation with respect to f and g one obtains the set of linearized equations

$$\begin{aligned} \Omega f &= \hat{H}_1 g + \hat{V} f + \hat{U}_1, \\ \Omega g &= \hat{H}_2 f + \hat{V} g + \hat{U}_2, \end{aligned} \tag{3.35}$$

$$\hat{H}_1 = \frac{\Delta_0^2}{4\pi}\left(-\nabla^2 + \frac{\nabla^2(\sin^2\Theta_0)}{\sin^2\Theta_0}\right), \hat{H}_2 = -\frac{\Delta_0^2}{4\pi}\nabla^2 + \left(\frac{\Delta_0^2}{4\pi r^2} - 1\right)\cos(2\Theta_0),$$

$$\hat{V} = \frac{m\Delta_0^2}{2\pi r^2}\cos\Theta_0,$$

where $\Omega = \omega/4\pi\gamma M_S$ is the normalized magnon frequency and $\hat{U}_i$ $(i = 1, 2)$, are integro-differential operators accounting for the volume magnetostatic effects.

Furthermore, an effective boundary condition appears from the linearization procedure, $G(k)=0$, which in the asymptotic regime $\beta \ll 1$ turns out to be

$$G(k)=\frac{\mathrm{d}g(R,k)}{\mathrm{d}r}+2I_m\frac{L}{\Delta_0^2}\ln(4/\beta)g(R,k), \tag{3.36}$$

with $I_0=2$ and $I_m=1$, $m\neq 0$. The magnetostatic operators $\hat{U}_i$ act as a perturbation on the system of equations (3.35) because $U_{\mathrm{d,v}}/4\pi M_S \simeq \beta \ll 1$. Therefore, a perturbative expansion of the functions f,g around the solutions corresponding to the $\hat{U}_i\equiv 0$ case is acceptable. In the case of the $|m|=1$ class of azimuthal excitations, these solutions are given by

$$g_0(r,k)=\sin\Theta_0\left[\frac{4\sqrt{\pi}}{\Delta_0}J_1(kr)-\frac{m\pi k}{2}Y_1(kr)\right], \quad f_0(r,k)=-\Omega_0 g_0(r,k), \tag{3.37}$$

where $Y_1(x)$ is the Neumann function of first order and $\Omega_0=k\Delta_0/2\sqrt{\pi}$. Introducing this perturbative expansion into Eqs. (3.35), one obtains the following equation for the normalized frequency:

$$(\Omega-\Omega_0)\int_0^R \mathrm{d}r\, r f_0 g_0=\frac{1}{8\pi}\int_0^R \mathrm{d}r\int_0^R \mathrm{d}r'\rho(r)S(r,r')\rho(r'), \tag{3.38}$$

$$\rho(r)=f_0\cos\Theta_0+\frac{\mathrm{d}(rg_0)}{\mathrm{d}r}, \quad S(r,r')=L\int_0^{2\pi}\frac{\cos\alpha\,\mathrm{d}\alpha}{\sqrt{r^2+r'^2-2rr'\cos\alpha+L^2/4}}. \tag{3.39}$$

Azimuthal modes belonging to the $|m|=1$ class must be compatible with the boundary condition $G(k)=0$ for their wave numbers, where G is given by Eq. (3.36). The gyrotropic mode is identified with the lowest zero of $G(k)$, which corresponds to the azimuthal number $m=-1$ and is given aproximately by $k_0\simeq \Delta_0/2\sqrt{\pi}R^2$. The other zeros of the boundary condition are closely distributed over **R**, forming doublets according to the two signs of $|m|$. Calculation of the eigenfrequencies associated with the excitation modes in each doublet leads to a square-root dependence on the aspect ratio (valid for small values of this parameter), $\Omega\sim\beta^{1/2}$, and to a doublet splitting that increases with larger values of β. The same formation of doublets is found at higher values of $|m|$. Even though this theory provides a prediction of the existence of doublets in the magnon spectrum of ferromagnetic micron-size circular disks and the expected dependences have been observed experimentally, it cannot be regarded as satisfactory in quantitive terms because the experimental splittings exceed the theoretical expectations [105].

The same authors also codeveloped a model describing the excitation spectrum of radially symmetric magnon modes in ferromagnetic submicron circular disks [106]: Small deviations from the static VS due to the presence of radially symmetric spin excitations are considered in the form of Eq. (3.33), with $\vartheta(r,\phi,t) \equiv \vartheta(r)$ and $\psi(r,\phi,t) \equiv \psi(t)$. Generalized momentum μ/γ conjugated with ψ within the Lagrangian formalism of the Landau-Lifshitz equation is given by the expression $\mu = LM_S \int_{D(0,R)} \mathrm{d}^2\vec{r} \cos\Theta$, so that the total Lagrangian becomes

$$\mathcal{L} = \frac{1}{\gamma}\mu\frac{\mathrm{d}\psi}{\mathrm{d}t} - E(\psi,\mu), \tag{3.40}$$

where $E(\psi,\mu)$ is the total energy of the system (exchange and magnetostatic contributions) expressed in the coordinate system (ψ,μ). The corresponding Hamilton's equation of motion yields the following expression for the eigenfrequencies of the excitation modes:

$$\Omega = 4\pi\gamma M_S \left[\frac{\beta}{\pi}\ln\left(\frac{\eta}{\beta}\right)\right]^{1/2}, \tag{3.41}$$

where $\eta \in [4,6]$ is a phenomenological parameter. This theoretical dependence is quite insensitive to the value of η and agrees well with the experimental values for the frequencies of this kind of excitations.

A (topological) gauge-potential approach was considered by K. Guslienko *et al.* to study the coupling of spin-wave excitations with non-uniform slowly moving magnetization distributions (for instance, the gyrotropic mode) [107]. Renormalization of the interaction Lagrangian between spin waves and the VS leads to a kinetic term of the form $\mathcal{L}_{\text{SW-VS}} = \frac{1}{2}M\dot{\vec{X}}^2$, where $M \simeq \frac{3}{2}\frac{L}{\gamma^2}$ is an effective mass of dynamical origin.

3.3 Temperature and pinning effects

Thermal and pinning effects enrich enormously the phenomenology of the vortex state. With respect to pinning, the presence in the disk of defects capable of trapping the VC into metastable pinning wells must affect the dynamics of the VS, especially the gyrotropic one (softest excitation mode). On the other hand, the effect of temperature on the properties of the VS is twofold. First, circular dots offer a rich landscape of ground states and transitions between them usually occur via thermal activation. Hence, transitions between two particular ground states (for instance SD→VS in the nucleation process) through intermediate metastable states (C state, S state, etc.) may be enhanced at high temperatures, which obviosuly would affect the static properties of the VS. Second, thermal activation dies out in the limit $T \to 0$ and therefore weaker pinning centers effectively trap the VC as the temperature decreases, that is, the landscape of pinning barriers becomes refined at low temperatures.

In Ref. [108] thermal dependence of hysteresis loops in single Py submicron-size dots with thickness $L = 50$ nm and radii $R \in [500, 900]$ nm was investigated by means of micro-Hall and bend-resistance magnetometry. These hysteresis loops presented the prototypical shape corresponding to circular disks with the VS (see Fig. 3.1), from which the experimental values for both nucleation and annihilation fields were extracted. From the set of smallest and biggest disks the authors observed the same thermal dependence for the magnetization reversal: H_{an} decreases monotonically with temperature, exhibiting two different slopes in the low/high T regimes. On the other hand, H_{n} is a nonmonotonic thermal function, increasing sharply on warming below a certain temperature, above which it slowly decreases. These behaviors are due to magnetization reversal ocurring via thermal activation (over an energy barrier) at low temperatures, whereas at high T these processes are dominated by the thermal dependence of M_S. This statement is supported by the fact that the experimental values can be fitted to the theoretical dependences $H_\star = H_{\star,0}(1 - \alpha_\star T^{3/2})$ and $H_\star = H_{\star,0}(1 + \beta_\star T)$, ($\star = \mathrm{n,an}$), at high and low temperatures, respectively. Small kinks in the magnetization at fields $H > H_{\mathrm{n}}$ are observed in the biggest disks, which are attributed to the development of a S state and a double-vortex prior to the single vortex nucleation. A rich landscape of modes of magnetization reversal unravels for disks of intermediate size, with complex thermal transitions among single-vortex, C state and double-vortex.

An exhaustive study of the annihilation process of magnetic vortices in Py disks at high temperatures, $T \in [290, 330]$ K, was conducted by J. Burgess *et al.* in Ref. [109]. DC-MOKE and AC-MOKE microscopies were used to measure hysteresis loops and magnetic susceptibilities of a square array of 15000 Py circular dots with $(L, R) = (32, 1000)$ nm and lattice spacing $d = 4$ μm, which ensures that magnetostatic interactions among the disks could be safely neglected. Extension of the RVM to third order in the VC displacement leads to the derivation of an expression for the magnetic susceptibility that fits well the experimental data within the vortex linear regime. The statistical distribution of the annihilation field is calculated from the difference between the experimental data and the extrapolated susceptibility at any field, which appears to be Gaussian distributed. The standard deviation turns out to decrease with increasing the temperature, a fact that supports the hypothesis of depinning-like processes triggering the decay. Thermal and sweep-rate dependences of the mean value of H_{an} can be described by means of the typical Néel-Brown model with account of the Bloch $T^{3/2}$ law for the saturation magnetization and a power-law scaling $(1 - H/H_0)^\alpha$ for the field-dependent annihilation energy barrier. The choice of $\alpha = 3/2$ for the power-law exponent was made by analogy with the case of domain-wall depinning, that is, pinning centers play an important role in the annihilation process.

G. Kakazei and coworkers conducted a study on the nucleation process of vortices in Py disks based on relaxation measurements [110]: A square array of Py circular dots with $(L, R) = (40, 250)$ nm and lattice period $d = 1$ μm was characterized magnetically in the range of temperatures $[200, 400]$ K. Interdot dipolar interactions could be neglected because $d > 2R$. The shape of the hysteresis loops was characteristic of the VS, with magnetization reversal occurring via displacement of the vortex structure outwards. Again, the monotonically decreasing behaviour of the annihilation field with T is reported. On the other hand, the nucleation field for these samples appears to be quite insensitive to the temperature in the range studied. States along the descending branch within the field range $[230, 320]$ Oe close to the nucleation field $H_\mathrm{n} = 250$ Oe were taken as initial states for the relaxation measurements. After a fast transient regime (~ 50 s) corresponding to the transition from the SD/onion state to a buckle state (C and S states), time evolution of the magnetization scales with $\ln(t/\tau_0)$, where t is the time and τ_0 is a characteristic time of the system. This long-time magnetization dynamics (~ 1 h) is related to the thermally assisted hopping of nucleation energy barriers, whose distribution is wide (logarithmic time dependence of the magnetization). The nucleation energy barrier is assumed to follow a field dependence of the form $\Delta E_\mathrm{n} = \beta(H/H_{\mathrm{n},0} - 1)^\alpha$, which can be fitted to the values derived from the experimental data of the magnetic viscosity. The corresponding value of the power-law exponent ranges between 3.6 and 4, which differs from the $\alpha = 3/2$ associated to depinning-like processes. The authors concluded that vortex nucleation occurs through deformation of the magnetization field of the C state.

Effects of pinning on the magnetic properties of a square array of Py ($\mathrm{Ni_{80}Fe_{20}}$) circular disks with $(L, R) = (100, 500)$ nm and lattice period $d = 1$ μm were studied in Ref. [111]. By means of SQUID magnetometry Shima *et al.* measured typical in-plane hysteresis loops for the VS [see Fig. 3.3] in a wide range of temperatures, $T \in [5, 250]$ K, and observed the existence of remnant magnetization. Due to the curling magnetization structure of the VS in a perfect cylindrical dot, in-plane magnetization at zero applied magnetic field should be almost zero. Therefore, VCs must be pinned at the minima of some pinning potential, away from the center of the disks. This fact is also upheld by the presence of a non-zero coercive field, indicating the existence of resistance to the vortex motion al low T. Both magnitudes decay exponentially with temperature due to thermal activation over the corresponding energy barriers. Initial susceptibility is found to be an increasing function of T. A pinning temperature $T_\mathrm{pin} \simeq 9.6$ K was introduced so that below T_pin the VC is pinned at a local minimum of the pinning potential, whereas the vortex escapes out of the metastable well via thermal activation for $T > T_\mathrm{pin}$. The authors suggested that the source of pinning centers could be the presence of defects in the dots, such as surface roughnesses and grain boundaries.

The question of how pinning affects the gyrotropic motion of the VC was answered by R. Compton and P. Crowell in Ref. [112]: Individual circular dots with thickness $L = 50$ nm and radii $R \in [0.3, 1.0]$ μm were patterned from two different Py ($\mathrm{Ni_{81}Fe_{19}}$) films, one with average grain diameter $d_A \simeq 35$ nm and average roughness $R_A \simeq 0.4$ nm (small-grain, SG), and the other with $d_A \simeq 85$ nm and $R_A \simeq 0.8$ nm (large-grain, LG). Orthogonal in-plane DC magnetic fields were used to move the VC across the disk plane and then the gyroscopic mode was excited by applying an in-plane magnetic field pulse with temporal width < 120 ps and variable amplitude between $2 - 13$ Oe. This excitation field was spatially uniform over the disk. Time evolution of the gyrotropic motion of the VC was recorded using time-resolved Kerr microscopy. The authors observed fluctuations in the values of the gyrofrequency as the VC moved over length scales ~ 10 nm (typical range of a pinning potential) for small enough amplitudes of the field pulse. These fluctuations are independent of the VC polarization. Characteristics of the defect at a pinning site determine a critical excitation amplitude of the field pulse above which the radius of the gyro-orbit exceeds the range of the pinning center, that is, the VC becomes depinned. In this regime the eigenfrequency of the gyrotropic motion is insensitive to the field amplitude and depends solely on the magnetostatic energy of the vortex structure [see Eq. (3.32)]. Spatial distribution of the pinning centers can be obtained by mapping fluctuations in the gyrofrequency according to this scheme, with the VC serving as a sensitive scanning probe, see Fig. 3.7. The authors conducted an extension of this work in Ref. [113]: They observed a positive correlation between the areal defect density and the areal grain density, which is indicative of grain boundaries being a prominent source of pinning. Furthermore, crystallographic grain structure is found to be weakly correlated with the spatial density of pinning centers and not to influence the average magnitude of frequency fluctuations. Independence of the average gyrofrequency shift on the disk radius suggests that it represents a mesure of the strength of the pinning potential at an individual defect. Pinning interaction between the VC and a single defect is estimated to be about 2.2 eV.

Quantitative detection of the Barkhausen effect, a prominent signature of the pinning of magnetic domain structures, was accomplished by Freeman's group recently [114]. By means of nanomechanical torque magnetometry the authors studied the stochastic jumps in the magnetization of a single Py disk with $(L, R) = (42, 500)$ nm, as the VC moves across the plane of the disk controlled by a set of two orthogonal static in-plane magnetic fields H_x and H_y. Measurement of the magnetization along 1D closed paths in the (H_x, H_y) plane led to hysteresis loops sensitive to pinning phenomena: During pinning the differential susceptibility is suppressed (but does not vanish) and transitions from one pinning center to another appear as steep sections. Therefore, pinning centers can be located in this way. Minor loops and bistability in the magnetization are masked at high temper-

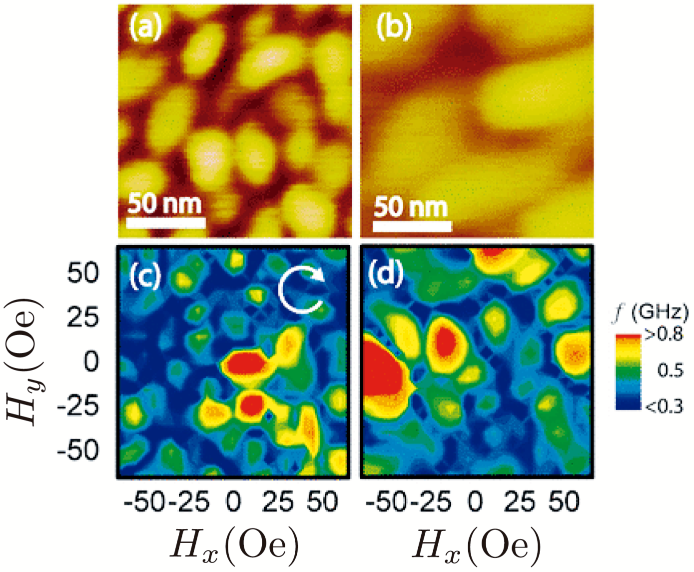

Figure 3.7: Atomic force microscopy images of the unpatterned (a) SG and (b) LG samples. Contour maps of ω_{G} for a disk with $R = 500$ nm made of (c) SG and (d) LG samples as a function of a static in-plane magnetic field. The pulse amplitude is about 7 Oe. The gyrofrequency is represented by a color scale and pinning centers appear as point-like regions of bright contrast in a background of low-frequency unpinned motion. The figure has been extracted from Ref. [112].

atures because of thermal activation of the VC over the intersite wells. Analysis of the Barkhausen noise present in the measurements of the magnetization along 2D (H_x, H_y)-paths in a neighborhood of a particular pinning site led J. Burgess and coauthors to build a 2D mapping of the corresponding pinning potential. Estimates of the height and width of the pinning barriers can be obtained from these maps, whose ranges are respectively $[0.3, 2.5]$ eV and $[7, 10]$ nm. These values are compatible with the ones derived in Refs. [112, 113].

3.4 Lagrangian mechanics of the vortex core

Rigidity of the VC has been an underlying assumption in the existing theoretical models of both static properties and spin excitations of sub-micron magnetic disks. Pinning of this soliton structure by linelike defects, which is conceptually similar to pinning of flux lines in type-II superconductors, contradicts this hypothesis: The VC should undergo a local deformation along the cylinder axis to adjust itself to the pinning (metastable) well at a particular defect. Therefore, the true nature of the VC line is that of an elastic string.

If deformations of the VC along the axis of the disk are ignored, the gyrotropic mode can be viewed as a uniform precession of the magnetic moment of the disk. While it is true that strong exchange interaction makes the vortex a well-defined independent entity, the question arises whether the gyrotropic mode allows spatial dispersion similar to spin waves of a finite wavelength in ferromagnets. The aim of this section is to study spin waves related specifically to the gyrotropic motion of the vortex. Such a wave is illustrated in Fig. 3.8. It must exist due to the finite elasticity of the vortex provided by the exchange interaction.

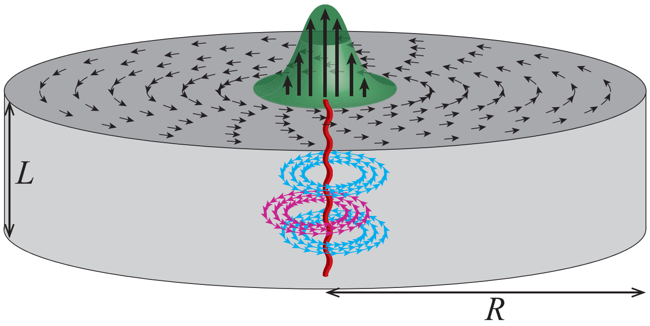

Figure 3.8: Gyroscopic spin wave in the vortex state of a mesoscopic magnetic disk.

Note that conceptually similar modes have been studied for vortices in liquid helium (Tkachenko modes) [115] and for Abrikosov vortices in superconductors

[116]. However, the dynamics of vortices in magnetic disks is very different from the dynamics of vortex lines in helium and in superconductors. From the mathematical point of view the above problem resembles the problem of the motion of a charged string in a potential well in the presence of the magnetic field. The latter problem is a generalization of the problem of Landau levels of an electron in a two-dimensional potential well in the magnetic field.

Most of the research on the gyrotropic motion of vortices in circularly polarized disks ignores the inertial mass of the VC. Such a mass has a dynamical origin stemming from the variation of the shape of the VC as it moves inside the disk. Meantime, experimental studies of vortex oscillations in micrometer Py rings [117] hinted towards a non-negligible vortex mass of order 10^{-24}kg. Despite the ring geometry in which it was measured, this value must provide a reasonable ballpark of the vortex mass in a disk because, as it will be shown in Sec. 3.8, the main contribution to the mass comes from distances far from the VC. (A similar situation exists for the electromagnetic structure of the Abrikosov vortex in a superconductor.) On a theoretical side the mass of the magnetic vortex has been previously computed in a two-dimensional Heisenberg model with anisotropic exchange interaction [87, 118, 119]. In disks made of soft ferromagnetic materials that have been experimented with, the exchange interaction is isotropic. It will be shown that in this case the finite mass density of the vortex originates from the geometrical confinement of the spin field and the magnetic dipole-dipole interactions.

The vortex line will be described by the vector field $\vec{X} = (x, y)$, where $x(t, z)$ and $y(t, z)$ are coordinates of the center of the VC in the XY plane. Landau-Lifshitz dynamics of the fixed-length magnetization vector (3.24) follows from the Lagrangian [93]

$$\mathcal{L}\Big[t; \Theta, \Phi, \dot{\Theta}, \dot{\Phi}, \partial_z\Theta, \partial_z\Phi\Big] = \int \mathrm{d}z\, \mathrm{d}^2\vec{r} \left[\frac{M_S}{\gamma}(D_t\Phi)\cos\Theta - \mathcal{E}(\Theta, \Phi, \partial_z\Theta, \partial_z\Phi)\right], \tag{3.42}$$

where $\mathcal{E}(\Theta, \Phi, \partial_z\Theta, \partial_z\Phi)$ is the energy density. The dependence of the Lagrangian on the partial derivatives ∂_z of the angular coordinates comes from the elastic nature of the vortex core. It is contained in the total energy, $\mathcal{E}$, that takes into account interaction between different layers of the vortex line, see below.

The spatial dependence of angular coordinates (Θ, Φ) for the VS is given by $\Theta = \Theta(t; \vec{r}, z) = \Theta[\vec{r} - \vec{X}(t, z), t]$ and $\Phi = \Phi(t; \vec{r}, z) = \Phi[\vec{r} - \vec{X}(t, z), t]$. Only long-wave solutions that do not deform the vortex core in any z-cross-section of the disk will be considered, which means that the angular coordinates depend on t and z via the coordinates of the vortex core $\vec{X}(t, z)$. The covariant derivative with respect to time, $D_t\Phi$, along the VC is given by

$$D_t\Phi = \nabla_{\dot{\vec{X}}(t,z)}\Phi = -\dot{\vec{X}}(t, z) \cdot \nabla_{\vec{r}}\Phi[\vec{r} - \vec{X}(t, z)], \tag{3.43}$$

where "dot" denotes partial derivative with respect to t.

Taking all these considerations into account, the above Lagrangian becomes

$$\mathcal{L}\left[t;\vec{X},\dot{\vec{X}},\partial_z\vec{X}\right]=\int \mathrm{d}z\tilde{\mathcal{L}}\left[t,z;\vec{X},\dot{\vec{X}},\partial_z\vec{X}\right] \tag{3.44}$$

with the Lagrangian density being

$$\tilde{\mathcal{L}}\left[t,z;\vec{X},\dot{\vec{X}},\partial_z\vec{X}\right]=\int \mathrm{d}^2\vec{r}\left[\frac{M_S}{\gamma}\left(-\dot{\vec{X}}(t,z)\cdot\nabla_{\vec{r}}\Phi\right)\cos\Theta-\mathcal{E}(\Theta,\Phi,\partial_z\Theta,\partial_z\Phi)\right]. \tag{3.45}$$

Thus the generalized momentum densities are given by

$$\begin{aligned}\vec{\Pi}_t\left[t,z;\vec{X},\dot{\vec{X}},\partial_z\vec{X}\right] &\equiv \frac{\delta\tilde{\mathcal{L}}}{\delta\left(\dot{\vec{X}}(t,z)\right)}=-\frac{M_S}{\gamma}\int \mathrm{d}^2\vec{r}\,(\nabla_{\vec{r}}\Phi)\cos\Theta, &(3.46)\\ \vec{\Pi}_z\left[t,z;\vec{X},\dot{\vec{X}},\partial_z\vec{X}\right] &\equiv \frac{\delta\tilde{\mathcal{L}}}{\delta\left(\partial_z\vec{X}(t,z)\right)}=-\frac{\delta\omega(\vec{X},\partial_z\vec{X})}{\delta(\partial_z\vec{X}(t,z))}, &(3.47)\end{aligned}$$

where $\omega(\vec{X},\partial_z\vec{X})=\int \mathrm{d}^2\vec{r}\ \mathcal{E}(\Theta,\Phi,\partial_z\Theta,\partial_z\Phi)$ is the linear energy density. The dynamics of the VC is governed by the Euler-Lagrange equation,

$$D_t\vec{\Pi}_t+\partial_z\vec{\Pi}_z-\frac{\delta\tilde{\mathcal{L}}}{\delta\vec{X}(t,z)}=0. \tag{3.48}$$

Notice that

$$\begin{aligned}D_t\Lambda(t,z;\vec{r},\vec{v}) &= \dot{\xi}(t,z)(\Lambda)=\frac{\partial}{\partial t}\Lambda(\vec{r}-\vec{X}(t,z),\dot{\vec{X}}(t,z)) \qquad (3.49)\\ &= -\dot{\vec{X}}(t,z)\cdot\nabla_{\vec{r}}\Lambda(\vec{r}-\vec{X}(t,z),\dot{\vec{X}}(t,z))+\ddot{\vec{X}}(t,z)\cdot\nabla_{\vec{v}}\Lambda(\vec{r}-\vec{X}(t,z),\dot{\vec{X}}(t,z))\end{aligned}$$

means covariant derivative along the curve that is tangent to the VC, $\xi(t,z)$. All terms involving $\dot{\vec{X}}(t,z)$ and $\ddot{\vec{X}}(t,z)$ in the Euler-Lagrange equation come from $D_t\vec{\Pi}_t$, which is given by

$$\begin{aligned}D_t\vec{\Pi}_t &= -\frac{M_S}{\gamma}\int \mathrm{d}^2\vec{r}\,D_t\left(\cos\Theta\nabla_{\vec{r}}\Phi\right)\\ &= -\frac{M_S}{\gamma}\int \mathrm{d}^2\vec{r}\left(\nabla_{\vec{r}}\left[-\dot{X}_j\partial_j\Phi+\ddot{X}_j\tilde{\partial}_j\Phi\right]\cos\Theta+\nabla_{\vec{r}}\Phi\left[-\dot{X}_j\partial_j\cos\Theta+\ddot{X}_j\tilde{\partial}_j\cos\Theta\right]\right)\\ &= \hat{e}_iM_{ij}\ddot{X}_j-\hat{e}_iK_{ij}\dot{X}_j, \qquad (3.50)\end{aligned}$$

where

$$
\begin{aligned}
M_{ij} &= -\frac{M_S}{\gamma}\int \mathrm{d}^2\vec{r}\,\Big[(\partial_i\tilde{\partial}_j\Phi)\cos\Theta + (\partial_i\Phi)\tilde{\partial}_j\cos\Theta\Big],\\
K_{ij} &= -\frac{M_S}{\gamma}\int \mathrm{d}^2\vec{r}\,\Big[(\partial_i\partial_j\Phi)\cos\Theta + (\partial_i\Phi)\partial_j\cos\Theta\Big],
\end{aligned}
\tag{3.51}
$$

and $\partial_j \equiv \nabla_{r_j}$, $\tilde{\partial}_j = \nabla_{v_j}$.

Transformation of the expression $\hat{e}_i K_{ij}\dot{X}_j$ into the form $\vec{\rho}_{\mathrm{G}} \times \dot{\vec{X}}$ results in the identity $\epsilon_{ijk}\rho_{\mathrm{G},j} = K_{ik}$. From this we obtain $\rho_{\mathrm{G},j} = -\frac{1}{2}\epsilon_{ikj}K_{ik}$, which translates into the vector form as

$$
\begin{aligned}
\vec{\rho}_{\mathrm{G}} &= \frac{M_S}{2\gamma}\int \mathrm{d}^2\vec{r}\epsilon_{ikj}\Big[(\partial_i\partial_k\Phi)\cos\Theta + (\partial_i\Phi)(\partial_k\cos\Theta)\Big]\hat{e}_j\\
&= \frac{M_S}{2\gamma}\int \mathrm{d}^2\vec{r}\,\Big[\big(\nabla_{\vec{r}}\times\nabla_{\vec{r}}\Phi\big)\cos\Theta + \nabla_{\vec{r}}\Phi\times\nabla_{\vec{r}}\cos\Theta\Big].
\end{aligned}
\tag{3.52}
$$

To compute the mass tensor and the gyrovector we have to find the solutions (Θ, Φ) of the Landau-Lifshitz equation in the low-dynamics regime that is characterized by the condition $|\dot{\vec{X}}| \ll 1$. In this regime solutions can be expanded as a perturbative series on the differential speed, $|\dot{\vec{X}}|$, of the VC,

$$
\begin{aligned}
\Theta(t,z;\vec{r}) &= \Theta^{(0)}(z;\vec{r}) + \Theta^{(1)}(t,z;\vec{r}) + \ldots,\\
\Phi(t,z;\vec{r}) &= \Phi^{(0)}(z;\vec{r}) + \Phi^{(1)}(t,z;\vec{r}) + \ldots
\end{aligned}
\tag{3.53}
$$

Notice that the zero-th order is time-independent, otherwise the gyrovector would depend on time.

The approach that neglects deformation of the vortex core in any z-cross-section of the disk is correct only for weak deviations of the centerline of the VC from the straight line along the Z-axis. Study of the Landau-Lifshitz equation for the set of variables (Θ, Φ) will lead to the conditions defining such weak bending regime. It can be obtained by applying the variational principle to the Lagrangian density

$$
\tilde{\mathcal{L}}\big[t,z;\Theta,\Phi,\dot{\Theta},\dot{\Phi},\partial_z\Theta,\partial_z\Phi\big] = \int \mathrm{d}^2\vec{r}\,\left[\frac{M_S}{\gamma}(D_t\Phi)\cos\Theta - \mathcal{E}(\Theta,\Phi,\nabla_{\vec{r}}\Theta,\nabla_{\vec{r}}\Phi,\partial_z\Theta,\partial_z\Phi)\right].
\tag{3.54}
$$

Notice that

$$
\mathcal{E}(\Theta,\Phi,\nabla_{\vec{r}}\Theta,\nabla_{\vec{r}}\Phi,\partial_z\Theta,\partial_z\Phi) = \mathcal{E}_{XY}(\Theta,\Phi,\nabla_{\vec{r}}\Theta,\nabla_{\vec{r}}\Phi) + \mathcal{E}_{\mathrm{el}}(\Theta,\Phi,\partial_z\Theta,\partial_z\Phi)
\tag{3.55}
$$

with $\mathcal{E}_{XY}(\Theta, \Phi, \nabla_{\vec{r}}\Theta, \nabla_{\vec{r}}\Phi)$ being the sum of the exchange, anisotropy and dipolar energy responsible for the formation of the vortex, and

$$\mathcal{E}_{\rm el}(\Theta, \Phi, \partial_z\Theta, \partial_z\Phi) = A_{\rm eff}\left[(\partial_z\Theta)^2 + \sin^2\Theta(\partial_z\Phi)^2\right] \tag{3.56}$$

being the elastic energy in which $A_{\rm eff}$ is a constant. It describes contribution of the exchange and dipolar forces to the elasticity of the vortex line, with the exchange playing a dominant role. Consequently, with good accuracy, $A_{\rm eff}$ can be identified with the exchange constant A.

The set of dynamical equations for (Θ, Φ) is

$$\begin{aligned} D_t\left(\frac{\delta\tilde{\mathcal{L}}}{\delta(D_t\Phi)}\right) + \partial_z\left(\frac{\delta\tilde{\mathcal{L}}}{\delta(\partial_z\Phi)}\right) - \frac{\delta\tilde{\mathcal{L}}}{\delta\Phi} &= 0, \\ \frac{M_S}{\gamma}\frac{\partial\cos\Theta}{\partial t} + \frac{\delta\mathcal{E}_{XY}}{\delta\Phi} - 2A_{\rm eff}\left[\sin 2\Theta\partial_z\Theta\partial_z\Phi + \sin^2\Theta\partial_z^2\Phi\right] &= 0, \end{aligned} \tag{3.57}$$

and

$$\begin{aligned} D_t\left(\frac{\delta\tilde{\mathcal{L}}}{\delta(D_t\Theta)}\right) + \partial_z\left(\frac{\delta\tilde{\mathcal{L}}}{\delta(\partial_z\Theta)}\right) - \frac{\delta\tilde{\mathcal{L}}}{\delta\Theta} &= 0, \\ \frac{M_S}{\gamma}\sin\Theta\frac{\partial\Phi}{\partial t} + \frac{\delta\mathcal{E}_{XY}}{\delta\Theta} - 2A_{\rm eff}\left[\partial_z^2\Theta - \frac{\sin 2\Theta}{2}(\partial_z\Phi)^2\right] &= 0. \end{aligned} \tag{3.58}$$

Performing a Fourier transform

$$\begin{aligned} \Phi(t, z; \vec{r}) &= \frac{1}{\sqrt{2\pi}}\int {\rm d}q\ \bar{\Phi}(t, q; \vec{r})e^{iqz}, \\ \Theta(t, z; \vec{r}) &= \frac{1}{\sqrt{2\pi}}\int {\rm d}q\ \bar{\Theta}(t, q; \vec{r})e^{iqz}, \end{aligned} \tag{3.59}$$

the following set of equations for the pair $(\bar{\Theta}, \bar{\Phi})$ is obtained:

$$\frac{M_S}{\gamma}\frac{\partial\,\overline{\cos\Theta}}{\partial t} + \frac{\overline{\delta\mathcal{E}_{XY}}}{\delta\Phi} + \frac{A_{\rm eff}q^2}{\pi}\left[\overline{\sin 2\Theta}\star\bar{\Theta}\star\bar{\Phi} + \overline{\sin\Theta}\star\overline{\sin\Theta}\star\bar{\Phi}\right] = 0, \tag{3.60}$$

$$\frac{1}{\sqrt{2\pi}}\frac{M_S}{\gamma}\overline{\sin\Theta}\star\frac{\partial\bar{\Phi}}{\partial t} + \frac{\overline{\delta\mathcal{E}_{XY}}}{\delta\Theta} + 2A_{\rm eff}q^2\left[\bar{\Theta} - \frac{\overline{\sin 2\Theta}}{4\pi}\star\bar{\Phi}\star\bar{\Phi}\right] = 0, \tag{3.61}$$

where $\star$ means Fourier convolution.

For a small bending of the vortex core, the boundary conditions on the angle Θ are the same as in the rigid VC case, i.e.: $\Theta \simeq 0$ or π in the limit $\tilde{r} \ll \Delta_0$, and $\Theta \simeq \pi/2$ in the limit $\tilde{r} \gg \Delta_0$, where $\tilde{r} = ||\vec{r} - \vec{X}(t, z)||_2$ is the radial distance from the VC center at any height z. Two limits can be considered here:

- Limit $\tilde{r} \ll \Delta_0$. In this case, $\sin\Theta \simeq 0$ and thus $\sin 2\Theta \partial_z \Theta \partial_z \Phi + \sin^2\Theta \partial_z^2 \Phi \simeq 0$. Hence, in the Fourier space Eq. (3.60) becomes

$$\frac{M_S}{\gamma}\frac{\partial\,\overline{\cos\Theta}}{\partial t} + \frac{\overline{\delta\mathcal{E}_{XY}}}{\delta\Phi} = 0. \tag{3.62}$$

- Limit $\tilde{r} \gg \Delta_0$. In this case, $\sin\Theta \simeq 1$ and thus $\sin 2\Theta \partial_z \Theta \partial_z \Phi + \sin^2\Theta \partial_z^2 \Phi \simeq \partial_z^2 \Phi$. Therefore, Eq. (3.60) turns into

$$\frac{M_S}{\gamma}\frac{\partial\,\overline{\cos\Theta}}{\partial t} + 2A_{\text{eff}}q^2\bar{\Phi} + \frac{\overline{\delta\mathcal{E}_{XY}}}{\delta\Phi} = 0. \tag{3.63}$$

Notice that in both limits $\sin 2\Theta \simeq 0$ and so $\partial_z^2\Theta - \frac{\sin 2\Theta}{2}(\partial_z\Phi)^2 \simeq \partial_z^2\Theta$. Consequently, in the Fourier space Eq. (3.61) becomes

$$\frac{1}{\sqrt{2\pi}}\frac{M_S}{\gamma}\overline{\sin\Theta} \star \frac{\partial\bar{\Phi}}{\partial t} + 2A_{\text{eff}}q^2\bar{\Theta} + \frac{\overline{\delta\mathcal{E}_{XY}}}{\delta\Theta} = 0. \tag{3.64}$$

Finally, in the limit of weak bending ($A_{\text{eff}}q^2 \ll 1$) the terms of the form $2A_{\text{eff}}q^2\bar{\xi}$ can be neglected in the above equations. In doing so, one recovers the standard Landau-Lifshitz equations for (Θ, Φ) at any z layer, with the VC center depending on the value of z. Introducing now the perturbative series (3.53) into the Landau-Lifshitz equation and splitting it into $O(|\dot{\vec{X}}|^n)$ terms, the equations of motion for the $\Phi^{(n)}$ and $\Theta^{(n)}$ terms are derived. In the case of the zero-th and first order terms, one recovers the static solution (3.24) and the first perturbative solution for the rigid vortex [see Sec. 3.8].

3.5 Elastic Thiele equation

The generalized Thiele equation describing spin waves in the VC of finite mass density is derived in this Section. First, one should compute the gyrovector and the mass density tensor. From Eq. (3.25) the following identities are straightforwardly deduced,

$$\begin{aligned} \nabla_{\vec{r}} \times \nabla_{\vec{r}}\Phi_0 &= 2\pi\mathcal{Q}\delta^{(2)}\left(\vec{r} - \vec{X}(t,z)\right)\hat{e}_z, \\ \nabla_{\vec{r}}^2\Phi_0 &= 0. \end{aligned} \tag{3.65}$$

The first term of Eq. (3.52) equals $(\pi\mathcal{Q}pM_S/\gamma)\hat{e}_z$ with account of these identities. The second term is evaluated at the zero-th order of the perturbative expansion of the angular coordinates in the low-dynamics regime, Eq. (3.25), taking into account that in the weak bending regime the deformation of the VC is small and one can consider $\tilde{r} \simeq r$ because $||\vec{X}(t,z)||_2 \ll 1$. In doing so, one obtains the expression $(\pi \mathcal{Q} p M_S/\gamma)\hat{e}_z$ again [95]. Thus the gyrovector becomes $\vec{\rho}_{\mathrm{G}} = \rho_{\mathrm{G}} p \mathcal{Q} \hat{e}_z$ with

$$\rho_{\mathrm{G}} = 2\pi M_S/\gamma. \tag{3.66}$$

Notice that $\vec{\rho}_{\mathrm{G}}$ is the gyrovector linear density as compared to the gyrovector in the Thiele equation for a rigid vortex [94].

Computation of the mass density tensor will be performed in Section 3.8. For circularly polarized disks it will be shown that this tensor reduces to a scalar, $M_{ij} = \rho_M \delta_{ij}$, with the VC mass density given by $\rho_M = \dfrac{1}{4\gamma^2}\ln(R/\Delta_0)$, where R is the radius of the disk. Only $\omega(\vec{X}, \partial_z \vec{X})$ contributes to the partial derivative $\delta\tilde{\mathcal{L}}/\delta\vec{X}$ in the slow dynamics regime, because $\vec{\Pi}_t = \rho_M \dot{\vec{X}}$ and so the term $\dot{\vec{X}} \cdot \vec{\Pi}_t$ equals $\rho_M \dot{\vec{X}}^2$. Consequently, the generalized Thiele equation becomes

$$\rho_M \ddot{\vec{X}}(t,z) + \dot{\vec{X}}(t,z) \times \vec{\rho}_{\mathrm{G}} + \partial_z \vec{\Pi}_z + \nabla_{\vec{X}}\omega = 0. \tag{3.67}$$

The linear energy density $\omega(\vec{X}, \partial_z \vec{X})$ is the sum of the magnetostatic and exchange contributions in the z-cross-section, $\omega_{XY}(\vec{X})$, and an elastic contribution due to the deformation of the VC line, $\omega_{\mathrm{el}}(\partial_z \vec{X})$. Zeeman contribution will be considered later. The dependence on the vortex core coordinates of the $\omega_{XY}(\vec{X})$ term is quadratic for small displacements [see Eq. (3.31)]:

$$\omega_{XY}(\vec{X}) = \frac{1}{2}\rho_M \omega_M^2 \epsilon_0 \vec{X}^2, \tag{3.68}$$

where $\omega_M = \rho_{\mathrm{G}}/\rho_M$ is the characteristic frequency of the system and $\epsilon_0 = \omega_{\mathrm{G}}/\omega_M$ is a dimensionless parameter. Recall that the conventional gyrofrequency ω_{G} is defined by Eq. (3.32). From the continuous spin-field model we know that

$$\omega_{\mathrm{el}}(\partial_z \vec{X}) = A_{\mathrm{eff}} \int \mathrm{d}^2\vec{r} \left[(\partial_z \Theta)^2 + \sin^2\Theta (\partial_z \Phi)^2\right]. \tag{3.69}$$

Noticing that $\partial_z \Theta = -\nabla_{\vec{r}}\Theta \cdot \partial_z \vec{X}$ and $\partial_z \Phi = -\nabla_{\vec{r}}\Phi \cdot \partial_z \vec{X}$, and taking into account the vector identity $(\vec{A}\times\vec{B})\cdot(\vec{C}\times\vec{D}) = (\vec{A}\cdot\vec{C})(\vec{B}\cdot\vec{D}) - (\vec{A}\cdot\vec{D})(\vec{B}\cdot\vec{C})$, with either $\vec{A} = \vec{D} = \nabla_{\vec{r}}\Theta$, $\vec{B} = \vec{C} = -\partial_z \vec{X}$ or $\vec{A} = \vec{D} = \nabla_{\vec{r}}\Phi$, $\vec{B} = \vec{C} = -\partial_z \vec{X}$, the following relations can be derived

$$\left(\nabla_{\vec{r}}\Theta \cdot \partial_z \vec{X}\right)^2 = (\nabla_{\vec{r}}\Theta)^2 \left(\partial_z \vec{X}\right)^2 - \left(\nabla_{\vec{r}}\Theta \times \partial_z \vec{X}\right)^2, \tag{3.70}$$

$$\left(\nabla_{\vec{r}}\Phi \cdot \partial_z \vec{X}\right)^2 = (\nabla_{\vec{r}}\Phi)^2 \left(\partial_z \vec{X}\right)^2 - \left(\nabla_{\vec{r}}\Phi \times \partial_z \vec{X}\right)^2. \tag{3.71}$$

The main contribution to the integral comes from the zero-th order in the perturbative expansion (3.53). Notice that $\Theta_0(\vec{r}) = \Theta_0(\tilde{r})$ and that $\nabla_{\vec{r}}\Phi_0 = \frac{Q}{\tilde{r}}\hat{e}_\phi$. As discussed before, in the weak bending regime one can use the approximation $\tilde{r} \simeq r$, so that $\nabla_{\vec{r}}\Phi_0 \times \partial_z\vec{X} = -\frac{Q}{r}\partial_z X_r \hat{e}_z$ and $\nabla_{\vec{r}}\Theta_0 \times \partial_z\vec{X} = \frac{\mathrm{d}\Theta_0}{\mathrm{d}r}\partial_z X_\phi \hat{e}_z$, where $X_r = \hat{e}_r \cdot \vec{X} = x\cos\theta + y\sin\theta$ and $X_\phi = \hat{e}_\phi \cdot \vec{X} = -x\sin\theta + y\cos\theta$. The elastic energy density finally becomes

$$\begin{aligned}\omega_{\mathrm{el}}(\partial_z\vec{X}) =& A_{\mathrm{eff}}\int \mathrm{d}^2\vec{r}\left[(\nabla_{\vec{r}}\Theta_0)^2 + \frac{\sin^2\Theta_0}{r^2}\right]\left(\frac{\partial\vec{X}}{\partial z}\right)^2 \\ &- A_{\mathrm{eff}}\int \mathrm{d}^2\vec{r}\left[\left(\frac{d\Theta_0}{dr}\right)^2\left(\frac{\partial X_\phi}{\partial z}\right)^2 + \frac{\sin^2\Theta_0}{r^2}\left(\frac{\partial X_r}{\partial z}\right)^2\right] \\ =& \pi A_{\mathrm{eff}}\int r\,\mathrm{d}r\left[\left(\frac{d\Theta_0}{dr}\right)^2 + \frac{\sin^2\Theta_0}{r^2}\right]\left(\frac{\partial\vec{X}}{\partial z}\right)^2,\end{aligned} \tag{3.72}$$

where the angular dependence of $(\partial_z X_r)^2$ and $(\partial_z X_\phi)^2$ has been integrated over θ. This energy density can be recast as $\omega_{\mathrm{el}}(\partial_z\vec{X}) = \dfrac{1}{2}\lambda\left(\dfrac{\partial\vec{X}}{\partial z}\right)^2$, where λ is the elastic constant given by

$$\lambda = 2\pi A_{\mathrm{eff}}\int r\,\mathrm{d}r\left[\left(\frac{d\Theta_0}{dr}\right)^2 + \frac{\sin^2\Theta_0}{r^2}\right]. \tag{3.73}$$

Making use of the variable $m_0(r) = \cos\Theta_0(r)$, the above equation can be rewritten as

$$\lambda = 2\pi A_{\mathrm{eff}}\int r\,\mathrm{d}r\left[\frac{1}{1-m_0^2}\left(\frac{dm_0}{dr}\right)^2 + \frac{1-m_0^2}{r^2}\right] \tag{3.74}$$

and using the spatial dependence (3.24) one gets

$$\frac{1}{1-m_0^2}\left(\frac{dm_0}{dr}\right)^2 + \frac{1-m_0^2}{r^2} = \begin{cases} \frac{\Delta_0^2}{2C_1r^2}\left(\frac{2pC_1}{\Delta_0^2}r\right)^2 + \frac{2C_1r^2}{\Delta_0^2}\frac{1}{r^2} = \frac{4C_1}{\Delta_0^2} & r \ll \Delta_0 \\ \frac{1}{\Delta_0^2}m_0^2 + \frac{1}{r^2} = \frac{C_2^2}{\Delta_0 r}\exp\left(-2r/\Delta_0\right) + \frac{1}{r^2} & r \gg \Delta_0 \end{cases} \tag{3.75}$$

Computing the integral (3.73) by splitting into two regions, $[0,\Delta_0]$ and $[\Delta_0, R]$, one obtains the expression

$$\lambda = 2\pi A_{\mathrm{eff}}\left[\frac{50}{49} + \ln(R/\Delta_0)\right]. \tag{3.76}$$

In the limit $R \gg \Delta_0$ the logarithmic term dominates and therefore λ becomes

$$\lambda = 2\pi A_{\mathrm{eff}}\ln(R/\Delta_0). \tag{3.77}$$

Finally, for the total energy density one obtains

$$\omega(\vec{X}, \partial_z \vec{X}) = \frac{1}{2}\rho_M \omega_M^2 \epsilon_0 \vec{X}^2 + \frac{1}{2}\lambda \left(\frac{\partial \vec{X}}{\partial z}\right)^2 \tag{3.78}$$

and thus the generalized Thiele equation for an elastic VC line becomes

$$\rho_M \ddot{\vec{X}}(t,z) - \lambda \partial_z^2 \vec{X}(t,z) + \dot{\vec{X}}(t,z) \times \vec{\rho}_{\mathrm{G}} + \rho_M \omega_M^2 \epsilon_0 \vec{X}(t,z) = 0. \tag{3.79}$$

3.6 Spin waves in the vortex core

Introducing the complex variable $\chi = x - iy$ we can recast Eq. (3.79) as the following complex partial differential equation:

$$\rho_M \ddot{\chi} - \lambda \partial_z^2 \chi + i\rho_{\mathrm{G}} \dot{\chi} + \rho_M \omega_M^2 \epsilon_0 \chi = 0. \tag{3.80}$$

Let $\chi_0(z)$ be the equilibrium complex center of the straight vortex core line. In the presence of the wave it gets perturbed and becomes $\chi(t,z) = \chi_0(z) + \chi_w(t,z)$, with $||\chi_w||_z \ll ||\chi_0||_z$. Switching to the Fourier transform,

$$\chi_w(t,z) = \frac{1}{2\pi} \int \mathrm{d}\omega \, \mathrm{d}q \chi_w(\omega, q) e^{i(\omega t - qz)}, \tag{3.81}$$

the following equation for $\chi_w(\omega, q)$ is derived:

$$\left[-\rho_M \omega^2 + \lambda q^2 - \rho_{\mathrm{G}} \omega + \rho_M \omega_M^2 \epsilon_0\right] \chi_w(\omega, q) = 0. \tag{3.82}$$

For non-zero amplitude of the wave the expression in the square parenthesis must vanish. This determines the spectrum of the waves:

$$\rho_M \omega^2 - \lambda q^2 + \rho_{\mathrm{G}} \omega - \rho_M \omega_M^2 \epsilon_0 = 0. \tag{3.83}$$

At $\rho_M \neq 0$ one can normalize Eq. (3.83) to get

$$\omega^2 + \omega_M \omega - \omega_M^2 \left(\epsilon_0 + \frac{\lambda}{\rho_M \omega_M^2} q^2\right) = 0. \tag{3.84}$$

Solving this equation one obtains the spectrum of VC excitations:

$$\omega_\pm(q) = \frac{\omega_M}{2} \left[\sqrt{(1 + 4\epsilon_0) + \frac{4\lambda q^2}{\rho_M \omega_M^2}} \pm 1\right]. \tag{3.85}$$

Condition $4\lambda q^2/\rho_M\omega_M^2 \ll 1$ is satisfied in the weak bending regime, so that the above square root can be expanded and therefore one obtains the following expression for the frequencies

$$\omega_\pm(q) = \frac{\omega_M}{2}\left(\sqrt{1+4\epsilon_0} \pm 1\right) + \frac{1}{\sqrt{1+4\epsilon_0}}\frac{\lambda}{\rho_{\mathrm{G}}}q^2, \tag{3.86}$$

where the relation $\rho_M\omega_M = \rho_{\mathrm{G}}$ has been used.

As it will be shown in Section 3.8 the parameter $\epsilon_0 = \omega_{\mathrm{G}}/\omega_M$ is normally small due to the smallness of $\beta = L/R$. Consequently,

$$\omega_-(q) \approx \omega_{\mathrm{G}} + \frac{\lambda}{\rho_{\mathrm{G}}}q^2, \tag{3.87}$$

$$\omega_+(q) \approx \omega_M + \frac{\lambda}{\rho_{\mathrm{G}}}q^2. \tag{3.88}$$

With the help of Eqs. (3.66) and (3.77) with $A_{\mathrm{eff}} \approx A = M_S^2\Delta_0^2$ the above equations can be written in a transparent form:

$$\omega_-(q) = \omega_{\mathrm{G}} + \gamma M_S(q\Delta_0)^2\ln(R/\Delta_0), \tag{3.89}$$

$$\omega_+(q) = \omega_M + \gamma M_S(q\Delta_0)^2\ln(R/\Delta_0). \tag{3.90}$$

Note that the weak bending regime corresponds to $q\Delta_0 \ll 1$.

3.7 Quantum mechanics of the excitations in the vortex core

In this section it will be shown that excitations of the VC can be also obtained in a rather non-trivial way from the quantum theory as well. This problem is interesting on its own as it turns out to be equivalent to the problem of quantum excitations of a charged string confined in a parabolic potential and subjected to the magnetic field.

It is straightforward to prove that the generalized Thiele equation (3.79) is the Euler-Lagrange equation associated with the following effective Lagrangian density that can be derived from Eq. (3.45):

$$\tilde{\mathcal{L}}(t, z; \vec{X}, \dot{\vec{X}}, \partial_z\vec{X}) = \frac{1}{2}\rho_M\dot{\vec{X}}^2 + \dot{\vec{X}}\cdot\vec{A}_{\rho_{\mathrm{G}}} - \omega(\vec{X}, \partial_z\vec{X}), \tag{3.91}$$

where $\vec{A}_{\rho_{\mathrm{G}}}$ is the gyrovector potential satisfying $\nabla_{\vec{X}} \times \vec{A}_{\rho_{\mathrm{G}}} = -\vec{\rho}_{\mathrm{G}}$. Thus the total Lagrangian becomes

$$\mathcal{L} = \int \mathrm{d}z\,\tilde{\mathcal{L}} = \int \mathrm{d}z\,\left[\frac{1}{2}\rho_M\dot{\vec{X}}^2 + \dot{\vec{X}}\cdot\vec{A}_{\rho_{\mathrm{G}}} - \omega(\vec{X}, \partial_z\vec{X})\right]. \tag{3.92}$$

Noticing that $\{\varphi_n(z)\}_{n\in\mathbf{N}} = \left\{\sqrt{\frac{2}{L}}\sin\left(q_n z\right)\right\}_{n\in\mathbf{N}}$, with $q_n = \frac{2\pi}{L}n$, is a Hilbert basis of the function subspace $\mathcal{W} = \{\varphi \in \mathcal{L}^2(0,L),\ \varphi(0) = \varphi(L) = 0\}$, one can expand $\vec{X}$ as

$$\vec{X}(t,z) = \vec{X}_0(t) + \sum_n \vec{X}_n(t)\varphi_n(z), \tag{3.93}$$

where $\vec{X}_0(t)$ is the center of the undisturbed vortex and $\vec{X}_n(t) =< \vec{X}(t,z), \varphi_n(z) >_{\mathcal{L}^2(0,L)}$. Introducing this expansion in Eq. (3.92) and taking into account the orthonormality of the Hilbert basis (and its spatial derivatives) the following identity is derived:

$$\begin{aligned} \mathcal{L}\left(t, \left\{\vec{X}_n\right\}_{n\in\mathbf{Z}^+}, \left\{\dot{\vec{X}}_n\right\}_{n\in\mathbf{Z}^+}\right) = \left[\frac{1}{2}M\dot{\vec{X}}_0^2 + \dot{\vec{X}}_0\cdot\vec{A}_0 - \frac{1}{2}M\omega_M^2\epsilon_0\vec{X}_0^2\right] + \\ \sum_{n>0}\left[\frac{1}{2}\rho_M\dot{\vec{X}}_n^2 + \dot{\vec{X}}_n\cdot\vec{A}_n - \frac{1}{2}\rho_M\omega_M^2\epsilon_0\vec{X}_n^2 - \frac{1}{2}\lambda q_n^2\vec{X}_n^2\right], \end{aligned} \tag{3.94}$$

where $\mathbf{Z}^+ = \{0\}\cup\mathbf{N}$, $M = \rho_M L$ is the total mass of the rigid vortex line and $\vec{A}_n$ is the gyrovector potential associated to the n-th coordinate $\vec{X}_n$, which satisfies $\nabla_{\vec{X}_0}\times\vec{A}_0 = -\vec{G}$ and $\nabla_{\vec{X}_n}\times\vec{A}_n = -\vec{\rho}_{\mathrm{G}}$, $n>0$, with $\vec{G} = \vec{\rho}_{\mathrm{G}}L$ being the gyrovector of the rigid vortex.

Applying the Laguerre transformation to the above Lagrangian one obtains the following expression for the Hamiltonian

$$\begin{aligned} \mathcal{H}\left(t, \left\{\vec{X}_n\right\}_{n\in\mathbf{Z}^+}, \left\{\vec{\Pi}_n\right\}_{n\in\mathbf{Z}^+}\right) = \left[\frac{1}{2M}(\vec{\Pi}_0 - \vec{A}_0)^2 + \frac{1}{2}M\omega_M^2\epsilon_0\vec{X}_0^2\right] + \\ \sum_{n>0}\left[\frac{1}{2\rho_M}(\vec{\Pi}_n - \vec{A}_n)^2 + \frac{1}{2}\rho_M\omega_M^2\left(\epsilon_0 + \frac{\lambda}{\rho_M\omega_M^2}q_n^2\right)\vec{X}_n^2\right], \end{aligned} \tag{3.95}$$

where $\vec{\Pi}_0 = M\dot{\vec{X}}_0 + \vec{A}_0$ and $\vec{\Pi}_n = \rho_M\dot{\vec{X}}_n + \vec{A}_n$, $n>0$ are the corresponding canonical momenta. Notice that Eq. (3.95) shows that $\mathcal{H}$ splits into the direct sum $\oplus_{m\in\mathbf{Z}^+}\mathcal{H}_m$, with $\mathcal{H}_m$ being the Hamiltonian defined over the phase space $(\vec{X}_m, \vec{\Pi}_m)$. It has a structure of the form

$$\mathcal{H}' = \frac{1}{2\eta}(\vec{\Pi} - \vec{A})^2 + \frac{1}{2}\eta\omega_M^2\xi\vec{X}^2, \tag{3.96}$$

where $(\vec{X}, \vec{\Pi})$ are the canonically conjugate variables, η, ξ are constants and $\vec{A}$ is the gyrovector satisfying $\nabla_{\vec{X}}\times\vec{A} = -\chi\hat{e}_z$, with χ being a constant. It is important to point out that $\chi/\eta = \omega_M$ in all cases.

From this point forward the case of the VC of a non-zero mass ($\eta \neq 0$) will be considered. It is convenient to choose a "symmetric gauge" given by

$$\vec{A} = \frac{1}{2}(-\chi \hat{e}_z) \times \vec{X} = \frac{\chi y}{2}\hat{e}_x - \frac{\chi x}{2}\hat{e}_y. \tag{3.97}$$

Firstly, one defines the kinetic momentum operators as $\vec{p} = \eta \dot{\vec{X}}$, so that $\vec{\Pi} = \vec{p} + \vec{A}$. Notice the following non-vanishing commutators

$$[p_j, p_k] = -i\hbar\chi\epsilon_{jk} \qquad j,k \in \{x,y\}, \tag{3.98}$$

where ϵ_{jk} is the antisymmetric tensor $\epsilon_{xy} = -\epsilon_{yx} = 1$. Secondly, one introduces the operators

$$\begin{aligned} a &= \sqrt{\frac{1}{2\hbar\chi}}\left(p_y + ip_x\right), \\ a^\dagger &= \sqrt{\frac{1}{2\hbar\chi}}\left(p_y - ip_x\right), \end{aligned} \tag{3.99}$$

which satisfy standard commutation relations for Bose operators, $\left[a, a^\dagger\right] = 1$. The number operator $N_a = a^\dagger a$ satisfies commutation relations $[N_a, a] = -a, \quad \left[N_a, a^\dagger\right] = a^\dagger$, and the following identity

$$\frac{1}{2\eta}\left(\vec{\Pi} - \vec{A}\right)^2 = \hbar\omega_M\left(N_a + \frac{1}{2}\right) \tag{3.100}$$

holds.

In analogy with the case of a charged particle in the electromagnetic field [120], one obtains that the gyrotropic translational group is generated by $\vec{T} = \vec{\Pi} + \vec{A}$,

$$T_x = p_x + \chi y, \qquad T_y = p_y - \chi x \tag{3.101}$$

which satisfies the following commutation relations,

$$[T_j, p_k] = 0, \qquad [T_j, T_k] = i\hbar\chi\epsilon_{jk}, \quad j,k \in \{x,y\}. \tag{3.102}$$

Now we introduce another set of Bose operators

$$\begin{aligned} b &= \sqrt{\frac{1}{2\hbar\chi}}\left(T_y - iT_x\right), \\ b^\dagger &= \sqrt{\frac{1}{2\hbar\chi}}\left(T_y + iT_x\right), \end{aligned} \tag{3.103}$$

which satisfy commutation relations

$$\left[b, b^{\dagger}\right] = 1, \quad [M_b, b] = -b, \quad \left[M_b, b^{\dagger}\right] = b^{\dagger},$$

where $M_b = b^{\dagger}b$ is the corresponding number operator. Notice that the commutation relations $[a, b] = \left[a, b^{\dagger}\right] = 0$ also hold.

Coordinates x and y can be expressed in terms of the above Bose operators:

$$\begin{aligned} x &= \frac{1}{\chi}\left(p_y - T_y\right), \\ y &= -\frac{1}{\chi}\left(p_x - T_x\right), \end{aligned} \tag{3.104}$$

so that

$$\frac{1}{2}\eta\omega_M^2\left(x^2 + y^2\right) = \hbar\omega_M\left(N_a + M_b - ab - a^{\dagger}b^{\dagger} + 1\right). \tag{3.105}$$

Consequently, the Hamiltonian (3.96) becomes

$$\mathcal{H}' = \hbar\omega_M\left[(1+\xi)N_a + \xi M_b - \xi(ab + a^{\dagger}b^{\dagger}) + \xi + \frac{1}{2}\right]. \tag{3.106}$$

It can be diagonalized with the help of Bogoliubov transformations

$$\bar{\alpha} = ua - vb^{\dagger}, \qquad \bar{\beta} = ub - va^{\dagger}, \tag{3.107}$$

with u, v being real numbers. These new operators satisfy Bose commutation relations if $u^2 - v^2 = 1$. Substituting the above equations into Eq. (3.106) one obtains

$$\begin{aligned} \mathcal{H}' =& \hbar\omega_M\Bigg[\bar{\alpha}^{\dagger}\bar{\alpha}\Big(u^2(1+\xi) + \xi v^2 - 2\xi uv\Big) + \bar{\beta}^{\dagger}\bar{\beta}\Big(v^2(1+\xi) + \xi u^2 - 2\xi uv\Big) + \\ & (\bar{\alpha}^{\dagger}\bar{\beta}^{\dagger} + \bar{\alpha}\bar{\beta})\Big(uv(1+2\xi) - \xi(u^2+v^2)\Big) + \Big(v^2(1+2\xi) - 2\xi uv + (\xi + 1/2)\Big)\Bigg]. \end{aligned} \tag{3.108}$$

To get a Hamiltonian in the oscillator form, the coefficient related to $(\bar{\alpha}^{\dagger}\bar{\beta}^{\dagger} + \bar{\alpha}\bar{\beta})$ should be zero, which requires

$$uv(1+2\xi) - \xi(u^2+v^2) = 0. \tag{3.109}$$

The solution is $u = \cosh(\theta)$, $v = \sinh(\theta)$, with

$$\tanh(2\theta) = \frac{2\xi}{1+2\xi}. \tag{3.110}$$

Finally, the coefficients of the terms $\bar{\alpha}^\dagger\bar{\alpha}$ and $\bar{\beta}^\dagger\bar{\beta}$ become

$$\begin{aligned} u^2(1+\xi)+\xi v^2-2\xi uv &= \frac{1}{2}\left[\frac{1+2\xi}{\cosh(2\theta)}+1\right]=\frac{1}{2}\left[\sqrt{1+4\xi}+1\right], \\ v^2(1+\xi)+\xi u^2-2\xi uv &= \frac{1}{2}\left[\frac{1+2\xi}{\cosh(2\theta)}-1\right]=\frac{1}{2}\left[\sqrt{1+4\xi}-1\right], \end{aligned} \tag{3.111}$$

and, consequently, the Hamiltonian in the second quantization formalism becomes

$$\mathcal{H}'=\hbar\omega_+\left(\bar{\alpha}^\dagger\bar{\alpha}+\frac{1}{2}\right)+\hbar\omega_-\left(\bar{\beta}^\dagger\bar{\beta}+\frac{1}{2}\right), \tag{3.112}$$

where

$$\omega_\pm=\frac{1}{2}\left[\sqrt{1+4\xi}\pm 1\right]\omega_M. \tag{3.113}$$

Noticing that for any $n\in\mathbf{Z}^+$ we have $\xi=\epsilon_0+\frac{\lambda}{\rho_M\omega_M^2}q_n^2$, the second quantization procedure yields the following form of Hamiltonian (3.95):

$$\mathcal{H}=\sum_{n\geq 0}\hbar\omega_n^+\left(\bar{\alpha}_n^\dagger\bar{\alpha}_n+\frac{1}{2}\right)+\sum_{n\geq 0}\hbar\omega_n^-\left(\bar{\beta}_n^\dagger\bar{\beta}_n+\frac{1}{2}\right), \tag{3.114}$$

where $\omega_n^\pm$ are the eigenfrequencies of the vortex state given by

$$\omega_n^\pm=\frac{1}{2}\left[\sqrt{(1+4\epsilon_0)+\frac{4\lambda}{\rho_M\omega_M^2}q_n^2}\pm 1\right]\omega_M, \tag{3.115}$$

which coincides with (3.85).

3.8 Computation of the vortex mass

As it has been discussed in Section 3.4, to calculate the vortex mass density tensor [see Eq. (3.51)] one needs to find solution $[\Phi(\vec{r},t),\Theta(\vec{r},t)]$ of the Landau-Lifshitz equation in the slow dynamics regime, that is in the first order on $|\dot{\vec{X}}|$. A more convenient set of variables for this problem is the pair (Φ,m), where $m\equiv m_z=\frac{M_z}{M_S}=\cos\Theta$ is the projection of the magnetic moment onto the Z axis. Notice that Landau-Lifshitz equation can be recast as the set of equations

$$\begin{aligned} D_t\Phi &= \frac{\gamma}{M_S}\frac{\delta E}{\delta m}, \\ D_t m &= -\frac{\gamma}{M_S}\frac{\delta E}{\delta\Phi}. \end{aligned} \tag{3.116}$$

The total energy density $\mathcal{E}(\Phi, m)$ splits into the sum

$$\begin{aligned}
\mathcal{E}(\Phi, m) &= \mathcal{E}_{\mathrm{ex}}(\Phi, m) + \mathcal{E}_{\mathrm{an}}(\Phi, m) + \mathcal{E}_{\mathrm{d}}(\Phi, m) \\
&= A\left[(\nabla\Theta)^2 + \sin^2\Theta(\nabla\Phi)^2\right] - K_{\parallel}\frac{M_x^2}{M_S^2} + K_{\perp}\frac{M_z^2}{M_S^2} - \frac{1}{2}\vec{M}\cdot\vec{H}_{\mathrm{d}} \\
&= A\left[\frac{1}{1-m^2}(\nabla m)^2 + (1-m^2)(\nabla\Phi)^2\right] - K_{\parallel}\cos^2\Phi(1-m^2) \\
&\quad + K_{\perp}m^2 - \frac{1}{2}\vec{M}\cdot\vec{H}_{\mathrm{d}},
\end{aligned} \tag{3.117}$$

with $K_{\parallel}$, $K_{\perp}$ being the anisotropy constants of the ferromagnetic material. Recall that $\vec{H}_{\mathrm{d}}(\vec{r}) = -\nabla U_{\mathrm{d}}(\vec{r})$, with $\nabla^2 U_{\mathrm{d}}(\vec{r}) = -4\pi\rho_{\mathrm{d}}$, and $\rho_{\mathrm{d}} = -\nabla\cdot\vec{M}$. Equivalently [93],

$$\begin{aligned}
U_{\mathrm{d}}(\vec{r}) &= \int_V \mathrm{d}^3\vec{r}\,'\vec{M}(\vec{r}\,')\cdot\nabla'\left(\frac{1}{|\vec{r}-\vec{r}\,'|}\right) \\
&= -\int_V \mathrm{d}^3\vec{r}\,'\frac{\nabla'\cdot\vec{M}(\vec{r}\,')}{|\vec{r}-\vec{r}\,'|} + \int_{\partial V}\mathrm{d}\vec{S}'\cdot\frac{\vec{M}(\vec{r}\,')}{|\vec{r}-\vec{r}\,'|} \\
&= \int_V \mathrm{d}^3\vec{r}\,'\frac{\rho_{\mathrm{d}}(\vec{r}\,')}{|\vec{r}-\vec{r}\,'|} + \int_{\partial V}\mathrm{d}^2\vec{r}\,'\frac{\sigma_{\mathrm{d}}(\vec{r}\,')}{|\vec{r}-\vec{r}\,'|},
\end{aligned} \tag{3.118}$$

with $\sigma_{\mathrm{d}} = \vec{M}\cdot\vec{n}$ being the effective surface "charge" density and V being the volume of the system. Consequently, the magnetostatic energy can be written as

$$E_{\mathrm{d}} = \frac{1}{2}\int_V \mathrm{d}^3\vec{r}\rho_{\mathrm{d}}(\vec{r})U_{\mathrm{d}}(\vec{r}) + \frac{1}{2}\int_{\partial V}\mathrm{d}^2\vec{r}\,\sigma_{\mathrm{d}}(\vec{r})U_{\mathrm{d}}(\vec{r}). \tag{3.119}$$

One deals with a 2D micrometric object, so the surface energy term dominates over the volume energy term. This surface term can be approximated by an effective easy plane anisotropy contribution given by

$$E_{\mathrm{d},S} = \int_V \mathrm{d}^3\vec{r}\,2\pi M_z^2(\vec{r}). \tag{3.120}$$

This gives for the total energy density

$$\begin{aligned}
\mathcal{E}(\Phi, m) &= A\left[\frac{1}{1-m^2}(\nabla m)^2 + (1-m^2)(\nabla\Phi)^2\right] - K_{\parallel}\cos^2\Phi(1-m^2) \\
&\quad + (K_{\perp} + 2\pi M_S^2)m^2,
\end{aligned} \tag{3.121}$$

and the equations of motion (3.116) become

$$\begin{aligned}\frac{M_S}{\gamma}D_t\Phi =& -\frac{2Am}{(1-m^2)^2}(\nabla m)^2 - \frac{2A}{1-m^2}\triangle m - 2Am(\nabla\Phi)^2 + 2K_{\parallel}\cos^2\Phi\, m\\ &+2(K_{\perp}+2\pi M_S^2)m,\\ \frac{M_S}{\gamma}D_t m =& -K_{\parallel}\sin(2\Phi)(1-m^2) - 4Am\nabla m\cdot\nabla\Phi + 2A(1-m^2)\triangle\Phi.\end{aligned} \tag{3.122}$$

In the slow dynamics regime ($|\dot{\vec{X}}| \ll 1$) solutions (Φ, m) can be split into $\Phi = \Phi_0+\Phi_1$ and $m = m_0+m_1$, where Φ_0 and m_0 are the static solutions of the Landau-Lifshitz equation (the anisotropy interaction is considered to be weak enough so that the static solutions of the Hamiltonian $E_{\text{ex}} + E_{\text{d}}$ are valid for our problem) and where Φ_1 and m_1 are linear on $|\dot{\vec{X}}|$. Static solutions are given by Eqs. (3.25). As discussed in Sec. 3.5, in the weak bending regime one can approximate $\tilde{r} \simeq r$ so that $\nabla\Phi_0 = \mathcal{Q}\dfrac{\hat{e}_\phi}{r}$ and $\nabla m_0 = \dfrac{dm_0}{dr}\hat{e}_r$.

Linearizing Eqs. (3.122) and taking into account that $D_t\Phi = -\dot{\vec{X}}\cdot\nabla\Phi$ and $D_t m = -\dot{\vec{X}}\cdot\nabla m$, one obtains the equations of motion

$$\begin{aligned}\frac{M_S}{\gamma}\dot{\vec{X}}\cdot\frac{\mathcal{Q}\hat{e}_\phi}{r} =& \frac{2A}{1-m_0^2}\triangle m_1 + m_1\left[\frac{2A(1+3m_0^2)}{(1-m_0^2)^3}\left(\frac{dm_0}{dr}\right)^2 + \frac{4Am_0\triangle m_0}{(1-m_0^2)^2}\right.\\ &\left.+\frac{2A}{r^2} - 2K_{\parallel}\cos^2\Phi_0 - 2(K_{\perp}+2\pi M_S^2)\right] + \frac{4A\,m_0}{(1-m_0^2)^2}\frac{dm_0}{dr}\hat{e}_r\cdot\nabla m_1\\ &+4A\mathcal{Q}\,m_0\frac{\hat{e}_\phi}{r}\cdot\nabla\Phi_1 + 2K_{\parallel}m_0\sin(2\Phi_0)\Phi_1,\\ \frac{M_S}{\gamma}\dot{\vec{X}}\cdot\hat{e}_r\frac{dm_0}{dr} =& -2A(1-m_0^2)\triangle\Phi_1 + 4A\mathcal{Q}\,m_0\nabla m_1\cdot\frac{\hat{e}_\phi}{r} + 4A\,m_0\frac{dm_0}{dr}\hat{e}_r\cdot\nabla\Phi_1\\ &-2K_{\parallel}\sin(2\Phi_0)m_0m_1 + 2K_{\parallel}\cos(2\Phi_0)(1-m_0^2)\Phi_1.\end{aligned} \tag{3.123}$$

Asymptotic expressions for the $O(|\dot{\vec{X}}|)$ corrections to the out-of-plane vortex shape can be determined by substituting Eqs. (3.25) into Eqs. (3.123). In doing so, one obtains

$$\begin{aligned}m_1 &= -\frac{M_S}{2\gamma}\mathcal{Q}\frac{\dot{\vec{X}}\cdot\hat{e}_\phi}{(K_{\perp}+2\pi M_S^2)+K_{\parallel}\cos^2\Phi_0}\frac{1}{r},\\ \Phi_1 &= \frac{C_2 M_S}{2\gamma A}\Delta_0^{3/2}(\dot{\vec{X}}\cdot\hat{e}_r)\frac{\exp\left(-r/\Delta_0\right)}{r^{1/2}}\end{aligned} \tag{3.124}$$

for $r \gg \Delta_0$, and

$$\begin{aligned} m_1 &= \frac{M_S C_1 \mathcal{Q}}{3\gamma A \Delta_0^2}(\dot{\vec{X}} \cdot \hat{e}_\phi) r^3, \\ \Phi_1 &= \frac{M_S}{\gamma}\frac{p}{12A}\dot{\vec{X}} \cdot \vec{r} \end{aligned} \tag{3.125}$$

for $r \ll \Delta_0$. Computation of the mass of the vortex core can be made via $\vec{\Pi}_t$, which should be proportional to $\dot{\vec{X}}$ in this limit:

$$\begin{aligned} \vec{\Pi}_t = -\frac{M_S}{\gamma}\int \mathrm{d}^2\vec{r}(\nabla\Phi)m &= -\frac{M_S}{\gamma}\int \mathrm{d}^2\vec{r}(\nabla\Phi_0)m_0 - \frac{M_S}{\gamma}\int \mathrm{d}^2\vec{r}(\nabla\Phi_0)m_1 \\ &- \frac{M_S}{\gamma}\int \mathrm{d}^2\vec{r}(\nabla\Phi_1)m_0 - \frac{M_S}{\gamma}\int \mathrm{d}^2\vec{r}(\nabla\Phi_1)m_1. \end{aligned} \tag{3.126}$$

Notice that $-\frac{M_S}{\gamma}\int \mathrm{d}^2\vec{r}(\nabla\Phi_0)m_0 = \vec{0}$ because it corresponds to the momentum of the static solution. The last term of Eq. (3.126) can be neglected because it is quadratic in $|\dot{\vec{X}}|$. Therefore it remains to calculate the second and third terms, which are given by

$$\begin{aligned} -\frac{M_S}{\gamma}\int \mathrm{d}^2\vec{r}(\nabla\Phi_0)m_1 &= -\frac{M_S}{\gamma}\int_{r\le\Delta_0} \mathrm{d}^2\vec{r}(\nabla\Phi_0)m_1 - \frac{M_S}{\gamma}\int_{r\ge\Delta_0} \mathrm{d}^2\vec{r}(\nabla\Phi_0)m_1 \\ &= \frac{\pi}{\gamma^2}\left[\frac{M_S^2}{K_\perp + 2\pi M_S^2}\frac{1/2}{\sqrt{1+\frac{K_\shortparallel}{K_\perp+2\pi M_S^2}}}\ln(R/\Delta_0) - \frac{1}{28}\right]\dot{\vec{X}}, \end{aligned} \tag{3.127}$$

and

$$\begin{aligned} -\frac{M_S}{\gamma}\int \mathrm{d}^2\vec{r}(\nabla\Phi_1)m_0 &= -\frac{M_S}{\gamma}\int_{r\le\Delta_0} \mathrm{d}^2\vec{r}(\nabla\Phi_1)m_0 - \frac{M_S}{\gamma}\int_{r\ge\Delta_0} \mathrm{d}^2\vec{r}(\nabla\Phi_1)m_0 \\ &= \frac{\pi}{\gamma^2}\left[-\frac{11}{168} + \frac{4}{49}\left(1 - \Xi\cdot e^2\right)\right]\dot{\vec{X}}, \end{aligned} \tag{3.128}$$

respectively. Notice that $\Xi = \int_1^{R/\Delta_0} \mathrm{d}x\frac{\exp(-2x)}{x} \simeq \int_1^\infty \mathrm{d}x\frac{\exp(-2x)}{x} = 0.049$ because one is interested in the limit $R \gg \Delta_0$.

Collecting all terms for the momentum, the total mass density becomes

$$\rho_M = \frac{\pi}{\gamma^2}\left[\frac{M_S^2}{K_\perp + 2\pi M_S^2}\frac{\ln(R/\Delta_0)}{2\sqrt{1+\frac{K_\shortparallel}{K_\perp+2\pi M_S^2}}} - 0.049\right]. \tag{3.129}$$

Notice that the term involving $\ln(R/\Delta_0)$ is the dominant one in the limit $R \gg \Delta_0$. Furthermore, redefining the exchange length by a factor close to unity one can always absorb the small numerical constant in Eq. (3.129) into the logarithmic term. Magneto-crystalline anisotropies, if they are sufficiently large, destroy the circularly polarized state. Consequently, materials like Py, used in the studies of the vortex state, have negligible magneto-crystalline anisotropy energy as compared to the demagnetizing energy. This means that the above expression for the vortex mass density can be reduced to

$$\rho_M \simeq \frac{1}{4\gamma^2} \ln(R/\Delta_0). \tag{3.130}$$

With account of this formula one obtains the following expressions for the parameters ω_M and ϵ_0 that determine eigenfrequencies in the equation (3.115):

$$\begin{aligned} \omega_M &= \frac{8\pi\gamma M_S}{\ln(R/\Delta_0)}, \\ \epsilon_0 &= \frac{5L}{18\pi R} \ln(R/\Delta_0). \end{aligned} \tag{3.131}$$

3.9 Effects of the magnetic field and dissipation

In this section the effects of a magnetic field on the excitation modes of the VS are studied. An arbitrarily directed magnetic field can be split into two components, one being in the plane of the disk and the other one being perpendicular to it. The effects of these two components can be investigated separately.

Consider first the case of a spatially uniform in-plane magnetic field, $\vec{H}_{\mathrm{in}} = h_x \hat{e}_x + h_y \hat{e}_y$. For small displacements along the disk, the magnetic vortex develops a linear density of in-plane magnetic moment given by [96]

$$\langle \vec{M}(\vec{X}) \rangle \big|_{\mathrm{L}} = -\mu \left[\hat{e}_z \times \vec{X} \right], \qquad \mu = (2\pi/3) C M_S R. \tag{3.132}$$

The Zeeman energy density term is

$$\omega_Z(\vec{X}) = -\langle \vec{M}(\vec{X}) \rangle \big|_{\mathrm{L}} \cdot \vec{H}_{\mathrm{in}} = -\mu \left[\hat{e}_z \times \vec{H}_{\mathrm{in}} \right] \cdot \vec{X} = \mu h_y x - \mu h_x y \tag{3.133}$$

and thus the total in-plane potential energy becomes

$$\begin{aligned} \omega_{XY}(\vec{X}) &= \frac{1}{2} \rho_M \omega_M^2 \epsilon_0 \left(x^2 + y^2 \right) + \mu h_y x - \mu h_x y = \\ & \frac{1}{2} \rho_M \omega_M^2 \epsilon_0 \left[\left(x + \frac{\mu h_y}{\rho_M \omega_M^2 \epsilon_0} \right)^2 + \left(y - \frac{\mu h_x}{\rho_M \omega_M^2 \epsilon_0} \right)^2 \right] - \frac{1}{2} \frac{\mu^2}{\rho_M \omega_M^2 \epsilon_0} \vec{H}_{\mathrm{in}}^2. \end{aligned} \tag{3.134}$$

Notice that by shifting the origin of the coordinate system one retrieves the original in-plane term of the total energy density (3.78) except for the constant term $-\frac{1}{2}\frac{\mu^2}{\rho_M\omega_M^2\epsilon_0}\vec{H}_{\text{in}}^2$, which is field dependent. Consequently, the application of an in-plane magnetic field does not modify the excitation modes given by (3.115).

Consider now the effect of the magnetic field perpendicular to the plane of the disk, $\vec{H}_\perp = H\hat{z}$. Application of such a field results in the precession of the magnetic moment of the vortex about the direction of the field, described by the Landau-Lifshitz equation [93],

$$\frac{\partial\vec{M}(t,\vec{X})}{\partial t} = -\gamma\left[\vec{M}(t,\vec{X})\times\vec{H}_\perp\right]. \tag{3.135}$$

Formally, this effect can be accounted for by adding an extra term to the gyrovector. Indeed, integration of Eq. (3.67) (with no potential energy) over time gives $\dot{\vec{X}} = \alpha\left[\vec{X}\times\vec{\rho}_{\text{G}}\right]$, where $\alpha = -1/\rho_M$. With account of Eq. (3.132), one has

$$\left[\hat{e}_z\times\dot{\vec{X}}\right] = -\gamma\left[\hat{e}_z\times\vec{X}\right]\times\vec{H}_\perp, \tag{3.136}$$

$$\alpha\left(\hat{e}_z\times\left[\vec{X}\times\vec{\rho}_{\text{G}}\right]\right) = -\gamma\left[\hat{e}_z\times\vec{X}\right]\times\vec{H}_\perp. \tag{3.137}$$

The vector identity $\vec{a}\times\vec{b}\times\vec{c} = (\vec{a}\cdot\vec{c})\vec{b} - (\vec{a}\cdot\vec{b})\vec{c}$ leads to $\alpha\rho_{\text{G}} = -\gamma H$. Consequently, the precessional effect of the perpendicular field can be absorbed into the gyrovector density if one adds the term $\vec{\rho}_{\text{G},\vec{H}_\perp} = -\frac{\gamma}{\alpha}\vec{H}_\perp = \rho_M\gamma\vec{H}_\perp$ to it. This adds the Larmor frequency to ω_M,

$$\omega_M(H) = \frac{\rho_{\text{G,tot}}}{\rho_M} = \omega_M + \frac{\rho_{\text{G},\vec{H}_\perp}}{\rho_M} = \omega_M + \gamma H, \tag{3.138}$$

so that the eigenfrequencies (3.115) become

$$\omega_n^\pm(H) = \frac{1}{2}\left[\sqrt{[1+4\epsilon(H)] + \frac{4\lambda}{\rho_M\omega_M^2(H)}q_n^2} \pm 1\right]\omega_M(H), \tag{3.139}$$

with $\epsilon(H)$ given by

$$\epsilon(H) = \frac{\omega_{\text{G}}(H)}{\omega_M(H)} = \frac{\omega_{XY}''(\vec{X}=\vec{0})}{\rho_M\omega_M^2(H)} = \frac{\epsilon_0}{(1+\gamma H/\omega_M)^2}. \tag{3.140}$$

Introducing dimensionless variables $h = \gamma H/\omega_M$ and $\bar{\omega}_n^\pm(h) = \omega_n^\pm(H)/\omega_M$, Eq.

(3.139) can be rewritten as

$$\begin{aligned}\bar{\omega}_n^{\pm}(h) &= \frac{1}{2}\left[\sqrt{1+\frac{4\epsilon_0}{(1+h)^2}+\frac{4\lambda}{\rho_M\omega_M^2(1+h)^2}q_n^2}\pm 1\right](1+h) \\ &\simeq \frac{1}{2}\left[\sqrt{1+\frac{4\epsilon_0}{(1+h)^2}}\pm 1\right](1+h)+\frac{\mathrm{sgn}(1+h)}{\sqrt{(1+h)^2+4\epsilon_0}}\frac{\lambda q_n^2}{\rho_M\omega_M^2}. \end{aligned} \tag{3.141}$$

The distance between ω_n^+ and ω_n^- equals $\Delta\omega = \omega_M + \gamma H$.

To conclude this Section, the effects of the dissipation on the excitation modes of magnetic vortices will be investigated. One considers only the zero field case. Derivation of the corresponding expressions when a magnetic field is applied is straightforward. Dissipation is introduced into the equation of motion by adding a damping term of the form $-D\dot{\vec{X}}$ [see Eqs. (3.26) and (3.28)], so that the elastic Thiele equation becomes

$$\rho_M\ddot{\vec{X}} - \lambda\partial_z^2\vec{X} + \dot{\vec{X}}\times\vec{\rho}_G - D\dot{\vec{X}} + \rho_M\omega_M^2\epsilon_0\vec{X} = 0. \tag{3.142}$$

Repeating the procedure of Sec. 3.6 with the above equation in the massive vortex case ($\rho_M \neq 0$) one obtains the following equation for the frequency modes

$$\omega^2 + (\omega_M + id)\omega - \omega_M^2\epsilon(q) = 0, \tag{3.143}$$

with $d = D/\rho_M$ and $\epsilon(q) = \epsilon_0 + \frac{\lambda}{\rho_M\omega_M^2}q^2$. The (complex) roots of this equation, $\omega_\pm = \mathrm{Re}(\omega_\pm) + i\mathrm{Im}(\omega_\pm)$, are given by

$$\begin{aligned}\mathrm{Re}(\omega_\pm) &= \mp\frac{r^{1/2}}{2}\cos(\theta/2) - \frac{\omega_M}{2}, \\ \mathrm{Im}(\omega_\pm) &= \mp\frac{r^{1/2}}{2}\sin(\theta/2) - \frac{d}{2},\end{aligned} \tag{3.144}$$

with

$$\begin{aligned} r &= \sqrt{\left[(1+4\epsilon(q))\omega_M^2 - d^2\right]^2 + 4d^2\omega_M^2}, \\ \theta &= \arg\left(\left[(1+4\epsilon(q))\omega_M^2 - d^2\right] + i\left[2d\omega_M\right]\right) \\ &= \tan^{-1}\left(\frac{2d\omega_M}{(1+4\epsilon(q))\omega_M^2 - d^2}\right). \end{aligned} \tag{3.145}$$

In the regime of weak dissipation, $d << \omega_M$, one has $\theta \simeq \tan^{-1}\left[\frac{2d}{(1+4\epsilon(q))\omega_M}\right]$ and $r \simeq (1+4\epsilon(q))\omega_M^2$. As $\cos[\tan^{-1}(x)/2] \simeq 1 - \frac{x^2}{8} + o(x^4)$ and $\sin[\tan^{-1}(x)/2] \simeq$

$\frac{x}{2} + o(x^3)$ if $|x| \ll 1$, one finally obtains

$$\begin{aligned}\mathrm{Re}(\omega_\pm) &= \mp\left[\frac{1}{2}\left(\sqrt{1+4\epsilon(q)} \pm 1\right) - \frac{1}{4}\frac{(d/\omega_M)^2}{(1+4\epsilon(q))^{3/2}}\right]\omega_M \\ &\simeq \mp\left[\frac{\omega_M}{2}\left(\sqrt{1+4\epsilon_0} \pm 1\right) - \frac{\omega_M}{4}\frac{(d/\omega_M)^2}{(1+4\epsilon_0)^{3/2}}\right. \\ &\quad \left. + \frac{\lambda}{\sqrt{1+4\epsilon_0}}\left(1 + \frac{3}{2}\frac{(d/\omega_M)^2}{(1+4\epsilon_0)^2}\right)\frac{q^2}{\rho_M \omega_M}\right], \end{aligned} \tag{3.146}$$

and

$$\mathrm{Im}(\omega_\pm) = \left(\mp\frac{1}{\sqrt{1+4\epsilon(q)}} - 1\right)\frac{d}{2}, \tag{3.147}$$

$$\frac{\mathrm{Im}(\omega_+)}{\mathrm{Im}(\omega_-)} = -\frac{1+\sqrt{1+4\epsilon(q)}}{1-\sqrt{1+4\epsilon(q)}} = \frac{(1+\sqrt{1+4\epsilon(q)})^2}{4\epsilon(q)}. \tag{3.148}$$

3.10 Discussion

Study of excitation modes of vortices in circularly polarized mesoscopic magnetic disks that correspond to the string-like gyrotropic waves in the VC has been conducted. This problem was studied by classical treatment based upon Landau-Lifshitz equation and by quantum treatment based upon Hamiltonian approach. The quantum problem is interesting on its own as it is equivalent to the problem of quantum oscillations of a charged string confined in a parabolic potential and subjected to the magnetic field, which in its turn, is a generalization of the problem of the field-induced orbital motion of the electron in a potential well. Both treatments rendered identical results. The solution presented here generalizes the expression for the frequency of the gyrotropic motion of the vortex for the case of the finite wave number q, as $\omega_-(q) = \omega_\mathrm{G} + \gamma M_S (q\Delta_0)^2 \ln(R/\Delta_0)$. This expression is valid in the long-wave limit $q\Delta_0 \ll 1$. The wave number is quantized, $q_n = 2\pi n/L$, where L is the thickness of the disk and n is an integer. For, e.g., a Py disk ($M_S \approx 8 \times 10^5$ A/m^2, $A \approx 1.3 \times 10^{-11}$ J/m) of thickness $L = 100$ nm and diameter $2R = 1.5$ μm, the $n = 1$ mode is separated from the uniform gyrotropic mode by $f = \omega/(2\pi) \approx 7$ GHz, while for $2R = 1$ μm and $L = 50$ nm the separation is about 25 GHz. This mode could be excited by, e.g., a tip of a force microscope or a micro-SQUID placed at the center of the disk. Such measurement, while challenging, is definitely within experimental reach.

Throughout this chapter a non-zero mass of the vortex was considered. The finite value of the mass splits the gyrotropic frequency into two modes, one with the gap ω_{G} and the other with the gap $\omega_M \gg \omega_{\mathrm{G}}$. The latter depends explicitly on the vortex mass. The vortex mass density has been computed here as a coefficient of proportionality, ρ_M, in the kinetic energy density of the moving vortex $\rho_M \dot{\vec{X}}^2/2$, and is given by $\rho_M \simeq 1/(4\gamma^2)\ln(R/\Delta_0)$. For a 25-nm-thick, micron-size Py disk this gives the vortex mass in the ball park of 10^{-23} kg, which is close to the experimental value estimated for a Py ring of comparable size [117]. K. Guslienko *et al.* derived a similar expression for the mass, $M \simeq (3/2)L/\gamma^2$, in Ref. [107]. Both expressions have a dynamical origin and depend linearly on the ratio L/γ^2, but the prefactor in the present case shows an explicit logarithmic dependence on the radius of the disk due to the major contribution of the long-range dipolar interactions to the shape variation of the VC profile.

The result obtained here for the mass gives $\omega_M = 8\pi\gamma M_S/\ln(R/\Delta_0)$. It is higher than the frequencies of the modes studied in Refs. [101, 106], and is typically in the same frequency range that the uniform ferromagnetic resonance of the magnetic material. It would be interesting to investigate this frequency range experimentally alongside with the low-frequency gyrotropic mode. One can also test experimentally the explicit field dependence of the vortex modes, computed here. So far, one has studied the low field that disturbs only slightly the VS formed in a zero field. Nevertheless, the statement concerning the existence of the additional mode due to the finite vortex mass should apply to higher fields as well. This case, however, defies analytical study and must employ full-scale numerical micromagnetic calculations. When the field is sufficient to fully polarize the disk in the perpendicular direction, one expects the high frequency mode to evolve into the uniform ferromagnetic resonance.

It is worth remarking that these axial excitation modes have been detected this same year by Adeyeye's group using broadband ferromagnetic resonance [121, 122]. The authors adapted the model presented here to interpret their experimental results, finding good agreement between theory and experiments.

Chapter 4

Quantum depinning of the magnetic vortex core

4.1 Magnetic irreversibility and relaxation measurements

The vortex core is a suitable candidate to observe macroscopic quantum phenomena. Because of the strong exchange interaction it behaves as an independent entity and, the VC being a nanoscopic object, is likely to exhibit quantum tunneling between classically stable configurations. The measurement of time relaxations of the magnetic moment is a simple way to observe this phenomenon. At finite temperatures these relaxations may occur via thermal activation, whereas in the limit $T \to 0$ these relaxations continue independently of the temperature due to under-barrier quantum tunneling. Macroscopic quantum tunneling (MQT) [see Chapter 2] determines that the relaxation rate decreases exponentially as $\exp(-S_{\text{eff}}/\hbar)$, where S_{eff} is the total action –including dissipation due to coupling with the environment– evaluated at the magnetic thermon for a given temperature. This behaviour has been widely observed in a large number of systems [32], which include single domain particles [123–126], magnetic clusters [127, 128], magnetic domain walls [42], flux lines in type-II superconductors [45, 129] and, very recently, Normal-Superconducting interfaces in type-I superconductors [see Chapters 1 and 2]. All these experimental evidences suggest that magnetic tunneling is a common phenomenon characterizing the low-temperature dynamics of magnetic materials in the mesoscopic scale.

As discussed in Sec. 3.3, dynamics of the VC can be affected by the presence of structural defects in the sample, the effect of pinning (effective strength of the pinning well) being enhanced as the temperature decreases. The gyrotropic motion of the VC can be induced via the application of an in-plane magnetic field, which displaces the VC out of its equilibrium position perpendicularly to the field direction –see Fig. 4.1a. In this section, the magnetic irreversibility and the dynamics of VCs in micron-size Py dot arrays are explored at low temperatures by means of the application of an in-plane magnetic field. Experimental evidence of the quantum depinning of magnetic VCs through relaxation measurements will be presented.

4.1.1 Experimental results

All measurements were performed in a commercial SQUID magnetometer capable of measuring at temperatures down to 2 K and to apply DC magnetic fields up to 5 T. The system is equipped with a Continuous Low Temperature Control (CLTC) and an Enhanced Thermometry Control (ETC) and it showed thermal stability better than 0.01 K at all times in any isothermal measurement. Two hexagonal arrays of Py ($Ni_{81}Fe_{19}$) disks were studied, with geometries given by the parameters $(L, R) = (95, 750)$ nm (S1) and $(L, R) = (60, 750)$ nm (S2), respectively. Their surface density was 0.15 dots/μm^2. Both arrays of Py disks were fabricated on a silicon wafer using optical lithography, and lift-off techniques. A single layer resist spin coating and highly directional electron-beam evaporation under UHV conditions were used to obtain circular dots with sharp edges. Identical properties such as grain size, distribution, orientation, and film thickness may be obtained over the whole array. The magnetic film was deposited on a water-cooled substrate from a Py ($Ni_{81}Fe_{19}$) target. The growth ratio was of about 1.5 Å/s. Both Py films showed a switching field of about 4 Oe and appeared to be pretty isotropic (in-plane). Figure 4.1b shows an AFM image of the array S1, the perspective being from a top-down view. Finally, samples were prepared by stacking four 5×5 mm^2 of these arrays with parallel sides and all magnetic measurements were performed using an in-plane configuration of the magnetic field. Samples were studied in the range of temperatures $T \in [2, 300]$ K and under applied magnetic fields up to 2 kOe.

Figure 4.2a shows the $M(H)$ curves of sample S1 at three different temperatures, $T \in \{2, 50, 300\}$ K, for positive applied magnetic fields. The first magnetization curves have been omitted. The values of the magnetization at negative fields can be obtained by noticing that these hysteretic cycles are antisymmetric. These hysteresis loops correspond to the onion state/SD↔VS transitions [see Sec. 3.1]. As the temperature is lowered, the nucleation field H_n decreases and the annihilation field H_{an} increases [see discussion in Sec. 3.3]. The vortex linear regime along the descending branch should extend from 300 Oe to −500 Oe at least in the range of temperatures explored. This has been confirmed by analyzing the numerical derivative of the DC hysteresis loops and by measuring the AC susceptibility along this hysteretic branch for comparison, a technique introduced

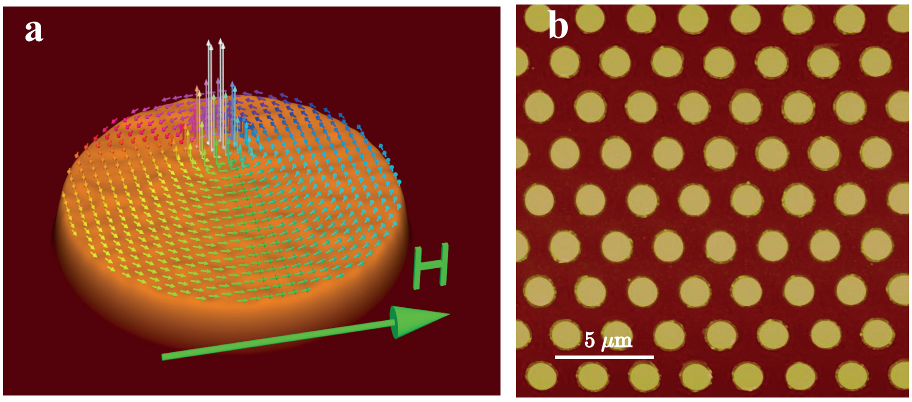

Figure 4.1: (a) Magnetization field of the vortex state in one of the Py disks considered in (b). The VC is displaced transversely to the direction of the applied magnetic field H. (b) AFM image of the array S1 of Py disks from a top-down view.

in Ref. [109]. Figure 4.2b shows the numerical derivative $\mathrm{d}M/\mathrm{d}H$ of these curves along the descending branch for positive values of the magnetic field, with a clear non-zero plateau in the field range $[0, 300]$ Oe. This is a characteristic signature of the vortex linear regime. The AC susceptibility measurements resulted in a similar behavior to that described in Ref. [109]. On the other hand, the descending and ascending branches do not overlap at any temperature within the linear regime. Furthermore, the remnant magnetization increases as T decreases [see Sec. 3.3]. From Fig. 4.1b one observes that the patterned disks have a fairly circular shape, so that the possibility of open hysteresis at zero field due to ellipticity (or shape defect) of the submicron-size disks can be neglected. In summary, the vortex linear regime exhibits magnetic irreversibility that is temperature dependent.

Metastability of magnetic vortices in sample S1 was explored by means of 1) ZFC-FC magnetization curves [M_{ZFC} and M_{FC}, respectively] at different magnetic fields, and 2) isothermal measurements of the magnetization along the descending branch of the hysteresis cycle from the onion/SD state [$M_{\mathrm{des}}(H)$] at different temperatures. In both protocols the values of T and H at which the magnetization was measured were the same. The ZFC process consists of the following steps: Firstly, minor cycles around $H = 0$ Oe are performed at $T = 150$ K, which leads to a zero-magnetization state at zero field. Secondly, the sample is cooled down to $T = 2$ K at zero field and then the desired magnetic field H is applied. Finally, the ZFC magnetization curve is measured from 2 K to 150 K. Sweeping the temperature back to 2 K one obtains the FC curve. Figure 4.3a shows both ZFC-FC curves measured at $H = 300$ Oe in the temperature range $T \in [2, 150]$ K. Notice that the magnetization increases strongly from an initial value at 2 K to

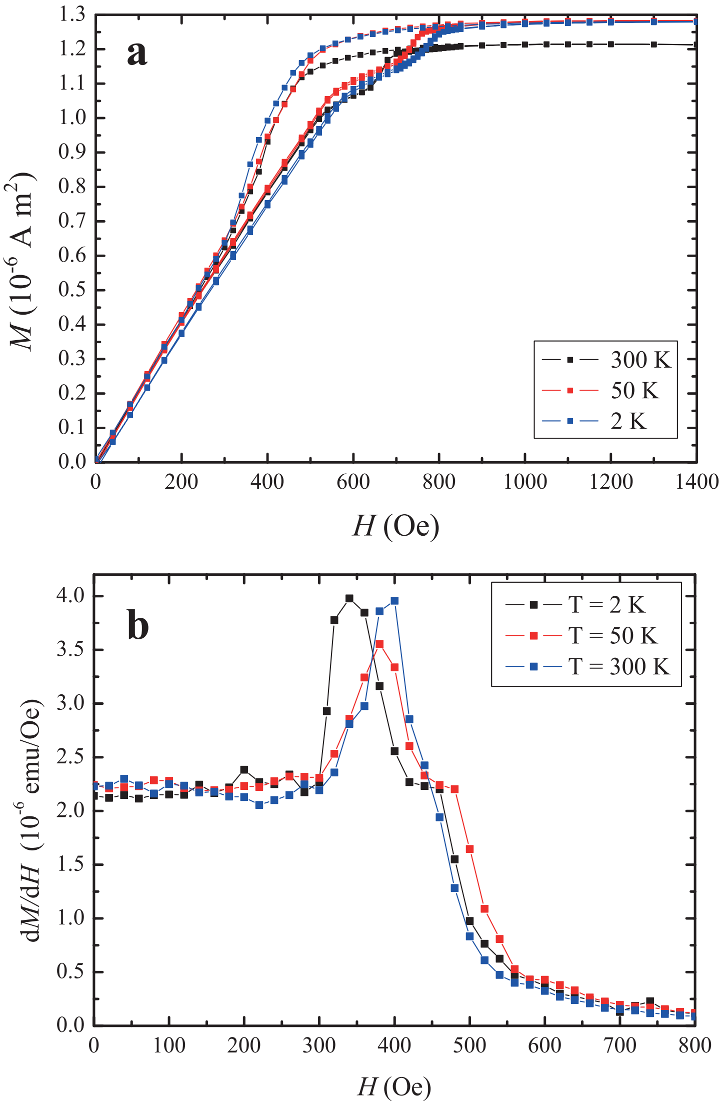

Figure 4.2: (a) Half hysteresis loops of sample S1 obtained at three different temperatures ($T = 2$, 50 and 300 K) for positive applied magnetic fields. The size of the points is bigger than the error bars. (b) Numerical derivative $\mathrm{d}M/\mathrm{d}H$ along the descending branch of the hysteresis loops plotted in (a).

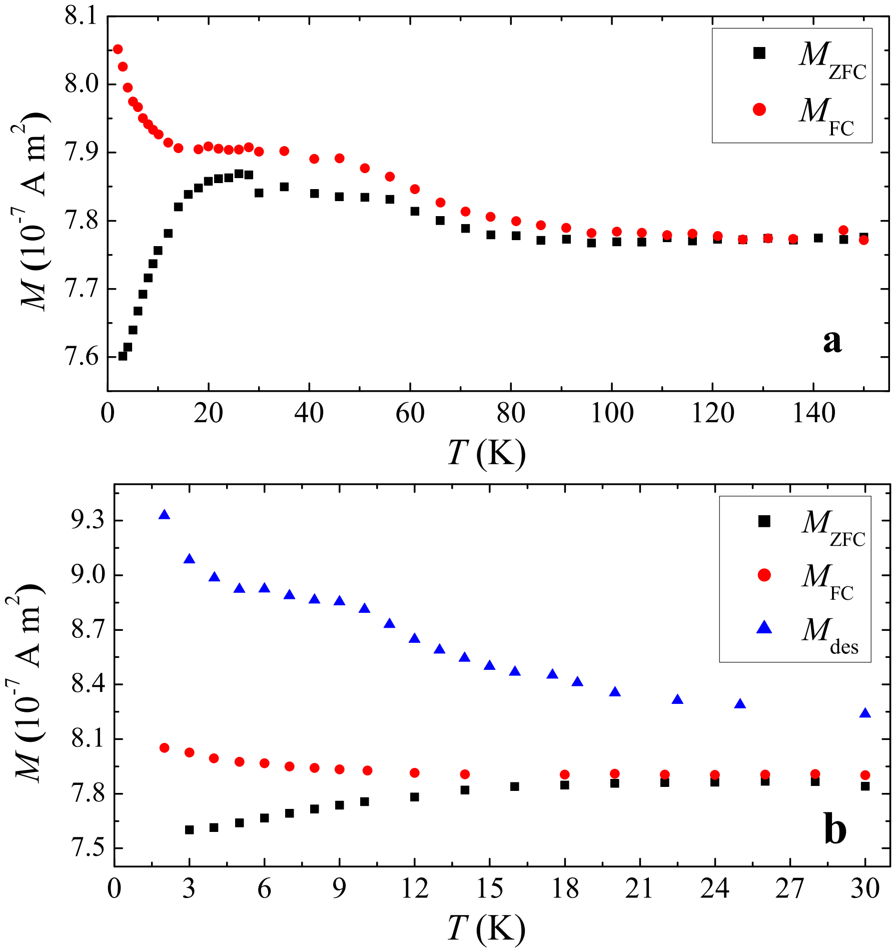

Figure 4.3: (a) Temperature dependence of M_{ZFC}(300 Oe) and M_{FC}(300 Oe) in the range $T \in [2, 150]$ K. (b) Thermal dependence of M_{des}(300 Oe), M_{ZFC}(300 Oe) and M_{FC}(300 Oe) in the range $T \in [2, 30]$ K. These measurements correspond to the sample S1.

a maximum around $T \sim 30$ K. Then it decreases smoothly and reaches a plateau at high temperatures. The dependence of the FC curve on temperature is similar to that of the ZFC case at high temperatures, but with slightly higher values of the magnetization. In the ballpark of $T \sim 20$ K, however, the magnetization of the FC process rises strongly, reaching its maximum value at $T = 2$ K. This thermal dependence of both $M_{\mathrm{ZFC}}(H)$ and $M_{\mathrm{FC}}(H)$ is characteristic of applied magnetic fields within the linear vortex regime. Additionally, isothermal magnetic measurements along the descending branch of the hysteresis cycle, $M_{\mathrm{des}}(H)$, were measured: Firstly, one saturates the sample in the onion/SD state by application of a $H = 1$ kOe magnetic field after fixing the temperature T. Secondly, the magnetic field is reduced to the desired value and then magnetization of the sample is recorded. In both protocols, measurements of M were taken at the same values of T. Figure 4.3b shows the thermal dependences of M_{des}, M_{ZFC} and M_{FC} evaluated at $H = 300$ Oe in the range $T \in [2, 30]$ K. The values of $M_{\mathrm{des}}(300\text{ Oe})$ decrease strongly as T increases within the range $T \in [2, 20]$ K and tend smoothly to those of the FC curve above $T \sim 30$ K. The divergence among the M_{ZFC}, M_{FC} and M_{des} curves in the range $T \in [2, 20]$ K indicates the existence of strong magnetic irreversibility in this region.

To confirm that the FC curve represents the magnetic equilibrium of the system two sets of measurements of the isothermal time evolution of the magnetization, $M(T, t)$, were taken for sample S1 as the temperature is swept in increments of 1 K every 30 minutes (a) from 15 K to 2 K and (b) from 2 K to 15 K, see Fig. 4.4. The initial magnetic state for each set of measurements was prepared by means of the ZFC process explained above down to the desired temperature, followed by the application of a magnetic field $H = 300$ Oe. In Fig. 4.4a magnetic relaxation of the sample is only observed at 15 and 14 K, the magnetization quickly reaching a stationary value corresponding to that of the FC curve. From this point forward, sweeping the temperature down to 2 K only leads to a variation of the magnetization of the sample according to the thermal dependence of the FC curve. On the other hand, Fig. 4.4b shows that, for this protocol, the magnetization relaxes in the whole range of temperatures. The initial magnetization value of each relaxation is determined by the time evolution of the previous process. Furthermore, the amount of relaxed magnetization in each relaxation process is approximately the same within the range $T \in [2, 9]$ K and progressively decreases to zero for $T \geq 10$ K, with the magnetization tending to the values of the FC curve. Analogous behavior with respect to the hysteresis loops, ZFC-FC magnetization curves and magnetization along the descending branch was found for sample S2.

A deeper insight into the metastability of both samples was gained by performing relaxation measurements within the vortex linear regime. The amount of magnetization available for relaxing is given by the difference $M_0 - M_{\mathrm{eq}}$, where

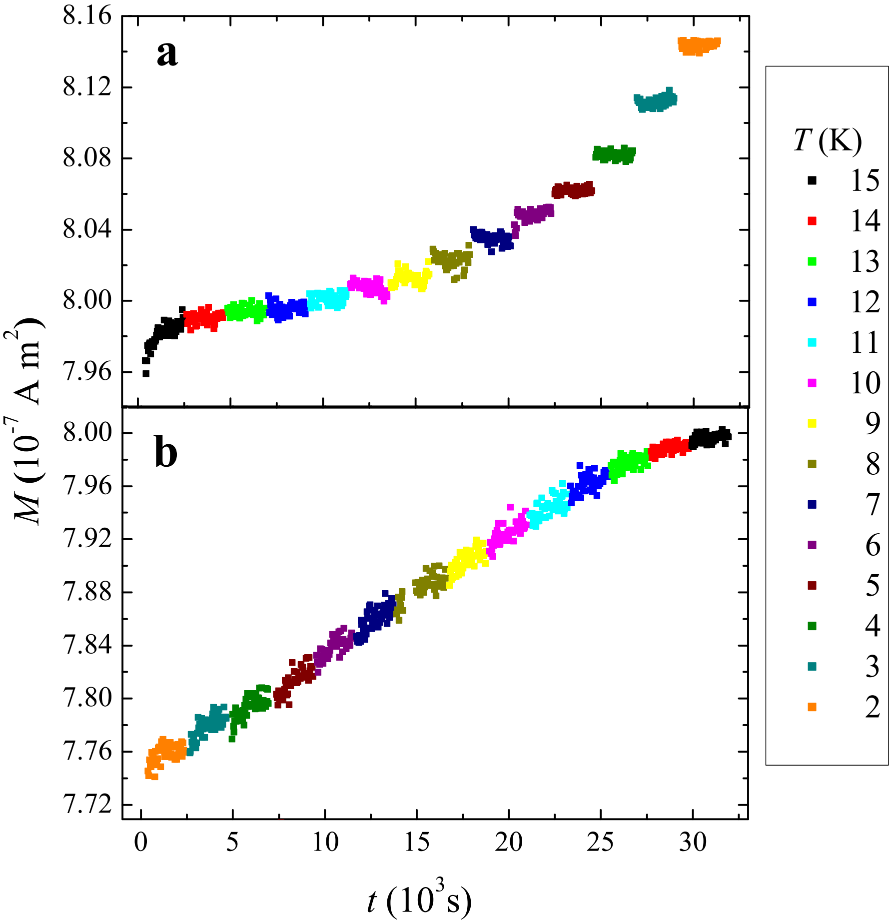

Figure 4.4: Isothermal time evolution of the magnetization of sample S1 in steps of 1 K every 30 minutes (a) from 15 K to 2 K and (b) from 2 K to 15 K.

M_0 is the initial magnetization and M_{eq} corresponds to the equilibrium magnetization. Therefore, the study focused on relaxation measurements of the VS from the metastable states along the descending hysteretic branch in the temperature range $T \in [2, 20]$ K (see Fig. 4.3b). Figure 4.5 shows the normalized irreversible magnetization [left term of Eq. (4.1)] vs. $\ln t$ curves measured at zero field within the temperature range $T \in [2, 10]$ K for samples S1 [panel (a)] and S2 [panel (b)]. In this case relaxation processes occur from the remnant state to the zero-magnetization state. Only below $T \sim 20$ K the magnetization of both samples follows very well a logarithmic time dependence.

Magnetic viscosity $S(T)$ of these relaxation measurements can be calculated in this range of temperatures by means of the theoretical expression [32]

$$\frac{M(t) - M_{\mathrm{eq}}}{M_0 - M_{\mathrm{eq}}} = 1 - S(T) \ln t, \tag{4.1}$$

with $M_0 = M_{\mathrm{r}}(T)$ and $M_{\mathrm{eq}} = 0$ in the case of Fig. 4.5. Figure 4.6 shows the magnetic viscosity as a function of temperature for both samples. Magnetic viscosity reaches a non-zero plateau below $T_{\mathrm{c}} = 6$ K, the crossover temperature of the system. Above T_{c} the magnetic viscosity increases up to a certain temperature —dependent on the sample—, from which it decreases again. The increase of viscosity with temperature above the crossover temperature is due to thermal activation over the pinning barriers. The drop of the magnetic viscosity is in agreement with the loss of magnetic irreversibility in the systems.

4.1.2 Discussion

A logarithmic time dependence of the magnetization in relaxation measurements indicates the existence of a broad distribution of energy barriers V in the system. Classically, these energy barriers can be overcome by thermal activation with probability proportional to the Arrhenius factor $\exp(-V/k_{\mathrm{B}}T)$. The so-called blocking temperature, T_{B}, sets apart the reversible ($T > T_{\mathrm{B}}$) and irreversible ($T < T_{\mathrm{B}}$) regimes when the sample is externally perturbed. Despite the slight differences between M_{ZFC} and M_{FC} and between M_{des} and M_{FC} at high temperatures, the strong divergence in magnetization observed in Fig. 4.3b suggests that the blocking temperature should be below $T \sim 20$ K.

The blocking temperature for weakly interacting systems can be estimated as the temperature at which the magnetic viscosity reaches its maximum [32]. From Fig. 4.6 one estimates the values $T_{\mathrm{B,S1}} \simeq 18$ K and $T_{\mathrm{B,S2}} \simeq 20$ K for samples S1 and S2, respectively. This is in good agreement with the gradual loss of logarithmic time dependence of these relaxation measurements at $T \gtrsim 20$ K. Notice that thermal activation of the energy barriers dies out in the limit $T \to 0$.

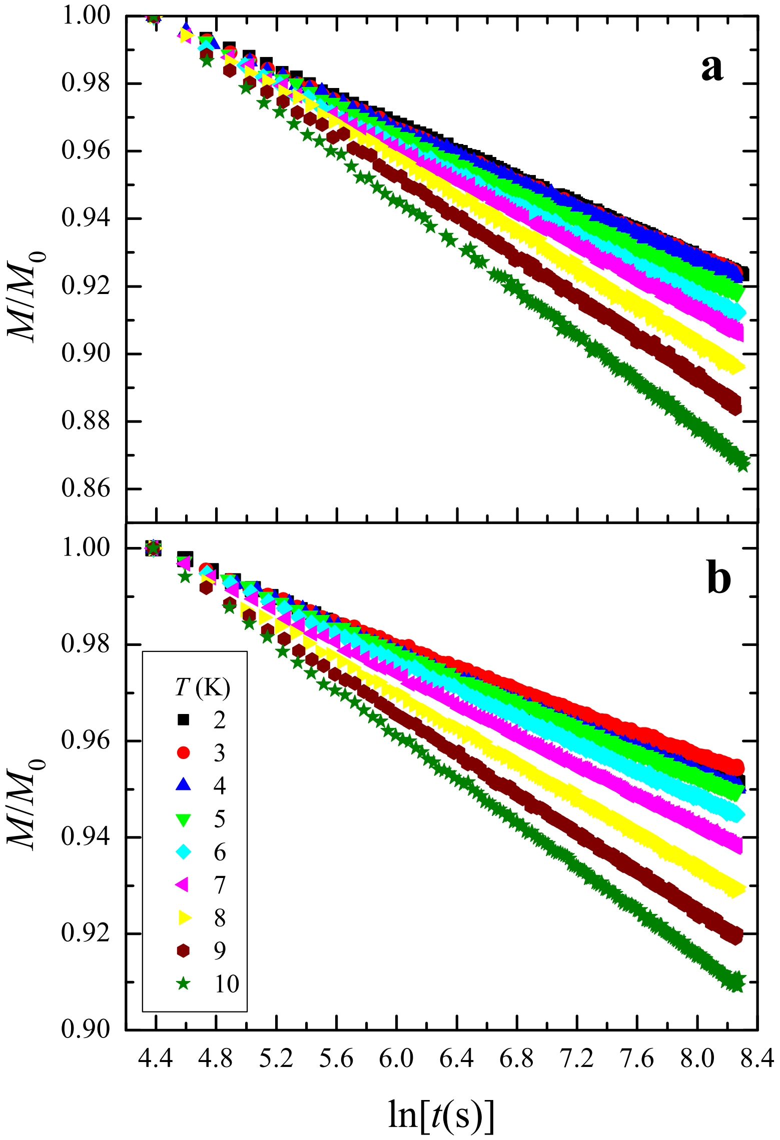

Figure 4.5: Relaxation measurements of magnetic vortices from the remnant state to equilibrium for samples (a) S1 and (b) S2.

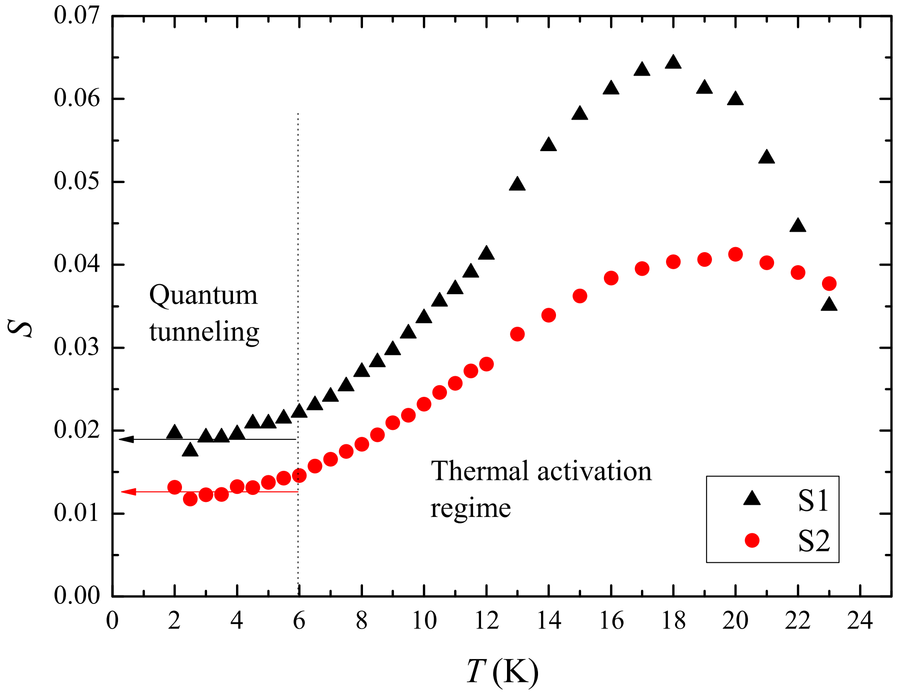

Figure 4.6: Magnetic viscosity versus temperature for both samples. The arrows point towards the non-zero value of the plateaus.

Therefore, the existence of the non-zero plateau in the thermal dependence of the magnetic viscosity as $T \to 0$ is the evidence of relaxations being non-thermal at very low temperatures. Equivalently, transitions from metastable states occur through underbarrier quantum tunneling below T_c. This interpretation is upheld by the graphic representation M vs. $T \ln(t/\tau_0)$ [126] of the relaxation processes in Fig. 4.7: τ_0 is the so-called characteristic attempt time of the system and its value is such that the magnetization of a relaxation process scales with $T \ln(t/\tau_0)$ in the thermal regime. Hence, its best estimate corresponds to the best scaling of the resulting $M\,[T \ln(t/\tau_0)]$ graphic representations. Notice that just the power dependences $\tau_0 = 10^p$, $p \in \mathbf{Z}^+$, are considered because only the order of magnitude is relevant to the relaxation process (see Ref. [32]). In the present case the estimates for samples S1 and S2 are $\tau_{0,\mathrm{S1}} \sim 10^{-11}$s and $\tau_{0,\mathrm{S2}} \sim 10^{-10}$s, respectively, so that magnetic relaxation curves only scale for temperatures above T_c. The loss of scaling below the crossover temperature corresponds to the quantum regime and is independent of the energy barrier distribution [126]. The increase of the viscosity between T_c and T_B corresponds to thermal overcoming of the (pinning) energy barriers. Above the blocking temperature, the decrease of the viscosity as T increases corresponds to the fact that there is a lower number of magnetic VCs in metastable states that should relax to the equilibrium magnetization —magnetic irreversibility decreases with temperature.

The onset of magnetic irreversibility occurs by sweeping the external magnetic field in both M_{ZFC} and M_{des} processes. The effect of the field (within the linear regime) on the VS is to move the VC across the disk plane and, thus, magnetic irreversibility should arise from this displacement. As discussed in Sec. 3.3, the presence of some sort of structural defects (grain boundaries, dislocations, etc.) affects the (gyrotropic) dynamics of the VS. Linelike defects are feasible candidates to provide the landscape of pinning barriers encountered by the VC during its low-temperature dynamics. Magnetic relaxation of the samples may, therefore, be interpreted simply as the dynamics of the VC as it escapes from the mestastable wells due to pinning centers towards the equilibrium. The crossover temperature being independent of the thickness of the submicron-size disks supports the hypothesis that just a small portion of the VC line takes part in the tunneling process via an elastic deformation. The VC line as a whole behaves classically, that is, the amount of spins configuring this magnetic soliton is large enough not to exhibit quantum tunneling phenomena collectively.

4.2 Theoretical model

As discussed in Secs. 3.4 and 3.5, the true nature of the VC line is that of an elastic string with finite elasticity provided by the exchange interaction. At low

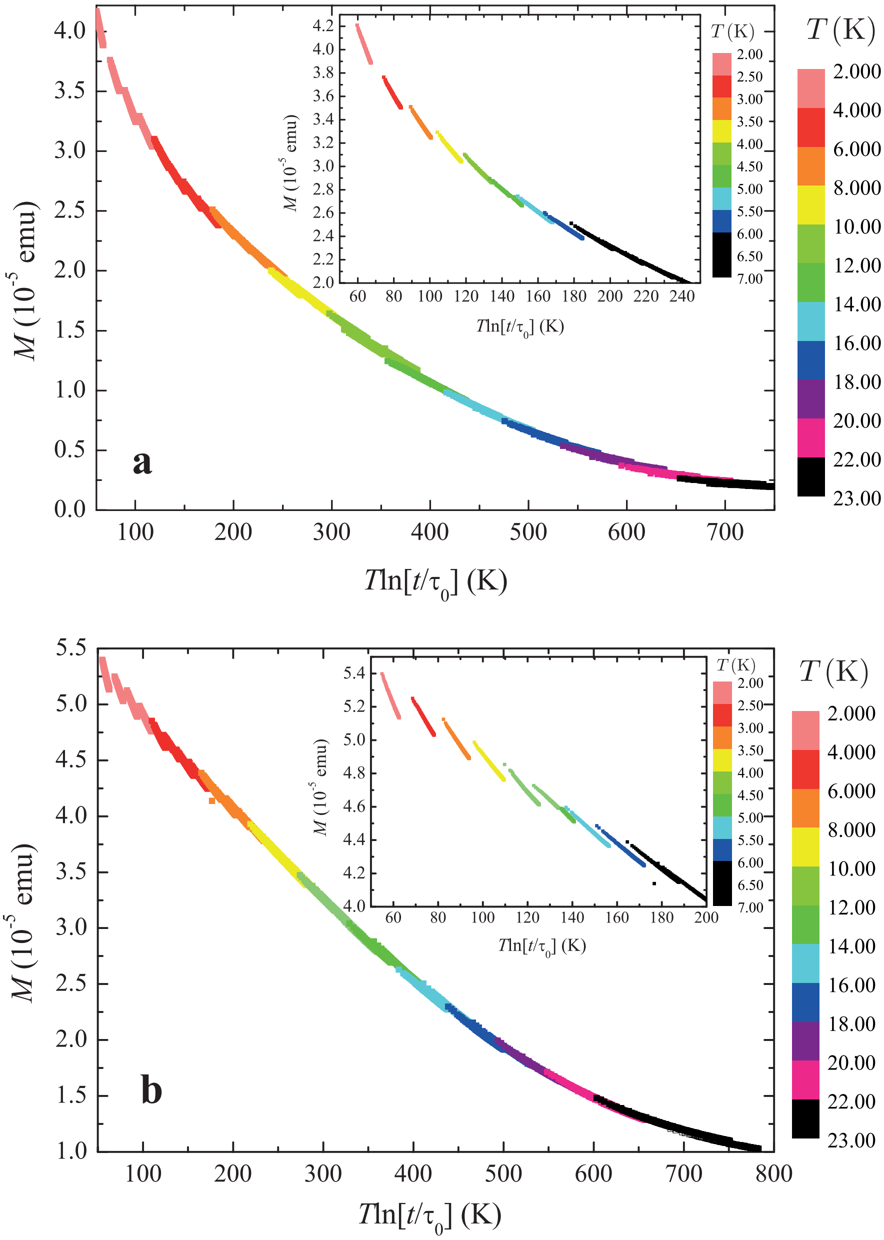

Figure 4.7: Magnetization vs. $T \ln t$ curves measured at zero field for samples (a) S1 and (b) S2. Insets show a zoom of the curves in the temperature range $T \in [2, 7]$ K. Above $T_c = 6$ K the scaling $M = M[T \ln(t/\tau_0)]$ is verified –black segments within the insets–, which corresponds to the case of thermal relaxation. Below T_c one finds a breakdown of this scaling associated with the quantum regime.

temperatures only the softest dynamical mode of the VS can be activated, which corresponds to the gyrotropic motion of the VC. The aim of this section is to study the mechanism of quantum tunneling of the elastic VC line through a pinning barrier during the gyrotropic motion. The attention will focus on line defects, which can be originated for instance by linear dislocations along the disk symmetry axis. This case may be relevant to the relaxation experiments discussed in Sec. 4.1 since linear defects provide the maximum pinning and, therefore, the VC line in the equilibrium state is likely to align locally with these defects. Such a situation would be similar to pinning of domain walls by interfaces and grain boundaries. Thus, the depinning of a small segment of the VC line from a line defect will be considered. The problem of quantum and thermal depinning of a massive elastic string trapped in a linear defect and subject to a small driving force was considered by Skvortsov [130]. The problem studied here is different as it involves gyrotropic motion of a massless vortex that is equivalent to the motion of a trapped charged string in a magnetic field [see Sec. 3.5]. This problem will be studied with account of Caldeira-Leggett-type dissipation [see Sec. 2.1.4].

4.2.1 Elastic Thiele's Lagrangian formalism and depinning rate

From this point forward, a circular disk geometry with parameters (L, R) and an in-plane configuration of the applied magnetic field will be considered. Furthermore, *linear density* (along the VC line) will be referred to simply as *density*. The VC line is pinned by the line defect going in the Z direction –symmetry axis of the disk– and located at the center of the disk. The VC line shall be described by the vector field $\vec{X} = (x, y)$, where $x(t, z)$ and $y(t, z)$ are coordinates of the center of the VC in the XY plane. The dependence on the Z-coordinate emerges from the elastic nature of this magnetic structure [see Sec. 3.5]. Figure 4.8 shows an sketch of the vortex line deformation due to pinning and its gyroscopic motion.

The softest dynamical mode of the VC, and hence of the whole vortex, originates from gyroscopic motion and is described by the generalized Thiele equation (3.79):

$$\dot{\vec{X}}(t, z) \times \vec{\rho}_{\mathrm{G}} + \partial_z \vec{\Pi}_z + \nabla_{\vec{X}} \omega = 0, \tag{4.2}$$

where 'dot' means time derivative. The gyrovector density $\vec{\rho}_{\mathrm{G}} = \rho_{\mathrm{G}} p \mathcal{Q} \hat{e}_z$ is responsible for the gyroscopic motion of the VC and its modulus is given by Eq. (3.66), with $p = \pm 1$ being the polarization of the VC and $\mathcal{Q} = 1$ being the vorticity of the magnetization field. The potential energy density $\omega(\vec{X}, \partial_z \vec{X})$ splits into the sum of two contributions, $\omega_1(\vec{X})$ and $\omega_2(\partial_z \vec{X})$. The latter is the elastic

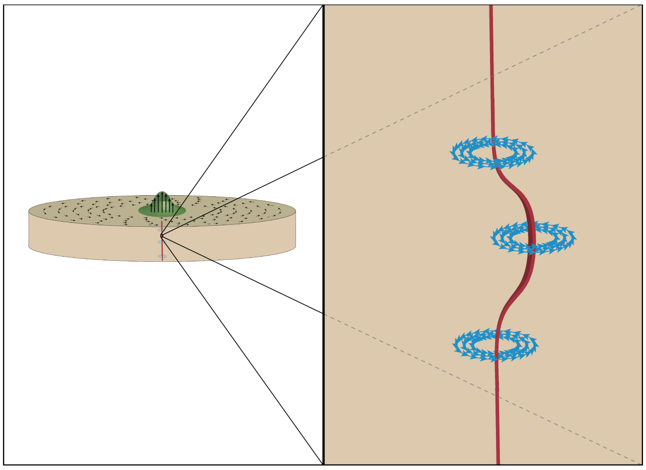

Figure 4.8: Vortex state and depinning via nucleation of the part of the VC line in a circular disk made of soft ferromagnetic material.

term, $\omega_2(\partial_z\vec{X}) = \frac{1}{2}\lambda\left(\frac{\partial\vec{X}}{\partial z}\right)^2$, provided by the exchange interaction. The elastic constant is given by Eq. (3.77). Finally, $\vec{\Pi}_z = -\delta\omega/\delta(\partial_z\vec{X}) = -\lambda\partial_z\vec{X}$ is the generalized momentum density with respect to Z. Hence, the generalized Thiele equation becomes

$$\dot{\vec{X}}(t,z)\times\vec{\rho}_{\mathrm{G}} - \lambda\partial_z^2\vec{X}(t,z) + \nabla_{\vec{X}}\omega = 0. \tag{4.3}$$

The Lagrangian corresponding to the above equation is given by [see Eq. 3.92]:

$$\mathcal{L}[t,\vec{X},\dot{\vec{X}},\partial_z\vec{X}] = \int_0^L \mathrm{d}z\left\{\dot{\vec{X}}\cdot\vec{A}_{\rho_{\mathrm{G}}} - \omega(\vec{X},\partial_z\vec{X})\right\}, \tag{4.4}$$

where $\vec{A}_{\rho_{\mathrm{G}}} = \rho_{\mathrm{G}}p\mathcal{Q}y\hat{e}_x$ is the gyrovector potential in a convenient gauge. Notice tha the symmetric gauge is used in Eq. (3.97) instead of this one. In both cases the gyrovector potential verifies the identity $\nabla_{\vec{X}}\times\vec{A}_{\rho_{\mathrm{G}}} = -\vec{\rho}_{\mathrm{G}}$. The VC is a mesoscopic object consisting of many degrees of freedom. Quantum depinning of such object must be considered within the semiclassical method of Caldeira-Leggett theory [see Sec. 2.1.4]: The depinning rate at a temperature T, $\Gamma(T) = A(T)\exp\left[-B(T)\right]$, is obtained by performing the imaginary-time path integral

$$\int D[x]\int D[y]\exp\left[\frac{-1}{\hbar}\oint \mathrm{d}\tau\mathcal{L}_{\mathrm{E}}\right] \tag{4.5}$$

over τ-periodic trajectories $\vec{X}_\tau \equiv \vec{X}(\tau, z)$ with period $\hbar/k_B T$. Notice that $\tau = it$ is the imaginary time and $\mathcal{L}_\mathrm{E}$ is the Euclidean version of Eq. (4.4). That is,

$$\mathcal{L}_E[\tau, \vec{X}_\tau, \dot{\vec{X}}_\tau, \partial_z \vec{X}_\tau] = \int_0^L \mathrm{d}z \left\{ - i\dot{\vec{X}}_\tau \cdot \vec{A}_{\rho_\mathrm{G}} + \omega(\vec{X}_\tau, \partial_z \vec{X}_\tau) \right\}. \tag{4.6}$$

The energy density $\omega_1(\vec{X}_\tau)$ splits into the sum of three terms. The first one, $\omega_{XY}(\vec{X}_\tau)$, represents the sum of the magnetostatic and exchange contributions in the z-cross-section, whose dependence on the VC coordinates is $\omega_{XY}(\vec{X}_\tau) \sim \vec{X}_\tau^2$ for small displacements [see Eq. (3.68)]. The second term, $\omega_\mathrm{dep}(\vec{X}_\tau)$, represents the pinning energy density associated with the line defect. Recent experimental works have reported an even quartic dependence of pinning potentials on the VC coordinates for small displacements in Py rings [131]. Therefore, it is legitimate to take the following functional dependence for the sum of both terms:

$$(\omega_{XY} + \omega_\mathrm{dep})(\vec{X}_\tau) = \frac{1}{2}\kappa \left(x_\tau^2 + y_\tau^2\right) - \frac{1}{4}\beta p_4(x_\tau, y_\tau), \tag{4.7}$$

where (κ, β) are the parameters of the model and $p_4(x, y)$ is a linear combination of monomials of degree four on variables x and y. The last term represents the Zeeman energy density, which is given by $\omega_Z(\vec{X}_\tau) = -\mu \left[\hat{e}_z \times \vec{H}_\mathrm{in}\right] \cdot \vec{X}_\tau$, $\mu = (2\pi/3) C M_S R$ for small displacements. It corresponds to the application of a weak in-plane uniform magnetic field $\vec{H}_\mathrm{in}$. A magnetic field $\vec{H}_\mathrm{in} = -H\hat{e}_y$ applied along the Y direction is chosen in the forthcoming calculations.

The simple dependence $p_4(x_\tau, y_\tau) = x_\tau^4$ keeps the main features of the pinning potential [see Sec. 4.2.4]. One also neglects the elastic term $\frac{1}{2}\lambda\left(\frac{\partial y_\tau}{\partial z}\right)^2$. The assumptions made regarding the structure of the potential can affect the values of factors of order unity but should not change the conclusions as to the magnitude of the effects studied here. From all these considerations the Lagrangian (4.6) becomes

$$\begin{aligned} \mathcal{L}_\mathrm{E}[\tau, \vec{X}_\tau, \dot{\vec{X}}_\tau, \partial_z \vec{X}_\tau] = & \\ \int_0^L \mathrm{d}z \left\{ - i\rho_\mathrm{G} p Q y_\tau \dot{x}_\tau - \mu H x_\tau + \frac{\kappa}{2} x_\tau^2 + \frac{\kappa}{2} y_\tau^2 - \frac{\beta}{4} x_\tau^4 + \frac{\lambda}{2}\left(\frac{\partial x_\tau}{\partial z}\right)^2 \right\}. \end{aligned} \tag{4.8}$$

Finally, Gaussian integration over y_τ [see Appendix B] reduces Eq. (4.5) to

$$\int D[x] \exp\left[\frac{-1}{\hbar} \oint \mathrm{d}\tau \mathcal{L}_\mathrm{E,eff}\right] \tag{4.9}$$

with

$$\mathcal{L}_{\mathrm{E,eff}}[\tau, x_\tau, \dot{x}_\tau, \partial_z x_\tau] = \int_0^L \mathrm{d}z \left\{ \frac{1}{2}\left(\frac{\rho_{\mathrm{G}}^2}{\kappa}\right)\dot{x}_\tau^2 - \mu H x_\tau + \frac{\kappa}{2}x_\tau^2 - \frac{\beta}{4}x_\tau^4 + \frac{\lambda}{2}\left(\frac{\partial x_\tau}{\partial z}\right)^2 \right\}. \tag{4.10}$$

Within the framework of the Caldeira-Leggett theory [see Sec. 2.1.4], dissipation is taken into account by adding a term

$$\frac{\eta}{4\pi}\int_0^L \mathrm{d}z \oint \mathrm{d}\tau \int_{\mathbf{R}} \mathrm{d}\tau_1 \frac{[x_\tau(\tau, z) - x_\tau(\tau_1, z)]^2}{(\tau - \tau_1)^2} \tag{4.11}$$

to the action of Eq. (4.9). The dissipative constant η is related to the damping of the magnetic VC [32] and from Eq. (3.30) one has $\eta \simeq 3\alpha_{\mathrm{LLG}}\rho_{\mathrm{G}}$, with α_{LLG} being the Gilbert damping parameter. Introducing dimensionless variables $\bar{\tau} = (\kappa/\sqrt{2}\rho_{\mathrm{G}})\tau$, $\bar{z} = (\kappa/2\lambda)^{1/2}z$ and $u = (2\beta/\kappa)^{1/2}x_\tau$, the depinning exponent becomes

$$B(T,h) = \frac{\rho_{\mathrm{G}}\sqrt{\lambda\kappa}}{2\hbar\beta}\int \mathrm{d}\bar{z}\oint \mathrm{d}\bar{\tau}\left[\frac{1}{2}\dot{u}^2 + \frac{1}{2}(u')^2 + V(u,h) + \frac{\eta}{2\sqrt{2}\pi\rho_{\mathrm{G}}}\int_{\mathbf{R}} \mathrm{d}\bar{\tau}_1 \frac{(u(\bar{\tau},\bar{z}) - u(\bar{\tau}_1,\bar{z}))^2}{(\bar{\tau} - \bar{\tau}_1)^2}\right] \tag{4.12}$$

where ' $'$ ' means derivative with respect to $\bar{z}$, $V(u,h) = -hu + u^2 - u^4/4$ is the normalized energy potential and $h = 2\sqrt{2\beta/\kappa^3}\mu H$. Let $u_0(h)$ be the relative minimum of V for a fixed value of h. By rescaling the energy potential $V(u,h) \to V(u,h) := V(u_0(h) + u, h) - V(u_0(h), h)$ and shifting the variable $u \to u_0(h) + u$ one obtains $V(u,h) = u^2\left[\left(1 - 3u_0^2(h)/2\right) - u_0(h)u - u^2/4\right]$.

4.2.2 Instantons of the dissipative 1+1 model

Quantum depinning of the VC line is given by the evaluation of the depinning exponent (4.12) at the instanton solution of the Euler-Lagrange equations of motion of the 1+1 field theory described by Eq. (4.12). This gives

$$\ddot{u} + u'' - \left[2 - 3u_0^2(h)\right]u + 3u_0(h)u^2 + u^3 - \frac{\sqrt{2}}{\pi}\frac{\eta}{\rho_G}\int_{\mathbf{R}} \mathrm{d}\bar{\tau}_1 \frac{u(\bar{\tau},\bar{z}) - u(\bar{\tau}_1,\bar{z})}{(\bar{\tau} - \bar{\tau}_1)^2} = 0 \tag{4.13}$$

with boundary conditions

$$\begin{aligned} u(-\Omega/2, \bar{z}) &= u(\Omega/2, \bar{z}) \qquad && \bar{z} \in \mathbf{R}, \\ \max_{\bar{\tau}\in[-\Omega/2,\Omega/2]} u(\bar{\tau}, \bar{z}) &= u(0, \bar{z}) \qquad && \bar{z} \in \mathbf{R}, \end{aligned} \tag{4.14}$$

that must be periodic on the imaginary time $\bar{\tau}$ with the period $\Omega = \frac{\kappa}{\sqrt{2}\rho_{\mathrm{G}}}\frac{\hbar}{k_{\mathrm{B}}T}$. This equation cannot be solved analytically, so we must proceed by means of numerical methods. Notice that in the computation of instantons one can safely extend the integration over $\bar{z}$ in Eq. (4.12) over the whole set of real numbers.

Zero temperature

In this case, application of the 2D Fourier transform

$$\hat{u}(\omega,\theta) = \frac{1}{2\pi}\int_{\mathbf{R}^2} \mathrm{d}\bar{\tau}\,\mathrm{d}\bar{z}\; u(\bar{\tau},\bar{z})e^{i(\omega\bar{\tau}+\theta\bar{z})} \tag{4.15}$$

to Eq. (4.13) yields the equation

$$\begin{aligned}\hat{u}(\omega,\theta) = {} & \frac{1}{\omega^2+\theta^2+\sqrt{2}|\omega|\eta/\rho_{\mathrm{G}}+2-3u_0^2(h)}\Bigg[\frac{3u_0(h)}{2\pi} \\ & \times\int_{\mathbf{R}^2}\mathrm{d}\omega_1\,\mathrm{d}\theta_1\hat{u}(\omega_1,\theta_1)\hat{u}(\omega-\omega_1,\theta-\theta_1)+\frac{1}{(2\pi)^2}\times \\ & \int_{\mathbf{R}^4}\mathrm{d}^2\vec{\omega}\,\mathrm{d}^2\vec{\theta}\;\hat{u}(\omega_2,\theta_2)\hat{u}(\omega_1-\omega_2,\theta_1-\theta_2)\hat{u}(\omega-\omega_1,\theta-\theta_1)\Bigg],\end{aligned} \tag{4.16}$$

which is an integral equation for $\hat{u}$. The depinning exponent (4.12) in the Fourier space becomes

$$\begin{aligned}B(T=0,h) = {} & \frac{\rho_{\mathrm{G}}\sqrt{\kappa\lambda}}{2\hbar\beta}\Bigg\{\int_{\mathbf{R}^2}\mathrm{d}\omega\,\mathrm{d}\theta\;\hat{u}(\omega,\theta)\hat{u}(-\omega,-\theta)\times \\ & \left[\left(1-\frac{3}{2}u_0^2(h)\right)+\frac{\omega^2+\theta^2}{2}+\frac{|\omega|}{\sqrt{2}}\frac{\eta}{\rho_{\mathrm{G}}}\right]-\frac{u_0(h)}{2\pi}\int_{\mathbf{R}^4}\mathrm{d}^2\vec{\omega}\,\mathrm{d}^2\vec{\theta} \\ & \hat{u}(\omega_1,\theta_1)\hat{u}(\omega_2,\theta_2)\hat{u}(-\omega_1-\omega_2,-\theta_1-\theta_2)-\frac{1}{(4\pi)^2}\int_{\mathbf{R}^6}\mathrm{d}^3\vec{\omega}\,\mathrm{d}^3\vec{\theta} \\ & \hat{u}(\omega_1,\theta_1)\hat{u}(\omega_2,\theta_2)\hat{u}(\omega_3,\theta_3)\hat{u}(-\omega_1-\omega_2-\omega_3,-\theta_1-\theta_2-\theta_3)\Bigg\}.\end{aligned} \tag{4.17}$$

The zero-temperature instanton is computed using an algorithm that is a field-theory extension of the algorithm introduced in Refs. [64], [65] for the problem of dissipative quantum tunneling of a particle. To begin with, one introduces the operator

$$O(\lambda,\alpha,\hat{u}(\omega,\theta),h)=\frac{1}{\omega^2+\theta^2+\sqrt{2}|\omega|\eta/\rho_{\mathrm{G}}+2-3u_0^2(h)} \times\left(\lambda\int_{\mathbf{R}^2}\mathrm{d}\omega_1\,\mathrm{d}\theta_1\hat{u}(\omega_1,\theta_1)\hat{u}(\omega-\omega_1,\theta-\theta_1)+ \alpha\int_{\mathbf{R}^4}\mathrm{d}^2\vec{\omega}\,\mathrm{d}^2\vec{\theta}\;\hat{u}(\omega_2,\theta_2)\hat{u}(\omega_1-\omega_2,\theta_1-\theta_2)\hat{u}(\omega-\omega_1,\theta-\theta_1)\right), \tag{4.18}$$

which generalizes the integral operator from Eq. (4.16). Notice that the equation of motion for the instanton in the Fourier space becomes $\hat{u}(\omega,\theta)=O(3u_0(h)/2\pi,1/(2\pi)^2, \hat{u}(\omega,\theta),h)$. Secondly, it is important to point out the *scaling property* of this operator because it will be used in the computation of Eq. (4.17): Given any triplet $(\lambda_0,\alpha_0,\hat{u}_0(\omega,\theta))$ satisfying the identity (4.16), so will any other triplet $(\lambda_1,\alpha_1,\hat{u}_1(\omega,\theta))$ provided that

$$\hat{u}_1(\omega,\theta)=\chi\hat{u}_0(\omega,\theta) \tag{4.19}$$
$$\lambda_1=\lambda_0/\chi \tag{4.20}$$
$$\alpha_1=\alpha_0/\chi^2, \tag{4.21}$$

where χ is a constant. This means that if a solution $(\lambda_1,\alpha_1,\hat{u}_1(\omega,\theta))$ can be found for arbitrary parameters (λ_1,α_1), then one can obtain the solution corresponding to the pair (λ_0,α_0) simply by rescaling $\hat{u}_1(\omega,\theta)$ by a factor $\chi=\lambda_1/\lambda_0$ as long as $(\lambda_1/\lambda_0)^2=\alpha_1/\alpha_0$ is verified.

The algorithm consists of the following steps:

1. Start with an initial $(\lambda_0,\alpha_0,\hat{u}_0(\omega,\theta))$.
2. Let $\hat{u}_1(\omega,\theta)=O(\lambda_0,\alpha_0,\hat{u}_0(\omega,\theta),h)$.
3. Calculate $\lambda_1=\lambda_0/\chi^2,\alpha_1=\alpha_0/\chi^3$, where $\chi=\hat{u}_1(\vec{0})/\hat{u}_0(\vec{0})$.
4. Find $\hat{u}_2(\omega,\theta)=O(\lambda_1,\alpha_1,\hat{u}_1(\omega,\theta),h)$.
5. Repeat steps (2)-(4) until the successive difference satisfies a preset convergence criterion.

The output is the triplet $(\lambda_n,\alpha_n,\hat{u}_n(\omega,\theta))$. The final step consists of rescaling $\hat{u}_n$ to obtain the solution corresponding to the pair $(\lambda,\alpha)=(3u_0(h)/2\pi,1/(2\pi)^2)$: The rescaling rules of the λ- and α- terms of Eq. (4.16) are different according to the scaling property. Therefore, to obtain an accurate approximation of the instanton solution one has to split $\hat{u}(\omega,\theta)$ into the sum of two functions $\hat{u}_1(\omega,\theta)$

and $\hat{u}_2(\omega, \theta)$ in the above algorithm, and calculate their next iteration by means of the λ-term and the α-term of the operator (4.18), respectively. Finally, one rescales $\hat{u}_{1,n}$ by a factor $2\pi\lambda_n/3u_0(h)$ and $\hat{u}_{2,n}$ by a factor $2\pi\sqrt{\alpha_n}$. The depinning rate is calculated by evaluation of Eq. (4.17) at this solution.

Non-zero temperature

Because of the thermon solution being periodic in $\bar{\tau}$ —with period Ω— at $T \neq 0$, a solution of the form

$$u(\bar{\tau}, \bar{z}) = \sum_{n\in\mathbf{Z}} u_n(\bar{z}) e^{-i\omega_n \bar{\tau}} \tag{4.22}$$

is considered, where $\omega_n = \dfrac{2\pi n}{\Omega}$ for all $n \in \mathbf{Z}$. Introducing this functional dependence into Eq. (4.13) and applying a 1D Fourier transform leads to the equation

$$\begin{aligned} \hat{u}_n(\theta) = {} & \frac{1}{\omega_n^2 + \theta^2 + \sqrt{2}|\omega_n|\eta/\rho_\mathrm{G} + 2 - 3u_0^2(h)} \times \\ & \left[\frac{3u_0(h)}{\sqrt{2\pi}} \sum_{p\in\mathbf{Z}} \int_{\mathbf{R}} \mathrm{d}\theta_1 \hat{u}_p(\theta_1)\hat{u}_{n-p}(\theta - \theta_1) + \right. \\ & \left. \frac{1}{2\pi} \sum_{p,q\in\mathbf{Z}} \int_{\mathbf{R}^2} \mathrm{d}^2\vec{\theta}\; \hat{u}_p(\theta_2)\hat{u}_q(\theta_1 - \theta_2)\hat{u}_{n-p-q}(\theta - \theta_1) \right], \end{aligned} \tag{4.23}$$

which is an integral equation for the set $\{\hat{u}_n\}_{n\in\mathbf{Z}}$ of Fourier coefficients. The depinning exponent (4.12) in the Fourier space becomes

$$\begin{aligned} B(T > 0, h) = {} & \frac{\rho_\mathrm{G}\sqrt{\kappa\lambda}}{2\hbar\beta} \left\{ \sum_{n\in\mathbf{Z}} \int_{\mathbf{R}} \mathrm{d}\theta\; \hat{u}_n(\theta)\hat{u}_{-n}(-\theta) \times \right. \\ & \left[\left(1 - \frac{3}{2}u_0^2(h)\right) + \frac{\omega_n^2 + \theta^2}{2} + \frac{|\omega_n|}{\sqrt{2}}\frac{\eta}{\rho_\mathrm{G}} \right] - \frac{u_0(h)}{\sqrt{2\pi}} \sum_{n,m\in\mathbf{Z}} \int_{\mathbf{R}^2} \mathrm{d}^2\vec{\theta} \\ & \hat{u}_n(\theta_1)\hat{u}_m(\theta_2)\hat{u}_{-n-m}(-\theta_1 - \theta_2) - \frac{1}{8\pi} \sum_{n,m,l\in\mathbf{Z}} \int_{\mathbf{R}^3} \mathrm{d}^3\vec{\theta} \\ & \left. \hat{u}_n(\theta_1)\hat{u}_m(\theta_2)\hat{u}_l(\theta_3)\hat{u}_{-n-m-l}(-\theta_1 - \theta_2 - \theta_3) \right\} \Omega. \end{aligned} \tag{4.24}$$

The numerical algorithm is analogous to that used in the zero-temperature case, but with account of the rescaling of $\{\hat{u}_p^1\}_{p\in\mathbf{Z}}$ and $\{\hat{u}_p^2\}_{p\in\mathbf{Z}}$ by factors $\sqrt{2\pi}\lambda_n/3u_0(h)$ and $\sqrt{2\pi\alpha_n}$, respectively, in the last step of the calculations.

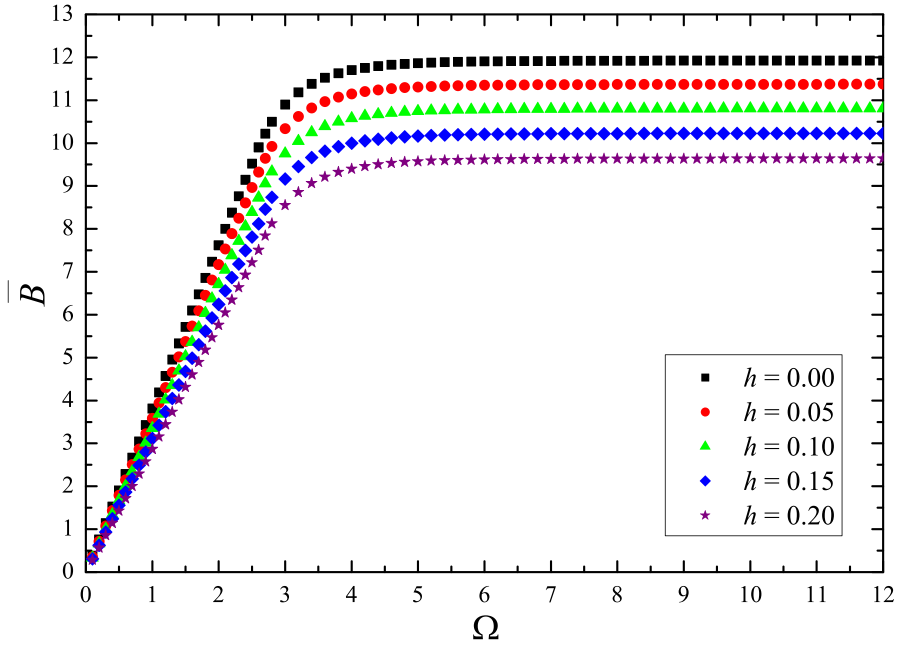

Figure 4.9: Temperature dependence of the depinning rate: Normalized action $\dfrac{2\hbar\beta}{\rho_{\rm G}\sqrt{\kappa\lambda}}B(T)$ vs. Ω at different values of the parameter h.

Figure 4.9 shows the normalized action $\bar{B}(T) = \dfrac{2\hbar\beta}{\rho_{\mathrm{G}}\sqrt{\kappa\lambda}} B(T)$ as a function of Ω at different values of the parameter h. In the simulations the standard value $\alpha_{\mathrm{LLG}} = 0.008$ for bulk Py has been taken [96].

4.2.3 Crossover temperature

The crossover temperature determines the transition from thermal to quantum tunneling regimes in the relaxation processes. It can be computed by means of theory of phase transitions [56, 58, 66]: Above T_c, the instanton solution minimizing Eq. (4.12) is a $\bar{\tau}$-independent function $u(\bar{\tau}, \bar{z}, h) = \bar{u}_0(\bar{z}, h)$, whereas just below T_c the instanton solution can be split into the sum of $\bar{u}_0$ and a small perturbation depending on $\bar{\tau}$,

$$u(\bar{\tau}, \bar{z}, h) = \bar{u}_0(\bar{z}, h) + \bar{u}_1(\bar{z}, h) \cos\left(\frac{2\pi}{\Omega}\bar{\tau}\right). \tag{4.25}$$

The depinning exponent (4.12) is proportional to

$$\int_{\mathbf{R}} \mathrm{d}\bar{z}\ \Phi(\bar{z}; \bar{u}_1, \bar{u}_1'), \tag{4.26}$$

where Φ is the spatial action density. Introducing the expansion (4.25) into Eq. (4.12) one obtains the following expansion for the above functional:

$$\Phi(\bar{z}; \bar{u}_1, \bar{u}_1') = \left[\frac{1}{2}(\bar{u}_0')^2 + V(\bar{u}_0, h)\right] \Omega\ + \frac{\Omega}{4}(\bar{u}_1')^2 + \Lambda \bar{u}_1^2 + O(4), \tag{4.27}$$

with

$$\Lambda = \frac{\Omega}{4} V''(\bar{u}_0, h) + \frac{\pi^2}{\Omega} + \frac{\pi}{\sqrt{2}} \frac{\eta}{\rho_{\mathrm{G}}}. \tag{4.28}$$

If $\Lambda > 0$ the only pair $(\bar{u}_1, \bar{u}_1')$ minimizing Φ is $\bar{u}_1 \equiv 0$. The crosover temperature is then defined by the equation $\min_{\bar{z}\in\mathbf{R}} \Lambda = 0$, that is

$$\frac{\Omega_{\mathrm{c}}}{4} \min_{\bar{z}\in\mathbf{R}} V''(\bar{u}_0, h) + \frac{\pi^2}{\Omega_{\mathrm{c}}} + \frac{\pi}{\sqrt{2}} \frac{\eta}{\rho_{\mathrm{G}}} = 0. \tag{4.29}$$

The equation of motion for a $\bar{\tau}$-independent instanton is

$$\bar{u}_0'' - [2 - 3u_0^2(h)]\bar{u}_0 + 3u_0(h)\bar{u}_0^2 + \bar{u}_0^3 = 0 \tag{4.30}$$

with boundary conditions: $\bar{u}_0 \to 0$ at $|\bar{z}| \to \infty$ and $\bar{u}_0(0,h) = -2u_0(h) + \sqrt{4-2u_0^2(h)} \equiv w(h)$, which is the width of the potential. Hence,

$$\begin{aligned}\min_{\bar{z}\in\mathbf{R}} V''(\bar{u}_0(\bar{z},h),h) &= \min_{\bar{u}_0\in[0,w(h)]} V''(\bar{u}_0,h) = \\ &\min_{\bar{u}_0\in[0,w(h)]} \left\{[2-3u_0^2(h)] - 6u_0(h)\bar{u}_0 - 3\bar{u}_0^2\right\} = \\ &-10 + 3u_0^2(h) + 6u_0(h)\sqrt{f(h)}\end{aligned} \tag{4.31}$$

with $f(h) = 4 - 2u_0^2(h)$. Solution of the quadratic equation for T_c given by Eq. (4.29) yields the following expression for the crossover temperature:

$$T_\mathrm{c}(h) = \frac{\hbar\kappa}{4\pi k_\mathrm{B}\rho_\mathrm{G}}\left[\sqrt{8+3f(h)-12u_0(h)\sqrt{f(h)}+\frac{\eta^2}{\rho_\mathrm{G}^2}} - \frac{\eta}{\rho_\mathrm{G}}\right]. \tag{4.32}$$

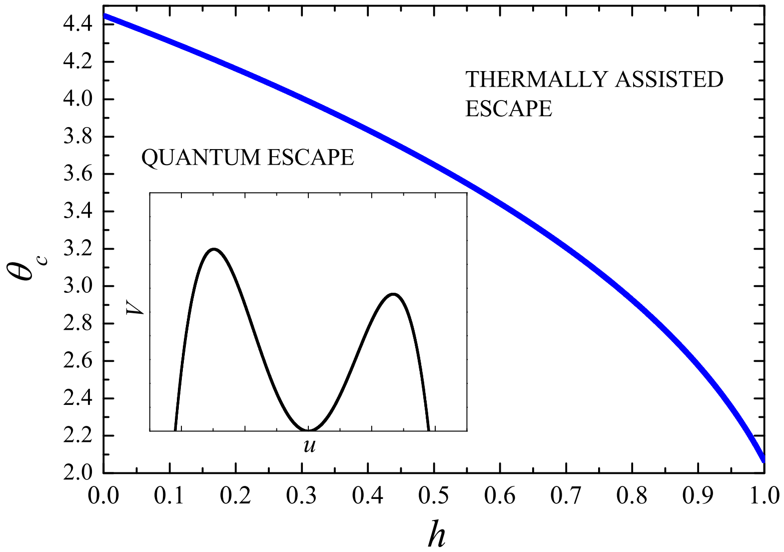

Figure 4.10: Magnetic field dependence of the dimensionless crossover temperature $\theta_\mathrm{c} = \dfrac{4\pi k_\mathrm{B}\rho_\mathrm{G}}{\hbar\kappa} T_c$. (Inset) Sketch of the potential $V(u, h = 0.1)$.

Figure 4.10 shows the dependence of the dimensionless crossover temperature $\theta_\mathrm{c} = \dfrac{4\pi k_\mathrm{B}\rho_\mathrm{G}}{\hbar\kappa} T_c$ on the generalized magnetic field h.

4.2.4 Discussion

Given any value of the generalized field h, two regimes in the dependence of the normalized action on Ω are clearly distinguished in Fig. 4.9: A linear regime is found below $\Omega_c(h)$, whereas the normalized action tends to a constant value above the crossover imaginary-time period. Notice that the transition from the linear to the plateau regime is smooth —that is, of second-order type. Above the crossover temperature the depinning rate becomes

$$B(T > T_c, h) = \frac{\rho_G\sqrt{\lambda\kappa}}{2\hbar\beta}\int d\bar{z}\left[\frac{1}{2}(\bar{u}_0')^2 + V(\bar{u}_0, h)\right]\Omega \qquad (4.33)$$

with $\bar{u}_0$ being the $\bar{\tau}$-independent instanton. By means of Eq. (4.30) this expression can be rewritten as [32]

$$B(T > T_c, h) = \frac{\rho_G\sqrt{\lambda\kappa}}{2\hbar\beta}\left[2\sqrt{2}\int_0^{w(h)} d\bar{u}_0\sqrt{V(\bar{u}_0, h)}\right]\Omega \qquad (4.34)$$

and, therefore, the slope of the normalized action $\bar{B}(\Omega)$ is equal to $2\sqrt{2}\times \int_0^{w(h)} d\bar{u}_0\sqrt{V(\bar{u}_0, h)}$ in the linear regime, which can be evaluated analytically. At all values of the generalized field h, the numerical slope calculated from Fig. 4.9 coincides with that calculated analytically within the numerical error of the simulations. This is indicative of the robustness of the algorithm presented here.

Quantum effects reported in Sec. 4.1 can be interpreted as being plausibly due to the depinning from line defects present in the disk. The size of the defects needs to exceed the nucleation length in order to pin the VC, but not to be as long as the thickness of the disk. Pinning of extended parts of the VC line by line defects would be justified by the fact that linear defects provide the strongest pinning so that the VC line, or at least some segments, would naturally fall into such traps. Thus, the present model can be test out on the experimental results obtained in Sec 4.1. The crossover temperature is relevant to the roughness of the fine-scale potential landscape due to linear defects at the bottom of the potential well created by the external and dipolar fields. Above T_c vortices diffuse in this potential by thermal activation, whereas below T_c they diffuse by quantum tunneling. This must determine the temperature dependence (independence) of the magnetic viscosity. T_c is, therefore, the measure of the fine-scale barriers due to linear defects. It can be measured experimentally and help to extract the width of the pinning potential.

Notice that the depinning rate should not exceed $30 - 40$ in order for the tunneling to occur on a reasonable time scale. Estimates of the model parameters (κ, β) are obtained by fitting the model to experimental data. Considering the experimental values $A = 1.3 \cdot 10^{-11}$ J/m and $M_S = 7.5 \cdot 10^5$ A/m for permalloy, fitting Eq. (4.32) and Eq. (4.17) to the values $T_c \sim 6$ K (see Fig. 4.6) and $B(T = 0, h = 0) \sim 30$, respectively, at zero field leads to the estimates

$$\kappa \sim 5.9 \cdot 10^7 \text{ J/m}^3, \qquad \beta \sim 6.9 \cdot 10^{27} \text{ J/m}^5. \qquad (4.35)$$

The width of the quartic potential can be found via the expression $w = \sqrt{2\kappa/\beta} \sim 0.13$ nm. This value is compatible with the width of the potential provided by a linear dislocation.

In conclusion, non-thermal dynamics of magnetic vortices in micron-size Py disks has been observed. It is attributed to the quantum escape of the VC line from a line defect in these disks. Experimental results let one conclude that the depinning process occurs in steps about 0.13 nm, which corresponds to the width of the energy potential.

Chapter 5

Josephson junction with a magnetic vortex

5.1 Introduction

A junction of two superconductors coupled via a weak link is known as a *Josephson junction*, where the link consists of a thin non-superconducting layer —insulating barrier, normal metal or ferromagnet. It exhibits the Josephson effect, a macroscopic quantum phenomenon consisting of the flow of supercurrent across the junction even in the absence of applied voltage. This is due to the tunneling of Cooper pairs through the energy barrier provided by the weak link separating both superconductors.

The first experimental observations of the (DC) Josephson effect were performed in 1960 by H. Meissner [132], J. Nicol *et al.* [133] and I. Giaever [134], even though it was attributed to the direct conduction of electrons through metallic shorts in the insulating layer. At that time, quasiparticle —electrons and holes— tunneling through an insulating barrier was widely known both theoretically and experimentally. On the contrary, underbarrier quantum tunneling of Cooper pairs was believed to occur with such low probability that it was unobservable for practical purposes.

The concept of symmetry breaking inherent in superconductivity [see Sec. 1.2.2] led B. Josephson to conclude that the phase difference between both superconductors, Φ_{21}, could be detected in case they exchange electrons —on the contrary, global superconducting phases cannot be observed experimentally. Furthermore, the total current flowing across a Josephson junction must depend explicitly on this phase difference. Josephson extended the calculation of the tunneling current across a superconductor-insulator-normal metal (S/I/N) junction by M. Cohen and coworkers [135] to the case of a Josephson junction with an insulating layer, obtaining the following expression for the total current [136]:

$$\begin{aligned} I(V) &= I_{\mathrm{qp}}(V) + I_{\mathrm{pair}}(V), \\ I_{\mathrm{pair}}(V) &= I_1(V)\cos(\Phi_{21}) + I_2(V)\sin(\Phi_{21}), \end{aligned} \tag{5.1}$$

where $I_{\mathrm{qp}}(V)$ and $I_{\mathrm{pair}}(V)$ represent the quasiparticle and pair tunneling currents, respectively. $I_2(V)$ is an even function of the applied voltage and does not vanish as $V \to 0$, whereas $I_{\mathrm{qp}}(0) = I_1(0) = 0$. Therefore, at zero voltage a non-zero current flows across the junction stemming from the tunneling of Cooper pairs. It is referred to as the Josephson supercurrent, $I_{\mathrm{J}}(V) = I_2(V)\sin(\Phi_{21})$. Giaever's heuristic formula for the tunneling current [134] corresponds to the quasiparticle tunneling current in Josephson's derivation. Notice that the Josephson current is of the same order of magnitude as the quasiparticle tunneling current, which contradicts the previous belief that the contribution of Cooper pairs to the tunneling current could be ignored. In fact, at zero temperature one has $I_2(T=0) = \dfrac{\pi\Delta(0)}{2eR_{\mathrm{N}}}$, with $\Delta(0)$ being the superconducting gap at such temperature and R_{N} being the normal-state junction resistance. Hence $I_1(T=0)/I_{\mathrm{qp}}(2\Delta(0)/e) = \pi/4$, where the quasiparticle current has been evaluated at the sum-gap voltage $2\Delta(0)/e$.

Experimental confirmation of the Josephson effect was provided by P. Anderson and J. Rowell in their study of low-resistance Josephson junctions [137]. In particular, these authors observed that the critical supercurrent was sensitive to magnetic fields and that the corresponding field dependence was in agreement with Josephson's predictions [137, 138], namely the critical supercurrent is reduced to a minimum whenever the junction contains integer multiples of the flux quantum Φ_0.

Josephson junctions play a crucial role in the design of quantum circuits for high-sensitive probing. Some remarkable examples are 1) the SQUID magnetometer, which consists of two Josephson junctions connected in parallel by superconducting leads forming a loop and achieves a field sensitivity of about 10^{-15} T; 2) The superconducting low-inductance undulatory galvanometer (SLUG) [139], consisting of an oxidized niobium wire completely surrounded by a blob of lead-tin solder and showing a sensitivity of 10^{-14} V with a time constant of 1 s; and 3) rapid single flux quantum (RSFQ) digital electronics to name a few.

The Josephson supercurrent can be formally derived within the framework of the Ginzburg-Landau theory for a superconductor-normal-superconductor (S/N/S) junction. The supercurrent density is given by Eq. (1.8):

$$\vec{j}(\vec{r}) = \frac{e^\star}{2m^\star}\left\{\bar{\psi}\Big[-i\hbar\nabla - \frac{e^\star}{c}\vec{A}\Big]\psi + \psi\Big[i\hbar\nabla - \frac{e^\star}{c}\vec{A}\Big]\bar{\psi}\right\}, \tag{5.2}$$

where $e^\star = -2e$ and $m^\star = 2m_e$ are the charge and the mass of the Cooper pair, respectively. Setting the frame of axes so that the interface of the Josephson junction goes along the XY plane at $z = 0$, the supercurrent flowing across is given by the Z component of the above equation, j_z. The most general boundary conditions for this kind of junction are given by the set of equations [6]

$$\Big[-i\hbar\frac{\partial\psi_1}{\partial z} - \frac{e^\star}{c}A_z\psi_1\Big](0-) = -i\hbar\frac{\psi_2}{\lambda_\mathrm{J}}(0+), \tag{5.3}$$

$$\Big[-i\hbar\frac{\partial\psi_2}{\partial z} - \frac{e^\star}{c}A_z\psi_2\Big](0+) = i\hbar\frac{\psi_1}{\lambda_\mathrm{J}}(0-), \tag{5.4}$$

with $\lambda_\mathrm{J} \in \mathbf{R}$ being the property of the junction. Label 1 (2) is set to refer to the superconducting region on the $z < 0$ ($z > 0$) side of the interface. An underlying consequence of these boundary conditions is that the supercurrent (5.2) is continuous across the junction, that is $j_z|_1(0-) = j_z|_2(0+)$. Introducing Eq. (5.3) and its complex conjugate into the Z component of Eq. (5.2) one obtains

$$j_z|_1(0-) = \left(\frac{-i\hbar e^\star}{2m^\star\lambda_\mathrm{J}}\right) 2i\,\mathrm{Im}\Big\{\bar{\psi}_1(0-)\psi_2(0+)\Big\} = j_m \sin\left(\Phi_{21}\right), \tag{5.5}$$

where $j_m = \dfrac{\hbar|e^\star|}{m^\star\lambda_\mathrm{J}}|\psi_1(0-)||\psi_2(0+)|$ is the maximum current density carried by the junction, $\Phi_{21} = \Phi_1 - \Phi_2$ is the phase difference between the two superconducting regions, and the polar form of the superconducting wave functions, $\Psi = |\Psi|e^{i\Phi}$, has been taken into account. This equation is known as the *current-phase relation* of the Josephson junction. If the coupling between the superconducting regions is weak, the moduli $|\psi_1(0-)|$ and $|\psi_2(0+)|$ differ slightly from the corresponding equilibrium bulk values.

The superconducting wave function $\psi(\vec{r})$ and the vector potential $\vec{A}(\vec{r})$ —describing a certain magnetic field— are modified according to Eqs. (1.14) under a gauge transformation, from which the following *gauge-invariant phase relation* can be derived:

$$\nabla\Phi - \frac{e^\star}{\hbar c}\vec{A} = 0. \tag{5.6}$$

Integration of this relation over the path {superconducting region 2 → superconducting region 1} leads to

$$\begin{aligned}\Phi_{21} &= \left[\Phi_1^0(0-) - \Phi_2^0(0+)\right] - \frac{|e^\star|}{\hbar c}\int_2^1 \vec{A}\cdot \mathrm{d}\vec{l} \\ &= \Phi_{21}^0 + \frac{2\pi}{\Phi_0}\int_1^2 \vec{A}\cdot \mathrm{d}\vec{l},\end{aligned} \tag{5.7}$$

where $\Phi_0 = hc/2e$ is the flux quantum and $\Phi_{21}^0 = \Phi_1^0(0-) - \Phi_2^0(0+)$ is the intrinsic phase difference between both superconductors.

Josephson tunneling through uniformly magnetized ferromagnetic layers has been intensively studied in the past [140]. In this chapter one is interested in the Josephson effect in the case when a ferromagnetic layer contains a vortex of the magnetization field. The interest in this problem is two-fold. Firstly, micron-size disks of soft ferromagnetic materials naturally form a vortex ground state due to magnetic dipolar interactions. The variety of spatial dimensions of such disks [see Sec. 3.1] ideally suites typical parameters of Josephson junctions, with the disks' thickness range being comparable to the values of the coherence-length of conventional superconductors.

Secondly, recent macroscopic evidence of quantum diffusion of vortices in the array of submicron and micron-size magnetic disks [see Sec. 4.1] raises question whether an individual vortex tunneling event can be observed by measuring the change in the tunneling current through the disk. The problem of quantum tunneling of the VC out of the potential well created by the pinning potential was discussed in Sec. 4.2.4. It was found that the low-temperature quantum diffusion of the VC occurs via steps of a few interatomic distances. Thermal diffusion at elevated temperatures may involve longer steps. Theoretical picture of macroscopic relaxational dynamics of vortices in the array of micron-size Py disks agreed with experiment. In this chapter one is asking the question whether the displacement of the VC by a few nanometers, or by a fraction of a nanometer, can be detected via measurement of the tunneling current through a Josephson junction that is made of a magnetic disk in the vortex state.

5.2 Formulation of the problem

A ferromagnetic Josephson junction (S/F/S), where the F-layer consists of a circularly polarized magnetic disk, is considered. This essentially non-uniform ground state is characterized by the curling of the magnetization in the plane of the disk and by the existence of the vortex that sticks out of the disk and carries small uncompensated magnetic moment, see Fig. 5.1.

Notice that, in general, ferromagnetism weakens the superconductivity at the S/F boundary due to the proximity effect. It disappears if the ferromagnetic and superconducting surfaces are separated by a thin non-magnetic insulating layer, leaving only electromagnetic interaction of the Josephson junction with the ferromagnet, which is the case studied here. For a S/F/S junction the maximum current j_m depends strongly on the magnetic properties of the ferromagnetic layer [140]. In the case of a circularly polarized magnetic disk, the curling of the magnetization provides a net zero in-plane magnetization for a centered vortex and the out-of-plane component of the magnetization due to the VC is very small —can be ignored. Moderate displacements of the VC from the center of the disk induce a

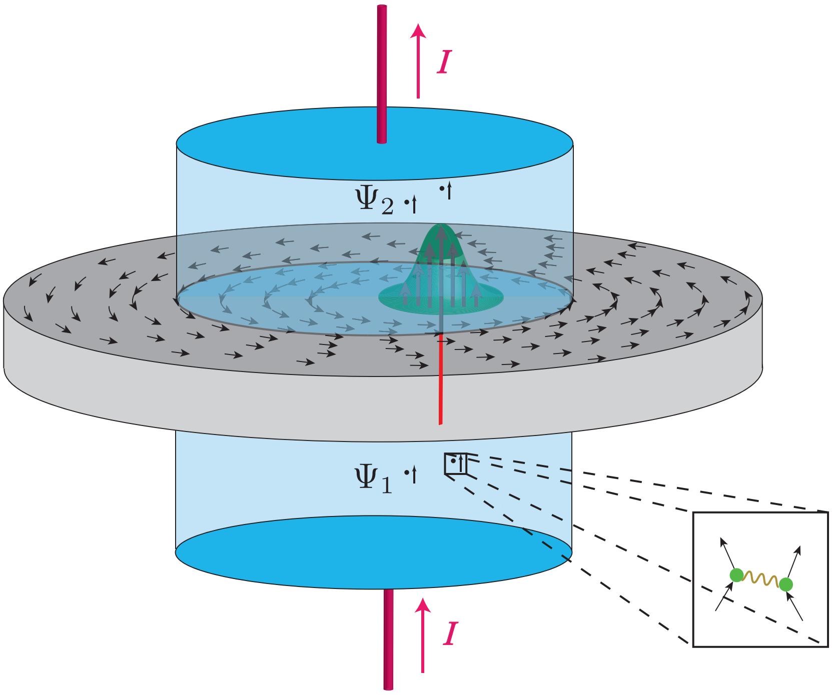

Figure 5.1: Josephson current through a circularly polarized magnetic disk.

total in-plane magnetic moment linear with it . Therefore, the current j_m is only slightly affected by the motion of the VC in the regime of tiny displacements and, from this point forward, it will be considered to be approximately constant. This means that the main effect of the magnetic vortex on the Josephson current occurs via the superconducting phase difference.

Under the practical condition that the lateral size of the junction is smaller than the radius of the disk, but much greater than the diameter of the nanoscale VC, the Josephson current through the junction can be calculated rigorously. It is dominated by the configuration of the magnetization in the disk that depends on the position of the VC. The latter can be displaced by the external magnetic field parallel to the disk. The VC can also exhibit circular motion that corresponds to a collective gyroscopic mode of the disk. It can also move spontaneously via thermal or quantum diffusion in the presence of weak pinning. The present aim is to find out whether the tiny movements of the vortex core can be detected by measuring the Josephson current.

Let (L, R) be respectively the thickness and the radius of the ferromagnetic disk. Again, the coordinate frame is set according to the symmetry of the system: The XY plane coincides with the plane of the disk and the Z axis coincides with the symmetry axis of the disk. The S/F boundaries are located at $z = \pm L/2$. According to the geometry of the system, the path integral in Eq. (5.7) must be performed along the Z axis between $z = -L/2$ (superconducting region 1/ferromagnet boundary) and $z = L/2$ (ferromagnet/superconducting region 2 boundary). Therefore, the gauge-invariant phase relation becomes

$$\Phi_{21} = \Phi_{21}^{(0)} + \frac{2\pi}{\Phi_0} \int_{-\frac{L}{2}}^{\frac{L}{2}} A_z(\vec{r})\,\mathrm{d}z, \tag{5.8}$$

where A_z is the projection of the vector potential onto the Z-axis. Notice that the vector potential $\vec{A}$ is determined by the magnetization field $\vec{M}$ within the volume V of the disk,

$$\vec{A}(\vec{r}) = \int_V \frac{\nabla' \times \vec{M}(\vec{r}\,')}{|\vec{r} - \vec{r}\,'|}\,\mathrm{d}^3\vec{r}\,' + \oint_{\partial V} \frac{\vec{M}(\vec{r}\,') \times \vec{n}'}{|\vec{r} - \vec{r}\,'|}\,\mathrm{d}^2 S'. \tag{5.9}$$

Here $\vec{n}'$ is the vector normal to the surface of the disk.

5.3 Computation of the phase difference

The magnetization field in the disk can be described by the fixed-length vector [see Eq. (3.24)]

$$\begin{aligned} \vec{M}(\Theta, \Phi) &= M_S(\cos\Phi \sin\Theta, \sin\Phi \sin\Theta, \cos\Theta) \\ &= M_S(\sqrt{1 - m^2}\cos\Phi, \sqrt{1 - m^2}\sin\Phi, m), \end{aligned} \tag{5.10}$$

where M_S is the saturation magnetization of the ferromagnetic material and $m = \cos\Theta$ is the projection of the normalized magnetic moment onto the Z axis. Let $\vec{X}_v(t, z) = \big(x_v(t, z), y_v(t, z)\big)$ be the coordinates of the center of the VC in the XY plane. Rigidity of the vortex structure is assumed, which translates into the VC coordinates being independent of the z variable. One uses a quasi-static approximation in which no time dependence of the VC coordinates is considered, which is always valid for the slow motion of the vortex. Because of this, the coordinate axis in the XY plane can be rotated so that $\vec{X}_v = x_v \hat{e}_x$. Let (r, ϕ) be the polar coordinates in the XY plane. The static solution of the magnetization field is [see Eq. (3.25)]

$$\begin{aligned} \Phi_0(x, y) &= \tan^{-1}(y/x - x_v) + \phi_0, \\ \cos\Theta_0(\tilde{r}) &= \begin{cases} p\left(1 - C_1\left(\frac{\tilde{r}}{\Delta_0}\right)^2\right) & \tilde{r} \ll \Delta_0, \\ C_2\left(\frac{\Delta_0}{\tilde{r}}\right)^{1/2} \exp(-\tilde{r}/\Delta_0) & \tilde{r} \gg \Delta_0, \end{cases} \end{aligned}$$

where

- $\tilde{r} = ||\vec{r} - \vec{X}_v||_2$ is the radial distance from the VC center,
- $p = \pm 1$ is the polarization of the magnetization,
- $\phi_0 = \pm\pi/2$ corresponds to CCW/CW rotation of the magnetization,
- $\Delta_0 = \sqrt{A/M_S^2}$ is the exchange length of the material, and
- $C_1 = \frac{3}{7}$ and $C_2 = \frac{4}{7}pe$.

Introducing the vector basis for cylindrical coordinates,

$$\hat{e}_r = \cos\phi\hat{e}_x + \sin\phi\hat{e}_y, \quad \hat{e}_\phi = -\sin\phi\hat{e}_x + \cos\phi\hat{e}_y, \tag{5.11}$$

the magnetization field can be split into $\vec{M}(r,\phi,z) = M_r\hat{e}_r + M_\phi\hat{e}_\phi + M_z\hat{e}_z$, with

$$M_r = \hat{e}_r \cdot \vec{M} = M_S\sqrt{1 - m_0^2}\cos(\Phi_0 - \phi), \tag{5.12}$$

$$M_\phi = \hat{e}_\phi \cdot \vec{M} = M_S\sqrt{1 - m_0^2}\sin(\Phi_0 - \phi), \tag{5.13}$$

$$M_z = M_S m_0. \tag{5.14}$$

Let $\tilde{\phi}_v = \tan^{-1}(y/x - x_v)$. Then $(\tilde{r}, \tilde{\phi}_v)$ are the polar coordinates in the XY plane from the VC center. Figure 5.2 shows the geometrical relation between both systems of polar coordinates, from which the following identities are straightforwardly deduced:

$$\begin{aligned} &\tilde{r} = ||\vec{r} - \vec{X}(t,z)||_2 = \sqrt{r^2 + x_v^2 - 2rx_v\cos\phi}, \\ &\sin\tilde{\phi}_v = \frac{r}{\tilde{r}}\sin\phi, \quad \cos\tilde{\phi}_v = \frac{1}{\tilde{r}}(r\cos\phi - x_v). \end{aligned} \tag{5.15}$$

According to the above asymptotic dependences of the static solution one has

$$\sqrt{1 - m_0^2} \simeq \begin{cases} \sqrt{2C_1}\frac{\tilde{r}}{\Delta_0} & \tilde{r} \ll \Delta_0, \\ 1 & \tilde{r} \gg \Delta_0, \end{cases} \tag{5.16}$$

and

$$\sin\Phi_0 = C\cos\tilde{\phi}_v, \qquad \cos\Phi_0 = -C\sin\tilde{\phi}_v, \tag{5.17}$$

where $C = \sin\phi_0 = \pm 1$ represents the chirality of the magnetization field of the ground state.

In this chapter the limit $R \gg L, \Delta_0$ is considered. Being interested in the tiny displacements of the VC due to, e.g., quantum tunneling, one also shall assume that $|x_v| \ll \Delta_0$. This allows one to obtain a perturbative expansion of the phase difference across the junction in terms of powers of x_v.

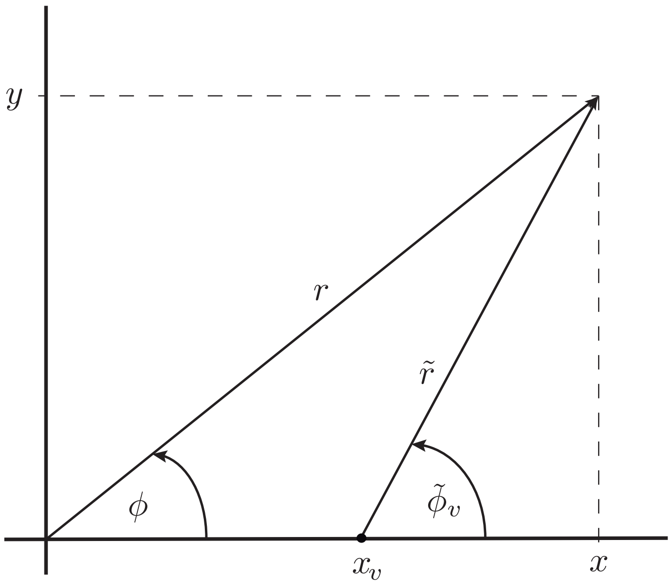

Figure 5.2: Relation between the systems of polar coordinates (r, ϕ) and $(\tilde{r}, \tilde{\phi}_v)$.

5.3.1 Surface contribution

The surface of the disk consists of three surfaces, $\partial V = S_1 \cup S_2 \cup S_3$, where S_1 and S_3 are respectively the top and the bottom surfaces of the disk, and S_2 is the lateral surface. The corresponding normal vectors are $\hat{n}_1 = -\hat{n}_3 = \hat{e}_z$ and $\hat{n}_2 = \hat{e}_r$. It is straightforward to prove the following identities:

$$\vec{M} \times \hat{n}|_{S_1} = -\vec{M} \times \hat{n}|_{S_3} = M_\phi \hat{e}_r - M_r \hat{e}_\phi, \tag{5.18}$$

$$\vec{M} \times \hat{n}|_{S_2} = M_z \hat{e}_\phi - M_\phi \hat{e}_z, \tag{5.19}$$

so that the surface contribution to A_z comes from integration over S_2. This means that

$$\begin{aligned} A_z(\vec{r})|_{\text{Surf}} &= \int_{S_2} \hat{e}_z \cdot \frac{\vec{M}(\vec{r}\,') \times \vec{n}'}{|\vec{r} - \vec{r}\,'|} \, \mathrm{d}^2 S' = \int_{S_2} r' \, \mathrm{d}\phi' \, \mathrm{d}z' \frac{-M_{\phi'}}{|\vec{r} - \vec{r}\,'|} = \\ &= R \int_{-\frac{L}{2}}^{\frac{L}{2}} \mathrm{d}z' \int_0^{2\pi} \mathrm{d}\phi' \frac{-M_{\phi'}}{|\vec{r} - \vec{r}\,'|} \bigg|_{S_2} . \end{aligned} \tag{5.20}$$

The Coulomb potential can be expanded in cylindrical coordinates as

$$\frac{1}{|\vec{r} - \vec{r}\,'|} = \int_0^\infty \mathrm{d}k \; J_0(kr^\star) e^{-k(z_> - z_<)}, \tag{5.21}$$

where $z_< = \min\{z, z'\}$, $z_> = \max\{z, z'\}$, $J_0(x)$ is the zero-order Bessel function of the first kind, and

$$r^\star = \sqrt{r^2 + r'^2 - 2rr'\cos(\phi - \phi')}. \tag{5.22}$$

If $z \neq z'$ one can switch to the integration over ϕ and k, which gives

$$\begin{aligned} \int_0^{2\pi} \mathrm{d}\phi'(-M_{\phi'}|_{S_2}) \int_0^\infty \mathrm{d}k\ J_0(kr^\star)|_{S_2} e^{-k(z_> - z_<)} = \\ \int_0^\infty \mathrm{d}k\ e^{-k(z_> - z_<)} \int_0^{2\pi} \mathrm{d}\phi' \left[-M_{\phi'} J_0(kr^\star)\right]\big|_{S_2}. \end{aligned} \tag{5.23}$$

By means of Eqs. (5.15), (5.16) and (5.17) the following asymptotic expressions for $M_{\phi'}$ are obtained:

$$M_{\phi'} \simeq \begin{cases} M_S \frac{C}{\Delta_0}\sqrt{2C_1}\,[r' - x_v\cos\phi'] & \tilde{r}' \ll \Delta_0, \\ \frac{M_S C}{\tilde{r}'}[r' - x_v\cos\phi'] & \tilde{r}' \gg \Delta_0. \end{cases} \tag{5.24}$$

Integration over surface S_2 corresponds to the asymptotic limit $\tilde{r}' \gg \Delta_0$, which leads to $r' \gg x_v$. Consequently, the following expansion of the Coulomb potential can be used:

$$\frac{1}{\tilde{r}'} \simeq \frac{1}{r'} + \frac{x_v\cos\phi'}{r'^2} \tag{5.25}$$

and, therefore, $M_{\phi'}|_{S_2} \simeq M_S C\,[1 + O((x_v/r')^2)]$.

Neumann's addition theorem for Bessel functions leads to the following expansion

$$J_0(kr^\star) = \sum_{m\geq 0} \epsilon_m J_m(kr) J_m(kr') \cos\left(m(\phi - \phi')\right), \tag{5.26}$$

where $\epsilon_0 = 1$ and $\epsilon_m = 2,\ m > 0$. With account of the orthogonality of the Fourier basis $\{1\} \cup \{\cos m\phi'\}_{m\in\mathbf{N}} \cup \{\sin m\phi'\}_{m\in\mathbf{N}}$ one obtains

$$\int_0^{2\pi} \mathrm{d}\phi' \left[-M_{\phi'} J_0(kr^\star)\right]\big|_{S_2} = -2\pi M_S C J_0(kr) J_0(kR) + O\left((x_v/R)^2\right). \tag{5.27}$$

On the other hand, one has the identity

$$\int_0^\infty \mathrm{d}k J_m(kr) J_m(kr') e^{-k(z_> - z_<)} = \frac{1}{\pi\sqrt{rr'}} Q_{m-\frac{1}{2}}\left[\frac{r^2 + r'^2 + (z - z')^2}{2rr'}\right], \tag{5.28}$$

where $Q_\lambda[z]$ is the Legendre function of second kind of the degree λ,

$$Q_\lambda[z] = \frac{\sqrt{\pi}}{2^{\lambda+1}} \frac{\Gamma(\lambda+1)}{\Gamma(\lambda+3/2)} \frac{1}{z^{\lambda+1}} {}_2F_1\left(\frac{\lambda+1}{2}, \frac{\lambda}{2}+1, \lambda+\frac{3}{2}; \frac{1}{z^2}\right), \tag{5.29}$$

with ${}_2F_1$ being the hypergeometric function. Consequently, Eqs. (5.21), (5.27) and (5.28) give

$$\begin{aligned}\int_0^{2\pi} \mathrm{d}\phi' \frac{-M_{\phi'}}{|\vec{r}-\vec{r}\,'|}\bigg|_{S_2} &= -\frac{2M_S C}{\sqrt{rR}} Q_{-\frac{1}{2}}\left[\frac{r^2+R^2+(z-z')^2}{2rR}\right] \\ &\quad + O\left((x_v/R)^2\right), \quad z \neq z'.\end{aligned} \tag{5.30}$$

The contribution of the ferromagnetic layer to the phase difference of the junction is given by the path integral [see Eq. (5.8)]

$$\Phi_{21}^F|_{\mathrm{Surf}} = \frac{2\pi R}{\Phi_0}\int_{-\frac{L}{2}}^{\frac{L}{2}} \mathrm{d}z \int_{-\frac{L}{2}}^{\frac{L}{2}} \mathrm{d}z' \int_0^{2\pi} \mathrm{d}\phi' \frac{-M_{\phi'}}{|\vec{r}-\vec{r}\,'|}\bigg|_{S_2}. \tag{5.31}$$

To deal with the singularity of the integrand when $\vec{r}\,'$ equals $\vec{r}$, one introduces the Cauchy principal value prescription to the integration over the z' variable, that is

$$\int_{-\frac{L}{2}}^{\frac{L}{2}} \mathrm{d}z' \Rightarrow \mathcal{P}\int_{-\frac{L}{2}}^{\frac{L}{2}} \mathrm{d}z' := \lim_{\epsilon\to 0+}\left\{\int_{-\frac{L}{2}}^{z-\epsilon} \mathrm{d}z' + \int_{z+\epsilon}^{\frac{L}{2}} \mathrm{d}z'\right\}. \tag{5.32}$$

With account of this prescription Eq. (5.23) can be always applied and so $\Phi_{21}^F|_{\mathrm{Surf}}$ becomes

$$\Phi_{21}^F|_{\mathrm{Surf}} = -\frac{4\pi M_S C}{\Phi_0}\sqrt{\frac{R}{r}}\int_{-\frac{L}{2}}^{\frac{L}{2}} \mathrm{d}z\, \mathcal{P}\int_{-\frac{L}{2}}^{\frac{L}{2}} \mathrm{d}z' Q_{-\frac{1}{2}}\left[\frac{r^2+R^2+(z-z')^2}{2rR}\right] + O(x_v^2). \tag{5.33}$$

5.3.2 Bulk contribution

The bulk contribution to the phase difference of the Josephson junction stems from the projection of the curl of the magnetization field onto the Z axis. That is,

$$\begin{aligned}A_z(\vec{r})|_{\mathrm{Bulk}} &= \int_V \frac{\hat{e}_z\cdot\left[\nabla'\times\vec{M}(\vec{r}\,')\right]}{|\vec{r}-\vec{r}\,'|}\mathrm{d}^3\vec{r}\,' \\ &= \int_{-\frac{L}{2}}^{\frac{L}{2}} \mathrm{d}z' \int_0^R \mathrm{d}r' \int_0^{2\pi} \mathrm{d}\phi' \frac{r'\left[\nabla'\times\vec{M}(\vec{r}\,')\right]}{|\vec{r}-\vec{r}\,'|}\cdot\hat{e}_z\end{aligned} \tag{5.34}$$

with the projection of $\nabla'\times\vec{M}(\vec{r}\,')$ onto the Z axis being

$$\hat{e}_z\cdot\left[\nabla'\times\vec{M}(\vec{r}\,')\right] = \frac{1}{r'}\left[\frac{\partial(r'M_{\phi'})}{\partial r'} - \frac{\partial M_{r'}}{\partial\phi'}\right]. \tag{5.35}$$

As in the previous subsection, with account of Eq. (5.21) for the cylindrical expansion of the Coulomb potential (if $z \neq z'$) one has

$$\begin{aligned}\int_0^{2\pi} \mathrm{d}\phi' \left[r'\hat{e}_z \cdot \left(\nabla' \times \vec{M}\right)\right] \int_0^{\infty} \mathrm{d}k\ J_0(kr^\star) e^{-k(z_> - z_<)} = \\ \int_0^{\infty} \mathrm{d}k\ e^{-k(z_> - z_<)} \int_0^{2\pi} \mathrm{d}\phi' J_0(kr^\star) \left[r'\hat{e}_z \cdot \left(\nabla' \times \vec{M}\right)\right].\end{aligned} \tag{5.36}$$

Let $\bar{z}^{(\prime)} = z^{(\prime)}/\Delta_0$ and $\rho^{(\prime)} = r^{(\prime)}/\Delta_0$ be the set of normalized spatial coordinates. With account of the normalized versions of Eqs. (5.15), (5.16), (5.17), (5.25), and of the approximation $\tilde{\rho}' \simeq \rho'$ in the asymptotic regime $\tilde{\rho}' \ll 1$, one has the following asymptotic expressions:

$$\hat{e}_z \cdot \left(\nabla' \times \vec{M}\right) \simeq \frac{M_S C \sqrt{2C_1}}{\Delta_0} \left[(2 - C_1\rho'^2) - 2\frac{x_v}{\Delta_0 \rho'}(2 - C_1\rho'^2) \cos\phi'\right] \tag{5.37}$$

for $\tilde{\rho}' \ll 1$, and

$$\hat{e}_z \cdot \left(\nabla' \times \vec{M}\right) \simeq \frac{M_S C}{\Delta_0 \rho'} \left[1 + \frac{x_v}{\Delta_0 \rho'} \cos\phi'\right] \tag{5.38}$$

in the asymptotic regime $\tilde{\rho}' \gg 1$.

Again, in the case of $z \neq z'$, the addition theorem (5.26), the orthogonality of the Fourier basis and the identity (5.28) lead to the following asymptotic expressions:

$$\begin{aligned}\int_0^{2\pi} \mathrm{d}\phi' \frac{r'\left(\nabla' \times \vec{M}\right)}{|\vec{r} - \vec{r}\,'|} \cdot \hat{e}_z \simeq \frac{2M_S C\sqrt{2C_1}}{\Delta_0\sqrt{\rho\rho'}} \times \\ \left[(2 - C_1\rho'^2)\rho' Q_{-\frac{1}{2}}[\chi] - 2\frac{x_v}{\Delta_0}(2 - C_1\rho'^2) Q_{\frac{1}{2}}[\chi] \cos\phi\right]\end{aligned} \tag{5.39}$$

for $\tilde{\rho}' \ll 1$, and

$$\int_0^{2\pi} \mathrm{d}\phi' \frac{r'\left(\nabla' \times \vec{M}\right)}{|\vec{r} - \vec{r}\,'|} \cdot \hat{e}_z \simeq \frac{2M_S C}{\Delta_0\sqrt{\rho\rho'}} \left[Q_{-\frac{1}{2}}[\chi] + \frac{x_v}{\Delta_0 \rho'} Q_{\frac{1}{2}}[\chi] \cos\phi\right] \tag{5.40}$$

in the asymptotic regime $\tilde{\rho}' \gg 1$, where the expansions in the right side have been performed up to first order in the VC displacement and

$$\chi = \frac{\rho^2 + \rho'^2 + (\bar{z} - \bar{z}')^2}{2\rho\rho'}. \tag{5.41}$$

In the same manner as in the previous subsection, the Cauchy principal value prescription is introduced to avoid singularities in the integrand of the bulk contribution to the phase difference. Therefore one obtains

$$
\begin{aligned}
\Phi_{21}^{F}|_{\text{Bulk}} &= \frac{2\pi}{\Phi_0}\int_{\frac{-L}{2}}^{\frac{L}{2}} A_z(\vec{r})|_{\text{Bulk}}\,\mathrm{d}z = \frac{2\pi}{\Phi_0}\Delta_0^3\int_{\frac{-L}{2\Delta_0}}^{\frac{L}{2\Delta_0}}\mathrm{d}\bar{z} \\
&\quad\times\mathcal{P}\int_{\frac{-L}{2\Delta_0}}^{\frac{L}{2\Delta_0}}\mathrm{d}\bar{z}'\int_0^{\frac{R}{\Delta_0}}\mathrm{d}\rho'\int_0^{2\pi}\mathrm{d}\phi'\frac{r'\left(\nabla'\times\vec{M}\right)\cdot\hat{e}_z}{|\vec{r}-\vec{r}\,'|} \\
&= \frac{4\pi}{\Phi_0}\frac{M_S C\Delta_0^2}{\sqrt{\rho}}\int_{\frac{-L}{2\Delta_0}}^{\frac{L}{2\Delta_0}}\mathrm{d}\bar{z}\,\mathcal{P}\int_{\frac{-L}{2\Delta_0}}^{\frac{L}{2\Delta_0}}\mathrm{d}\bar{z}'\Bigg\{\sqrt{2C_1}\int_0^1\frac{\mathrm{d}\rho'}{\sqrt{\rho'}} \\
&\quad\times\left[(2-C_1\rho'^2)\rho' Q_{-\frac{1}{2}}[\chi]-2\frac{x_v}{\Delta_0}(2-C_1\rho'^2)Q_{\frac{1}{2}}[\chi]\cos\phi\right] \\
&\quad+\int_1^{\frac{R}{\Delta_0}}\frac{\mathrm{d}\rho'}{\sqrt{\rho'}}\left[Q_{-\frac{1}{2}}[\chi]+\frac{x_v}{\Delta_0\rho'}Q_{\frac{1}{2}}[\chi]\cos\phi\right]\Bigg\},
\end{aligned}
\tag{5.42}
$$

where integration over ρ' has been split into the domains $[0,1]$ and $[1,R/\Delta_0]$ corresponding to the asymptotic expansions of the integrand [see Eqs. (5.39) and (5.40)]. As before, one is working under the assumption of an infinitesimal displacement of the VC from the center of the disk, $x_v \ll 1$, so that the deformation of the VC area with respect to the centered case ($\rho' \leq 1$) is small and can be safely neglected in the integration process, simplifying the calculations.

5.4 Computation of the Josephson current

According to the gauge-invariant phase relation [Eq. (5.8)], the superconducting phase difference splits into the sum of the intrinsic component and of both surface and bulk contributions, which are given by Eqs. (5.33) and (5.42) respectively, due to the presence of the F-layer. That is,

$$
\Phi_{21}(\rho,\phi) = \Phi_{21}^{0} + \Phi_{21}^{F}|_{\text{Surf}} + \Phi_{21}^{F}|_{\text{Bulk}} = \Phi_{21}^{0} + a(\rho) + b(\rho)\cos\phi,
$$

where the functions $a(\rho)$ and $b(\rho)$ are given by

$$\begin{aligned} a(\rho) =& \frac{4\pi M_S C\Delta_0^2}{\Phi_0\sqrt{\rho}} \int_{\frac{-L}{2\Delta_0}}^{\frac{L}{2\Delta_0}} \mathrm{d}\bar{z}\, \mathcal{P} \int_{\frac{-L}{2\Delta_0}}^{\frac{L}{2\Delta_0}} \mathrm{d}\bar{z}' \times \qquad (5.43) \\ & \left\{ \sqrt{2C_1} \int_0^1 \frac{\mathrm{d}\rho'}{\sqrt{\rho'}} (2 - C_1\rho'^2)\rho' Q_{-\frac{1}{2}}[\chi] + \int_1^{\frac{R}{\Delta_0}} \frac{\mathrm{d}\rho'}{\sqrt{\rho'}}\, Q_{-\frac{1}{2}}[\chi] \right. \\ & \left. - \sqrt{\frac{R}{\Delta_0}} Q_{-\frac{1}{2}} \left[\frac{\rho^2 + (R/\Delta_0)^2 + (\bar{z} - \bar{z}')^2}{2\rho R/\Delta_0} \right] \right\}, \\ b(\rho) =& \frac{x_v}{\Delta_0} \frac{4\pi M_S C\Delta_0^2}{\Phi_0\sqrt{\rho}} \int_{\frac{-L}{2\Delta_0}}^{\frac{L}{2\Delta_0}} \mathrm{d}\bar{z}\, \mathcal{P} \int_{\frac{-L}{2\Delta_0}}^{\frac{L}{2\Delta_0}} \mathrm{d}\bar{z}' \times \qquad (5.44) \\ & \left\{ \int_1^{\frac{R}{\Delta_0}} \frac{\mathrm{d}\rho'}{\rho'^{3/2}}\, Q_{\frac{1}{2}}[\chi] - 2\sqrt{2C_1} \int_0^1 \frac{\mathrm{d}\rho'}{\sqrt{\rho'}} (2 - C_1\rho'^2) Q_{\frac{1}{2}}[\chi] \right\}. \end{aligned}$$

The current density across the junction is given by the current-phase relation (5.5):

$$j = j_m \sin\big(\Phi_{21}^0 + a(\rho) + b(\rho)\cos\phi\big). \qquad (5.45)$$

With account of the Jacobi-Anger expansions

$$\begin{aligned} \cos(b(\rho)\cos\phi) &= J_0(b(\rho)) + 2\sum_{n\geq 1} (-1)^n J_{2n}(b(\rho)) \cos(2n\phi), \\ \sin(b(\rho)\cos\phi) &= 2\sum_{n\geq 0} (-1)^n J_{2n+1}(b(\rho)) \cos\big((2n+1)\phi\big), \qquad (5.46) \end{aligned}$$

and of the uniform convergence of these series $-b(\rho)$ is a bounded function over the domain $[0, R/\Delta_0]$– one has the identities

$$\int_0^{2\pi} \mathrm{d}\phi\, \sin\big(b(\rho)\cos\phi\big) = 0, \qquad (5.47)$$

$$\int_0^{2\pi} \mathrm{d}\phi\, \cos\big(b(\rho)\cos\phi\big) = 2\pi J_0(b(\rho)). \qquad (5.48)$$

Combined with the trigonometric identity $\sin(\Phi_{21}^0 + a(\rho) + b(\rho)\cos\phi) = \sin\big(\Phi_{21}^0 + a(\rho)\big)\cos(b(\rho)\cos\phi) + \cos\big(\Phi_{21}^0 + a(\rho)\big)\sin(b(\rho)\cos\phi)$ they lead to the following expression:

$$\int_0^{2\pi} \mathrm{d}\phi\, \sin\big(\Phi_{21}^0 + a(\rho) + b(\rho)\cos\phi\big) = 2\pi J_0\big(b(\rho)\big)\sin\big(\Phi_{21}^0 + a(\rho)\big). \qquad (5.49)$$

The total current can be obtained by integrating Eq. (5.45) over the surface, $S_\mathrm{J} = \pi R_0^2$, of the junction of radius R_0, centered at the origin of the XYZ coordinate frame. Therefore, the following expression for the total current is obtained

$$I = \int_{S_\mathrm{J}} \mathrm{d}^2\vec{r}\, j_m \sin \Phi_{21} = I_m \int_0^{R_0/\Delta_0} \rho\, \mathrm{d}\rho\; J_0\big(b(\rho)\big) \sin\big(\Phi_{21}^0 + a(\rho)\big), \tag{5.50}$$

where $I_m = 2\pi j_m \Delta_0^2$ is the maximum current carried by the junction.

In estimating the effect of the displacement of the VC one shall assume that the intrinsic phase difference of the junction, Φ_{21}^0, is zero. Figure 5.3 shows variation of the Josephson current, $\Delta I = I_0 - I$, resulting from small displacements of the VC with respect to the center of the disk, for different values of the parameter $\lambda = R_0/R$. The variation of the current is normalized to $I_0 = I(x_v = 0)$. As an illustration of this effect, the computation has been performed for a Py disk of normalized radius $R/\Delta_0 = 100$ and normalized thickness $L/\Delta_0 = 6$. The experimental values $M_S = 7.5 \cdot 10^5$ A/m and $A = 1.3 \cdot 10^{-11}$ J/m for Py have been used, which give $\Delta_0 \simeq 15.2$ nm.

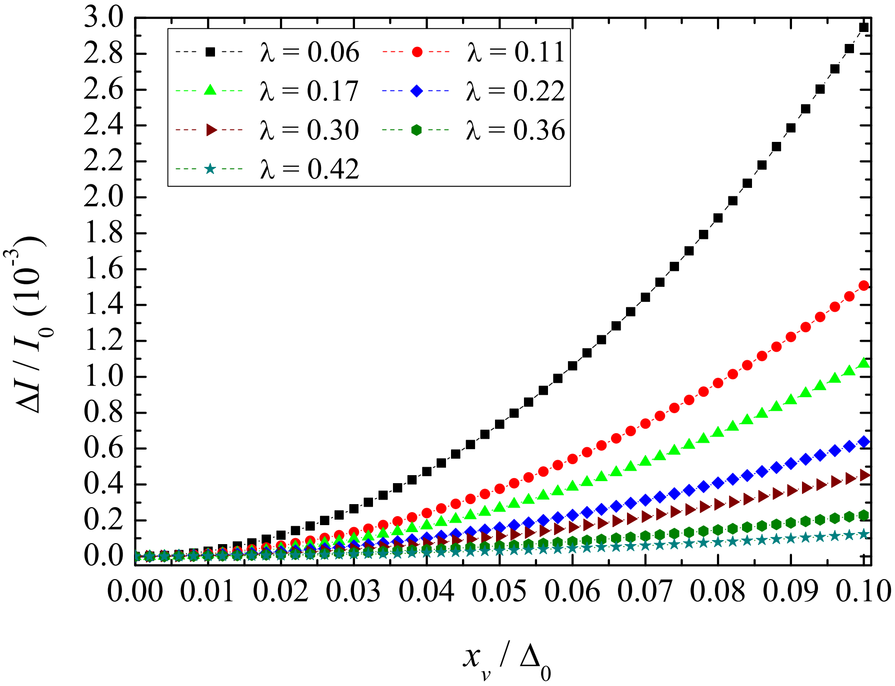

Figure 5.3: Variation of the Josephson current for different values of the parameter $\lambda = R_0/R$ as a function of the normalized VC displacement from the center of the disk. The current is normalized to $I_0 = I(x_v = 0)$.

5.5 Discussion

One has studied how the tunneling current through the Josephson junction containing a circularly polarized magnetic disk changes when the center of the vortex is displaced by a tiny distance due to, e.g, thermal activation or quantum tunneling. The numerical work has been done for a disk of a thickness that is few times greater than the diameter of the VC. The latter in Py is about 15 nm, which for $L/\Delta_0 = 6$ used in the plot of Fig. 5.3 corresponds to the disks of thickness of 90 nm. Such disks have been studied in Chapter 4, where thermal and quantum diffusion of vortices has been observed.

The change in the Josephson current due to the displacement of the VC from the center of the disk has been computed in the range up to $x_v \sim 0.1\Delta_0$, which corresponds to 1.5 nm for a Py disk. The maximal change in the Josephson current in this range of the displacement is of order of a few tenths of a percent, which is within experimental range. It grows fast with the displacement for R_0/R below 0.1, which for a disk of diameter of 1.5 μm –like those studied in Chapter 4– corresponds to the Josephson junction of the lateral size 150 nm. While in calculations a circular junction was used, its geometry does not really matter as long as its size $R_0 < R$ is large compared to Δ_0. Smaller junctions produce stronger effect.

The present calculation and numerical estimates clearly illustrate that a Josephson junction with a magnetic disk in the VS would be an interesting physical system that could be used to measure the nanoscale motion of the VC. Manufacturing of such junctions and experimenting with them may open up an exciting field of research on quantum and classical dynamics of magnetic vortices.

Chapter 6

Conclusions and future perspectives

6.1 Conclusions

The conclusions of the thesis are briefly outlined in this section. A more detailed account of them can be found in the sections ”Discussion” of the previous chapters. The summary splits into three parts according to the topics covered in this thesis.

Quantum tunneling of normal-superconductor interfaces in type-I superconductors

The nature of the mechanism of magnetic relaxation in a disk-shaped type-I Pb superconductor has been explored as a function of temperature and magnetic field for initial states along the descending branch of the magnetic hysteresis cycle. As the sample is cooled down, a transition from a thermal to a quantum regime has been observed in the temperature dependence of the magnetic relaxation rate. The crossover temperature between both regimes has been found to exhibit an inverse dependence on the magnetic field that impedes the detection of the quantum regime at high enough magnetic field values. On rising the magnetic field, the relaxation rate has been observed to change from a slowly increasing regime, in which no thermal effects are detected, to a steeply incremental region that is noticeably affected by temperature. Comparison between the experimental data and a model for quantum tunneling of normal-superconductor interfaces through energy barriers defined by structural defects in the sample implies that the bumps generated at the interfaces, which are responsible for the magnetic relaxation, become flatter when the magnetic field increases. Quantum transitions cease above a certain combination of values of temperature and magnetic field, but the interfaces are still pinned by the defects and depinning occurs by thermal activation until a threshold for quasi-free flux motion is reached.

Macroscopic quantum tunneling of interfaces separating normal and superconducting regions in type-I superconductors has been studied theoretically. A mathematical model has been developed that describes dissipative quantum escape of a two-dimensional elastic manifold from a planar potential well. It corresponds to, e.g., a current-driven quantum depinning of the interface from a grain boundary or from an artificially manufactured pinning layer. The Euclidean dynamics of the interface in a type-I superconductor is entirely dissipative, described by integro-differential equations in 2+1 dimensions. The model describes quantitatively the thermal dependence of the magnetic viscosity of lead at zero field and estimates the width of the pinning well to be about 3.6 nm. Together with the observation of nonthermal low-temperature magnetic relaxation in lead, the model suggests the possibility of a controlled measurement of quantum depinning of the interface in a type-I superconductor.

Axial excitation modes of the vortex state and quantum depinning of the vortex core

Classical and quantum theory of spin waves in the vortex state of a mesoscopic submicron magnetic disk has been developed with account of the finite mass density of the vortex. Oscillations of the vortex core resemble oscillations of a charged string in a potential well in the presence of the magnetic field. Conventional gyrotropic frequency appears as a gap in the spectrum of spin waves of the vortex. In the long-wave limit $q\Delta_0 \ll 1$ this spectrum becomes $\omega_-(q) = \omega_\mathrm{G} + \gamma M_S (q\Delta_0)^2 \ln(R/\Delta_0)$, where ω_G is the conventional gyrofrequency, γ is the gyromagnetic ratio, M_S is the saturation magnetization, Δ_0 is the exchange length, and R is the radius of the disk. The finite mass of the vortex, $M \simeq L/(4\gamma^2)\ln(R/\Delta_0)$ with L being the thickness of the disk, agrees with experimental findings. It originates from the geometrical confinement of the spin field and the magnetic dipole-dipole interactions. Finite vortex mass generates a high-frequency branch of spin waves, with a gap given by $\omega_M = 8\pi\gamma M_S/\ln(R/\Delta_0)$ that belongs to the same frequency range that the uniform ferromagnetic resonance of the magnetic material. The effect of an external magnetic field applied perpendicularly to the disk plane on the spectra of the vortex can be described by adding the Larmor frequency to ω_M.

Dynamics of the vortex core can be affected by the presence of structural defects in the sample. The magnetic irreversibility and the dynamics of vortex cores in micron-size Py ($\mathrm{Ni}_{81}\mathrm{Fe}_{19}$) dot arrays have been explored at low temperatures by means of the application of an in-plane magnetic field. Experimental evidence of the quantum depinning of magnetic vortex cores was found through relaxation measurements. It is attributed to the quantum tunneling of a small portion of the vortex core line –via an elastic deformation– through pinning barriers towards the equilibrium. Linelike defects are the most feasible candidates to provide the landscape of pinning barriers encountered by the vortex core during its low-temperature dynamics. A model of quantum depinning of magnetic vortex cores from line defects in a disk geometry and under the application of an in-plane magnetic field has been developed within the framework of the Caldeira-Leggett theory. The Euclidean dynamics of the vortex core is dissipative, described by integro-differential equations in 1+1 dimensions. The depinning process occurs in steps of about 0.13 nm, which corresponds to the width of the pinning well.

Josephson junction with the vortex state

Josephson tunneling through a circularly polarized micron or submicron-size disk of a soft ferromagnetic material has been studied. The change in the Josephson current that is related to a tiny displacement of the vortex core has been computed analytically. The maximal change in the range of displacements $x_v \in [0, 0.1\Delta_0]$ is of order of a few tenths of a percent for a disk with thickness $L = 90$ nm, which is within experimental range. The change in the Josephson current grows fast with the displacement for R_0/R below 0.1, where $2R_0$ is the lateral size of the junction. Therefore, a Josephson junction with a magnetic disk in the vortex state can be an interesting physical system that may be used to measure the nanoscale motion of the magnetic vortex.

6.2 Future perspectives

Further work can be performed concerning the research presented in this thesis. The aim of this section is to outline some future extensions of it.

To begin with, as discussed in Chapter 2, the model of quantum tunneling of normal-superconductor interfaces can be naturally extended to the case of an arbitrary applied magnetic field. Some setbacks need to be taken into account in order to succeed. First, the pattern geometry of normal-superconductor interfaces is cumbersome because it strongly depends on the shape of the specimen and the distribution of defects (pinning centers) across the sample. Analytical theory describing the formation of these labyrinthine patterns is absent and, therefore, calculation of the prefactor $N(h)$ should be done numerically by solving the Ginzburg-Landau equations with account of demagnetizing and pinning effects. The same happens to the reduction of the effective energy barrier with the magnetic field strength, because the magnetic tension force depends on the shape of the normal-superconductor interfaces. A first attempt could be made with account of the laminar model for normal and superconducting domains, but the results derived from this would be valid for (quasi)defect-free samples.

Secondly, the theoretical model of spin-waves associated with the gyrotropic motion of the elastic vortex core was built under the assumption of small displacements of the vortex core within the XY-plane along the Z axis. This assumption is correct for the quantum depinning problem, where some segments of the vortex core line diffuse through a pinning well of subnanometric size. This allows to use the quadratic dependence (3.68) for the magnetostatic and exchange energy potentials. This model can be extended to the case of moderate axial vortex-core deformations if the general expression for the energy density ω_{XY} within the 2VSCFM is considered. Furthermore, the elastic energy density should be also modified –the hypothesis $\tilde{r} \simeq r$ is no longer valid. On the other hand, the present model can be extended to other flat geometries –ellipses, stadiums, etc.– if an ansatz for the magnetization field of the corresponding vortex ground state is provided. With respect to the quantum depinning of the vortex core line in disks with the vortex state, it would be interesting to extend the model to the case of random pinning potentials. This task is really cumbersome because the replica method technique used in problems of the same kind leads to an effective action that couples explicitly the coordinates (x_τ, y_τ), so that the algorithmic approach used in this thesis cannot be applied.

Thirdly, it would be interesting to study dynamical effects in a ferromagnetic Josephson junction with the vortex state. Temporal dynamics of this system is likely to couple Josephson oscillations with the oscillations of the magnetic vortex in the disk. The idea is to derive a system of equations that couples Thiele equation for the vortex state with the equation for the Josephson phase. Since oscillations of the Josephson current can be controlled by the voltage, the question of practical interest is whether the motion of the vortex core inside the disk can also be controlled by the voltage through the junction. In case such a control becomes possible, it would open the way to a new method of electronic manipulation of magnetic memory based upon submicron disks.

Appendices

Appendix A

Functional derivative

This Appendix deals with the formal definition of functional derivation and with the explicit calculation of the functional derivative for some functionals appearing in this thesis. One will focus on the space of complex differentiable functions defined over $\mathbf{R}^n$, to which the different functions of the models presented in this manuscript belong. Notice that the following definitions can be extended to more general functional spaces.

A.1 Functional derivative

Let Ω be a non-empty open subset of $\mathbf{R}^n$ and $\mathcal{E}(\Omega)$ be the Fréchet space of all C^∞ complex functions on Ω endowed with the locally convex topology of the local uniform convergence of functions and derivatives. Given any $f \in \mathcal{E}(\Omega)$, its support is defined as $\mathrm{supp}(f) = \overline{\{x \in \Omega \mid f(x) \neq 0\}}$, where "$\overline{}$" denotes topological closure. The space of *test functions*, $\mathcal{D}(\Omega)$, is defined as the vector subspace of $\mathcal{E}(\Omega)$ consisting of functions with compact support. Let $F : \mathcal{E}(\Omega) \to \mathbf{C}$ be a functional. Then the *functional* (or *variational*) *derivative* of $F[u]$, $\dfrac{\delta F}{\delta u(\vec{r})}$, is defined as

$$\lim_{\epsilon \to 0} \frac{F[u + \epsilon\varphi] - F[u]}{\epsilon} = \int_\Omega \mathrm{d}^n\vec{r} \frac{\delta F}{\delta u(\vec{r})} \varphi(\vec{r}), \quad \forall \varphi \in \mathcal{D}(\Omega), \tag{A.1}$$

whenever F is Fréchet differentiable at u.

A.1.1 Density functional

Let $V \subset \mathbf{R}^3$ be an oriented 3D smooth manifold. Let Ω_1 be an open subset of $\mathbf{R}^3$ containing the manifold V. A function $u : V \to \mathbf{C}$ is said to belong to the C^∞ class if there exists $\bar{u} \in \mathcal{E}(\Omega_1)$ such that $\bar{u}|_V \equiv u$. $\mathcal{E}(V)$ denotes the Fréchet space of C^∞ complex functions on V endowed with the corresponding subspace topology. Consider a functional of the form

$$F[u] = \int_V f\left(\vec{r}, u(\vec{r}), \nabla u(\vec{r})\right) \, \mathrm{d}^3\vec{r}, \tag{A.2}$$

where $u \in \mathcal{E}(V)$ and f is a differentiable function. Let $\varphi \in \mathcal{D}(\Omega)$, with $\Omega = \overset{\circ}{V}$ —interior of V. Therefore, for an arbitrary $\epsilon > 0$ one has

$$\begin{aligned} F[u+\epsilon\varphi] - F[u] &= \int_V \mathrm{d}^3\vec{r} \big[f\left(\vec{r}, u(\vec{r}) + \epsilon\varphi(\vec{r}), \nabla u(\vec{r}) + \epsilon\nabla\varphi(\vec{r})\right) - f\left(\vec{r}, u(\vec{r}), \nabla u(\vec{r})\right) \big] \\ &= \epsilon \int_V \mathrm{d}^3\vec{r} \left[\frac{\partial f}{\partial u}\varphi(\vec{r}) + \frac{\partial f}{\partial \nabla u} \cdot \nabla\varphi(\vec{r}) + O(\epsilon) \right], \end{aligned} \tag{A.3}$$

which leads to the expression

$$\lim_{\epsilon\to 0} \frac{F[u+\epsilon\varphi] - F[u]}{\epsilon} = \int_V \mathrm{d}^3\vec{r} \left[\frac{\partial f}{\partial u}\varphi(\vec{r}) + \frac{\partial f}{\partial \nabla u} \cdot \nabla\varphi(\vec{r}) \right]. \tag{A.4}$$

Notice that

$$\int_V \mathrm{d}^3\vec{r} \, \frac{\partial f}{\partial \nabla u} \cdot \nabla\varphi(\vec{r}) = \int_V \mathrm{d}^3\vec{r} \left[\nabla \cdot \left(\frac{\partial f}{\partial \nabla u}\varphi(\vec{r}) \right) - \left(\nabla \cdot \frac{\partial f}{\partial \nabla u} \right) \varphi(\vec{r}) \right], \tag{A.5}$$

where the first term on the right side vanishes as a consequence of the divergence theorem and φ being compactly supported on Ω. Hence, one finally obtains

$$\lim_{\epsilon\to 0} \frac{F[u+\epsilon\varphi] - F[u]}{\epsilon} = \int_V \mathrm{d}^3\vec{r} \left[\frac{\partial f}{\partial u} - \nabla \cdot \frac{\partial f}{\partial \nabla u} \right] \varphi(\vec{r}). \tag{A.6}$$

Application of the du Bois-Reymond lemma yields the following expression for the functional derivative of F:

$$\frac{\delta F}{\delta u(\vec{r})} = \frac{\partial f}{\partial u} - \nabla \cdot \frac{\partial f}{\partial \nabla u}. \tag{A.7}$$

This expression can be generalized in a straightforward manner to the case where the density f depends on other first-order differential operators —curl and divergence— and on higher order derivatives. On the other hand, in the above derivation one can weaken the condition $\varphi \in \mathcal{D}(\Omega)$ and consider $\varphi \in \mathcal{E}(V)$. In doing so the first term on the right side of Eq. (A.5) does not vanish for all φ —not compactly supported on $\overset{\circ}{V}$ anymore. Application of the divergence theorem leads to a surface term of the form

$$\int_{\partial V} \mathrm{d}^2\vec{r} \left(\frac{\partial f}{\partial \nabla u} \cdot \vec{n} \right) \varphi(\vec{r}), \tag{A.8}$$

where $\vec{n}$ is the normal vector to the boundary ∂V. Vanishing of this term is usually considered, which can be obtained by imposing the boundary condition

$$\frac{\partial f}{\partial \nabla u} \cdot \vec{n} = 0, \quad \text{on } \partial V. \tag{A.9}$$

In the particular case of the Ginzburg-Landau functional, the surface term leads to the boundary condition (1.9) valid for an Insulator-Superconductor interface.

A.1.2 Caldeira-Leggett functional

The Caldeira-Leggett functional is given by [see Eq. (2.37)]

$$F_{\mathrm{CL}}[u] = \int_0^{\hbar\beta} \mathrm{d}\tau \int_0^{\hbar\beta} \mathrm{d}\tau' D(\tau - \tau') u(\tau) u(\tau'), \tag{A.10}$$

with $D(\tau) = \frac{1}{2\hbar\beta} \sum_{n \in \mathbf{Z}} \eta |\nu_n| e^{i\nu_n \tau}$ being the kernel of the integral operator [see Eq. (2.41)] and $\nu_n, n \in \mathbf{Z}$, being the Matsubara frequencies. The function u belongs to the space $\mathcal{E}_{\mathrm{p}}(\mathbf{R})$, where the subscript "$_{\mathrm{p}}$" denotes periodic real-valued functions with period $\hbar\beta$. Let $\tilde{\varphi}$ be an arbitrary real-valued function compactly supported on $(0, \hbar\beta)$. The periodic extension of $\tilde{\varphi}|_{[0,\hbar\beta]}$ over $\mathbf{R}$ with period $\hbar\beta$ is denoted by φ. Thus, for $\epsilon > 0$ one has

$$F_{\mathrm{CL}}[u + \epsilon\varphi] - F_{\mathrm{CL}}[u] = \epsilon \int_0^{\hbar\beta} \mathrm{d}\tau \int_0^{\hbar\beta} \mathrm{d}\tau' D(\tau - \tau') \left[u(\tau)\varphi(\tau') + u(\tau')\varphi(\tau) + O(\epsilon) \right], \tag{A.11}$$

which leads to the expression

$$\lim_{\epsilon \to 0} \frac{F_{\mathrm{CL}}[u + \epsilon\varphi] - F_{\mathrm{CL}}[u]}{\epsilon} = \int_0^{\hbar\beta} \mathrm{d}\tau \left\{ 2 \int_0^{\hbar\beta} \mathrm{d}\tau' D(\tau - \tau') u(\tau') \right\} \varphi(\tau), \tag{A.12}$$

where a change of variables $\tau \mapsto \tau'$; $\tau' \mapsto \tau$ has been applied at the first term on the right side of Eq. (A.11). With account of the du Bois-Reymond lemma the following expression for the functional derivative of F_{CL} is obtained:

$$\frac{\delta F_{\mathrm{CL}}}{\delta u(\tau)} = 2 \int_0^{\hbar\beta} \mathrm{d}\tau' D(\tau - \tau') u(\tau'). \tag{A.13}$$

It is straightforward to prove, using the Fourier expansion of $u(\tau')$ over the set of Matsubara frequencies, that the above functional derivative is equivalent to

$$\frac{\delta F_{\mathrm{CL}}}{\delta u(\tau)} = \frac{\eta}{\pi} \int_{\mathbf{R}} \mathrm{d}\tau' \frac{u(\tau) - u(\tau')}{(\tau - \tau')^2}. \tag{A.14}$$

Appendix B

Gaussian integration

In this Appendix a useful formula to calculate path integrals of Gaussian type is given. A detailed treatment of the path-integral formalism is beyond the scope of this manuscript. A deep insight into this subject is provided by Refs. [141, 142].

B.1 Gaussian integration

Let $K \in L^2(\mathbf{R}^n \times \mathbf{R}^n, \mathbf{R})$ be a symmetric real-valued kernel $-K(\vec{x}, \vec{y}) = K(\vec{y}, \vec{x})$ for all $\vec{x}, \vec{y} \in \mathbf{R}^n-$ and let $f, \phi \in L^2(\mathbf{R}^n, \mathbf{R})$ be arbitrary square-integrable functions. Therefore, the following identity between Gaussian path integrals holds:

$$\frac{\int \mathcal{D}[f] \exp\left[-\frac{i}{2}\int_{\mathbf{R}^n\times\mathbf{R}^n} f(\vec{x})K(\vec{x},\vec{y})f(\vec{y})\,\mathrm{d}^n\vec{x}\,\mathrm{d}^n\vec{y} + i\int_{\mathbf{R}^n}\phi(\vec{y})f(\vec{y})\,\mathrm{d}^n\vec{y}\right]}{\int \mathcal{D}[f] \exp\left[-\frac{i}{2}\int_{\mathbf{R}^n\times\mathbf{R}^n} f(\vec{x})K(\vec{x},\vec{y})f(\vec{y})\,\mathrm{d}^n\vec{x}\,\mathrm{d}^n\vec{y}\right]} =$$
$$\exp\left[\frac{i}{2}\int_{\mathbf{R}^n\times\mathbf{R}^n}\phi(\vec{x})K^{-1}(\vec{x},\vec{y})\phi(\vec{y})\,\mathrm{d}^n\vec{x}\,\mathrm{d}^n\vec{y}\right], \tag{B.1}$$

where $K^{-1}(x, y)$ denotes the inverse kernel and satisfies the integral equation

$$\int_{\mathbf{R}^n} K(\vec{x},\vec{z})K^{-1}(\vec{z},\vec{y})\,\mathrm{d}^n\vec{z} = \delta^{(n)}(\vec{x}-\vec{y}). \tag{B.2}$$

List of Publications

[1] R. Zarzuela, E. M. Chudnovsky and J. Tejada. ”Dissipative macroscopic quantum tunneling in type-I superconductors”. *Phys. Rev. B* 84, 184525 (2011).

[2] Saül Vélez, Ricardo Zarzuela, Antoni García-Santiago and Javier Tejada. ”Magnetic field dependence of the quantum tunneling of normal-superconductor interfaces in a type-I Pb superconductor”. *Phys. Rev. B* 85, 064506 (2012).

[3] Ricardo Zarzuela, Saül Vélez, Joan Manel Hernandez, Javier Tejada and Valentyn Novosad. ”Quantum depinning of the magnetic vortex core in micron-size permalloy disks”. *Phys. Rev. B* 85, 180401(R) (2012).

[4] R. Zarzuela, E. M. Chudnovsky and J. Tejada. ”Excitation modes of vortices in submicron magnetic disks”. *Phys. Rev. B* 87, 014413 (2013).

[5] R. Zarzuela, E. M. Chudnovsky, J. M. Hernandez and J. Tejada. ”Quantum dynamics of vortices in mesoscopic magnetic disks”. *Phys. Rev. B* 87, 144420 (2013).

[6] Eugene M. Chudnovsky, Javier Tejada and Ricardo Zarzuela. ”Quantum forces in solids with two-state systems: Example of molecular magnets”. *Phys. Rev. B* 88, 220409(R) (2013).

[7] R. Zarzuela, E. M. Chudnovsky and J. Tejada. ”Josephson junction with a magnetic vortex”. *Submitted to Phys. Rev. B* (2014).

[8] S. Lendinez, R. Zarzuela, J. Tejada, M. W. Terban, S. J. L. Billinge, J. Espin, I. Imaz, D. Maspoch and E. M. Chudnovsky. ”Resonant Spin Tunneling in Randomly Oriented Nanospheres of Mn_{12} Acetate”. *Submitted to Phys. Rev. B* (2014).

Bibliography

[1] H. Kammerlingh-Onnes. In: *Leiden Commun.* 120b, 122b, 124c (1911) (cit. on p. 1).

[2] W. Meissner and R. Ochsenfeld. In: *Naturwissen* 21.787 (1933) (cit. on p. 1).

[3] V. L. Ginzburg and L. D. Landau. In: *Zh. Eksp. Teor. Fiz.* 20.1064 (1950) (cit. on pp. 3, 6).

[4] L. D. Landau. "On The Theory of Phase Transitions". In: *Zh. Eksp. Teor. Fiz.* 7 (1937), pp. 19–32 (cit. on p. 3).

[5] L. Gor'kov. "Microscopic Derivation of the Ginzburg-Landau equation in the theory of superconductivity". In: *Sov. Phys. JETP* 36 (1959), pp. 1918–1923 (cit. on p. 3).

[6] P. De Gennes. "Boundary Effects in Superconductors". In: *Reviews of Modern Physics* 36.1 (1964), pp. 225–237. DOI: `10.1103/RevModPhys.36.225` (cit. on pp. 6, 143).

[7] P. Anderson. "Plasmons, Gauge Invariance, and Mass". In: *Physical Review* 130.1 (1963), pp. 439–442. DOI: `10.1103/PhysRev.130.439` (cit. on p. 8).

[8] P. Higgs. "Broken Symmetries and the Masses of Gauge Bosons". In: *Physical Review Letters* 13.16 (1964), pp. 508–509. DOI: `10.1103/PhysRevLett.13.508` (cit. on p. 8).

[9] H. Hess, R. Robinson, R. Dynes, J. Valles, and J. Waszczak. "Scanning-Tunneling-Microscope Observation of the Abrikosov Flux Lattice and the Density of States near and inside a Fluxoid". In: *Physical Review Letters* 62.2 (1989), pp. 214–216. DOI: `10.1103/PhysRevLett.62.214` (cit. on p. 16).

[10] P. E. Goa, H. Hauglin, M. Baziljevich, E. Il'yashenko, P. L. Gammel, and T. H. Johansen. "Real-time magneto-optical imaging of vortices in super-

conducting $NbSe_2$". In: *Superconductor Science and Technology* 14.9 (2001), pp. 729–731. DOI: 10.1088/0953-2048/14/9/320 (cit. on p. 16).

[11] A. Abrikosov. "On the Magnetic Properties of Superconductors of the Second Group". In: *Zh. Eksp. Teor. Fiz.* 32 (1957), p. 1442 (cit. on p. 17).

[12] P. De Gennes and J. Matricon. "Collective Modes of Vortex Lines in Superconductors of the Second Kind". In: *Reviews of Modern Physics* 36.1 (1964), pp. 45–49. DOI: 10.1103/RevModPhys.36.45 (cit. on p. 17).

[13] Y. Kim, C. Hempstead, and A. Strnad. "Flux-Flow Resistance in Type-II Superconductors". In: *Physical Review* 139.4A (1965), A1163–A1172. DOI: 10.1103/PhysRev.139.A1163 (cit. on p. 18).

[14] A. Fortini and E. Paumier. "Thermodynamics of the Domain Structure and Determination of the Transition Fields in Type-1 Superconductors". In: *Physical Review B* 5.5 (1972), pp. 1850–1858. DOI: 10.1103/PhysRevB.5.1850 (cit. on p. 23).

[15] L. D. Landau. "On the theory of the intermediate state of superconductors". In: *Zh. Eksp. Teor. Fiz.* 13 (1943), p. 377 (cit. on p. 25).

[16] A. Meshkovsky and A. Shalnikov. In: *Zh. Eksp. Teor. Fiz.* 11 (1947), p. 1 (cit. on p. 25).

[17] A. Meshkovsky and A. Shalnikov. In: *Zh. Eksp. Teor. Fiz.* 34 (1958), p. 312 (cit. on p. 25).

[18] B. Balashova and Y. V. Sharvin. In: *Zh. Eksp. Teor. Fiz.* 31 (1956), p. 40 (cit. on p. 25).

[19] W. DeSorbo. "Study of the Intermediate State in Superconductors using Cerium Phosphate Glass". In: *Physical Review Letters* 4.8 (1960), pp. 406–408. DOI: 10.1103/PhysRevLett.4.406 (cit. on p. 26).

[20] W. DeSorbo and V. L. Newhouse. "Optical Detection of Domain Structure and Current Flow in Superconducting Lead Films". In: *Journal of Applied Physics* 33.3 (1962), p. 1004. DOI: 10.1063/1.1777152 (cit. on p. 26).

[21] B. Goodman and M. Wertheimer. "Observation of the speed of flux jumps in superconducting niobium". In: *Physics Letters* 18.3 (1965), pp. 236–238. DOI: 10.1016/0031-9163(65)90308-2 (cit. on p. 26).

[22] B. Goodman, A. Lacaze, and M. Wertheimer. In: *Compt. Rend.* 262 (1966), p. 12 (cit. on p. 26).

[23] R. Prozorov, R. W. Giannetta, A. A. Polyanskii, and G. K. Perkins. “Topological hysteresis in the intermediate state of type-I superconductors”. In: *Physical Review B* 72.21 (2005), p. 212508. DOI: 10.1103/PhysRevB.72.212508 (cit. on pp. 26, 30–31).

[24] R. Prozorov. “Equilibrium Topology of the Intermediate State in Type-I Superconductors of Different Shapes”. In: *Physical Review Letters* 98.25 (2007), p. 257001. DOI: 10.1103/PhysRevLett.98.257001 (cit. on pp. 26, 30–31).

[25] A. Kuznetsov, D. Eremenko, and V. Trofimov. “Onset of flux penetration into a type-I superconductor disk”. In: *Physical Review B* 57.9 (1998), pp. 5412–5418. DOI: 10.1103/PhysRevB.57.5412 (cit. on pp. 27–29).

[26] W. DeSorbo and W. Healy. “The intermediate state of some superconductors”. In: *Cryogenics* 4.5 (1964), pp. 257–323. DOI: 10.1016/0011-2275(64)90104-3 (cit. on p. 29).

[27] R. Prozorov, A. F. Fidler, J. R. Hoberg, and P. C. Canfield. “Suprafroth in type-I superconductors”. In: *Nature Physics* 4.4 (2008), pp. 327–332. DOI: 10.1038/nphys888 (cit. on p. 30).

[28] E. M. Chudnovsky, S. Vélez, A. García-Santiago, J. M. Hernandez, and J. Tejada. “Quantum tunneling of the interfaces between normal-metal and superconducting regions of a type-I Pb superconductor”. In: *Physical Review B* 83.6 (2011), p. 064507. DOI: 10.1103/PhysRevB.83.064507 (cit. on pp. 32, 39, 56, 65).

[29] A. C. Rose-Innes and E. H. Rhoderick. *Introduction to Superconductivity*. Pergamon Press, Oxford, 1969 (cit. on p. 34).

[30] R. Flükiger et al. *Superconductors: Transition Temperatures and Characterization Of Elements, Alloys and Compounds: O (without cuprates) ... Sc*. Ed. by R. Flükiger and W. Klose. Vol. 21c. Landolt-Börnstein - Group III Condensed Matter. Berlin/Heidelberg: Springer-Verlag, 1997, p. 29. DOI: 10.1007/b42902 (cit. on p. 34).

[31] S. Vélez, A. García-Santiago, J. M. Hernandez, and J. Tejada. “The role of temperature in the magnetic irreversibility of type-I Pb superconductors.” In: *Journal of physics. Condensed matter : an Institute of Physics journal* 24.48 (2012), p. 485701. DOI: 10.1088/0953-8984/24/48/485701 (cit. on pp. 34, 39).

[32] E. M. Chudnovsky and J. Tejada. *Macroscopic Quantum Tunneling of the Magnetic Moment*. Cambridge, England: Cambridge University Press, 1998 (cit. on pp. 37, 41, 53, 117, 124, 127, 132, 139).

[33] G. Van Den Berg. "The electrical resistance of potassium, tungsten, copper, tin and lead at low temperatures". In: *Physica* 14.2-3 (1948), pp. 111–138. DOI: `10.1016/0031-8914(48)90031-7` (cit. on p. 39).

[34] A. O. Caldeira and A. J. Leggett. "Influence of Dissipation on Quantum Tunneling in Macroscopic Systems". In: *Physical Review Letters* 46.4 (1981), pp. 211–214. DOI: `10.1103/PhysRevLett.46.211` (cit. on pp. 41, 50).

[35] A. O. Caldeira and A. J. Leggett. "Quantum tunnelling in a dissipative system". In: *Annals of Physics* 149.2 (1983), pp. 374–456. DOI: `10.1016/0003-4916(83)90202-6` (cit. on pp. 41, 50).

[36] J. Clarke, A. N. Cleland, M. H. Devoret, D. Esteve, and J. M. Martinis. "Quantum mechanics of a macroscopic variable: the phase difference of a Josephson junction." In: *Science (New York, N.Y.)* 239.4843 (1988), pp. 992–7. DOI: `10.1126/science.239.4843.992` (cit. on p. 41).

[37] G. Blatter, M. V. Feigel'man, V. B. Geshkenbein, A. I. Larkin, and V. M. Vinokur. "Vortices in high-temperature superconductors". In: *Reviews of Modern Physics* 66.4 (1994), pp. 1125–1388. DOI: `10.1103/RevModPhys.66.1125` (cit. on p. 41).

[38] Y. Yeshurun, A. Malozemoff, and A. Shaulov. "Magnetic relaxation in high-temperature superconductors". In: *Reviews of Modern Physics* 68.3 (1996), pp. 911–949. DOI: `10.1103/RevModPhys.68.911` (cit. on p. 41).

[39] T. Nattermann and S. Scheidl. "Vortex-glass phases in type-II superconductors". In: *Advances in Physics* 49.5 (2000), pp. 607–704. DOI: `10.1080/000187300412257` (cit. on p. 41).

[40] E. M. Chudnovsky, O. Iglesias, and P. C. E. Stamp. "Quantum tunneling of domain walls in ferromagnets". In: *Physical Review B* 46.9 (1992), pp. 5392–5404. DOI: `10.1103/PhysRevB.46.5392` (cit. on pp. 41, 55).

[41] K. Hong and N. Giordano. "Evidence for domain wall tunnelling in a quasi-one dimensional ferromagnet". In: *Journal of Physics: Condensed Matter* 8.19 (1996), pp. L301–L306. DOI: `10.1088/0953-8984/8/19/001` (cit. on p. 41).

[42] J. Brooke, T. F. Rosenbaum, and G. Aeppli. "Tunable quantum tunnelling of magnetic domain walls." In: *Nature* 413.6856 (2001), pp. 610–613. DOI: 10.1038/35098037 (cit. on pp. 41, 117).

[43] G. Blatter, V. Geshkenbein, and V. Vinokur. "Quantum collective creep". In: *Physical Review Letters* 66.25 (1991), pp. 3297–3300. DOI: 10.1103/PhysRevLett.66.3297 (cit. on p. 41).

[44] B. I. Ivlev, Y. N. Ovchinnikov, and R. S. Thompson. "Quantum flux creep in layered high-Tc superconductors". In: *Physical Review B* 44.13 (1991), pp. 7023–7027. DOI: 10.1103/PhysRevB.44.7023 (cit. on pp. 41, 55).

[45] J. Tejada, E. M. Chudnovsky, and A. García. "Quantum tunneling of vortices in the Tl2CaBa2Cu2O8 superconductor". In: *Physical Review B* 47.17 (1993), pp. 11552–11554. DOI: 10.1103/PhysRevB.47.11552 (cit. on pp. 41, 117).

[46] P. Ao and D. J. Thouless. "Tunneling of a quantized vortex: Roles of pinning and dissipation". In: *Physical Review Letters* 72.1 (1994), pp. 132–135. DOI: 10.1103/PhysRevLett.72.132 (cit. on p. 41).

[47] M. J. Stephen. "Quantum tunneling of vortex lines". In: *Physical Review Letters* 72.10 (1994), pp. 1534–1536. DOI: 10.1103/PhysRevLett.72.1534 (cit. on p. 41).

[48] K. Vogel, W. P. Schleich, T. Kato, D. Koelle, R. Kleiner, and E. Goldobin. "Theory of fractional vortex escape in a long Josephson junction". In: *Physical Review B* 80.13 (2009), p. 134515. DOI: 10.1103/PhysRevB.80.134515 (cit. on pp. 41, 55).

[49] U. Kienzle, T. Gaber, K. Buckenmaier, K. Ilin, M. Siegel, D. Koelle, R. Kleiner, and E. Goldobin. "Thermal escape of fractional vortices in long Josephson junctions". In: *Physical Review B* 80.1 (2009), p. 014504. DOI: 10.1103/PhysRevB.80.014504 (cit. on p. 41).

[50] S. Coleman. "Fate of the false vacuum: Semiclassical theory". In: *Physical Review D* 15.10 (1977), pp. 2929–2936. DOI: 10.1103/PhysRevD.15.2929 (cit. on pp. 41, 47).

[51] C. Callan and S. Coleman. "Fate of the false vacuum. II. First quantum corrections". In: *Physical Review D* 16.6 (1977), pp. 1762–1768. DOI: 10.1103/PhysRevD.16.1762 (cit. on pp. 41, 47, 53).

[52] H. Kramers. "Brownian motion in a field of force and the diffusion model of chemical reactions". In: *Physica* 7.4 (1940), pp. 284–304. DOI: 10.1016/S0031-8914(40)90098-2 (cit. on p. 43).

[53] J. Sakurai. *Modern Quantum Mechanics*. Ed. by S. F. Tuan. Revised Ed. Addison-Wesley, 1994, p. 500 (cit. on p. 44).

[54] S. A. Rice and A. R. Dinner, eds. *Advances in Chemical Physics, Volume 147*. Advances in Chemical Physics. Hoboken, NJ, USA: John Wiley & Sons, Inc., 2011. DOI: 10.1002/9781118135242 (cit. on p. 46).

[55] J. Langer. "Theory of the condensation point". In: *Annals of Physics* 41.1 (1967), pp. 108–157. DOI: 10.1016/0003-4916(67)90200-X (cit. on p. 47).

[56] I. Affleck. "Quantum-Statistical Metastability". In: *Physical Review Letters* 46.6 (1981), pp. 388–391. DOI: 10.1103/PhysRevLett.46.388 (cit. on pp. 47, 62–63, 137).

[57] M. H. Poincaré. "Sur la dynamique de l'électron". In: *Rendiconti del Circolo matematico di Palermo* 21.1 (1906), pp. 129–175. DOI: 10.1007/BF03013466 (cit. on p. 48).

[58] A. I. Larkin and Y. N. Ovchinnikov. "Quantum tunneling with dissipation". In: *Pis'ma Zh. Eksp. Teor. Fiz.* 37.7 (1983), p. 322 (cit. on pp. 50, 62–63, 137).

[59] J. Zinn-Justin. *Path Integrals in Quantum Mechanics*. Oxford University Press, 2005, p. 317 (cit. on p. 53).

[60] E. M. Chudnovsky, A. Ferrera, and A. Vilenkin. "Quantum depinning of flux lines from columnar defects". In: *Physical Review B* 51.2 (1995), pp. 1181–1184. DOI: 10.1103/PhysRevB.51.1181 (cit. on p. 55).

[61] E. M. Chudnovsky and L. Gunther. "Quantum theory of nucleation in ferromagnets". In: *Physical Review B* 37.16 (1988), pp. 9455–9459. DOI: 10.1103/PhysRevB.37.9455 (cit. on p. 55).

[62] A. Ferrera and E. M. Chudnovsky. "Quantum nucleation of magnetic bubbles". In: *Physical Review B* 53.1 (1996), pp. 354–358. DOI: 10.1103/PhysRevB.53.354 (cit. on p. 55).

[63] E. M. Lifshitz and L. P. Pitaevskii. *Statistical Physics: Theory of the Condensed State (Course of Theoretical Physics Vol. 9)*. Oxford, England: Butterworth-Heinemann, 1980, p. 387 (cit. on p. 56).

[64] L.-D. Chang and S. Chakravarty. “Quantum decay in a dissipative system”. In: *Physical Review B* 29.1 (1984), pp. 130–137. DOI: `10.1103/PhysRevB.29.130` (cit. on pp. 60, 133).

[65] D. Waxman and A. J. Leggett. “Dissipative quantum tunneling at finite temperatures”. In: *Physical Review B* 32.7 (1985), pp. 4450–4468. DOI: `10.1103/PhysRevB.32.4450` (cit. on pp. 61, 133).

[66] E. M. Chudnovsky. “Phase transitions in the problem of the decay of a metastable state”. In: *Physical Review A* 46.12 (1992), pp. 8011–8014. DOI: `10.1103/PhysRevA.46.8011` (cit. on pp. 62–63, 137).

[67] S. S. P. Parkin, M. Hayashi, and L. Thomas. “Magnetic domain-wall racetrack memory.” In: *Science (New York, N.Y.)* 320.5873 (2008), pp. 190–194. DOI: `10.1126/science.1145799` (cit. on p. 68).

[68] S. Y. Chou. “Patterned magnetic nanostructures and quantized magnetic disks”. In: *Proceedings of the IEEE* 85.4 (1997), pp. 652–671. DOI: `10.1109/5.573754` (cit. on p. 68).

[69] R. P. Cowburn, D. K. Koltsov, A. O. Adeyeye, and M. E. Welland. “Sensing magnetic fields using superparamagnetic nanomagnets”. In: *Journal of Applied Physics* 87.9 (2000), p. 7082. DOI: `10.1063/1.372938` (cit. on p. 68).

[70] E. A. Rozhkova, V. Novosad, D.-H. Kim, J. Pearson, R. Divan, T. Rajh, and S. D. Bader. “Ferromagnetic microdisks as carriers for biomedical applications”. In: *Journal of Applied Physics* 105.7 (2009), 07B306. DOI: `10.1063/1.3061685` (cit. on p. 68).

[71] D.-H. Kim, E. A. Rozhkova, I. V. Ulasov, S. D. Bader, T. Rajh, M. S. Lesniak, and V. Novosad. “Biofunctionalized magnetic-vortex microdiscs for targeted cancer-cell destruction.” In: *Nature Materials* 9.2 (2010), pp. 165–171. DOI: `10.1038/nmat2591` (cit. on p. 68).

[72] J. K. Ha, R. Hertel, and J. Kirschner. “Micromagnetic study of magnetic configurations in submicron permalloy disks”. In: *Physical Review B* 67.22 (2003), p. 224432. DOI: `10.1103/PhysRevB.67.224432` (cit. on pp. 68–70).

[73] R. P. Cowburn, D. K. Koltsov, A. O. Adeyeye, and M. E. Welland. “Single-Domain Circular Nanomagnets”. In: *Physical Review Letters* 83.5 (1999), pp. 1042–1045. DOI: `10.1103/PhysRevLett.83.1042` (cit. on p. 71).

[74] T. Shinjo, T. Okuno, R. Hassdorf, K. Shigeto, and T. Ono. “Magnetic Vortex Core Observation in Circular Dots of Permalloy”. In: *Science* 289.5481 (2000), pp. 930–932. DOI: `10.1126/science.289.5481.930` (cit. on p. 73).

[75] M. Schneider, H. Hoffmann, and J. Zweck. “Lorentz microscopy of circular ferromagnetic permalloy nanodisks”. In: *Applied Physics Letters* 77.18 (2000), p. 2909. DOI: `10.1063/1.1320465` (cit. on p. 73).

[76] T. Okuno, K. Shigeto, T. Ono, K. Mibu, and T. Shinjo. “MFM study of magnetic vortex cores in circular permalloy dots: behavior in external field”. In: *Journal of Magnetism and Magnetic Materials* 240.1-3 (2002), pp. 1–6. DOI: `10.1016/S0304-8853(01)00708-9` (cit. on p. 73).

[77] M. Grimsditch, P. Vavassori, V. Novosad, V. Metlushko, H. Shima, Y. Otani, and K. Fukamichi. “Vortex chirality in an array of ferromagnetic dots”. In: *Physical Review B* 65.17 (2002), p. 172419. DOI: `10.1103/PhysRevB.65.172419` (cit. on p. 74).

[78] V. Novosad et al. “Effect of interdot magnetostatic interaction on magnetization reversal in circular dot arrays”. In: *Physical Review B* 65.6 (2002), p. 060402. DOI: `10.1103/PhysRevB.65.060402` (cit. on p. 74).

[79] A. A. Belavin and A. M. Polyakov. “Metastable states of two-dimensional isotropic ferromagnets”. In: *JETP Letters* 22.10 (1975), pp. 503–506 (cit. on p. 76).

[80] D. J. Gross. “Meron configurations in the two-dimensional O(3) σ-model”. In: *Nuclear Physics B* 132.5 (1978), pp. 439–456. DOI: `10.1016/0550-3213(78)90470-4` (cit. on p. 76).

[81] N. A. Usov and S. E. Peschany. “Magnetization curling in a fine cylindrical particle”. In: *Journal of Magnetism and Magnetic Materials* 118.3 (1993), pp. L290–L294. DOI: `10.1016/0304-8853(93)90428-5` (cit. on pp. 77, 81).

[82] N. A. Usov and S. E. Peschany. “Magnetization curling in a thin ferromagnetic cylinder”. In: *Fiz. Met. Metal* 12 (1994), pp. 13–24 (cit. on pp. 77, 81).

[83] K. Y. Guslienko, V. Novosad, Y. Otani, H. Shima, and K. Fukamichi. “Field evolution of magnetic vortex state in ferromagnetic disks”. In: *Applied Physics Letters* 78.24 (2001), p. 3848. DOI: `10.1063/1.1377850` (cit. on pp. 77, 80).

[84] K. Y. Guslienko, V. Novosad, Y. Otani, H. Shima, and K. Fukamichi. “Magnetization reversal due to vortex nucleation, displacement, and annihilation

in submicron ferromagnetic dot arrays". In: *Physical Review B* 65.2 (2001), p. 024414. DOI: 10.1103/PhysRevB.65.024414 (cit. on pp. 77, 79).

[85] K. Y. Guslienko and K. L. Metlov. "Evolution and stability of a magnetic vortex in a small cylindrical ferromagnetic particle under applied field". In: *Physical Review B* 63.10 (2001), p. 100403. DOI: 10.1103/PhysRevB.63.100403 (cit. on pp. 77, 79–80).

[86] A. Aharoni. "Upper bound to a single-domain behavior of a ferromagnetic cylinder". In: *Journal of Applied Physics* 68.6 (1990), p. 2892. DOI: 10.1063/1.346422 (cit. on p. 81).

[87] M. E. Gouva, G. M. Wysin, A. R. Bishop, and F. G. Mertens. "Vortices in the classical two-dimensional anisotropic Heisenberg model". In: *Physical Review B* 39.16 (1989), pp. 11840–11849. DOI: 10.1103/PhysRevB.39.11840 (cit. on pp. 81, 96).

[88] J. P. Park, P. Eames, D. M. Engebretson, J. Berezovsky, and P. A. Crowell. "Imaging of spin dynamics in closure domain and vortex structures". In: *Physical Review B* 67.2 (2003), p. 020403. DOI: 10.1103/PhysRevB.67.020403 (cit. on p. 82).

[89] S.-B. Choe, Y. Acremann, A. Scholl, A. Bauer, A. Doran, J. Stöhr, and H. A. Padmore. "Vortex core-driven magnetization dynamics." In: *Science (New York, N.Y.)* 304.5669 (2004), pp. 420–422. DOI: 10.1126/science.1095068 (cit. on pp. 82, 85).

[90] V. Novosad, F. Y. Fradin, P. E. Roy, K. S. Buchanan, K. Y. Guslienko, and S. D. Bader. "Magnetic vortex resonance in patterned ferromagnetic dots". In: *Physical Review B* 72.2 (2005), p. 024455. DOI: 10.1103/PhysRevB.72.024455 (cit. on p. 82).

[91] B. Van Waeyenberge et al. "Magnetic vortex core reversal by excitation with short bursts of an alternating field." In: *Nature* 444.7118 (2006), pp. 461–4. DOI: 10.1038/nature05240 (cit. on p. 83).

[92] G. de Loubens et al. "Bistability of Vortex Core Dynamics in a Single Perpendicularly Magnetized Nanodisk". In: *Physical Review Letters* 102.17 (2009), p. 177602. DOI: 10.1103/PhysRevLett.102.177602 (cit. on p. 83).

[93] E. M. Chudnovsky and J. Tejada. *Lectures on Magnetism.* Princeton, NJ: Rinton Press, 2006 (cit. on pp. 84, 96, 109, 113).

[94] A. A. Thiele. “Steady-State Motion of Magnetic Domains”. In: *Physical Review Letters* 30.6 (1973), pp. 230–233. DOI: 10.1103/PhysRevLett.30.230 (cit. on pp. 84, 101).

[95] D. L. Huber. “Dynamics of spin vortices in two-dimensional planar magnets”. In: *Physical Review B* 26.7 (1982), pp. 3758–3765. DOI: 10.1103/PhysRevB.26.3758 (cit. on pp. 84, 101).

[96] K. Y. Guslienko. “Low-frequency vortex dynamic susceptibility and relaxation in mesoscopic ferromagnetic dots”. In: *Applied Physics Letters* 89.2 (2006), p. 022510. DOI: 10.1063/1.2221904 (cit. on pp. 84, 112, 137).

[97] K. Y. Guslienko, B. A. Ivanov, V. Novosad, Y. Otani, H. Shima, and K. Fukamichi. “Eigenfrequencies of vortex state excitations in magnetic submicron-size disks”. In: *Journal of Applied Physics* 91.10 (2002), p. 8037. DOI: 10.1063/1.1450816 (cit. on pp. 85–86).

[98] K. Y. Guslienko, X. F. Han, D. J. Keavney, R. Divan, and S. D. Bader. “Magnetic Vortex Core Dynamics in Cylindrical Ferromagnetic Dots”. In: *Physical Review Letters* 96.6 (2006), p. 067205. DOI: 10.1103/PhysRevLett.96.067205 (cit. on pp. 85–86).

[99] V. Novosad, M. Grimsditch, K. Y. Guslienko, P. Vavassori, Y. Otani, and S. D. Bader. “Spin excitations of magnetic vortices in ferromagnetic nanodots”. In: *Physical Review B* 66.5 (2002), p. 052407. DOI: 10.1103/PhysRevB.66.052407 (cit. on pp. 85, 88).

[100] L. Giovannini, F. Montoncello, F. Nizzoli, G. Gubbiotti, G. Carlotti, T. Okuno, T. Shinjo, and M. Grimsditch. “Spin excitations of nanometric cylindrical dots in vortex and saturated magnetic states”. In: *Physical Review B* 70.17 (2004), p. 172404. DOI: 10.1103/PhysRevB.70.172404 (cit. on p. 86).

[101] C. E. Zaspel, B. A. Ivanov, J. P. Park, and P. A. Crowell. “Excitations in vortex-state permalloy dots”. In: *Physical Review B* 72.2 (2005), p. 024427. DOI: 10.1103/PhysRevB.72.024427 (cit. on pp. 86–88, 116).

[102] B. A. Ivanov and C. E. Zaspel. “High Frequency Modes in Vortex-State Nanomagnets”. In: *Physical Review Letters* 94.2 (2005), p. 027205. DOI: 10.1103/PhysRevLett.94.027205 (cit. on pp. 87–88).

[103] X. Zhu, Z. Liu, V. Metlushko, P. Grütter, and M. Freeman. “Broadband spin dynamics of the magnetic vortex state: Effect of the pulsed field direction”. In: *Physical Review B* 71.18 (2005), p. 180408. DOI: 10.1103/PhysRevB.71.180408 (cit. on p. 87).

[104] J. P. Park and P. A. Crowell. “Interactions of Spin Waves with a Magnetic Vortex”. In: *Physical Review Letters* 95.16 (2005), p. 167201. DOI: `10.1103/PhysRevLett.95.167201` (cit. on p. 87).

[105] F. Hoffmann, G. Woltersdorf, K. Perzlmaier, A. N. Slavin, V. S. Tiberkevich, A. Bischof, D. Weiss, and C. H. Back. “Mode degeneracy due to vortex core removal in magnetic disks”. In: *Physical Review B* 76.1 (2007), p. 014416. DOI: `10.1103/PhysRevB.76.014416` (cit. on pp. 87, 89).

[106] C. E. Zaspel, E. S. Wright, A. Y. Galkin, and B. A. Ivanov. “Frequencies of radially symmetric excitations in vortex state disks”. In: *Physical Review B* 80.9 (2009), p. 094415. DOI: `10.1103/PhysRevB.80.094415` (cit. on pp. 89, 116).

[107] K. Y. Guslienko, G. R. Aranda, and J. M. Gonzalez. “Topological gauge field in nanomagnets: Spin-wave excitations over a slowly moving magnetization background”. In: *Physical Review B* 81.1 (2010), p. 014414. DOI: `10.1103/PhysRevB.81.014414` (cit. on pp. 90, 116).

[108] G. Mihajlović, M. S. Patrick, J. E. Pearson, V. Novosad, S. D. Bader, M. Field, G. J. Sullivan, and A. Hoffmann. “Temperature dependent nucleation and annihilation of individual magnetic vortices”. In: *Applied Physics Letters* 96.11 (2010), p. 112501. DOI: `10.1063/1.3360841` (cit. on p. 91).

[109] J. A. J. Burgess, D. C. Fortin, J. E. Losby, D. Grombacher, J. P. Davis, and M. R. Freeman. “Thermally activated decay of magnetic vortices”. In: *Physical Review B* 82.14 (2010), p. 144403. DOI: `10.1103/PhysRevB.82.144403` (cit. on pp. 91, 119).

[110] G. N. Kakazei et al. “Slow magnetization dynamics and energy barriers near vortex state nucleation in circular permalloy dots”. In: *Applied Physics Letters* 99.5 (2011), p. 052512. DOI: `10.1063/1.3619846` (cit. on p. 92).

[111] H. Shima, V. Novosad, Y. Otani, K. Fukamichi, N. Kikuchi, O. Kitakamai, and Y. Shimada. “Pinning of magnetic vortices in microfabricated permalloy dot arrays”. In: *Journal of Applied Physics* 92.3 (2002), p. 1473. DOI: `10.1063/1.1485110` (cit. on p. 92).

[112] R. L. Compton and P. A. Crowell. “Dynamics of a Pinned Magnetic Vortex”. In: *Physical Review Letters* 97.13 (2006), p. 137202. DOI: `10.1103/PhysRevLett.97.137202` (cit. on pp. 93–95).

[113] R. L. Compton, T. Y. Chen, and P. A. Crowell. “Magnetic vortex dynamics in the presence of pinning”. In: *Physical Review B* 81.14 (2010), p. 144412. DOI: `10.1103/PhysRevB.81.144412` (cit. on pp. 93, 95).

[114] J. A. J. Burgess, A. E. Fraser, F. F. Sani, D. Vick, B. D. Hauer, J. P. Davis, and M. R. Freeman. "Quantitative magneto-mechanical detection and control of the Barkhausen effect." In: *Science (New York, N.Y.)* 339.6123 (2013), pp. 1051–4. DOI: 10.1126/science.1231390 (cit. on p. 93).

[115] E. B. Sonin. "Vortex oscillations and hydrodynamics of rotating superfluids". In: *Reviews of Modern Physics* 59.1 (1987), pp. 87–155. DOI: 10.1103/RevModPhys.59.87 (cit. on p. 95).

[116] A. T. Dorsey. "Vortex motion and the Hall effect in type-II superconductors: A time-dependent Ginzburg-Landau theory approach". In: *Physical Review B* 46.13 (1992), pp. 8376–8392. DOI: 10.1103/PhysRevB.46.8376 (cit. on p. 96).

[117] D. Bedau, M. Kläui, S. Krzyk, U. Rüdiger, G. Faini, and L. Vila. "Detection of Current-Induced Resonance of Geometrically Confined Domain Walls". In: *Physical Review Letters* 99.14 (2007), p. 146601. DOI: 10.1103/PhysRevLett.99.146601 (cit. on pp. 96, 116).

[118] G. M. Wysin. "Magnetic vortex mass in two-dimensional easy-plane magnets". In: *Physical Review B* 54.21 (1996), pp. 15156–15162. DOI: 10.1103/PhysRevB.54.15156 (cit. on p. 96).

[119] B. A. Ivanov and G. M. Wysin. "Magnon modes for a circular two-dimensional easy-plane ferromagnet in the cone state". In: *Physical Review B* 65.13 (2002), p. 134434. DOI: 10.1103/PhysRevB.65.134434 (cit. on p. 96).

[120] J. Zak. "Magnetic Translation Group". In: *Physical Review* 134.6A (1964), A1602–A1606. DOI: 10.1103/PhysRev.134.A1602 (cit. on p. 106).

[121] J. Ding, G. N. Kakazei, X. Liu, K. Y. Guslienko, and A. O. Adeyeye. "Higher order vortex gyrotropic modes in circular ferromagnetic nanodots." In: *Scientific reports* 4 (2014), p. 4796. DOI: 10.1038/srep04796 (cit. on p. 116).

[122] J. Ding, G. N. Kakazei, X. M. Liu, K. Y. Guslienko, and A. O. Adeyeye. "Intensity inversion of vortex gyrotropic modes in thick ferromagnetic nanodots". In: *Applied Physics Letters* 104.19 (2014), p. 192405. DOI: 10.1063/1.4878617 (cit. on p. 116).

[123] J. Tejada and X. Zhang. "Experiments in quantum magnetic relaxation". In: *Journal of Magnetism and Magnetic Materials* 140-144 (1995), pp. 1815–1818. DOI: 10.1016/0304-8853(94)00497-8 (cit. on p. 117).

[124] R. Sappey, E. Vincent, M. Ocio, and J. Hammann. "Disentangling distribution effects and nature of the dynamics in relaxation measurements: the

RMR method". In: *Journal of Magnetism and Magnetic Materials* 221.1-2 (2000), pp. 87–98. DOI: 10.1016/S0304-8853(00)00378-4 (cit. on p. 117).

[125] D. D. Awschalom, J. F. Smyth, G. Grinstein, D. P. DiVincenzo, and D. Loss. "Macroscopic quantum tunneling in magnetic proteins". In: *Physical Review Letters* 68.20 (1992), pp. 3092–3095. DOI: 10.1103/PhysRevLett.68.3092 (cit. on p. 117).

[126] E. Vincent, J. Hammann, P. Prené, and E. Tronc. "Low temperature dynamics of small γ-Fe_2O_3 particles". In: *Journal de Physique I* 4.2 (1994), pp. 273–282. DOI: 10.1051/jp1:1994137 (cit. on pp. 117, 127).

[127] J. R. Friedman, M. P. Sarachik, J. Tejada, and R. Ziolo. "Macroscopic Measurement of Resonant Magnetization Tunneling in High-Spin Molecules". In: *Phys. Rev. Lett.* 76.20 (1996), pp. 3830–3833. DOI: 10.1103/PhysRevLett.76.3830 (cit. on p. 117).

[128] J. M. Hernandez, X. X. Zhang, F. Luis, J. Tejada, J. R. Friedman, M. P. Sarachik, and R. Ziolo. "Evidence for resonant tunneling of magnetization in Mn_{12} acetate complex". In: *Physical Review B* 55.9 (1997), pp. 5858–5865. DOI: 10.1103/PhysRevB.55.5858 (cit. on p. 117).

[129] A. Hamzic, L. Fruchter, and I. A. Campbell. "Non-activated magnetic relaxation in a high-Tc superconductor". In: *Nature* 345.6275 (1990), pp. 515–516. DOI: 10.1038/345515a0 (cit. on p. 117).

[130] M. A. Skvortsov. "Quantum and thermal depinning of a string from a linear defect". In: *Physical Review B* 55.1 (1997), pp. 515–521. DOI: 10.1103/PhysRevB.55.515 (cit. on p. 129).

[131] D. Bedau, M. Kläui, M. T. Hua, S. Krzyk, U. Rüdiger, G. Faini, and L. Vila. "Quantitative Determination of the Nonlinear Pinning Potential for a Magnetic Domain Wall". In: *Physical Review Letters* 101.25 (2008), p. 256602. DOI: 10.1103/PhysRevLett.101.256602 (cit. on p. 131).

[132] H. Meissner. "Superconductivity of Contacts with Interposed Barriers". In: *Physical Review* 117.3 (1960), pp. 672–680. DOI: 10.1103/PhysRev.117.672 (cit. on p. 141).

[133] J. Nicol, S. Shapiro, and P. Smith. "Direct Measurement of the Superconducting Energy Gap". In: *Physical Review Letters* 5.10 (1960), pp. 461–464. DOI: 10.1103/PhysRevLett.5.461 (cit. on p. 141).

[134] I. Giaever. “Electron Tunneling Between Two Superconductors”. In: *Physical Review Letters* 5.10 (1960), pp. 464–466. DOI: `10.1103/PhysRevLett.5.464` (cit. on pp. 141–142).

[135] M. Cohen, L. Falicov, and J. Phillips. “Superconductive Tunneling”. In: *Physical Review Letters* 8.8 (1962), pp. 316–318. DOI: `10.1103/PhysRevLett.8.316` (cit. on p. 141).

[136] B. Josephson. “Possible new effects in superconductive tunnelling”. In: *Physics Letters* 1.7 (1962), pp. 251–253. DOI: `10.1016/0031-9163(62)91369-0` (cit. on p. 142).

[137] P. Anderson and J. Rowell. “Probable Observation of the Josephson Superconducting Tunneling Effect”. In: *Physical Review Letters* 10.6 (1963), pp. 230–232. DOI: `10.1103/PhysRevLett.10.230` (cit. on p. 142).

[138] J. Rowell. “Magnetic Field Dependence of the Josephson Tunnel Current”. In: *Physical Review Letters* 11.5 (1963), pp. 200–202. DOI: `10.1103/PhysRevLett.11.200` (cit. on p. 142).

[139] J. Clarke. “A superconducting galvanometer employing Josephson tunnelling”. In: *Philosophical Magazine* 13.121 (1966), pp. 115–127. DOI: `10.1080/14786436608211991` (cit. on p. 142).

[140] A. Buzdin. “Proximity effects in superconductor-ferromagnet heterostructures”. In: *Reviews of Modern Physics* 77.3 (2005), pp. 935–976. DOI: `10.1103/RevModPhys.77.935` (cit. on p. 144).

[141] M. Chaichian and A. Demichev. *Path Integrals in Physics Volume I: Stochastic Processes and Quantum Mechanics*. London, England: Taylor & Francis, 2001, p. 336 (cit. on p. 167).

[142] R. P. Feynman, A. R. Hibbs, and D. F. Styer. *Quantum Mechanics and Path Integrals: Emended Edition*. New York: Dover Publications, 2010, p. 384 (cit. on p. 167).